A Theoretical And Experimental Investigation Of Two-phase Bubbly Turbulent Flow In A Curved Duct.

INFORMATION TO USERS

This manuscript has been reproduced from the microfilm master. UMI films the text directly from the original or copy submitted. Thus, some thesis and dissertation copies are in typewriter face, while others may be from any type of computer printer.

The quality of this reproduction is dependent upon the quality of the copy submitted. Broken or indistinct print, colored or poor quality illustrations and photographs, print bleedthrough, substandard margins, and improper alignment can adversely affect reproduction.

In the unlikely event that the author did not send UMI a complete manuscript and there are missing pages, these will be noted. Also, if unauthorized copyright material had to be removed, a note will indicate the deletion.

Oversize materials (e.g., maps, drawings, charts) are reproduced by sectioning the original, beginning at the upper left-hand corner and continuing from left to right in equal sections with small overlaps. Each original is also photographed in one exposure and is included in reduced form at the back of the book.

Photographs included in the original manuscript have been reproduced xerographically in this copy. Higher quality 6" x 9" black and white photographic prints are available for any photographs or illustrations appearing in this copy for an additional charge. Contact UMI directly to order.

UMI

A Bell & Howell Information Company
300 North Zeeb Road, Ann Arbor MI 48106-1346 USA
313/761-4700 800/521-0600

A THEORETICAL AND EXPERIMENTAL INVESTIGATION OF TWO-PHASE BUBBLY TURBULENT FLOW IN A CURVED DUCT

by

Edward Graf

Presented to the Graduate and Research Committee

of Lehigh University

in Candidacy for the Degree of

Doctor of Philosophy

in

Mechanical Engineering and Mechanics

Lehigh University

1996

Approved and recommended for acceptance as a dissertation in partial fulfillment of the requirements for the degree of Doctor of Philosophy.

Sept 24, 1996
Date

Dissertation Director
Professor Sudhakar Neti

Sept. 24, 1996
Accepted Date

Committee Members:

Professor Sudhakar Neti
Committee Chairman
M.E. Dept.

Professor Hugo Caram
Chem.E. Dept

Professor John C. Chen
Chem. E. Dept.

Professor Stanley H. Johnson
M.E. Dept.

Professor Antonios Liakopoulos
M.E. Dept.

ACKNOWLEDGMENTS

I would like to thank Professor S. Neti, my thesis advisor, for his continued advice, assistance and general support during the course of this work. His experience and technical intuition were invaluable to me during the last few years.

Professors H. Caram, J. Chen, S. Johnson and A. Liakopoulos, the members of my doctoral committee, were always available with helpful suggestions--through General Exams and progress reports, etc.-- during the entire extent of my stay at Lehigh.

It is difficult to fully put into words my thanks for my wife, Rosemary, who persevered along with me through these long years. Thanks for putting up with my absences.

I would like to remind my children, Suzanne, Ed and Andrew, that learning is a lifetime activity and hope that they get as much satisfaction from their academic work as this work has brought me.

My earliest remembrances of my parents, Carl and Anna, include their constant encouragement of learning and education. I just wish Dad were alive today to share in this accomplishment because without Mom and Dad I would never have cultivated my present interest in learning.

I would like to thank Dr. Paul Cooper at Ingersoll-Dresser Pumps for his constant encouragement over these long years and moral support.

Finally, I would like to thank the management at Ingersoll-Dresser Pumps for their sponsorship of this work. Especially noteworthy over the years has been the support from Mr. Walter Schmidt, who encouraged me during the early years of this undertaking, and Mr. Bill Ord.

Table of Contents

Figures

ABSTRACT

A three-dimensional Eulerian/Eulerian multi-phase computational algorithm has been developed and applied to predict various two-phase flow problems. These include both laminar and turbulent flows. The benefit of this approach as contrasted with the Eulerian/Lagrangian approach is that high void fraction flows can be computed economically. Two and three-dimensional single and two-phase problems have been extensively computed and include favorable comparisons with existing experimentally derived data whose analytical predictions have not been previously reported in the literature. The two-phase flow computations were validated by measurements in a two-phase test loop in the laboratory. The predicted results for 5 mm bubbles in a 25.4 mm square cross section duct (d_{bub}/D_H = 0.20) were compared to measurements and flow visualizations made in the test loop which comprises a vertical section followed by a 90° bend followed by a horizontal section. Void fractions were predicted to peak along the end walls at levels reported in the literature for bubbly up-flow. As the flow moves through the bend the bubbles quickly concentrate towards the inner wall. Finally the bubbles move towards the outside or top wall as the flow enters the horizontal section. The present numerical algorithm also correctly computes the expected trends of very small bubble diameter. When bubbles of 1 mm diameter (d_{bub}/D_H = 0.04) were simulated they were not predicted to segregate along the inner bend or at the top of the horizontal duct but rather follow the flow much better. The code is robust and predicted local void fraction of close to zero in some places and close to unity in others.

This dissertation discusses some of the turbulence models employed here: an assumption that the turbulent viscosity of the dispersed phase equals that of the continuous phase; a two-

phase modified k -ε model used for both phases and another model with a variable turbulent Prandtl number (i.e., ratio of the turbulent viscosity of the distributed phase to that of the continuous phase) based on Tchen's theory (1947) of a particle in a turbulent stream.

1. INTRODUCTION

Flows that involve one or more media that include more than one thermodynamic phase are called two-phase flows. Two-phase flows occur in numerous industrial settings, including: turbomachinery, nuclear reactors, refinery and pipeline equipment. Sometimes the flows are anticipated to be two-phase and at other times local superheating of the fluid causes vapor formation and thus an unexpected two-phase flow is generated. The formation of vapor negatively affects the critical heat flux in nuclear reactors. There has been extensive investigation into the heat transfer aspect of nuclear reactor loss-of-coolant accidents, LOCA, [J.C. Chen, (1982)]. The vapor generation rate models for post critical heat flux developed there could be included in the present framework to refine the LOCA simulations. The presence of vapor or a gas degrades the performance of pump components, including impeller cavitation damage, bearing and seal cavity overheating caused by a decrease in the heat transfer rate, etc.

Two phase flows are normally classified into the following flow regimes: bubbly, slug, annular and mist flows. These four classes can be further subdivided. Of these four regimes, bubbly flow occurs with the lowest gas/liquid volume ratio. Such flow regimes, and flow maps, are discussed further in a later section under *Literature Review.*

Two-phase flows that occur in the presence of strong pressure gradients, such as those induced by strong curvature as found in pipe elbows, labyrinth seal passages or pump impellers or body forces such as gravity, tend to segregate and become non-homogeneous. The majority of the existing two-phase flow experimental data is for homogeneous flows and thus is of little help in understanding these more complex flows. Numerical models which utilize an Eulerian description of the continuous phase and a Lagrangian "tracking" model of the dispersed phase are inefficient

when the flow field has regions where the local volume fraction of the dispersed phase is high. The present work utilizes a two-fluid model (i.e., an Eulerian/Eulerian description) in which a complete set of continuity and momentum equations are solved for each phase. Interaction terms that are present in these equations couple the exchange of mass and momentum between the phases. An algorithm to compute volume fractions has been developed based on the work of Carver (1982 & 1984) and has been shown to be stable even as the volume fraction approaches the limits of zero or unity. The two-fluid model applied herein requires the solution of as many as six coupled partial differential equations for each phase. The present three-dimensional algorithm has been used successfully with very low void fractions and up to an inlet void fraction of 0.3. The upper void fraction limit is set to 0.3 because this is an accepted limit on void fraction above which the flow regime transitions to slug or churn flow [Mishima and Ishii, (1984)]. At very high void fractions the bubbles may begin to coalesce into slugs and might require modification of constitutive equations to model this flow regime.

Previous two-fluid algorithms reported in the literature have used either algebraic turbulence models or employed higher level turbulence models only for the continuous phase. Often the dispersed phase turbulent eddy viscosity was assumed equal to some constant times the continuous phase diffusivity (i.e., a particle Prandtl number). Another approach for computing the turbulent eddy viscosity of the distributed phase, as used by Mostafa, et. al. (1987), is to relate it to the continuous phase turbulent viscosity by means of an algebraic equation based on the work of Tchen (1947) and Peskin (1959) for a particle in a turbulent flow field. Turbulent flows have been computed utilizing both a constant particle Prandtl number and also by applying a two-phase modified two-equation k-ε model to the distributed phase as well as the continuous phase.

The intent of this dissertation is to develop and validate a three-dimensional numerical algorithm capable of predicting complex two-phase flows. This development methodology started by considering various laminar and turbulent two and three-dimensional single phase flow problems and validating the governing equations and associated numerical procedures with single phase data available in the literature. Some of the single phase computations are compared to empirically derived data in the literature which has not previously been computed. This is especially true of the laminar and turbulent curved duct pressure loss data correlated for the square and rectangular cross sectional ducts.

The qualitative and quantitative predictions of the present numerical algorithm for two-phase flow in a square cross section composite duct consisting of an inlet vertical section followed by a 90^{o} bend and exhausting through a straight horizontal section were compared to data taken in the laboratory. The comparison between predictions and data will be discussed in a later section (see *Results*). There are three related geometries that consist of straight/curved/straight sections in series. These are: 1) the first straight section horizontal and the last straight section vertical down flow; 2) the first straight section vertical down flow and the last straight section horizontal; 3) the first straight section horizontal and the last straight section vertical up flow. While in single phase flow there would be no difference among these configurations, such is not the case for two-phase flow: all of these additional three geometries will result in different bubble trajectories. For instance, when the first straight section is horizontal (rather than vertical) the bubbles will be segregated by gravity before reaching the 90^{o} bend rather than symmetrically distributed. All four of the geometries are unique in two-phase flow. While obtaining experimental data would mean constructing four different test loops these geometries can be immediately predicted numerically with the present algorithm. However,

because the test loop was of one fixed geometry these additional geometries have not been computed in the present work. It will be interesting to compute the additional geometries as additional experimental data becomes available to support the predictions.

Just as the associated straight/curved/straight duct geometries can be rather straightforwardly computed so too can cross sections other than square. Single-phase rectangular cross section curved ducts were computed since single-phase loss data was available for these ducts. The agreement between the present numerical predictions and the empirical data for single phase losses in a curved duct of rectangular cross section was very good. Once experimental data for two-phase flows in rectangular cross section ducts is available the associated numerical predictions can be verified.

The above two examples indicate that an accurate and robust two-fluid algorithm is a powerful tool and offers the promise of minimizing experimental investigations to establish loss correlations for different geometries.

2. LITERATURE REVIEW

Literature pertaining to the various single and two-phase phenomena studied in this work are presented here. This includes laminar and turbulent single and two-phase flows in a driven cavity, in straight and curved ducts of non-circular cross section.

2.1 Single Phase

2.1.1 Introduction

The development of the two fluid model consisted of building upwards from a foundation built from numerous single phase computations of increasing complexity. This early development phase started with single phase laminar straight duct flow and then progressed to single phase turbulent straight duct flow. Next the single phase laminar curved duct flow capability was added. This required the derivation of the momentum equations in toroidal equations, followed by the correct discretization and coding and program development. Laminar flow, curved duct validation cases based on data and computations in the literature were run. The next stage of the development cycle required the derivation of the turbulent transport equations for single phase in toroidal coordinates. The details are given in Appendices VI and VII. These two equations were appropriately discretized and coded. Turbulent flow curved, duct validation cases were run.

Most of the single phase calculations performed were compared to computations existing in the literature. However, some of the computations performed were compared to experimental data in the literature; and to the author's knowledge, have not been previously computed

numerically. An example is the computation of the loss coefficient for turbulent flow in curved ducts with rectangular cross section.

2.1.2. Laminar Flows

Two-Dimensional Driven Cavity

The problem of the driven cavity was considered by Burggraf (1966) who was interested in this problem as a model for the study of the steady recirculating eddy that exists downstream of a bluff body at moderate Reynolds numbers. The steady state version of the problem consists of a cavity filled with fluid that is set in motion by the moving top wall. Batchelor (1956) has presented a theory for steady flows with finite viscosity. In two-dimensional closed flows the vorticity is uniform in a region where viscous forces are small. As the Reynolds number becomes larger the region of the fluid in which viscous forces are not negligible becomes smaller and smaller. The application of Batchelor's theory to the driven cavity problem might seem promising, especially if the rigid boundaries are viewed as singular surfaces away from which Batchelor's uniform vorticity solution should hold. However, this approach would by assumption neglect the singular surface that occurs off the solid boundaries that divides the flow into the region of the primary cell and a secondary eddy that occurs in the corner. Burggraf solved the Navier-Stokes equations in a square cavity by using the streamfunction-vorticity formulation of the governing equations and a relaxation numerical finite difference method. His results showed

that secondary vortices of opposite vorticity could be generated in the bottom corners of the cavity. The center of the primary vortex is located on the line of symmetry for infinitely small Reynolds numbers and moves laterally in the direction of movement of the top wall for Reynolds numbers up to 100. Above this limit, the vortex center begins to move slightly back towards the line of symmetry and also begins to move closer to the bottom wall as the secondary vortex gains in strength. The single phase version of the driven cavity problem was used as a test case of the two-dimensional limit of the present three-dimensional algorithm.

Three-Dimensional

Straight Duct

The study of steady internal flows in ducts is best divided into developing flows and fully developed flows. Flows which enter a duct with uniform axial velocity immediately experience a retarding force on the perimeter due to fluid shearing at the walls. The three dimensional boundary layer region begins to thicken on the walls as the fluid progresses down the duct. Beyond this viscous stress dominated region lies a potential core at the duct's center; however, the extent of this core diminishes with distance along the duct as the boundary layer grows. The velocity profile, pressure gradient and wall shear stress continue to change until the viscosity dominated wall regions merge. The distance required from the inlet to achieve the hydrodynamic condition where all of the flow variables are independent of distance in the longitudinal direction is called the hydrodynamic entry length. From this point on the flow is fully developed and a simplified two dimensional analysis of the flow is possible since all terms with gradients in the longitudinal direction can be neglected in the governing equations. The lateral velocities are equal to zero. The local friction coefficient, f_x, is now independent of distance in the longitudinal direction. The Fanning friction factor based on local shear is an important characteristic of a flow in a duct.

$$f_x = \frac{\tau}{\frac{\rho V^2}{2}} \qquad [2.1.2\text{-}1]$$

The Darcy friction factor based on pressure drop used in hydraulics is four times larger.

At the duct's inlet the local friction factor is large; it decreases asymptotically to the fully developed value of 14.227/Re for a square cross section duct (the classic value for a circular cross section duct is 16/Re). The local friction factor for fully developed flow in a rectangular cross section duct is greater than that in a square duct--with the limiting value for an infinite aspect ratio duct being 24.0/Re [Shah, (1978)]. The exact hydrodynamic development length varies with the duct's cross section [Sparrow, et. al., (1967) and McComas, (1967)]. The hydraulic entry length is approximately 0.075*D*Re when based on the local friction factor [(Kays, (1966)]. A friction factor can also be defined based on the wall shear stress integrated from inlet to the local longitudinal distance. This definition, which contains the history of the local shear stress, results in a friction factor which is higher than f_x . A third friction factor can be defined based on the pressure drop from the inlet to the local position. This results in the largest friction factor. This is because there is an additional pressure drop beyond that associated with the shear stress. This additional drop in the developing region is a result of the increase in momentum flux associated with the velocity profile change from uniform inlet velocity to a fully-developed profile with a peak centerline velocity. For fully developed flow the change in pressure is linearly proportional to axial:

$$\frac{p(0)-p(z)}{\frac{1}{2}\rho\overline{W}^2} = C\frac{z/D_H}{\mathrm{Re}} \qquad [2.1.2\text{-}2]$$

where the left hand side represents the nondimensional pressure drop over the distance z and C is the constant of proportionality, D_H is the hydraulic diameter of the section and Re is the Reynolds number based on D_H.

In the early entrance region, the pressure gradient is very large and decreases with length until it is constant at the end of the developing region. The high initial gradient is due to the large wall shear stresses and the rapid change in fluid momentum. In the developing region Sparrow et. al. (1967) show that the pressure drop is given by:

$$\frac{p(0)-p(z)}{\frac{1}{2}\rho\overline{W}^2} = C\frac{z/D_e}{\mathrm{Re}} + K(z) \qquad [2.1.2\text{-}3]$$

where K(z) is an incremental pressure drop attributable to the momentum change. It vanishes asymptotically as the fully developed condition is reached.

Curved Duct

Laminar flow in curved ducts is characterized by the Dean number for curvature effects and Reynolds number for inertial and viscous effects. Along with Reynolds number Dean number is a correlating parameter in asymptotic expansion of the momentum equations for curved pipes of small curvature (i.e., R/D >>1), see Dean (1928). Dean number, K_D, is defined as:

$K_D \equiv \frac{\mathrm{Re}}{\sqrt{\frac{\overline{R}}{D_H}}}$. Data pertaining to pipe flow (i.e., internal flow within a circular cross section) usually uses a Dean number based on pipe radius, a, in place of the hydraulic diameter, D_H. This Dean number will be indicated by K_a. (Note: $K_a = 0.707\ K_D$). However, data for duct flow (i.e., internal flow within a square cross section) does not always reference a Dean number

based on R/D_H; (sometimes $R/[0.5\ D_H]$ is used (e.g., Humphrey, et.al. 1977). In all these cases the Reynolds number is always based on D_H.

The Dean number is based on Dean's 1928 work, in which he solved the flow in curved pipes with mild curvature. The equations were solved using an asymptotic expansion in terms of a/R. Thus, Dean number can be rigorously shown to be a controlling parameter only for laminar duct flow with a/R<<1. In fact, White (1929) found that friction factor for turbulent flow in a curved duct was not correlated solely by the Dean number. For laminar flows, the friction factor in a curved section of pipe relative to that in a straight pipe is (Berger and Talbot, 1983) :

$$\frac{f}{f_s} = 0.0969\sqrt{K_a} + 0.556 \qquad [2.1.2\text{-}4]$$

The flow in curved ducts results in secondary flow patterns on lateral planes that centrifuge the fluid toward the outer radius at locations midway between the top and bottom walls. The static pressure is higher at the outer bend to balance the centrifugal force. Low momentum fluid in the boundary layers along the top and bottom walls is forced from the high pressure outer radii toward the low pressure region of the inner radius. This forms two pair of counter-rotating vortices. As the Dean number is increased, an additional pair of counter rotating vortices appear near the midline symmetry plane and close to the outer radius. Cheng et. al. (1976) solved the governing equations for fully developed flow in a curved duct by using a streamfunction-vorticity formulation for the lateral velocity components along with the axial momentum equation. Results are given for fully developed flow in rectangular cross section ducts of aspect ratios of 0.5, 1.0, 2.0 and 5.0. These results show that the critical Dean number is 202, above which the additional pair of vortices are predicted to occur. The maximum

longitudinal velocity is predicted to occur approximately three-quarter of the way towards the outer bend below the critical Dean number and somewhat closer to the center of the duct above the critical Dean number. The centerline velocity decreases with increasing Dean numbers: it is about 1.9 at a Dean number of 55 and approximately 1.45 for Dean numbers between 202 and 500.

Humphrey et. al. (1977) solved the curved duct problem with fully developed flow entering the curved section by including a long upstream tangent section. A 90° bend with R/D = 2.3 was analyzed at a Dean number of 368. Data is presented for the longitudinal velocity at various stations throughout the test section. Results there indicate that the location of maximum velocity occurs near the outer wall, approximately 85 percent away from the inner wall. Lateral velocities as high as 65 percent of the longitudinal velocity were computed. Small regions of separation were observed in the outer corners of the duct between 0° and 25° and in the upstream section. Because of this separation a fully elliptic numerical procedure had to be used for the numerical predictions.

Ghia et. al. (1976) present an analysis of developing laminar flow in curved ducts of rectangular cross section. A critical Dean number of 143 is predicted in this work. This is lower than the Cheng (1976) limit of 202. Ghia's paper indicted that Cheng's search was too coarse and missed the actual Dean number at which the extra pair of vortices first occurs. The angular distance required to achieve fully developed flow is less at the higher Dean number: 103° at a Dean number of 55 but only 60° at a Dean number of 210. However, the longitudinal distance, as measured by $\bar{R}\, d\theta$ is larger at the higher Dean number. The location of the maximum velocity and its level agree well with Cheng's work. The axial pressure drop from inlet to a downstream

station is given in a format similar to that for straight duct developing flow. The trends are very similar to what occur in straight duct flow--an initial developing region where the pressure gradient is high followed by a region for which the pressure gradient is constant--i.e., the fully developed region. The developing region has about the same pressure gradient for all Dean numbers. The pressure gradient in the developed section is proportional to Dean number. For very low Dean numbers the pressure gradient begins to approach the value for the straight duct. The friction factor for a curved duct at a Dean number of 55 is approximately 1.25 times that of the straight duct; and this ratio increases to 2.0 at a Dean number of 300. Numerical studies of laminar flow in a curved square duct with a mean radius of curvature four times the hydraulic diameter have been reported by Cheng et. al., (1987). A short straight section straight section (0.01 hydraulic diameters for the high Dean number case of 267 and 0.025 for a Dean number of 107) preceded the 90° and 180° bends. Slight separation is predicted to occur at 18° near the outer bend corners.

The works pertaining to laminar curved duct flow discussed above have distinctly different inlet boundary conditions: two fully developed, one developing and one somewhere in between. The inlet velocity profile is very important in determining the flow pattern in the curved section. A profile that is relatively uniform on entering the curved section will have only weak secondary flows since the secondary vorticity is proportional to deflection times the gradient of the lateral velocity normal to the duct side wall, see Squire and Winter (1951). The weaker secondary flows may be insufficient to avoid flow separation.

2.1.3 Turbulent Flows

Flows with duct Reynolds numbers beyond 2000 display instabilities and the well defined streamlines associated with laminar flow begin to become unstable and the flow develops fluctuations superimposed on the mean flow. For larger Reynolds numbers, the flow eventually transitions to turbulent flow. Turbulent flows are much more difficult to predict since the local velocity varies not only spatially but also temporally. Turbulent flows have been successfully modeled since the 1930's by thinking of the flow as consisting of a mean time averaged component together with turbulent fluctuations about that mean. The Navier-Stokes equations are re-written with all velocity and pressures consisting of a mean and time-varying component. The equations are time averaged and the resulting set is called the Reynolds Averaged Navier-Stokes equations. These equations include terms representing turbulent fluctuations of the various local velocities that can be thought of as additional stresses and are called the Reynolds stresses. They can be combined with the laminar molecular shear stresses to form a set of effective turbulent stress. Constitutive equations for these stresses need to be formed so as to close the equation set. The 'science' of forming these constitutive equations is called"turbulence modeling".

The prescription of the Reynolds stresses requires the description of a velocity and length scale (related to the size of the turbulent eddies). This can be done algebraically by using distance from the wall, etc. This formulation is the simplest and can be effective for simple boundary layer like flows. This approach is called a "zero order" equation. Partial differential equations can be written for the transport of one or more turbulent quantities. If only a single PDE is written which may be supplemented by algebraic equations, this would be called a one-

equation set. If two PDE's are used in the turbulence model, then the model is called a two-equation system.

The most often used two-equation set determines the eddy viscosity from the local values of the turbulence kinetic energy (k) and its dissipation rate (ε). These quantities are obtained by simultaneously solving two transport differential equations for k andε. A gradient type model is used to relate the turbulent fluxes to the mean flow field with the use of an isotropic eddy viscosity:

$$\rho \overline{u'_i u'_j} = -\mu_t S_{ij} + \frac{2}{3}\delta_{ij}\rho k \qquad [2.1.3\text{-}1]$$

$$\text{where: } S_{ij} = \frac{1}{2}\left(\frac{\partial U_i}{\partial x_j} + \frac{\partial U_j}{\partial x_i}\right) \text{ and } \mu_t = \rho C_\mu \frac{k^2}{\varepsilon} \qquad [2.1.3\text{-}2]$$

This model is a first order closure model. In complex flows where significant rate-of-strain components might be present due to streamline curvature or rotation or separation, etc. the above equations can be modified in an attempt to incorporate such effects. Since these modifications are done on an ad-hoc basis they often work only for a specific class of problems. A more sophisticated approach is to model each of the individual Reynolds stresses by solving a transport equation for each of them. This approach is called second-moment closure. The most accurate modeling uses a PDE to describe each of the six Reynolds stresses. This results in the addition of six more PDE. This is computationally taxing and introduces several additional unknowns to the equation set. An intermediate approach is to use algebraic equations for the transport of the Reynolds stresses. This is called an Algebraic Reynolds Stress Model (i.e., ARSM).

The prediction of turbulence driven secondary flows under fully developed condition in ducts requires a non-isotropic eddy viscosity formulation. The ARSM calculations used in this work [similar to that of Neti and Eichhorn (1978)] showed the expected corner vortices while an isotropic k-ε model calculation would not. Launder and Ying (1973) note that these secondary motions are due to gradients of the Reynolds stresses acting in the cross sectional plane of the duct. However, these stresses arise as a consequence of mean rates of strain in planes orthogonal to it. This fact is the reason that the scalar turbulent viscosity is insufficient for predicting these secondary velocities. A scalar turbulent viscosity implies that the principal axes of stress and strain are aligned and thus would not be suitable for such duct flows.

Launder and Ying formulate the Reynolds stresses in the lateral plane (i.e., x-y plane) as:

$$\overline{u^2} - \overline{v^2} = C\frac{k}{\varepsilon}\left[\overline{uw}\frac{\partial W}{\partial x} - \overline{vw}\frac{\partial W}{\partial y}\right] \qquad [2.3.1-3]$$

$$\overline{uv} = C\frac{k}{\varepsilon}\left[\overline{vw}\frac{\partial W}{\partial x} - \overline{uw}\frac{\partial W}{\partial y}\right] \qquad [2.3.1-4]$$

Naot et. al. (1974) propose a turbulence model which solves a transport equation for each of the six Reynolds stresses. To minimize the computational effort they prescribe the length

scale through an algebraic formulation in place of a transport equation for the dissipation of turbulence.

Most of the computations reported in the present work used a two-equation isotropic k-ε formulation. Curvature correction models were used to supplement the standard k-ε equation set for some of the curved duct calculations.

Three-Dimensional Turbulent Flows

Straight Ducts

As the flow approaches fully developed conditions, for laminar flow in ducts, lateral velocities vanish--they exist only for developing laminar duct flow. Lateral velocities are required for uniform axial velocity distributions to be changed to the parabolic distribution of fully developed laminar flow. Fluid moves from the perimeter of the duct to the center during the transition in the developing region. Once the laminar flow is fully developed there will be no lateral velocities. Nikuradse (1926) found that in contradistinction to the laminar flows, secondary flows do exist for fully developed turbulent flows in ducts of non-circular cross section. (Fully developed turbulent flow in circular cross section pipes do not have such secondary flows.) There are two counter rotating vortices in each corner. These serve to add momentum to the corner region (at the line of symmetry). The flow returns to the center near the wall midway between corners. Thus there is a momentum excess in the corners and momentum deficit along the wall midway between corners. Thus the flow streamlines do not simply move downstream in this flow but rather form helical patterns. The variation in turbulent axial velocity across the lateral plane of square and rectangular cross sections was measured by Leutheusser (1963). He also measured shear stress distributions along the wall and determined that a maximum in the shear stress existed approximately 40 percent between the corner and the midpoint of a duct wall. Brundrett and Baines (1963) measured the turbulence generated secondary flows using a constant current hot-wire anemometer and also predicted their

occurrence using a vorticity formulation. They showed that secondary flows are accompanied by a longitudinal component of vorticity. Vorticity production involves second derivatives of the Reynolds stresses and thus these secondary flows cannot exist in laminar flow.

Launder and Ying (1972) added further clarification to the nature of these secondary flows by showing that the secondary velocities are fairly independent of Reynolds number if normalized by the friction velocity. The variation in peak axial velocity with longitudinal distance was measured by Ahmed and Brundrett (1971) and Melling (1975). A peak in the axial velocity was observed at approximately 27.5 hydraulic diameters from the duct inlet. This peak velocity when normalized by the duct average velocity was measured to be 1.275 by Melling and 1.295 by Ahmed and Brundrett.

Curved Ducts

The transition to turbulent flow from laminar flow in a straight pipe or duct occurs when the Reynolds number (based on pipe hydraulic diameter) exceeds the critical Reynolds, approximately 2,300. The critical Reynolds number is higher than 2,300 for flows in curved ducts.

Ito (1959) proposed a correlation for critical Reynolds number for ducts of dimensionless radius of curvature, R/a , between 15 and 860:

$$Re_{Critical} = 2x10^4\left(\frac{D_H/2}{R}\right)^{0.32} \qquad [2.3.1\text{-}5]$$

This is based on a curve fit data for mildly curved ducts and is good to within about 15 percent for $R/(D_H/2)$ larger than 15.

Citing Taylor's (1929) test with a curved pipe of radius ratio a/R=1/31.9 Berger and Talbot (1983) propose a criterion based on Dean number: $K_{critical} = 1.6 \times 10^6$ where $K = (2a/R)(W_{max}a/\nu)^2$. Since $K_a = (2K)^{1/2}$ the proposed critical Dean number, $K_{a(critical)}$, is 1780. The assumption is implicitly made that the Dean number is the correlating parameter whereas Ito (1959) found that the critical Dean number increased with increasing critical Reynolds number. Berger and Talbot's proposed criterion would indicate that the critical Reynolds number is: $Re_{critical} = 1780\sqrt{\frac{R}{a}}$. This does not approach the straight pipe value as R/a gets large, whereas, Equation [2.3.1-5] does.

Numerical predictions of single phase turbulent flow in curved pipes and ducts are reported by Patankar, Pratap and Spalding (1974); Pratap and Spalding (1975); Pratap (1976) and Humphrey (1977). Patankar, Pratap and Spalding (1974) computed turbulent flow in curved circular pipes of mild curvature (R/a ranging from 16.4 to 40) and high Reynolds number (68,000 to 236,000) using a fully parabolic scheme. Half-symmetry was utilized to minimize the computational effort. A standard two-equation turbulence model was used with the equations cast in a (r,θ,ϕ) coordinate system. Computed longitudinal velocity profiles showed qualitative agreement with available data, while the computed local friction factors were underpredicted. Pratap and Spalding (1975) used a partially parabolic scheme to predict the turbulent single phase flow in a rectangular curved duct ($R/D_H = 5.17$) with an aspect ratio of 0.25 (the duct dimension in the radial direction is four times that normal to it). Again, symmetry was utilized to minimize the computational effort. The computed results are carried out so as to best simulate the laboratory test configuration. Unfortunately, because of screens in the test loop and a very short straight inlet section, the inlet velocity profiles used were specific to their test loop. The

inlet velocity profiles showed two peaks; one at approximately 20 percent and the other at approximately 80 percent from the inner wall.

Almost all of the analytical or experimental data reported in the literature is for one of two inlet boundary conditions: uniform inlet velocity or fully developed profile. The discharge condition of the air flow experimental rig is also of concern: the end of the 90° duct discharges immediately to the ambient. This constant exit static pressure condition is at odds with the radial pressure gradient that the curved duct imposes on the flow. Thus flow readjustments prior to the end of the bend are noticeable. Results of computations of turbulent flows in curved ducts done as part of this work are presented in the *Results* section.

Humphrey (1977) developed a fully elliptic procedure and used it to predict laminar and turbulent flows in a square duct of high curvature (i.e., $R/D_H = 2.3$). The laminar flow cases show separation and recirculating flows at approximately 6°-12°on the outer wall. To avoid separation, the centrifugal force would have to be balanced by a pressure gradient with a higher pressure at the outer wall. If the flow has a near uniform inlet static pressure then the flow along the outer wall will experience an adverse pressure gradient in the initial part of the bend as the pressure on the outer bend increases towards the elevated level. This is possibly the explanation for the separation. If the secondary flows are strong enough, the low momentum fluid from the outer wall may be moved towards the inner wall and separation at the outer wall could be avoided. However, there is a possibility that the flow could separate on the inner wall near the exit of the bend. This is also caused by the lateral pressure gradient: the initial portion of the bend along the inner wall experiences an acceleration as the near uniform inlet pressure approaches a lower pressure level on the inner wall mid-way through the bend. This lower pressure level midway through the bend must eventually return to a near uniform pressure at the

exit and so an adverse pressure gradient could develop on the inner wall between approximately 60^{o} and 90^{o}.

Humphrey, Whitelaw and Yee (1981) presented extensive measurements for both laminar and turbulent flow in a square cross section curved duct with radius ratio ($R/D_{H)}$ of 2.3. A 45 diameter inlet section was used to assure a fully developed profile into the curved duct. Unlike the laminar case, no separation for the turbulent flow was seen. The peak longitudinal velocities occur near the centerline of the duct from inlet up to 71^{o} ; close to the duct exit this peak moves to approximately three-quarters of the way towards the outer wall. Up to around 45^{o} , the longitudinal velocities near the inner wall are larger than those adjacent to the outer wall; this trend is reversed past 71^{o}. In addition, the longitudinal diffusion is less than 2 percent of the longitudinal convection for the present geometry. Thus it would appear that a fully elliptic procedure is not warranted for this turbulent curved duct of radius ratio $R/D_H = 2.3$. The lateral velocities are as large as 28 percent of the through flow in the duct's center and directed away from the center of curvature, and as large as 15 percent along the walls directed towards the center of curvature. Measurements indicate that the destabilizing curvature of the concave walls result in increased levels of turbulent kinetic energy and Reynolds shear stresses at the outer wall.

Taylor, Whitelaw and Yianneskis presented measurements in a duct similar to the one used by Humphrey, et. al. (1981), ($R/D_H = 2.3$) and also in a duct with milder curvature (R/D_H= 7) but with no long inlet section so that the flow developed as it proceeded through the bend. The peak longitudinal velocities are displaced towards the inner radius from inlet to about 60^{o}; from here to the exit the peak velocities move somewhat beyond the duct's centerline towards the outer wall. The inlet boundary layers in this curved duct are thinner than with the duct with the

long inlet section ahead and give rise to smaller secondary flow velocities. After 60°, the results for both ducts are similar (i.e., regardless of their inlet condition).

The work cited above considered radius ratios of 2.3 and 7. Curved ducts with a radius of curvature larger than 2.3 will quickly approach the qualitative features of the curved duct of radius ratio 7 since the strength of the lateral pressure gradient varies inversely with the square of the normalized radius of curvature, and the strength of the secondary velocities vary inversely with the square root of the normalized radius of curvature.

Experimental laser doppler data for developing turbulent flow in a curved duct of square cross section with normalized curvature of 1.5 has been given by Liu and Liou (1984). The turbulence intensity was found to be very large in the region of the extra pair of vortices found for high Dean numbers. The longitudinal velocities are higher near the inner wall for angles less than approximately 70° but after this a serious velocity defect in the longitudinal velocity is seen near the inner wall.

Curvature Correction Models for Single Phase Flow

Experiments with curved diffusers indicate pronounced effects of curvature on turbulence quantities, Parsons and Hill (1973). The flow on the convex wall is stabilized, while the flow on the concave side is destabilized, has enhanced turbulence kinetic energy production and an increased turbulence length scale. In fact any flow in which the streamlines are curved will experience such effects, even if the curvature is local. Local curvature effects of turbulence were reported for a backward facing step by Cheng and Farokhi (1992). Since the standard k-ε

turbulence model, which has been widely employed in turbulent flow, has had limited success in predicting complex shear flows which are subjected to curvature or rotation, it may be preferable to employ a transport equation for each of the Reynolds stresses so as to rigorously account for the extra rate of strain induced by curvature. However, this greatly increases computational effort. As a compromise, a number of approaches have been tried which seek an algebraic modification to the standard k-ε turbulence model. Cheng et. al. describe an algebraic formulation for the eddy viscosity that is a function of the flux Richardson number:

$$Ri = \frac{2U/R}{\left(1+\frac{n}{R}\right)\frac{\partial U}{\partial n}+\frac{U}{R}} \qquad [2.3.1\text{-}6]$$

where: n is the coordinate normal to the wall;
U is the local tangential velocity;
R is the local radius of curvature

Their modification is based on Rodi's (1976) algebraic Reynolds stress model for the Reynolds stresses:

$$\mu_t = \rho\frac{k^2}{\varepsilon}\frac{2\phi}{3}\left[1-Ri-\phi\frac{\mathrm{Pr}}{\varepsilon}\left(\frac{Ri^2+4Ri+1}{1-Ri}\right)\right] \qquad [2.3.1\text{-}7]$$

where: $\phi = \dfrac{1-C_2}{C_1-1+\dfrac{\mathrm{Pr}}{\varepsilon}}$ where: Pr and ε are the production and dissipation rate of turbulent kinetic energy, respectively.

Note that on the concave outer wall, $\frac{\partial U}{\partial n}$ is less than zero so that Ri is negative, while on the convex wall $\frac{\partial U}{\partial n}$ is greater than zero and the Richardson number is positive. Thus the eddy viscosity is diminished for convex curvature and stability is enhanced.

Parsons (1973) suggests modifying the mixing length based on Richardson number:

$$\frac{l}{l_o} = 1 - K^* Ri \qquad \text{; where K is on the order of 4.} \qquad [2.3.1\text{-}8]$$

Narasimhan et. al. (1991) suggest modification of the turbulence constant C_μ based on local curvature. Employing such an empirical model for wake flow behind an airfoil in a curved duct showed improvement on the inner wall but resulted in poorer agreement with data on the outer wall.

Pourahmade and Humphrey (1983) modified the standard two-equation turbulence model by making the constant C_μ a function of streamline curvature similar to Narasimhan (1991).

Bergstrom et. al. (1993) modified the dissipation rate equation based on curvature so that the resulting turbulence length scale became dependent on the local curvature. This allowed them to compute the enhancement of the turbulent shear stress at the concave surface and the corresponding reduction at the convex surface.

Some of these modifications to the standard k-ε turbulence model were tried in the present work in computing the curved duct studied by Humphrey. The results were mixed as will be seen in the *Results* section.

2.2 Two-Phase

2.2.1 Introduction

Bubbly flow is one of four flow regimes which can occur in two-phase flows. These flow regimes include bubbly, slug, annular and mist flow; even these four classes can be further subdivided. The flow regimes above are listed in order of increasing gas/liquid volume. Bubbly flow consists of discrete bubbles dispersed in a continuous flow of liquid. Slug flow is marked by the presence of cylindrical bubbles and liquid slugs passing alternately through a given station. The annular flow regime consists of the liquid phase flowing along the channel wall in the form of an annulus and the gas phase confined to the core. Mist flow is characterized by discrete liquid droplets dispersed in a continuous gas phase. Some authors make finer flow regime divisions: dispersed annular, churned slug, etc. which are combinations of the basic flow regimes defined above. Note that bubbly flow and mist flow are topologically similar-- a dispersed phase inside of a continuous phase. Slug flow and annular flow are also topologically similar: the phases segregated longitudinally in slug flow and segregated transversely in annular flow. Various authors over the last twenty-five years have proposed flow maps which are intended to determine the flow regime based on overall flow conditions. Oshinowo and Charles (1974) proposed a map which used the square root of the delivered gas to liquid volume ratio as the ordinate of the graph and the Froude number modified by liquid properties as the abscissa. Weisman (1981) gave a flow map derived from nuclear reactor loss-of-coolant tests. His map is based on superficial liquid and gas velocities. Mishima and Ishii (1984) also give a regime flow map based on the superficial velocities, (see Figure 2.2.1-1). Bubbly flow is seen to occur for the lowest range of superficial gas velocity. Hsu (1976) presents a regime map with the ordinate given by the ratio of

the gas to the total volumetric flow rate and the abscissa by the Froude number. This map is shown in Figure 2.2.1-2.

Modern approaches for the modeling of two-phase bubbly flow can be divided into two broad classes: 1) Locally Homogeneous Flow Analysis and 2) Separated Flow Analysis. Separated Flow Analysis can be further divided into Mixture (or Drift Flux) models; Eulerian/Lagrangian models and Eulerian/Eulerian (i.e., Two-Fluid) models. Direct Numerical Simulation (DNS) solves the three-dimensional, time dependent Navier Stokes equations with sufficient spatial and temporal resolution so as to resolve all scales of the turbulent motion. Direct numerical simulation of two-phase flows at realistic Reynolds numbers may become a reality sometime in the future. DNS has been used recently by Rouson and Eaton (1994) to predict particle laden flows in two-dimensional channels at a Reynolds number of 1552. Lagrangian tracking was used for the particles.

Locally homogeneous analysis is applicable when the interphasial momentum transfer is much greater than momentum transfer between each fluid and its environment. In this case, the two phases will have the same velocity. The fluid can be treated as a homogeneous single-phase fluid of variable density. While this formulation applies strictly only to dispersed bubbles approaching zero diameter, useful practical solutions have been computed using this model ,e.g. two-phase pump inducer calculations by Cooper (1967).

Separated flow analyses allow for a finite interphase transport rate and thereby allowing the two phases to have differing velocities. The difference in phase velocities is called slip. The simplest form of this analysis is the Drift-Flux model. Governing equations are written for conservation of mixture mass and momentum and incorporate unequal phase velocities by defining expressions for the slip.

The Eulerian/Lagrangian separated flow model solves a complete set of conservation equations for the continuous phase and numerically integrates a differential equation(s) representing the equation of motion for a particle. The Eulerian/Lagrangian algorithms can be further subdivided into deterministic and stochastic models. The deterministic model accounts for interactions between the bubbles and the mean properties of the continuous phase and has been used by Mohamed (1988) to successfully compute axisymmetric pipe flows. The stochastic approach models the instantaneous interaction of the continuous and the distributed phases by sampling a probability density function based on the liquid's turbulence intensity. This approach has been successfully applied to model axisymmetric flows by Neti et. al. (1990). Eulerian/Lagrangian methods are generally a good choice for flows with low volume fractions or a dispersed phase which includes a wide size range. Eulerian/Lagrangian descriptions often need several iterations between the main flow and the particle displacement equation based on the main flow since the interaction is developed explicitly. When the void fraction (i.e., the volume fraction of the distributed phase) is high it is more efficient to employ a Two-Fluid Model which develops the distributed phase's velocity implicitly.

The Two-Fluid model often allows for the most accurate description of the physics of the problem. Each phase is considered separately via two sets of conservation equations. These equations contain terms which model the interaction between the two phases, i.e., the interphase momentum transfer terms. The two fluids are viewed as co-existing in the flow domain, each occupying its fraction of the flow volume. This approach is thus also called the Interpenetrating Continua method. Details of the microscopic interactions at bubble interfaces are considered collectively in a macroscopic sense. The dynamics and trajectories of bubbles of varying diameters can be simulated by adding another "phase" for another bubble class/size resulting in a

Multi-Fluid model. However, the overall flow parameters, such as pressure loss, for a distributed phase with various diameters can be modeled using the present computational algorithm with a single phase of bubble size given by the Sauter mean radius, R_{SM}, where:

R_{SM} = 3*(Volume of the bubbles)/Surface Area of the bubbles.

The present work simulates a two-phase bubbly flow using a Two-Fluid Model. Terms are added to the momentum equations to account for the interphase momentum exchange. The present computer algorithm is capable of handling two-phase two-component problems (i.e., with no mass exchange between the phases). This is appropriate for water and air (or other noncondensable gas) or water/oil flows considered in this work. Water and steam flows would require additional terms in the continuity and energy equations.

The various levels of simulation sophistication result in increased understanding of the details of the flow at the expense of computational effort. If the slip velocity between phases is not too large then a simpler model, such as the homogeneous, may result in acceptable overall performance predictions. However, if the details of the flow are required, such as the local number of bubbles per second in different parts of a complex geometry then the two-fluid approach will be required. An example would be flow in a nuclear reactor core where the local heat rate is important and where because of the flow passage geometry the dispersed phase may segregate. If an acceptable model exists to describe the local slip velocity then a simpler model, such as the drift-flux model, may suffice. However, such data probably does not exist for geometries that have not been previously investigated.

Previous two-fluid algorithms in the literature have used either algebraic turbulence models or employed higher level turbulence models only for the continuous phase. The dispersed phase turbulent eddy viscosity in these works has often been assumed equal to some constant

times the continuous phase diffusivity (i.e., a particle Prandtl number). Another approach for computing the turbulent eddy viscosity of the distributed phase is to relate it to the continuous phase turbulent viscosity by means of an algebraic equation. The theory of a particle dispersed in a turbulent flow field based on the work of Tchen (1947) and Peskin (1959) provides such an algebraic equation. This modeling approach has been by Mostafa, et. al. (1987). In this work turbulent flows have been computed utilizing both a constant particle Prandtl number as well as by applying a two-phase modified two-equation k-ε model to the distributed phase as well as the continuous phase.

Some two-fluid algorithms in the literature have reported convergence problems when the density ratio of the two-phases exceeded approximately ten. Problems were reported for Shah's algorithm (1978); the IPSA code (Spalding 1980) and the KFIX code of Rivard and Torrey(1978). This topic will be discussed further in the *Numerical Solution Algorithm* chapter later in this work. The algorithm presented here is robust and can handle water/air flows with a density ratio of 1000:1. However, in the developmental stage the present author found it very useful to compute water/oil flows (density ratio 1.13:1), especially for developing the algorithms for void fraction computation and the lateral forces in a vertical duct of long length (i.e., Z/D_H =45).

Carver and Salcudean (1986) and. Carver (1988) developed a two-fluid model for bubbly flow in circular cross section elbows and return bends. This computational algorithm was used to predict the flow in two circular cross section pipe bends that had been tested by Gardner and Neller (1970). Their computations began at the inlet to the bend even though the test configuration of Gardner and Neller was proceeded by a long vertical straight section. Carver and Salcudean used a sinusoidal distribution of void fraction as an inlet boundary condition. This

is physically unrealistic. Their model of the interfacial momentum transfer forces included only the drag force and not the lateral lift force. Thus it is not expected that they would have been able to properly predict the void fraction peaking at the end of the vertical straight duct.

A numerical two-fluid scheme for one dimensional flow with heat transfer was presented by Dykhuizen et. al. (1984). A momentum equation was solved for the mixture and for the lighter phase. An upwind differencing scheme is used, which is expected to be accurate only for convection dominated flows. Their numerical procedure requires that the equations be cast in a form such that the resulting matrices representing the equations are lower triangular. It is not clear that this can be done for the general three-dimensional problem.

A two-fluid code has been developed by the United Kingdom Atomic Energy Authority's Harwell Laboratory, and has been reported by Lo (1989 and 1990). Spalding's numerical procedure (1980) was used for computing the void fraction. Numerical predictions for various two-dimensional problems were presented, including a free surface problem.

A two-dimensional two-fluid code for the prediction of oxygen droplet dispersion in a hydrogen gas flow was presented by Simonin et. al. (1991). Turbulent predictions of the dispersed phase were made by using Tchen's theory of dispersion of particles in a turbulent stream.

Dilute (i.e., less than 10 percent void fraction) bubbly two-phase axisymmetric jets in vertical up-flow were predicted and measured by Sun and Faeth (1986). Laser Doppler Anemometry was used to measure bubble velocities and flash photography was used to measure bubble size and distribution. Predictions were made assuming 1 mm diameter utilizing a locally homogeneous flow analysis; using a deterministic separated flow Eulerian/Lagrangian scheme as well as a stochastic separated flow Eulerian/Lagrangian code. The motion of the bubbles was

predicted using a Lagrangian approach based on the Basset-Boussinesq-Oseen equation. This includes the influence of gravity, virtual mass, drag and the Basset history forces. Both of the separated flow models employed similar schemes for determining the bubble motion. In the deterministic model, the bubbles interact with the mean liquid properties while in the stochastic model the bubbles interact with the instantaneous liquid properties via a random walk method. A statistically significant number of bubbles are tracked (typically a few thousand). The bubbles are assumed to interact with eddies whose properties are found by making a random selection from the velocity probability density function of the continuous phase. Theses Gaussian probability density function are assumed to have a standard deviation of $(2k/3)^{0.5}$. A primary goal of their work was to quantify the importance of the virtual mass and Basset force for bubbly flow. (These forces can be seen to be negligible for particle laden flows.) It is expected that these forces could be more important in bubbly flows than in particle laden gas flows. Their work indicated that the inclusion of the Basset force only marginally improved the accuracy of their predictions while significantly increasing the computational effort resulting in the conclusion that the calculation of the Basset force was not warranted.

A two-fluid model that combined the solution of an additional equation for the fluctuating kinetic energy equation of the particles in a particle laden gas/solid flow with the momentum equation of both phases is reported by Gidaspow et. al. (1991). The pressure term in the momentum equations of the particulate phase is considered to consist of the static normal stress and the dynamic stress, called solids pressure, which arises due to the collision of particles. A kinetic theory is used to model the solids phase pressure. A similar approach could be used to extend the method used in this work to compute particle laden flows. Experimental data for

fluidized beds including velocity profiles have been measured by Randelman, Benkrid and Caram. Numerical simulations of these beds is a future possibility.

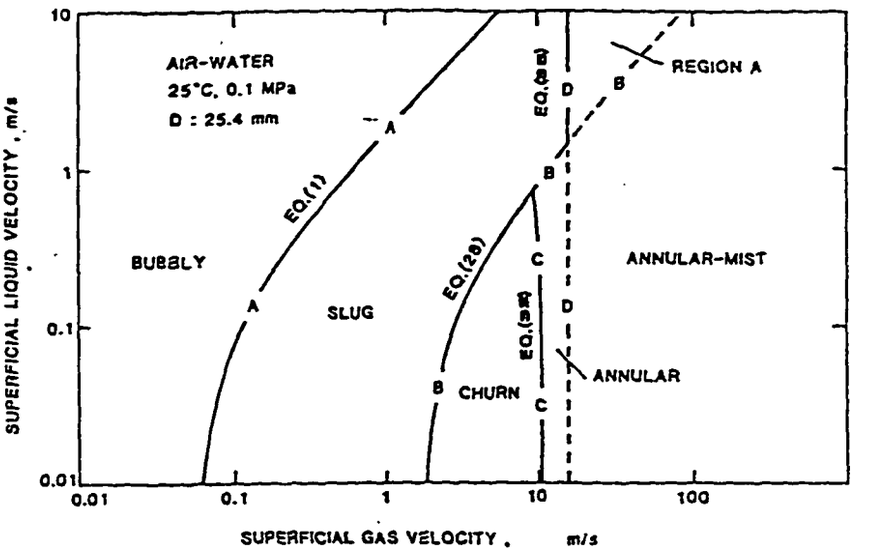

Figure 2.2.1-1Flow Regime Map (Mishima and Ishii)

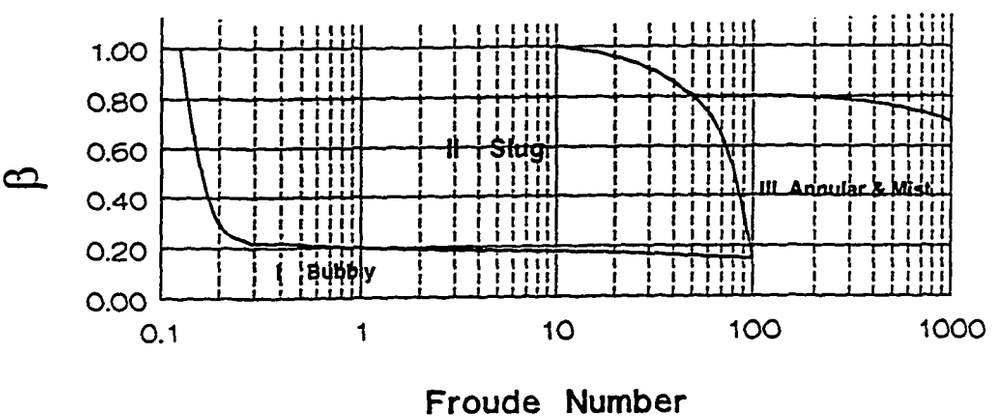

where: $\beta = \frac{Q_g}{Q_L+Q_G}$; $Fr = \frac{[(Q_L+Q_G)/A_{Duct}]^2}{gD_{Duct}}$

Figure 2.2.1-2 Flow Regime Map (Hsu)

2.2.2 Flow Geometries

Free Shear Flow Problems

A theoretical and experimental investigation into particle laden turbulent jets is report by Shuen (1984). Three different analyses were used: 1) a locally homogeneous flow model (slip between phases is neglected); 2) a deterministic Lagrangian/Eulerian approach; 3) a stochastic Lagrangian/Eulerian calculation. All three models used a k-ε turbulence model. The third approach yielded the most accurate predictions.

Particle laden axisymmetric turbulent jets have been computed using a two-fluid model by Elghobashi (1984). A two-equation turbulence model for incompressible dilute two-phase flows is presented which requires new numerical constants evaluated on the basis of two-phase jet spreading data. The turbulent eddy viscosity of the liquid droplets is evaluated by introducing a droplet Prandtl number. The universality of their proposed turbulence model is yet to be proven.

Lagrangian/Eulerian calculations of two-phase bubbly jet flows are reported by Sun (1985) and Sun and Faeth (1986). Measurements were made in a water tank in which a bubble ejector at the bottom was used to create an upwardly flowing jet. Two variants of Lagrangian/Eulerian calculations were made: a deterministic and a stochastic calculation that were described earlier. The stochastic approach yielded more accurate predictions and is recommended by the authors of this work.

A very similar paper to the one above was written two years later in which particle-laden turbulent water jets in still water were measured and computed by the same deterministic and

stochastic Eulerian/Lagrangian approach. The major difference found was that the present flows possessed higher relative turbulence intensities. This resulted in increased particle drag relative to calculations based on a standard drag law.

Mostafa and Mongia (1987) compared two-fluid (Eulerian/Eulerian) predictions to those from an Eulerian/Lagrangian stochastic formulation for turbulent evaporating dilute sprays. They concluded that the Eulerian/Eulerian model yielded results closer to the available data and that it was more efficient (in terms of run times). The authors do point out that there are certainly cases when the opposite might be true--such as flows in which rebounds from the walls are important.) The turbulent eddy viscosity of the dispersed phase used in the two-fluid model was calculated based on a local droplet Prandtl number defined as the ratio of the droplet eddy viscosity to the continuous phase turbulent eddy viscosity.

From the above discussion, it is apparent that none of the models reviewed above accounted for lateral lift forces. It is possible that this effect is not important since the lateral gradients of velocity are smaller than those in internal duct flow problems.

Straight Ducts

Mohammed (1988) used a deterministic Lagrangian/Eulerian calculation and Neti and Mohammed (1991) used a stochastic Lagrangian/Eulerian calculation to compute low void fraction bubbly upflow in a circular cross section pipe. The mixing length was adjusted for two phase-flows by utilizing a two-phase flow multiplier dependent on local quality. The deterministic separated flow model was found to underestimate the region containing bubbles; while the stochastic separated flow model was deemed superior.

A two-fluid model was applied to vertical up-flow in a circular cross section pipe with low Reynolds number by Antal et. al. (1991). Because of the low Reynolds number assumption the turbulent Reynolds stresses were not included and hence no turbulence modeling is necessary. A Galerkin finite element method was used to solve the equation set. The lateral lift force formulation of Drew and Lahey (1987) was used. The paper presents some comparisons with data, although the authors note that data is limited for low Reynolds numbers. The near wall peaking of the void fraction which was evident in the data was properly predicted.

Turbulent two-phase bubbly water and air flows in a pipe of circular cross section were experimentally investigated for both vertical up and down flows [Wang et. al. (1987)]. Measurements were made with a three wire hot-film anemometer. A peak in the void fraction close to the walls was measured for up flow. For the vertical down flows, the bubbles were found to move toward the center of the pipe causing void coring. It was found that at moderate and high Reynolds (23,000 to 44,000) numbers the turbulence increased monotonically with void fraction. However, at the highest Reynolds numbers it was found that the turbulence levels reached an asymptotic limit with increasing void fraction and at extremely high Reynolds number the turbulence actually decreased with increasing void fraction. A possible explanation is that while the turbulence generation increases with void fraction the increase in dissipation may eventually offset the generation.

The radial distribution of turbulent kinetic energy production, dissipation and diffusion for bubbly up-flow in a vertical circular cross section pipe was studied by Kataoka and Serizawa (1993). Turbulence generation and dissipation is shown to be largest at the pipe center. The Reynolds number was 30,000. The diffusion contribution was fairly constant across the section.

Bubbly up flow with a sudden expansion was analyzed with a two-fluid model in a circular cross section pipe. For such flows the presence of the interfacial drag force in the momentum equations introduces source terms into the transport equations for both the turbulent kinetic energy and for dissipation of turbulent kinetic energy. These source terms were first identified by Gosman et. al. (1992).

A two-fluid Eulerian/Eulerian model for particle laden flows is applied to the flows inside a fluidized bed combustor by Gidaspow, et. al. (1991). The combustor and an electrostatic separator were modeled as two-dimensional flow problems. The solids phase pressure was calculated by using a kinetic theory model. Solids volume fractions as high as 0.4 existed at the bottom of the combustor bed. The solids circulation was predicted as well as the hold-up in the combustor.

Turbulence modeling for particle laden jet flows was studied via a two-fluid model by Elghobashi et. al. (1984). The turbulent eddy viscosity of the distributed phase was calculated based on a local turbulent Prandtl number (i.e., the ratio of turbulent eddy viscosity of the dispersed phase to that of the continuous phase). This in turn is based on the theory of an isolated particle in a turbulent fluid as given by Tchen (1947) and later refined by Peskin and Soo (1967).

Curved Ducts

Two-dimensional planar two-phase curved channel computations were made by Carver (1982 and 1984). He extended his work for axisymmetric circular cross section pipe flows (1986 and 1987). In the latter work an inlet void fraction profile at the start of the duct was assumed. Unfortunately, the distribution chosen is not a realistic distribution for vertical up flow a sinusoidal curve with its peak value located at the duct's center was used. Carver was able to

successfully compute both velocity and void fraction profiles for the flow in bends for water/air flows.

Carver's (1984) work reviewed the various approaches for constructing a void fraction algorithm. Two equations of mass conservation are available, one from each phase. One of those equations could be used to develop the pressure correction equation, while the other used for constructing the void fraction algorithm. This approach, however, is not successful when the two phases have widely disparate densities since the effect of the heavier phase overwhelms the lighter phase. In the Spalding IPSA method (1980) volume fractions for each phase are computed separately from their mass conservation equation; and then the imbalance in volume fraction (the difference by which they do not sum to unity) is used to derive a pressure correction. Carver argues that this procedure suffers from convergence problems when the density ratio is large as the heavier phase dominates. Carver recommends first normalizing each mass conservation equation by its own reference density and then summing the two equations to form an equation that will be used to determine the pressure correction. The two normalized mass conservation equations are then subtracted to develop the equation for determining the void fraction. This basic approach with some modification is used in the present work.

Carver used a standard single phase k-ε turbulence model for the continuous phase and assumed a turbulent Prandtl number of unity to determine the turbulent eddy viscosity of the distributed phase. However, Carver's turbulence model neglected the effect of the presence of the bubbles on the continuous phase's turbulence. A description of the present approach to this problem is given in Section 4, *Mathematical Models*.

2.2.3 Fluid Turbulence Modification Induced by Bubbles

The interaction of the dispersed phase (bubbles/particles) with the continuum phase fluid tends to modify the fluid turbulence. Qualitative changes in turbulence due to the presence of particles have been reported by Tsuji (1991) for reacting flows. It is reasonably apparent that the presence of bubbles or particles in a flow should induce additional turbulence. Consider the changes induced in the present curved duct test rig when bubbles are injected into what is originally a single phase flow. There are strong lateral and longitudinal pressure gradients in the flow. These pressure gradients will generate different fluid and bubble accelerations due to the mass differences between the two phases. This relative acceleration between the two phases can be expected to cause additional velocity fluctuations.

It is still unclear how relevant data based on heavier particle laden flows is to bubbly (lighter) flows. It is reasonably apparent that relatively light bubbles moving in the fluid turbulence could enhance turbulence and the presence of heavy particles in a particle laden flow may also be expected to dampen turbulent fluctuations. A primary concern of present research, is to determine conditions under which turbulence is enhanced and under what conditions it may be suppressed. Gore and Crowe (1989) performed experiments of particle laden flows as well as bubbly flows. They found the correlating parameter to be the ratio of the particle or bubble diameter, d_{bub}, to the turbulent length scale, l_e. The turbulent length scale is based on the most energetic eddy. The ratio of $d_{bub}/l_e = 0.1$ appears to be the determining factor as to whether turbulence is increased or decreased.

A rather different view of the controlling phenomenon was advanced by Hetsroni (1989) who explains the enhanced turbulence by the vortex shedding of the particle or bubble and hence

focuses on a relative velocity. He proposes that the presence of the distributed phase with a low bubble Reynolds number tends to suppress the fluid turbulence while flows with high bubble Reynolds number tend to increase the turbulence.

A modified turbulence model based on the standard k-ε model is presented by Besnard et. al. (1991). This model accounts for the fluctuating energy induced by the particles or bubbles. This energy is either fed into turbulence or dissipated directly as heat.

The effect of the dispersed phase on mean quantities of velocity and void fraction led to theories in which the von Karman constant is modified by the presence of the bubbles. Hino (1963) and Neti and Mohammed (1990) report theories in which the von Karman constant is modified to account for the local presence of the distributed phase.

Boundary layer studies have shown that wall turbulence is not only random but consists of organized motions. The burst phenomenon has been studied: ejection of low-momentum fluid from the wall region to the main stream followed by an in-rush of high momentum fluid into the wall region [Walker et. al., (1989)]. The burst process seems to be a major contributor to the Reynolds stresses and may play an important role in two-phase flows to the degree that the dispersed phase is affected by the turbulent eddies.

In the present work a two-phase turbulence model is used that appears naturally from the derivation of the transport equations. These equations are derived from the momentum equations, which for two-phase flows include a momentum interchange force. When the transport equations are derived (see Appendices VI and VII) additional terms result which are included as source terms for both the k and ε equations (these are denoted as S_k and S_ε, respectively). The present turbulence model as derived in this work is consistent with that given by Wang, et. al. (1994).

This is unlikely to be the last word on two-phase turbulence transport modeling, but a plausible model that will be improved upon with further experimental and numerical studies.

3. EXPERIMENTS

Pressure drop measurements in an air/water bubbly flow have been made as part of this work. The measurements were made in a Plexiglas test section which permitted viewing and photographing the bubble trajectories throughout the test section. This chapter describes details pertaining to the experimental set-up, measurement details and results.

3.1 Description of Setup

A single and two-phase closed loop flow test rig has been built and instrumented to obtain flow data that can be used to validate the numerical predictions. The present loop is a modification of the loop built by Neti et. al. [1983]. The test section was made of transparent Plexiglas. The duct cross section was square with a 25 mm side. A 48 hydraulic diameters long inlet vertical section of duct precedes a 90^{o} elbow. This curved duct section has a mean radius-to-hydraulic diameter ratio of 5.5. The curved duct is followed by a horizontal square section which is 15 hydraulic diameters long. Air bubbles could be injected at the bottom of the vertical inlet section. The air injection hardware consisted of a compressor and regulator to supply air to a manifold arrangement of small tubes which run across the duct cross section. These tubes have been drilled with 0.5 mm diameter holes which admit air bubbles to the duct. The air injection rate is measured by a gas rotameter which is located between the compressor and the manifold. A schematic of the test section plus the other components of the test loop are shown in Figure 3.1-1. The test section and the bubble manifold described above and piping to permit the water flow to be diverted to a weigh tank for flow instrumentation calibration has been added during

this work. A 10 gpm centrifugal pump (STA-Rite 1/3 hp , 115 volt) was used to circulate the water. It was driven by an electric induction motor: Model S48H2EC11.

Water flow was measured with a rotameter located between the pump discharge and the inlet to the test section. Air flow was measured by an air rotameter that was located between the air compressor regulator and the bubble injector. Both the air and water rotameters consist of a scribed vertical cylinder through which the fluid passes. A float rests inside of the cylinder at its base when there is no flow. As flow is increased the float rises up the tube. At equilibrium the downward force exerted on the float by its mass is balanced by the float's buoyancy and the drag force of the fluid which is flowing vertically upwards. The flow loop could be run at duct Reynolds numbers as high as approximately 30,000. A resistive heater allowed the water temperature to be increased to achieve higher Reynolds numbers.

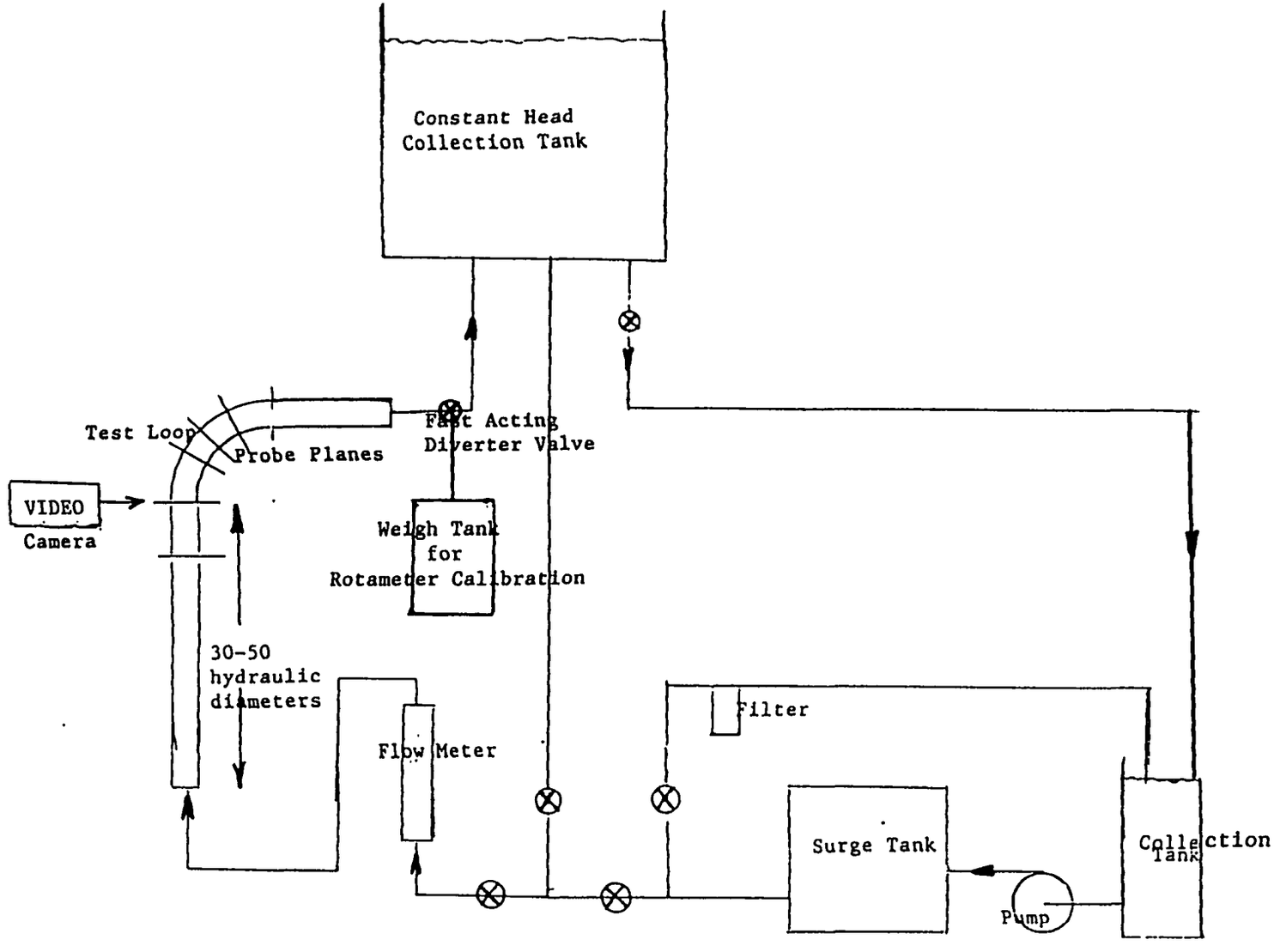

Figure 3.1-1 Flow Test Loop

3.2 Instrumentation

The test section was instrumented with sixteen pressure taps, (see Figure 3.2-1). Pressure taps were located 5 hydraulic diameters upstream of the elbow. The 90^{o} curved duct had eight pressure taps: at the inlet, at 30^{o}, at 60^{o} and at the exit of ninety degree bend. Taps were located on the inside and outside of the duct at each of these stations. Six taps were located in the horizontal duct downstream of the curved duct. Taps were located on all four faces of the duct at a downstream location of five hydraulic diameters. Pressure transducer tubing is attached to the pressure tap in the duct's side wall by the permanent addition of a nipple which blocks the view of the bubble patterns as they transit the test section. So, taps were not generally located on the forward face of the duct so as to maximize the optical access.

Bubble trajectories were recorded on a NTSC compatible video camera. Camera output could be monitored real-time and amplified and directed to a commercial frame grabber board. Data Translation's DT55-LC board is used with an IBM compatible personal computer. The board provided image acquisition, image display of the acquired signal and image storage. A high speed memory buffer stored the array of pixel values corresponding to a frame in real-time. The board and attendant software for displaying and saving an image is intended for scientific imaging and includes a phase locked loop at the input end to synchronize the board to the video camera; does not compress/decompress data which can lead to a loss of accuracy and utilizes 8-bit grayscale. The board acquires images in real time, i.e., was able to acquire the 512 pixels per line and 480 lines per frame in 1/30th of a second with an A/D converter with a throughput of 10 MHz. The captured images could be save in TIFF format. Image processing software can be used to improve contrast and brightness and to detect images. The commercially available

imaging utility "Halo Desktop Imager" from Media Cybernetics was used for this purpose. These images were used to determine the void fraction distribution at different locations in the test loop for comparison with the numerical predictions.

The pressures were recorded with a Validyne diaphragm type differential pressure transducer. The transducer range is 0 to 50 mm H_2O with a 0.02 mm resolution. The output of the transducer is a DC voltage which could be read on a multimeter as well as being input to the IBM compatible PC data acquisition analog to digital board. The differential pressure transducer has two ports which supply a test pressures to each side of the active diaphragm. All of the pressure measurements were referenced to tap #7 which is at the inlet to the 90° curved duct (Figure 3.2-1) by leaving the pressure tubing connected between this tap and one of the transducer's ports. The other transducer tap was sequentially connected to each of the pressure taps and the pressure at that tap read and recorded to the A to D board.

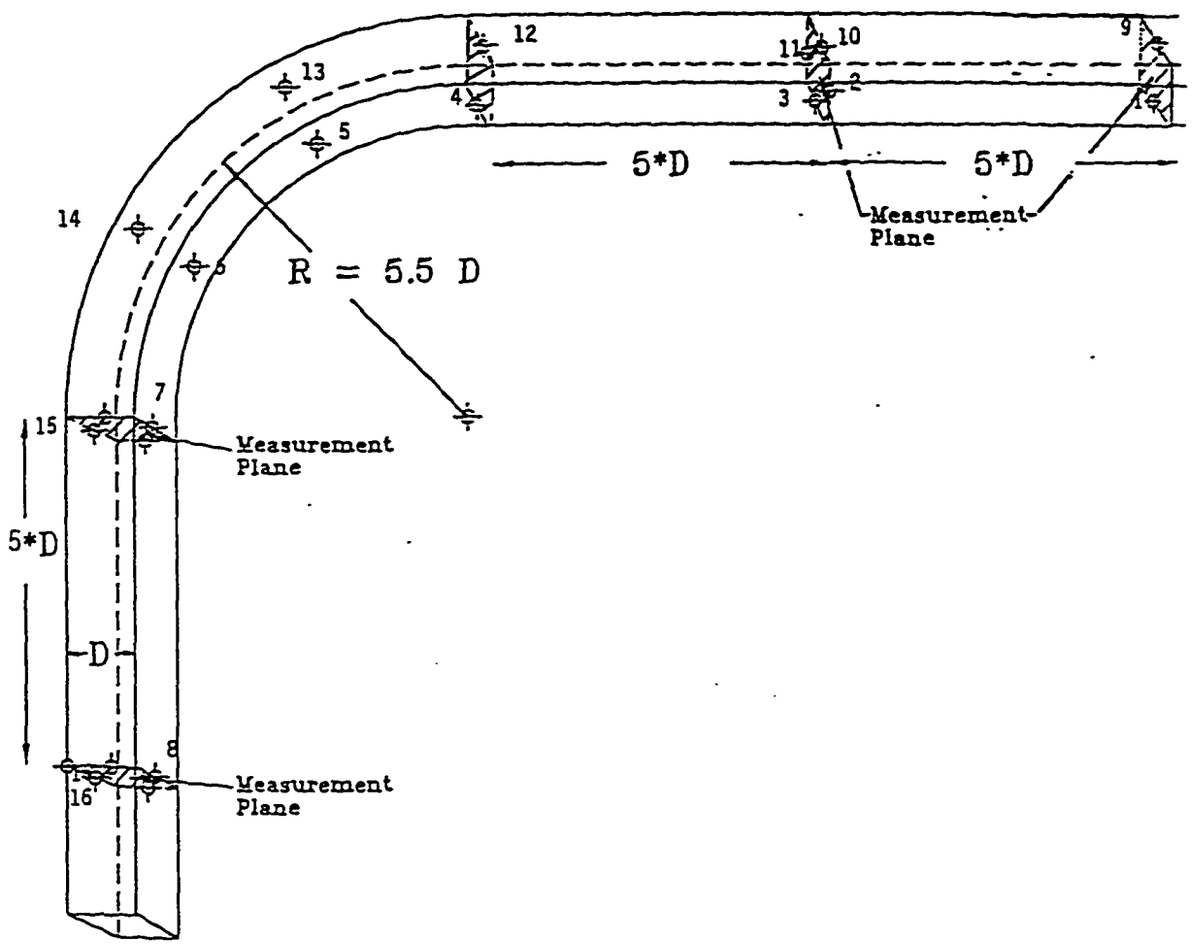

Figure 3.2-1 Test Loop Constructed for this Investigation
(illustrating static pressure tap locations)

3.3 Experimental Procedure

3.3.1 Calibration of the Rotameters

The rotameters were calibrated by correlating the float position with a volume flow rate which is measured by a precise secondary means. The water rotameter calibration was performed by running the loop at a flow rate and using a fast acting valve thrown to divert the flow to a weigh tank. The time to collect a given mass was recorded. Typically 100 lbm of water was collected, that would take on the order of several minutes. This calibration was done with water temperatures at 70° F and 100° F. The volumetric flow rate was thus correlated with a rotameter height reading. Figure 3.3.1-1 is the calibration curve of Reynolds number (based on the 25 mm hydraulic diameter duct) versus rotameter reading as a function of temperature.

A calibration curve for air flow rate with rotameter reading was established by using an Orsat apparatus (volumetric air displacement). This calibration curve is given in Figure 3.3.1-2.

The output of the Validyne pressure transducer and display unit was a D.C. voltage linearly proportional to pressure. The transducer calibration was verified by applying pressure to both the transducer and an inclined manometer via tubing with a tee. The pressure transducer reading is:

$$\text{mm } H_2O = 0.5(\text{Voltage Reading}) \qquad [3.3.1\text{-}1]$$

Pressures were read and automatically logged into a PC by using the data acquisition software. Each pressure was read as 100 voltage values taken at 0.1 second intervals, and were then averaged. The pressure data was then transferred to a spread sheet program, along with other parameters and reduced the data. Samples of spread sheet data are shown in Figure 3.3.1-3 and 3.3.1-4.

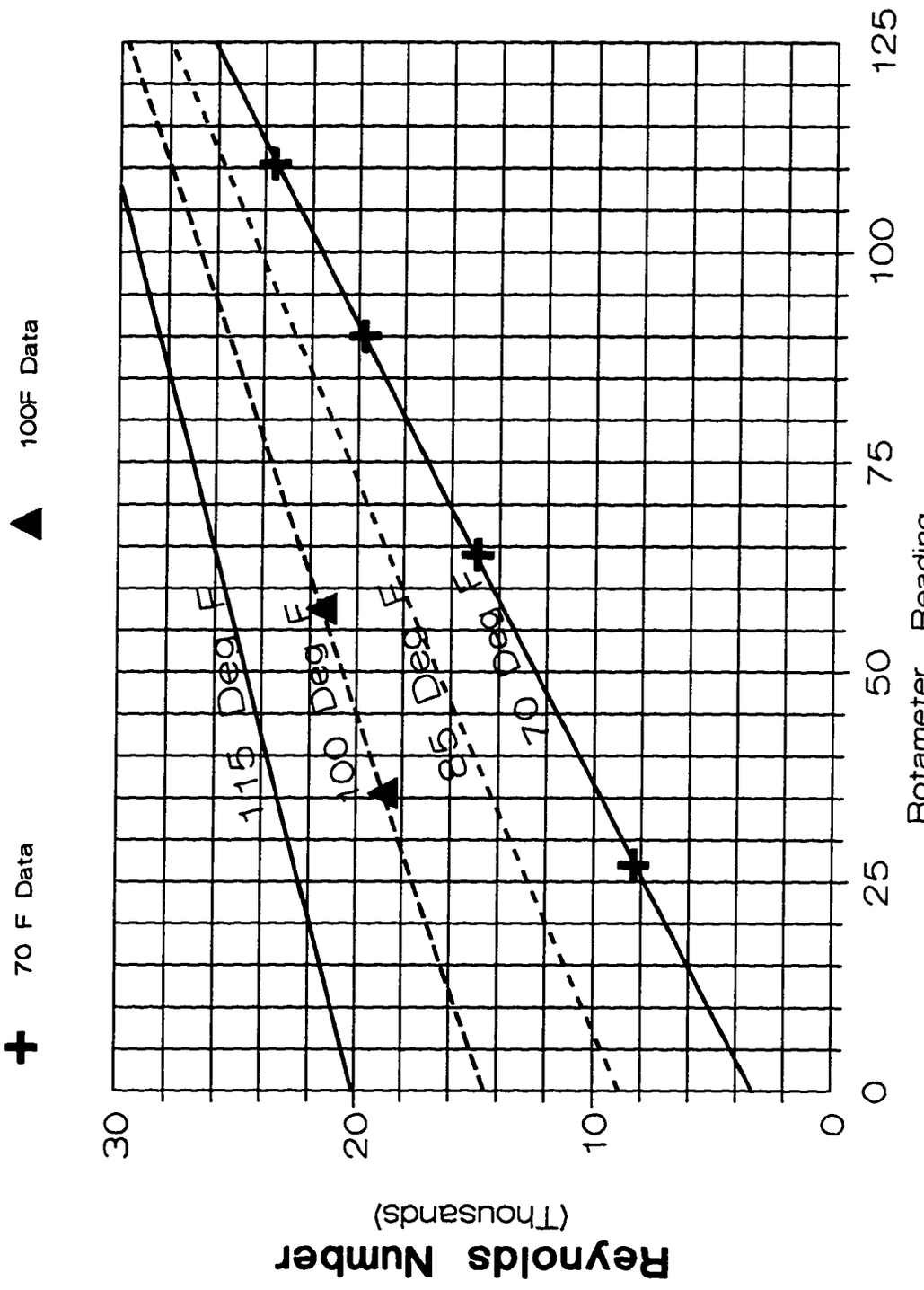

Figure 3.3.1-1 Water Rotameter Calibration

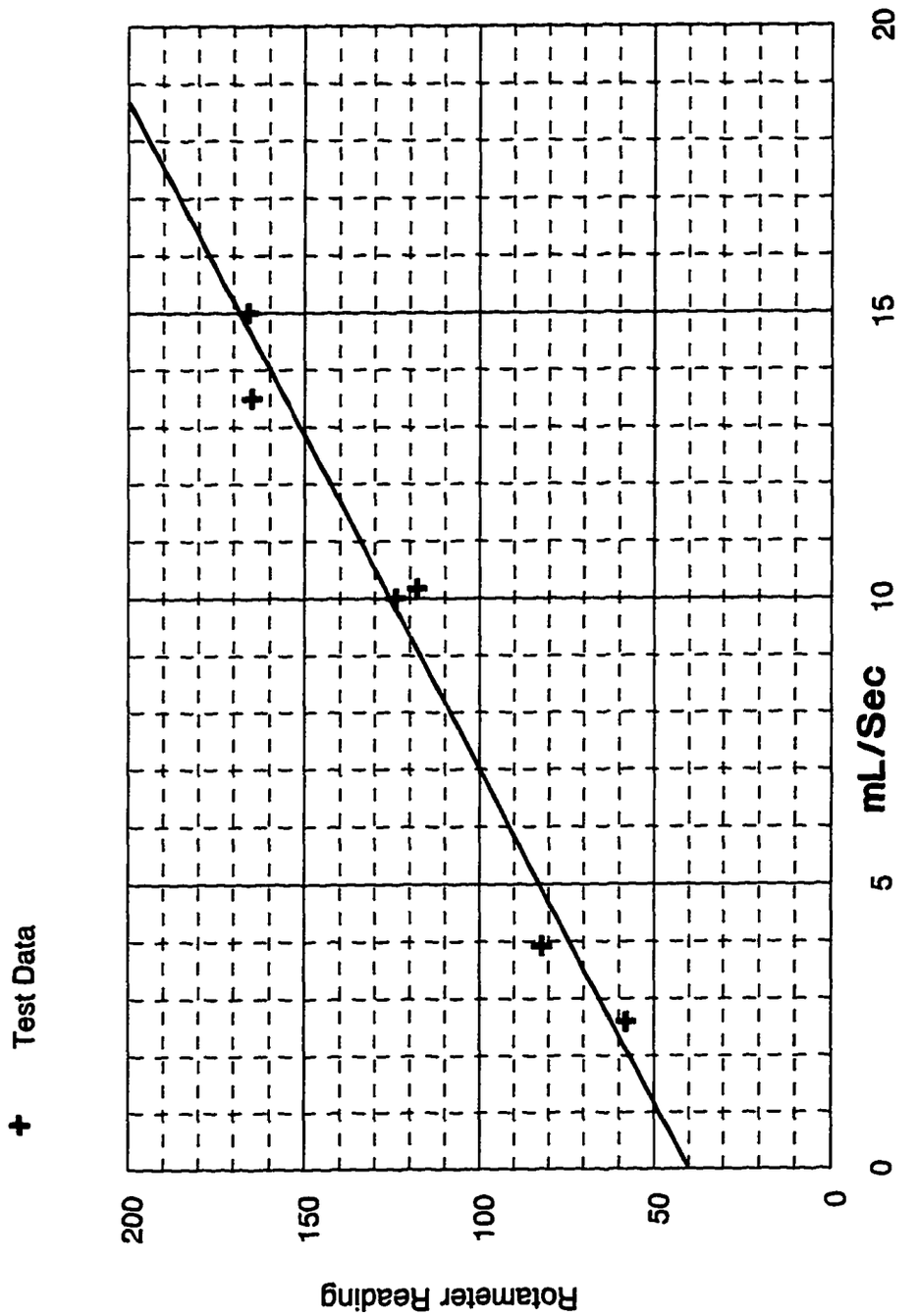

Figure 3.3.1-2 Air Rotameter Calibration

		Two-Phase	***Flow Test***	***with***	***Data Acq***	***System***			
3) Two-Phase	Repeat of 2)						E. Graf 9/15/94		
Note: Any	tap at an	elev. that	is diff from 7	'needs to hav	its press				
adjusted: i.e.	x_7 true reading is :		x_7 (mm H20	= 0.5(Validyne Voltage)		- Z x (1-SG)			
		where:	Z is distance	measured	in mm above	tap 7 loc.			
			Water	Air	Test	09/15/94			
Water	Temp=		114.3						
Water	Rota	Reading=	57.5		ML/SEC=	387.166667	IN**3/SEC=	23.6221273	
Air	Rota	Reading=	169		ML/SEC=	15.0566			
Validyne	Zero at	Start=	0		Void Fraction=	0.0388892		X=324.5	
	Note: Mv Zero	accounted for	In data acq		SG =	0.9611108			
Probe	Validyne	Press(mm)	Dist to _7(mm	Static Head	Rel Press (mn	Notes			
4_7	-1.3742	-0.6871	111.8	-4.347812	-5.034912				
15_7	6.13555	3.067775	0	0	3.067775		P on outside	greater--not u	iform
12_7	10.8035	5.40175	139.7	-5.4328205	-0.0310705		P on out. muc	greater (see 4	7)
5_7	17.8885	8.94425	104.5	-4.0639209	4.88032912				
13_7	-1.0324	-0.5162	126.5	-4.9194832	-5.4356832				
2_7	-3.3762	-1.6881	124.5	-4.8417048	-6.5298048				
11_7	-4.426	-2.213	124.5	-4.8417048	-7.0547048				
8_7	-1.18867	-0.594335	-127	4.93892777	4.34459277				
16_7	-1.2473	-0.62365	-127	4.93892777	4.31527777				
3_7	-5.7102	-2.8551	111.8	-4.347812	-7.202912				

Figure 3.3.1-3 Spread Sheet for Data Reduction

1_7	-11.97	-5.985	111.8	-4.347812	-10.332812				
Calculated	Data:								
	Kinematic Visc	6.759E-06							
	Vel Avg =	1.96851061							
	Re Number =	24271.4607							
	V**2/2g =	0.06021996							
(5 L/D EXT)	K elbow =	0.31247123							
(10 L/D EXT)	K elbow =	0.34184631							
	Vertical 5" Los	Frict Fact f =	0.03046626		K inlet =	0.1523313			
First	Horizontal 5"	Frict Fact f =	0.04864703						
Second	Horizontal 5"	Frict Fact f =	0.03634128						

Figure 3.3.1-4 Spread Sheet for Data Reduction, continued

3.4 Data and Results

Single and two-phase pressure loss data for the bend was measured using the methodology suggested by Ito (1960) and Blevins (1984). The pressure drop was measured between stations located in the vertical straight inlet duct before the bend and in the horizontal straight duct after the bend. The velocity profile at the bend's exit is distorted. It recovers to a uniform velocity profile at some distance downstream and there could be significant pressure changes associated with this. Pressure loss for fully developed straight duct flow in a length equal to the combined length of the inlet and exit straight sections was subtracted from the overall measured loss. In this way the total loss associated with the bend is measured, including the mixing loss which occurs downstream of the bend.

Single phase loss data taken in the present test loop is compared to the empirical correlation given by Blevins on Figure 3.4-1. Agreement is good at the higher Reynolds numbers (24,500). The present measurements of loss coefficient are twelve percent higher than the Blevins correlation at lower Reynolds numbers (15,400).

Water/air two-phase pressure loss data for the curved duct measured in the present test loop is compared with the Chisholm empirical correlation (1980) for the curved duct geometry (i.e., R/D = 5.5) in Figure 3.4-2. The agreement is very good. The two-phase multiplier for the present data is a few percent higher than Chisholm's empirical correlation.

Two-phase pressure loss data for the flow in the horizontal straight section is shown in Figure 3.4-3. This figure compares the present data to the Lockhart-Martinelli correlation [Wallis (1969)]. Presently measured two-phase loss multiplier is approximately 25 percent greater than that given by the Lockhart-Martinelli correlation.

Two-phase pressure loss data for the flow in the vertical straight section is shown in Figure 3.4-4. The figure shows a comparison of the present data to that of Lockhart-Martinelli correlation [Wallis(1969)]. The presently measured two-phase loss multiplier is approximately 35 percent greater than that given by the Lockhart-Martinelli correlation.

The difference between the present straight duct loss measurements, whether in the horizontal or the vertical section, and the empirically derived correlation in the literature can be attributed to the lack of sufficiently long straight sections in the present test loop to make this measurement accurately. The present test loop was not designed for the purpose of making these straight duct measurements. The measurement section for the straight section is only five hydraulic diameters long. This measurement section for the horizontal duct starts just five hydraulic diameters after the bend exit. The flow is probably not fully recovered at this point so the horizontal duct loss may include some of the loss attributable to the bend. The test section for determining the vertical straight loss ends immediately at the start of the 90^{o} bend. It is possible that some elliptic effects of the bend cause an acceleration of the flow at the bend inlet that is then recorded as excess total pressure loss over the straight measuring section.

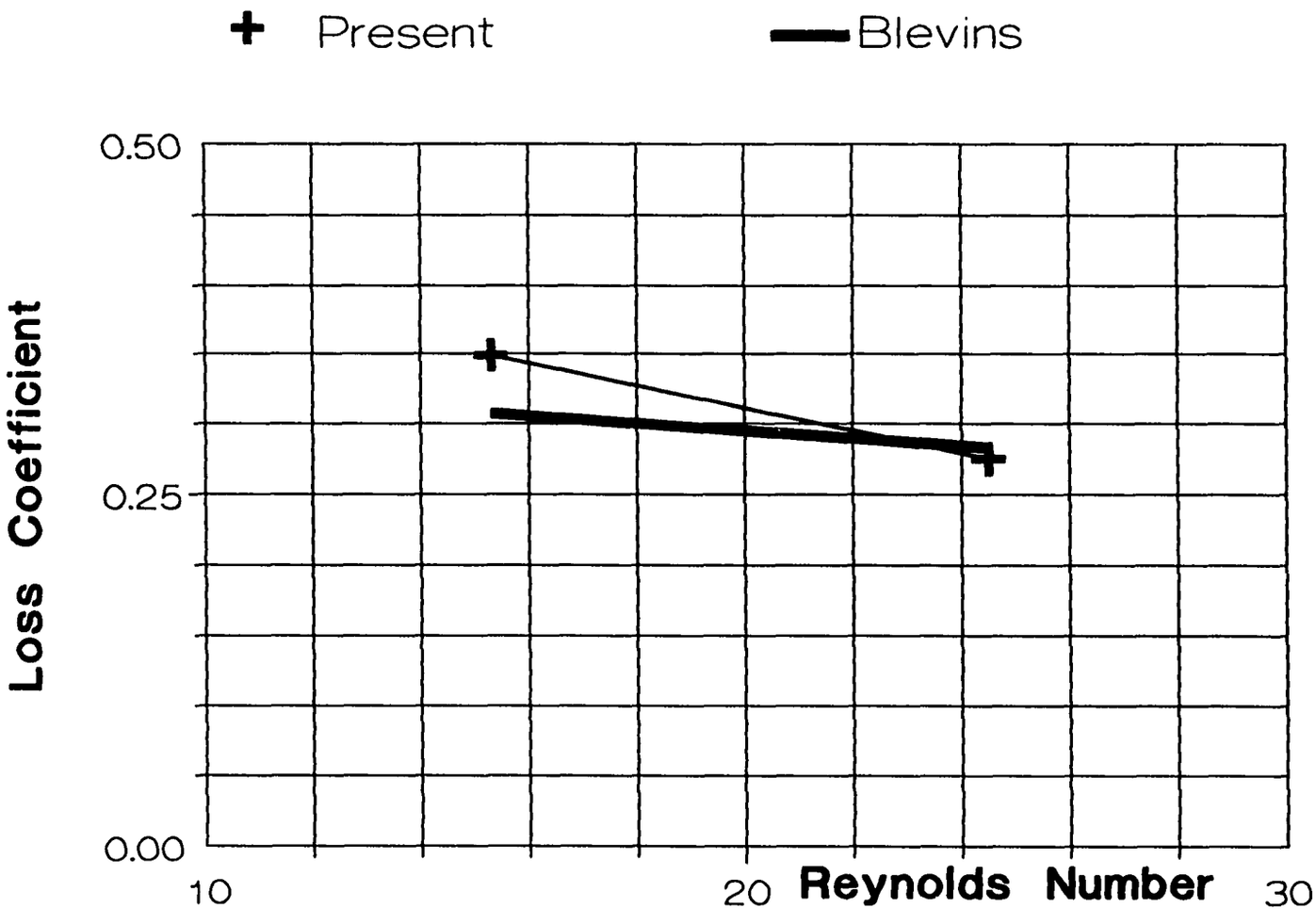

Figure 3.4-1 Loss Coefficient for 90° Curved Duct Flow
R/Dh=5.5; Square Cross-Section Duct

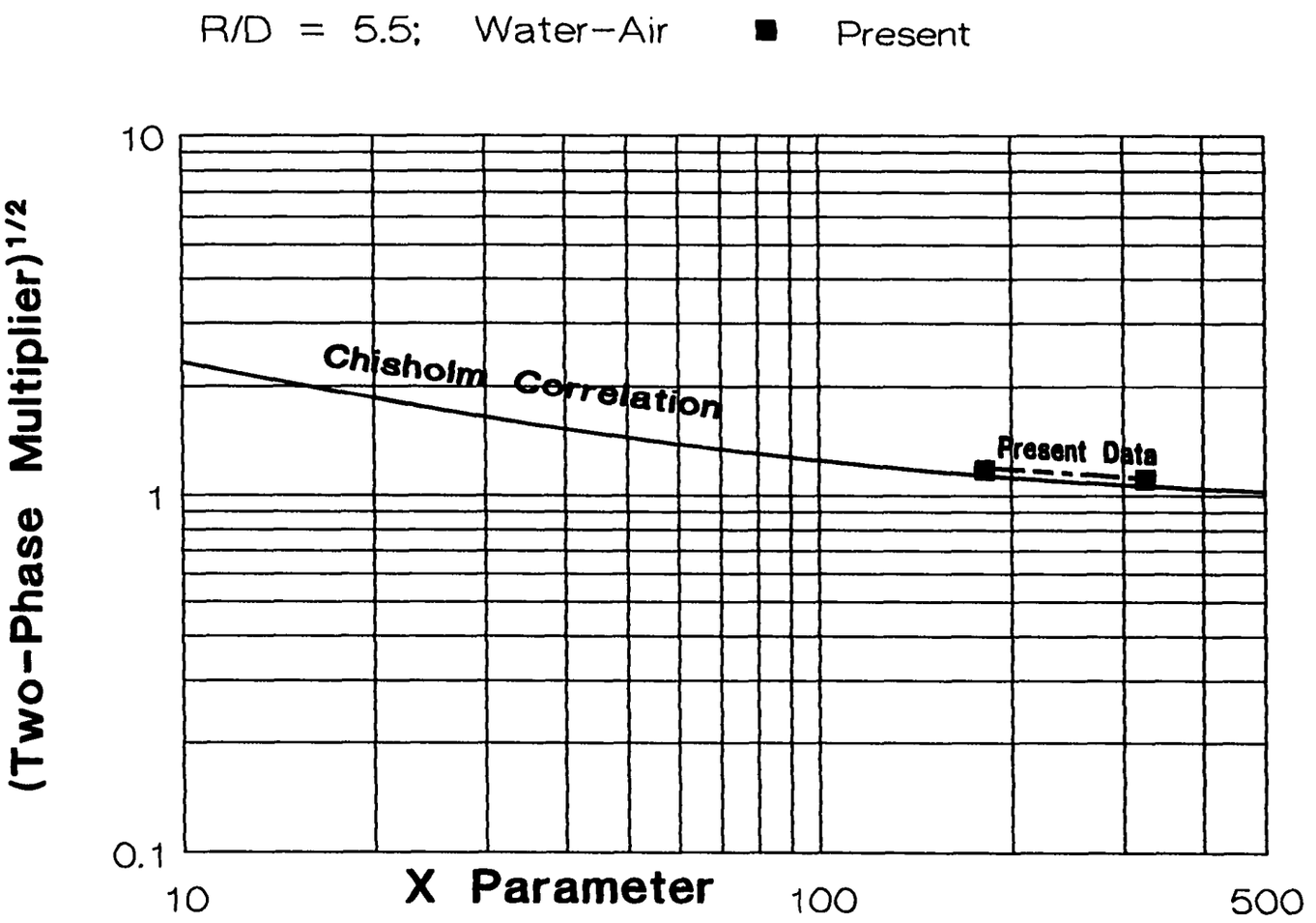

Figure 3.4-2 Two-Phase Loss Multiplier for 90° Curved Duct Flow
R/Dh=5.5; Square Cross-Section Duct

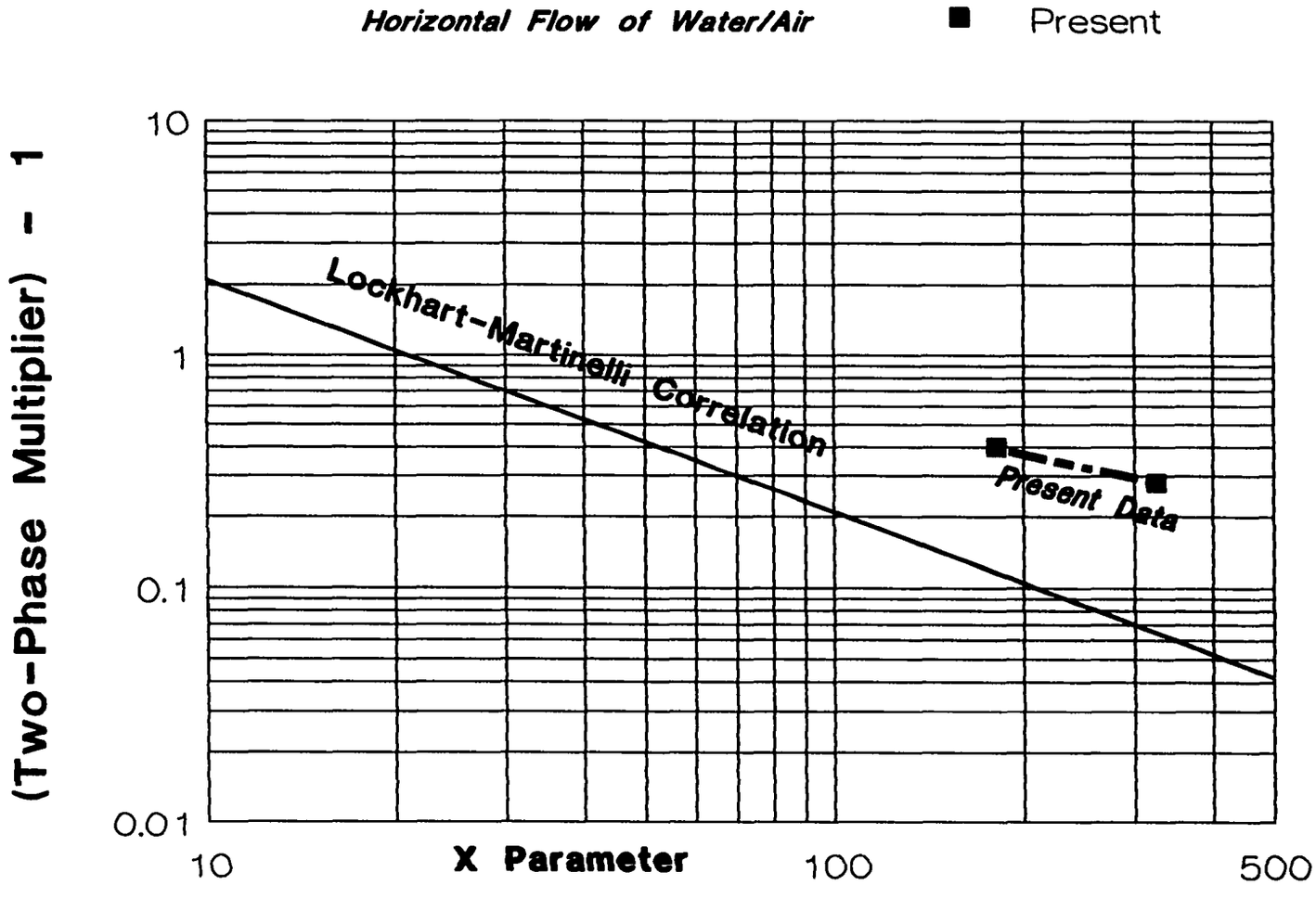

Figure 3.4-3 Two-Phase Loss Multiplier for Horizontal Duct Flow Square Cross Section

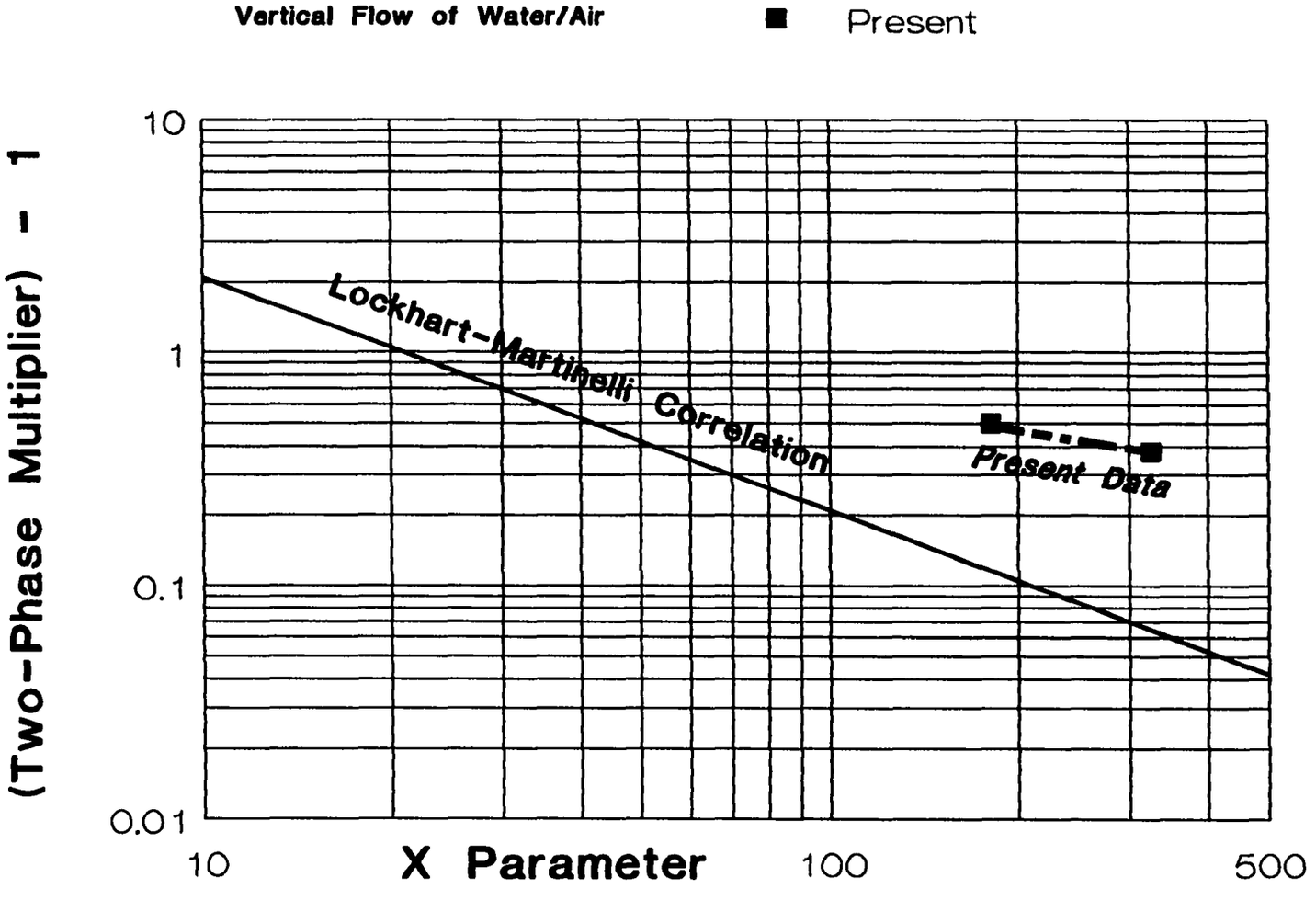

Figure 3.4-4 Two-Phase Loss Multiplier for Vertical Duct Flow
Square Cross-Section Duct

3.5 Experimental Uncertainty

Measurements of the pressure drop and the continuous phase average velocity are used to compute the loss coefficients reported in the previous section:

$$K = \frac{\Delta P}{\frac{1}{2}\rho V^2} \qquad [3.5\text{-}1]$$

Logarithmic differentiation of the equation for the loss coefficient indicates that the experimental uncertainty in the loss coefficient is:

$$\frac{\Delta K}{K} = \frac{\Delta P}{P} - 2\frac{\Delta V}{V} \qquad [3.5\text{-}2]$$

The liquid velocity is determined from the calibrated rotameter. Its uncertainty is 3 percent. The pressure drop is read from the calibrated pressure transducer whose uncertainty is 4 percent. Thus the overall uncertainty in the loss coefficient is:

$$\frac{\Delta K}{K} = 0.04 + 2(0.03) = 0.10 \quad or \quad \pm 10\,\% \qquad [3.5\text{-}3]$$

This analysis represents the random error. The loss coefficients determined in this work for the curved duct agree with the data in the literature to within this random error uncertainty.

As explained in the previous section, the loss coefficient determined for the vertical section is based on the pressure drop across a straight section immediately before the curved duct. Any elliptic effect from the bend that induces an acceleration at this plane will be interpreted as part of the straight section's pressure drop, potentially resulting in too large of a loss coefficient. Similarly, the loss for the horizontal section is determined by the pressure change in a section which is just five hydraulic diameters long and starts just five hydraulic diameters downstream of the bend. Thus some of the flow distortion induced by the bend may be interpreted as increased loss in the horizontal section. Therefore the measurements in the straight ducts include not only the random error analyzed above as approximately 10 percent, but also a bias error. This bias error is in the direction of increased loss coefficient for both the vertical straight duct and the horizontal straight duct. As noted above also, the intent of the present experimental study was to investigate the curved bend and not necessarily the straight duct.

4. MATHEMATICAL MODELS

4.1 Introduction

The analysis of two-phase bubbly flows presented herein is based on a "Two-Fluid" model (also called a Eulerian/Eulerian model). Each phase is considered to be a continuous medium which interpenetrates the other; thus the name "interpenetrating continuum" is also used for this basic modeling approach. It is assumed that both phases occupy each point in the mixture simultaneously. Conservation equations are written for each phase in an Eulerian frame. The dependent variables that arise from the solution of this equation set represent a time average at a given physical location in the computational domain. An observer viewing the two-phase test loop would see, for instance, many bubbles tracking on the inside radius of the curved duct and fewer on the outside of the bend. At any instance in a given location there is either an air bubble or water present. If however , an average is taken over a "long" period (t>>L/W), an average void fraction at each location can be found and its value would lie in the range <0.0,1.0>. This is the interpretation of the void fraction computed by the two-fluid model. Thus the details of the instantaneous flow conditions have been lost to the averaging process and the interaction of the continuous phase and the distributed phase are modeled "collectively".

Water/air or water/oil problems are considered in the present work. The two-fluid model can be employed when the distributed phase is composed of bubbles of only one size. Then the numerical computations accurately model not only the overall flow parameters (such as pressure loss) but also the details of the trajectories. However, the overall flow parameters, such as pressure loss, for a distributed phase with various diameters can be modeled using the present

two-fluid model for a two-phase flow with a distribution of bubble sizes represented by their Sauter mean radius, R_{SM}, where:

R_{SM} = 3*(Volume of the bubbles)/Surface Area of the bubbles.

If the detailed trajectories are required of a dispersed phase which is composed of bubbles of two different diameters then it would be necessary to include another "fluid" in the computations. Additional bubble diameters could be included in the computations by adding other "fluids" for each new diameter introduced. In such a case the approach would be considered a "multi-fluid" model.

4.2 Dimensional Analysis for Two-Phase Flow

There are twelve independent variables for two-phase flow in a straight-curved duct. These are:

$$\alpha_2, \rho_1, \rho_2, W_1, W_2, g, \bar{R}, d_b, \sigma, D_H, \nu_1, \nu_2$$

where: α_2 is the void fraction

ρ is the density

ν is the kinematic viscosity

W is the mean axial velocity

with subscripts 1 and 2 representing the two phases

For the flow phenomenon in question, there are three fundamental quantities: force, length and time. Buckingham-Pi theorem specifies nine (12-3 = 9) independent dimensionless parameters for the problem. Figure 4.2-1 lists the nine dimensionless parameters. These include four familiar groups: two Reynolds numbers (one for each phase), Froude number and Weber

number. Several other combinations of dimensionless groups can be formed to total nine. Described below is one such possible set.

The fifth dimensionless group is the ratio of body forces to drag. This parameter defines how important the shear forces are in the development of the flow. The body force would tend to move the dispersed phase in its preferred direction. Were it not for the drag exerted by the continuous phase on the dispersed phase, all of the dispersed phase would move rapidly in the direction of the body force. The body forces include gravity, centrifugal forces and the lateral lift force. In vertical up flow (along +Z direction) the dominant force in the lateral direction (i.e., x direction in the lateral plane) is the lateral lift force which tends to increase the void fraction along the duct's side walls. This can be seen from this dimensionless group where there is no gravitational effect since the sine of zero degrees is zero and there is no centrifugal effect since the radius of curvature is infinite. In the curved portion of the duct, gravity and the centrifugal terms compete: at small angles in the curved duct, the centrifugal term dominates; however, near the end of the duct (close to 90^{o}) gravity dominates. In between, midway through the curved portion the two forces are comparable in magnitude. The lateral lift force is a second order effect in the bend since centrifugal force is proportinal to W_1^2 while the lateral lift force is proportional to $W_1(W_1-W_2)$.

The sixth dimensionless group is formed by the ratio of inertial forces to drag force. This defines how well the dispersed phase can follow the continuous phase. When this parameter is large the dispersed phase will not follow the continuum flow well. By considering this group it is seen that this can occur if the bubble is large or very light compared to the continuous phase; if the drag is very low or if the relative velocity is low.

The seventh group is the ratio of bubble diameter to the hydraulic diameter of the duct. This parameter is seen to be important when attempting to use subscale model for the testing of two-phase flow problems to determine the full scale fluid mechanics of a complex geometry, such as subscale model testing of flows in nuclear reactor cores or large pumping systems.

The eighth group is the ratio of densities of the two phases. This is an important parameter as many numerical experimenters can testify when attempting to model water/air flow where the density is nearly a thousand to one.

The ninth group is the ratio of centripetal force to viscous force.

12 Independent variables: $\alpha_2, \rho_1, \rho_2, W_1, W_2, g, \overline{R}, d_b, \sigma, D_H, \nu_1, \nu_2$

$\Rightarrow 9$ *Dimensionless Parameters*

1- Inertia/Viscous Forces (Phase 1): $\frac{W_1 D_H}{\nu_1}$ Reynolds Number

2-Inertia/Viscous Forces (Phase 2): $\frac{W_2 D_H}{\nu_2}$ Reynolds Number

3-Inertia/Gravity: $\frac{\alpha_1 W_1^2 + \alpha_2 W_2^2}{g D_H}$ Froude Number

4-Inertia/Surface Tension: $\frac{\left(\alpha_1 W_1^2 + \alpha_2 W_2^2\right)\rho_1 d_b}{\sigma}$ Weber Number

5-Body Forces/Drag: $\frac{(\rho_1-\rho_2)\left\{g\sin\theta - \frac{\left[\alpha_1 W_1^2 + \alpha_2 W_2^2\right]}{\bar{R}} + (W_1 - W_2)\frac{W_1}{D_H}\right\}}{\frac{C_D \rho_1 (W_2 - W_1)^2}{d_b}}$

6-Inertia/Drag: $\left(\frac{\rho_1}{\rho_2}\right)\left(\frac{\alpha_1}{\alpha_2}\right)\left(\frac{d_b}{D_H}\right)\frac{1}{C_D\left\{1-\frac{W_1}{W_2}\right\}}$

7-Geometric Parameter: $\frac{d_b}{D_H}$

8-Density Ratio: $\frac{\rho_2}{\rho_1}$

9-Centripetal/Viscous: $\frac{\frac{\left(\alpha_1 W_1 + \alpha_2 W_2\right) D_H}{\nu_1}}{\frac{\bar{R}}{D_H}}$

Figure 4.2-1 Dimensional Analysis for Straight and/or Curved Duct

4.3 Governing Equations

4.3.1 Introduction

The two-fluid equations are derived by Eulerian time (or statistical) averaging of the Navier-Stokes equations with the interaction between phases incorporated into an interfacial momentum force. This averaging technique results in a "filtered" set of equations which do not contain the details of the interfacial interactions [Drew (1983)]. While these details are essentially unwanted, the averaging process does result in a loss of information which is then supplemented by constitutive equations, employed to model the interfacial momentum forces. These constitutive equations are one of the areas of investigation that merits additional work. The constitutive equations which are used in the present work are applicable to bubbly flows; void fractions limited to approximately 0.3 to 0.5. At higher void fractions bubbles coalesce to forms slugs and at even higher void fractions can stratify completely and/or form annular flow. The present code has been demonstrated to be robust and stable even as local void fractions approach unity (but with bubbly flow constitutive equations). However, additions to the constitutive equations are needed to treat such regions rigorously.

4.3.2 Interfacial Momentum Transfer

The interfacial force used in this work comprises the drag force and the lateral lift force. Additional forces which under certain circumstances might also be considered are the virtual mass and the Basset forces. The virtual mass and Basset forces are transient forces which would be included as the present algorithm is extended to compute unsteady flow processes. The virtual

mass force is the force required to accelerate the apparent mass of the continuous phase when the relative velocity between the phases change. The Basset force arises from the acceleration induced changes of the viscous drag and the unsteady boundary-layer development.

4.3.2.1 Drag Force

The drag force is modeled by a constitutive relation based on the steady-state drag of an isolated spherical particle. The model used was that utilized in the Los Alamos code TRAC (1978):

$$C_D = 240 \qquad \text{for } Re_b < 0.1 \qquad [4.3.2.1\text{-}1]$$

$$C_D = 24/Re_b \qquad \text{for } 0.1 < Re_b < 2 \qquad [4.3.2.1\text{-}2]$$

$$C_D = 9.35/Re_b^{0.68} \qquad \text{for } Re_b > 2 \qquad [4.3.2.1\text{-}3]$$

$$C_D = 0.1 \qquad \text{for } Re_b > 300{,}000 \qquad [4.3.2.1\text{-}4]$$

$$\text{where } Re_b \text{ is the bubble Reynolds number} = \frac{\rho_l V_{rel} d_{bub}}{\mu_l}$$

For very low Reynolds numbers the drag is given by the Stokes formulation (i.e., $24/Re_b$) which is analytically derived by neglecting inertial terms. This is only good for symmetric flow around a sphere, generally $Re_b < 2.0$. At moderate Reynolds numbers, inertial forces cause an asymmetric flow and the boundary layer separates and a stationary ring vortex forms behind the sphere. As the Reynolds number increases the ring vortex oscillates until it detaches and forms a wake downstream of the sphere for a Reynolds number of 500. The drag coefficient can be approximated in these last two regimes as $9.35/Re^{0.68}$. This correlation fairly fits the drag coefficient that decreases smoothly to about 0.4 at a Reynolds number of about 300,000. This is

called the critical Reynolds number. At this point the boundary layer becomes turbulent and the point of separation is delayed from about 82° to 120°. The drag coefficient is reduced to 0.1. The drag coefficient then slowly increases with increasing Reynolds numbers. Although the bubble Reynolds number varies locally in the duct problem, typical levels of Reynolds number are 100-300.

Other factors which affect the drag coefficient are non-sphericity of bubbles, surface roughness (which could be important for particle laden flows) and relative turbulence intensity. A distributed phase which is not spherical will have an increased drag coefficient. Some correlations based on a sphericity factor were given in Jayanti and Hewitt (1991). Increased surface roughness can lower the critical Reynolds number and hence cause a lowering of the drag coefficient. A similar effect of lowering the critical Reynolds number can occur as the turbulence intensity levels increase.

4.3.2.2 Lateral Lift Force

Lateral or transverse lift forces are generated on the distributed spherical phase due to particle rotation or because the distributed phase moves through a velocity gradient or shear flow.

In the case of particle rotation, velocity is added to the side of the sphere where the velocity is in the same direction of rotation and thus effectively increasing the velocity on this side while retarding it on the other side. Due to the associated static pressure change, the particle tends to move towards the direction of higher relative velocity. This is often called the Magnus effect. Drew and Lahey (1987) and Antal, Lahey and Flaherty (1991) compute a lateral lift force on particles by postulating that the particles rotate with an angular velocity equal to one-half of

the local velocity gradient. However, experimental verification of bubble rotation rates has not been published so that the physical underpinning of this theory has not been established.

Saffman (1965 and 1968) computed the lift force for a sphere moving through a simple shear flow:

$$F_{lateral} = \frac{81.2}{4\pi} \frac{\mu V_{rel} R^2_{bub} \kappa^{0.5}}{\nu^{0.5}} \qquad \text{where: } \kappa = \nabla \bar{V}_{abs} \qquad [4.3.2.2\text{-}1]$$

This result is valid only for very small Reynolds numbers and low shear rates. Mei and Klausner (1994) extended Saffman's work for finite Reynolds number and finite shear rates. Their lift force reduces to Saffman's as the Reynolds number approaches zero but has a lower value elsewhere.

Zun (1980) studied the forces that a bubble in vertical flow experiences. These include: the Magnus effect; the influence of the liquid velocity gradient; the static pressure change over the cross section due to turbulence; and the Magnus force due to circulation of liquid around the bubble together with the Bernoulli force due to stronger back flow on the wall side of the bubble. He concluded that the effect of the liquid velocity gradient is the largest influence on bubble migration.

The shear lift force on solid particles with both phases going downwards in a pipe with a sudden expansion was studied by Founti et. al. (1994). They conclude that the dominant lateral force is that to due to the transverse lift force due to shear gradient as formulated by Saffman. Their analysis shows that the Magnus effect is of second order compared to the Saffman effect. For the vertical down flow, the solid particle velocity is greater than the corresponding velocity of the fluid. The transverse shear lift act to disperse the solid particles towards the pipe walls.

The theory of Saffman with Mei and Klausner's correction was used in this work.

4.3.3 Fluid Turbulence Modification Induced by the Bubbles

The transport equations for k and ε are given below in *section 4.3.4 Equation Development.* These equations include additional source terms S_k in the turbulent kinetic energy equation and S_ε in the dissipation equation. These additional terms arise in the development of the two-phase turbulent transport equations from the momentum equations. The presence of the interfacial momentum exchange force term in the momentum equation results in these terms appearing in the turbulence model.

$$S_k = 2*CNST2\,(C_t\text{-}1)\,k \qquad \text{and} \qquad [4.3.3\text{-}1]$$

$$S_\varepsilon = 2*CNST2\,(C_t\text{-}1)\,\varepsilon \qquad [4.3.3\text{–}2]$$

where: C_t is the ratio of dispersed phase to continuous phase turbulent velocity fluctuation. It is set equal to 1.5 in this work based on Wang (1994).

These source terms result in an increase in turbulent kinetic energy by approximately 10 percent for two-phase (inlet void fraction of 0.07) computations compared to the same with everything else the same but with these terms turned off.

The mixing length relation, $l = \kappa y$, is modified to account for the presence of the distributed phase. A two-phase flow multiplier is used to account for this.

The present computation uses modified von Karman's constant, given below:

$$\kappa_{TP} = \Phi_{LO}^2\,\kappa \qquad [4.3.3\text{-}3]$$

where: $$\Phi_{LO}^2 = \left[1 - x_2 \frac{d_{bub}}{D_H}\left(\frac{\rho_2}{\rho_1} - 1\right)\right]$$

and x_v is the quality or mass fraction of the dispersed phase

The concept of Neti and Mohammed (1990) has been modified to include the ratio of bubble diameter to duct hydraulic diameter. This modification is suggested by the bubble rise velocity correlations presented by Govier and Aziz (1972). Bubble rise velocities in an infinite medium can be calculated by equating the drag of a spherical particle to its buoyancy. Govier and Aziz (1972) present an empirical correlation for bubble rise velocities in ducts in which the ratio of d_{bub}/D_H is a parameter. This concept was adapted to the present algorithm for the two-phase correction to the von Karman constant. This modification to the Neti and Mohammed (1990) approach seems to be necessary in the present computations for two reasons. The void fractions studied currently (as high as 0.3) are much higher than previous bubbly two-phase flow computations. Additionally, the ratio of bubble diameter to duct hydraulic diameter is also much larger.

4.3.4 Equation Development of the Governing Equations

The two-phase turbulent flow calculations reported in *Section 6, Computational Results*, required the solution of ten partial differential equations at each node. This includes three momentum equations for each of the two phases, a pressure correction equation, a void fraction equation, transport equations for the continuous phase's turbulent kinetic energy and turbulence kinetic energy dissipation rate. Some calculations were performed with a separate k-ε model for the distributed phase and for these calculations twelve partial differential equations were solved.

The sections below give a brief overview of the governing equations. More details are given in the Appendices:

Appendix I	Φ Momentum Equation
Appendix II	X Momentum Equation
Appendix III	Y Momentum Equation
Appendix IV	Pressure Correction Equation
Appendix V	Void Fraction Equation
Appendix VI	Transport Equation of Turbulent Kinetic Energy
Appendix VII	Transport Equation for the Dissipation

4.3.4.1-the Momentum Equations

$$\nabla \bullet \left(\alpha \rho U_i U_j\right)_k = -\alpha_k \nabla p + \nabla \bullet \alpha_k \tau + \alpha_k \rho_k \bar{g} + \bar{F}_D = 0 \qquad [4.3.4.1\text{-}1]$$

where: k=1 is the continuous phase and k=2 is the distributed phase

j=1 through 3 denotes the three coordinate directions

i= 1 for U Momentum Equation; 2 for V Momentum Equation and

3 for W Momentum Equation

These equations represent the Reynolds time averaged equations. Inertial forces must balance the sum of the pressure forces, shear forces, body forces and the interfacial momentum

exchange force. In the present work the interfacial momentum exchange force, F_D , includes drag forces and the lateral lift force. Unsteady calculations would incorporate the virtual mass force and the Basset force also into this term. These terms are discussed in *Section 4.3.2, Interfacial Momentum Transfer.*

4.3.4.2 Continuity Equations

There are two continuity equations for the two-phase flow problem. These equations must be used to determine the local pressure and the volume fraction of the two phases. Because the volume fractions must sum to unity there are two unknowns: the pressure and the void fraction (i.e., the volume fraction of the dispersed phase). In the interest of accuracy it is preferable to solve for the smaller volume fraction. It would be possible to use one of the species' mass conservation equations to determine the pressure and the other for the void fraction. However, as the two fluids are at the same pressure at any given location it would be physically unrealistic to derive the pressure solely by considering one of the phases. Since the continuity equations are linear the two equations can be combined. The two equations are summed to derive the pressure correction equation. The two equations are subtracted to form the void fraction equation. However, if this approach is taken it is clear that when the densities of the two phases are disparate the heavier phase will dominate the equation. This can result in poor conservation of the lighter phase (Carver, 1986). To help with this each of the continuity equations are divided by its reference density before they are combined.

4.3.4.2.1-Pressure Correction Equation

$$\frac{\nabla \bullet (\alpha \rho U_i)_1}{\rho_{1_{ref}}} + \frac{\nabla \bullet (\alpha \rho U_i)_2}{\rho_{2_{ref}}} = 0 \qquad [4.3.4.2.1\text{-}1]$$

The above equation is used to derive an equation in p', which is the pressure correction. This is done by relating the velocity component corrections to the pressure correction. Further details are given in *Section 5.4.2.2 Details of the Pressure Correction Algorithm.*

4.3.4.2.2-Void Fraction Equation

$$\frac{\nabla \bullet (\alpha \rho U_i)_1}{\rho_{1_{ref}}} - \frac{\nabla \bullet (\alpha \rho U_i)_2}{\rho_{2_{ref}}} = 0 \qquad [4.3.4.2.2\text{-}1]$$

The above equation is used to derive an equation in α_2 , the void fraction. The present experience indicates that this is the critical step in the creation of a stable and robust two-fluid algorithm. The void fraction algorithm is discussed in detail in *Section 5.4.2.1 Details of the Present Void Fraction Algorithm.*

4.3.4.3 Turbulence Transport Equations for the Continuous Phase

The governing equation for the transport of turbulent kinetic energy k is:

$$\rho U_i \bullet \nabla k = \nabla \bullet (\Gamma_k \nabla k) + G - \rho \varepsilon + S_k \qquad [4.3.4.3\text{-}1]$$

The convection of turbulent kinetic energy is balanced by diffusion, production and dissipation and bubble induced turbulent kinetic energy. The derivation of these equations follows the general suggestions found in Launder and Spalding (1972). Details pertaining to the development of these equations are given in Appendices VI and VII.

The governing equation for the dissipation of turbulent kinetic energy ε is:

$$\rho U_i \bullet \nabla \varepsilon = \nabla \bullet \left(\Gamma_\varepsilon \nabla \varepsilon\right) + \frac{C_1 \varepsilon}{k} G - \frac{C_2 \rho \varepsilon^2}{k} + S_\varepsilon \qquad [4.3.4.3\text{-}2]$$

where: C_1 and C_2 are empirical constants

G is the production of turbulent kinetic energy

ε is the turbulent kinetic energy dissipation rate

k is the turbulent kinetic energy

S_k and S_ε are the source terms due to the presence of the distributed phase

Γ_k and Γ_ε are the diffusion coefficients for k and ε, respectively

Convection is balanced by diffusion, production and dissipation and a bubble induced contribution.

The bubble induced production and dissipation of turbulent kinetic energy is discussed in *Section 4.33, Fluid Turbulence Modification Induced by Bubbles.*

4.4 Turbulence Modeling for the Dispersed Phase

It is expected that for bubbly flows the turbulence in the dispersed phase will be much less important in determining the overall flow field compared to the turbulence in the continuous

phase [Besnard et. al., (1991)]. Then it might be sufficient to model the dispersed phase turbulent eddy viscosity by treating the bubbles as particles suspended in a turbulent stream. The theory of Tchen (1947) and Peskin (1959) as modified by Soo (1967) gives a ratio of particle turbulent viscosity to the continuous phase turbulent viscosity ("particle turbulent Prandtl number") by computing the statistics of an individual particle interacting with the turbulent eddies of the continuous phase. The particle turbulent Prandtl number depends on the ratio of particle impulse response time to the time a fluid particle remains in a velocity correlated region; this ratio is called the impulse response parameter and is denoted by K. It is similar to the momentum exchange coefficient. Figure 4.4-1 is a reprint from Soo (1967) which shows the relationship between particle turbulent Prandtl number and the impulse response parameter. The ratio of the Lagrangian microscale of turbulence to the Eulerian scale (i.e., λ/λ_E) is important in determining this relationship. For a spherical particle or bubble:

$$K = \frac{\sqrt{\pi}}{18} \mathrm{Re}_{particle} \frac{\rho_{particle}}{\rho_{continuous}} \frac{d_{particle}}{\lambda} \qquad [4.4\text{-}1]$$

When the "particle" is an air bubble in a liquid the density ratio is approximately 1/1000, and K is small. Thus the particle eddy diffusivity is seen to approach unity. Most of the calculations in this dissertation were carried out by setting the bubble turbulent Prandtl number equal to unity.

Computations were also done with two two-equation turbulence models (i.e., a four equation model). These calculations when performed for the bubbly two-phase water/air flow did not differ recognizably from the simpler model with turbulent Prandtl number equal to unity. This is reasonable based on the discussion above for very light particles. The four equation

model was also used for the water/oil driven cavity problem. In this case the density ratio is not as high as 1000:1 but close to 1.13:1. It might then be expected that the simple assumption of unity turbulent Prandtl number would perhaps not be completely adequate. Indeed the results were sometimes better for the water/oil flow when using the more elaborate turbulence model (*see Section 6.2.1, 2D Driven Cavity)*. There is little reported in the literature concerning the use of a separate k-ε turbulence model for the distributed phase. Kashiwa and Gore report on a four equation turbulence model which is similar to that used here except that the contribution from the source terms S_k and S_ε are partitioned between the two-phases based on a partitioning function a_{kl} which expresses the fraction of energy due to the result of interpenetrating motion going into phase k. This parameter is determined based on classical dynamics. When two masses undergo an elastic collision, a portion of the kinetic energy is converted into disordered kinetic energy. If the masses of the two colliding bodies are m_1 and m_2 then:

$$a_{12} = \frac{m_2}{m_1 + m_2} \qquad [4.4\text{-}2]$$

By analogy with the inelastic collision problem the partitioning function for a two-phase water/air flow is given as:

$$a_{water/air} = \frac{\rho_{air}}{\rho_{water}\left(\frac{k_{water}}{k_{air}}\right)^3 + \rho_{air}} \qquad [4.4\text{-}3]$$

There is an intermediate approach between assuming a bubble turbulent Prandtl number equal to unity and solving an additional two-equation turbulence model. The theory of Tchen (1974) and Peskin (1959) [which is the basis of Figure 4.4-1] can be incorporated into the model, so that a local bubble turbulent Prandtl number is implicitly calculated. This approach appears to be promising especially for flows where the bubble or particle density approaches (or exceeds) that of the continuous phase. This approach has been used by Mostafa and Mongia (1987) for turbulent bubbly jet flows.

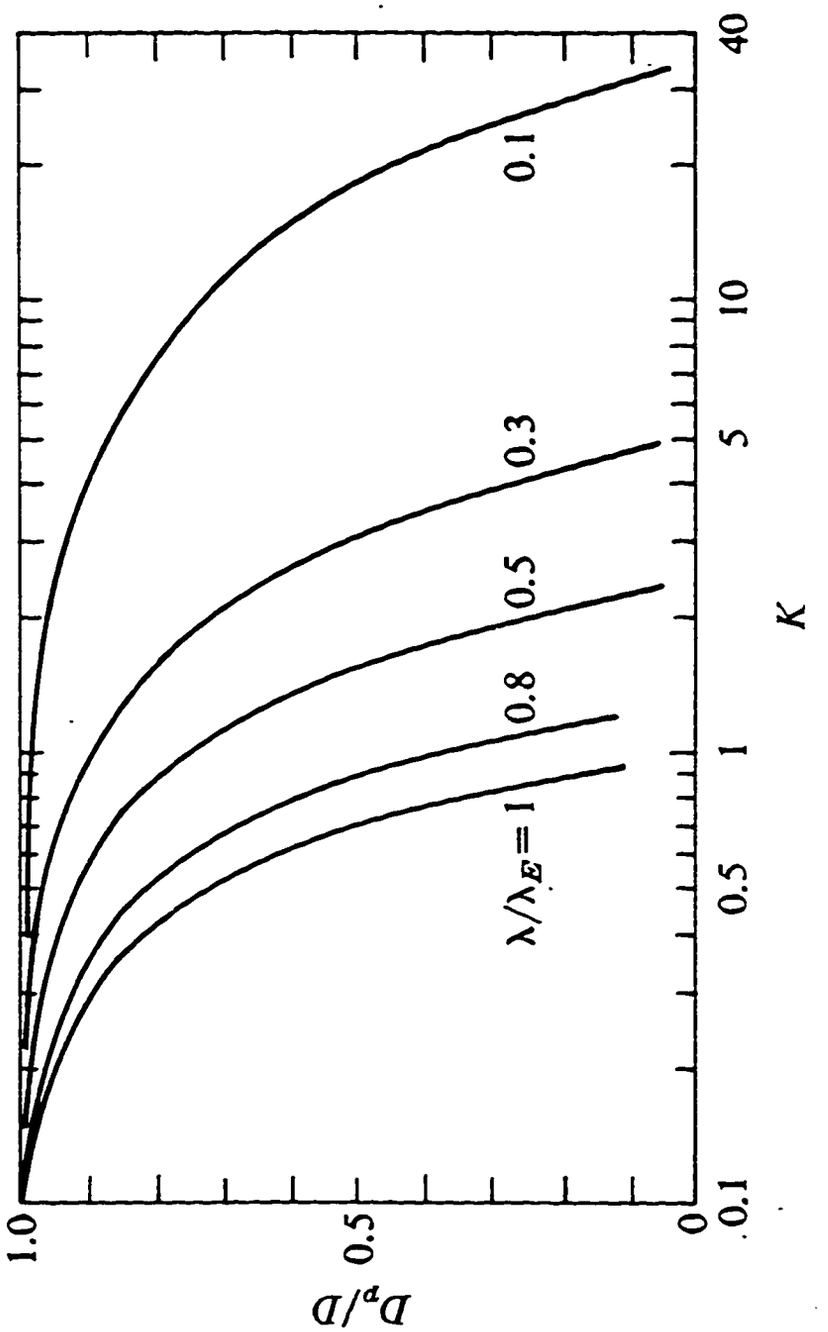

Figure 4.4-1 Ratio of Dispersed Phase's to Continuous Phase's Turbulent Diffusivity vs Impulse Response Function

4.5 Classification of Flow Problem Solution

Differential equations modeling flow and heat transfer and the associated numerical solution techniques can be classified as parabolic, elliptic and hyperbolic. An important additional class is the partially parabolic technique which lies somewhere between parabolic and elliptic. Equations describing subsonic flows are actually elliptic in nature, with pressure disturbances being transmitted in all directions. Supersonic flows or unsteady subsonic flows are governed by hyperbolic equations in which information is transferred in preferred directions called characteristics. Problems which in rigorous terms must be conceded to be elliptic can often be approximated by a parabolic (or marching) solution. The most well known parabolic approach is a boundary layer calculation, which can use the velocity distribution in the longitudinal direction along a body to march downstream from lateral plane to the next plane. This procedure is numerically efficient as data needs to be stored only at the current lateral plane. In the parabolic procedure, information is transmitted downstream by convection alone, with diffusion and pressure transmission taken to be of second order.

The conditions for curved duct flow which require a fully elliptic procedure were discussed in *Section 2, Literature Review*. It was seen there that curved duct flow with a mean radius to hydraulic diameter of 2.3 or less would require a fully elliptic solver for laminar flows. Restrictions pertaining to turbulent duct flow would not be as stringent: an elliptic solver would not be required until the duct mean radius reached approximately 1.5 or smaller.

A partially parabolic approach was proposed by Pratap and Spalding (1976) so as to relax some of the constraints of the parabolic procedure while still maintaining an efficient computational algorithm. Their partially parabolic procedure requires that the flow be free of

separation and recirculation zones, so that convection operates only in the downstream direction; that the Reynolds number be high enough so that diffusion in the longitudinal direction may be neglected; and that pressure is the dominant transmitter of downstream influences.

The present procedure is a hybridization of the parabolic and partially parabolic procedures. The present algorithm was written to be partially parabolic. The pressure at each node is stored three-dimensionally. Some test cases were run to show that downstream influences were felt upstream (a simulated screen in the duct was run, and the presence of the screen was seen in the solution at stations upstream of the screen). The complete partially parabolic procedure is accomplished by allowing multiple sweeps through the computational domain. Multiple sweeps through the domain for the two-phase flow is computationally very expensive. The multiple sweeps allow the pressure downstream to influence the upstream planes. However, for the presently used duct radius ratio of 5.5 the complete partially-parabolic procedure is not required. It will be seen in *Section 6.,Computational Results*, that reasonable agreement with the Humphrey data for a curved duct with a radius ratio of 2.3 was achieved with the present numerical procedure. However, it is recognized that at radius ratios smaller than 5.5 the complete partially parabolic procedure might yield improved predictions, just as the completely elliptic procedure will be required at radius ratios of approximately 1.5 or lower.

The present computational procedure is not a complete partially parabolic procedure since only one pass is done through the computational domain. It differs from a fully parabolic technique in the way that the pressure gradient term in the longitudinal momentum equation is handled. In the fully parabolic approach two separate pressure fields are used: one for the lateral plane and another for the longitudinal direction. The longitudinal momentum equation in the fully parabolic procedure assumes the same value of pressure *at all nodes on a given lateral*

plane for the pressure gradient term, $\frac{\partial \bar{p}}{\partial z}$, which is calculated from conservation of global mass across a lateral plane. The present procedure uses the same pressure field for all three momentum equations, and thus calculates a pressure gradient that varies from node to node. Because of this varying pressure gradient in the lateral plane for the longitudinal momentum equation the resulting longitudinal velocities will be different from that obtained in a fully parabolic procedure. Thus there will be a gradient of the term $\frac{\partial p}{\partial z}$ in the radial direction inside the curved duct. This gradient would not exist in the fully parabolic procedure of Patankar and Spalding (1972). This present procedure is expected to better resolve the radial variation of flow variables, such as the void fraction (see *Section 6. Computational Results)* which varies strongly in the radial direction.

5. NUMERICAL SOLUTION ALGORITHM

5.1 Introduction

The partial differential equations which must be solved to predict single and two-phase flow in the straight/curved/straight duct have been presented in an earlier section (4.3*Governing Equations*). Closed form solutions for such equations are not feasible and it is necessary to resort to numerical techniques to obtain a solution. The partial differential equations must be "discretized", i.e., written in an algebraic form and then the set of linearized equations at discrete points over the computational space. The following sections explain the details of the finite difference grid (i.e., the discrete points at which parametric variables are computed); the discretizing of the partial differential equations and the solution technique of the resulting system of linear algebraic equations.

5.2 The Finite Difference Grid

The system of equations will be solved on a curvilinear, orthogonal grid. This means that the coordinate system may have one or more axes that are curved in space and that at any node in the grid the three coordinate axes [i.e., (x,y,z) for the straight duct or (x,y,ϕ) for the curved duct] are orthogonal. Figure 5.2-1 shows the axis system both in the straight and in the curved sections of the duct. The cross section is pictured as a general rectangular section. While the experimental work was done in a loop constructed with a square cross section, computational runs were made for rectangular cross sections of various aspect ratios.

The primitive variables pressure (p), turbulent kinetic energy (k), dissipation rate (ε),and void fraction (α) are resolved on primary nodes, i.e., the intersection point of the three axes. The three velocity components are determined at secondary nodes which are at locations shifted mid-way between primary nodes in the x direction for the u velocity component; shifted in the y direction for the v component and shifted in the z direction for the w component. Such a mesh is called a "staggered grid" [Patankar, (1980)]. The staggered grid is shown for the u and v velocity components on two-dimensional slices through the three-dimensional space in Figure 5.2-2. The locations of the u and v velocity grids are more evident here. Figure 5.2-3 shows the location of the w component along a longitudinal slice through the computational domain. W velocity component is defined halfway between primary nodes in the z direction. The control volume projection onto this two-dimensional plane is also shown in this figure. This figure also illustrates the fact that while the u and v velocities are shifted in the x and y directions respectively, that they are *not* shifted in the z direction (consider the location of the v component in Figure 5.2-3). The control volume for the u velocity component is shown on a lateral plane in Figure 5.2-4. By using the staggered grid the pressure gradient in the x direction for the u velocity component will be located exactly at the two ends of the control volume (i.e., nodes P and W). This figure also illustrates the subscript nomenclature for the v velocity components used in the equation development carried out in the appendices. Generally, the compass directions N, S, E and W are used to describe the location of a component or node. The control volume for the v velocity component is shown in Figure 5.2-5. Again, the pressures required in the Y momentum equation will be those at the end of the faces of the control volume (i.e., nodes P and S). The subscript notation for the u component velocities is shown on this figure. The three-dimensional control volumes for u, v, w and the variables p, k, ε, and α are shown in

Figures 5.2-6 through 5.2-9. Although these are somewhat more complex than the two-dimensional projections of Figures 5.2-2 through 5.2-5 it is these three-dimensional volumes that are used when discretizing the governing equations. As noted above, all three velocity components show that they are shifted a half node space in their respective direction (i.e., x direction for the u component, y direction for the v component and z direction for the w component). Figure 5.2-9 shows that the variables pressure, turbulent kinetic energy, dissipation of turbulent kinetic energy and void fraction are defined at the primary nodes. Any other transported properties, such as temperature, would also be defined at these primary nodes.

The benefits of using a staggered grid are:

1- The procedure enhances stability of the algorithm. The staggered grid is one of the most common approaches (although not the only one) to solving a problem that arises in the solution of the incompressible Navier Stokes equations. In such a set of equations pressure does not appear explicitly in either the momentum equations or the continuity equation. Pressure occurs only as a gradient term, (i.e., dP/dx). This does not occur for compressible flow, since the continuity equation contains the unknown density, to which pressure is directly related (e.g., pressure is directly proportional to density if the perfect gas law is being used). In calculating the velocities, the pressure to either side of a node will be used if the velocity components are solved for at a primary node. As illustrated by Patankar (1980), with a one-dimensional explanation, a pressure field computed at adjacent nodes in the x direction of: 500 100 500 100 500 100 500 would be acceptable (although obviously quite physically unreasonable) since at any node the gradient dP/dx would be computed as zero. This is called the "checkerboard" problem from the two-dimensional equivalent of the example cited above.

2- the calculation of the continuity equation is made easier since the fluxes required at the faces of the volume are explicitly defined (with the shifted u, v, etc.).

3- the calculation of any of the transported quantities (such as turbulent kinetic energy or dissipation of TKE or void fraction) is simplified since the required fluxes are readily available.

4- the calculation of the velocity components themselves is simplified since the pressures needed at the faces of the control volumes are explicitly given.

While the staggered grid does offer the benefits listed immediately above, the specification of boundary conditions becomes more complex.

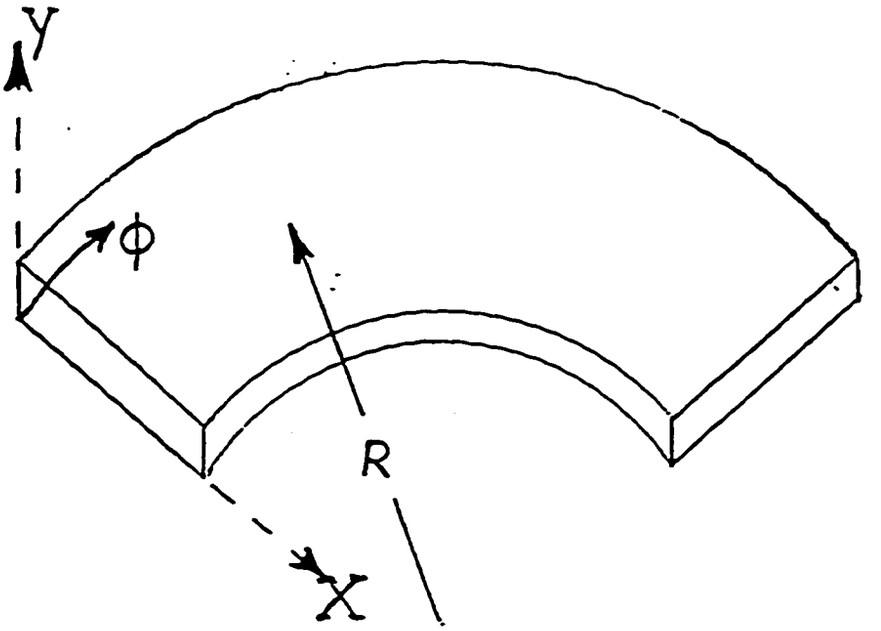

CURVED DUCT

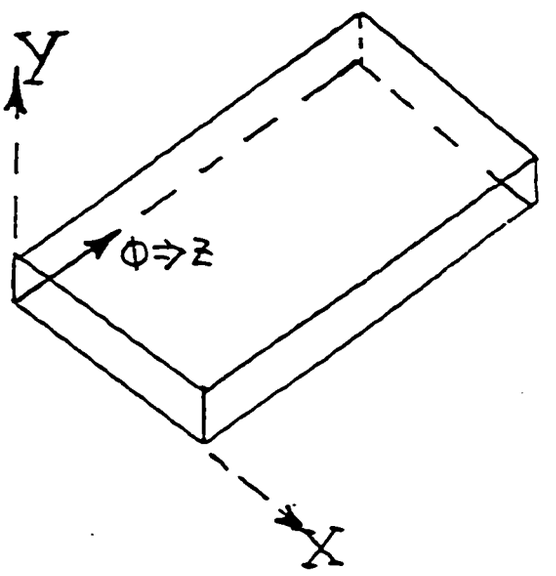

STRAIGHT DUCT

Figure 5.2-1 Axis System

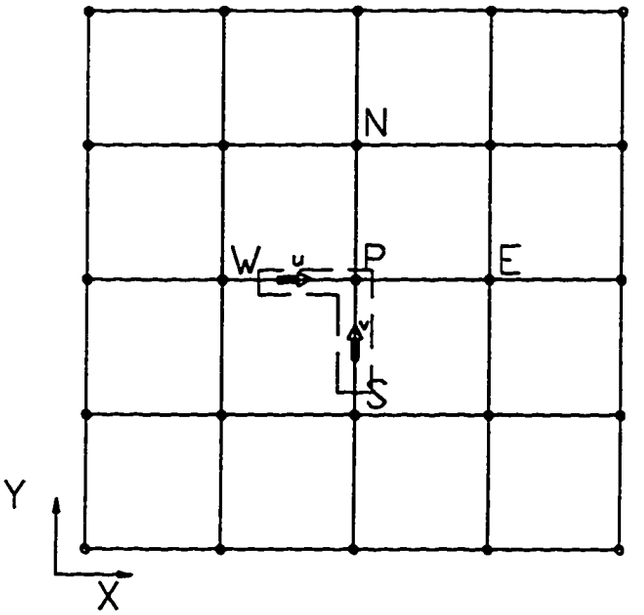

Lateral Plane (i.e. X - Y Plane)
Location of u and v velocities

Figure 5.2-2

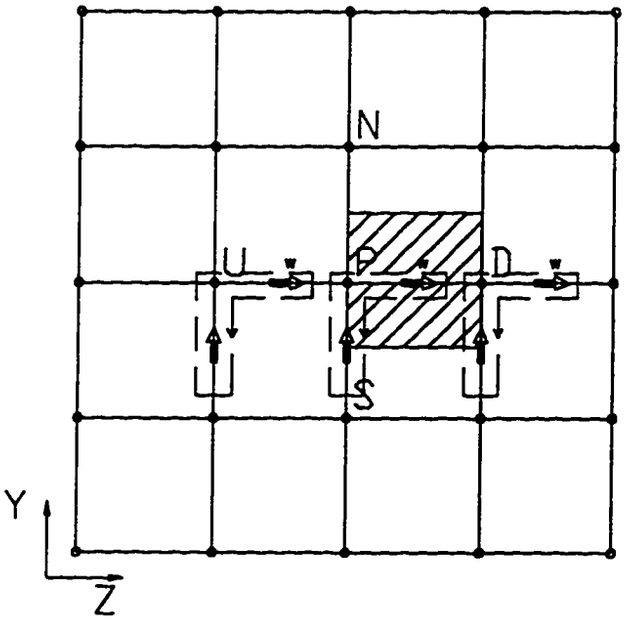

Longitudinal Plane (i.e. Y - Z Plane)
Location of w velocities
and Control Volume for W Velocity

Figure 5.2-3

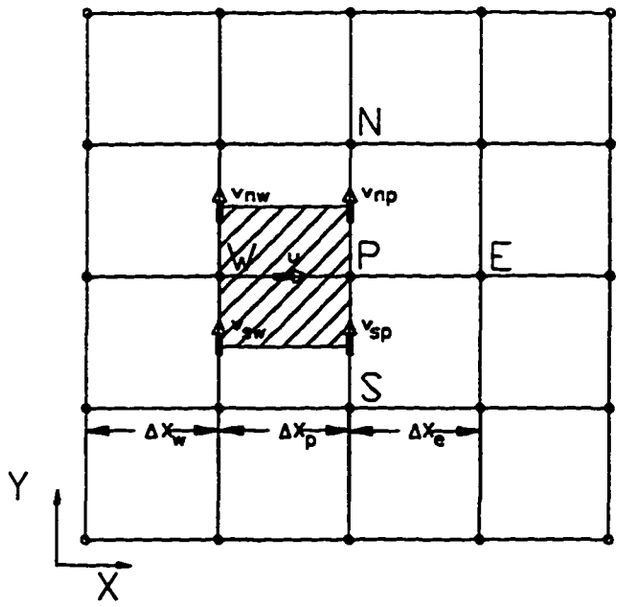

Lateral Plane (i.e., X - Y Plane)
Control Volume for U Velocity

Figure 5.2–4

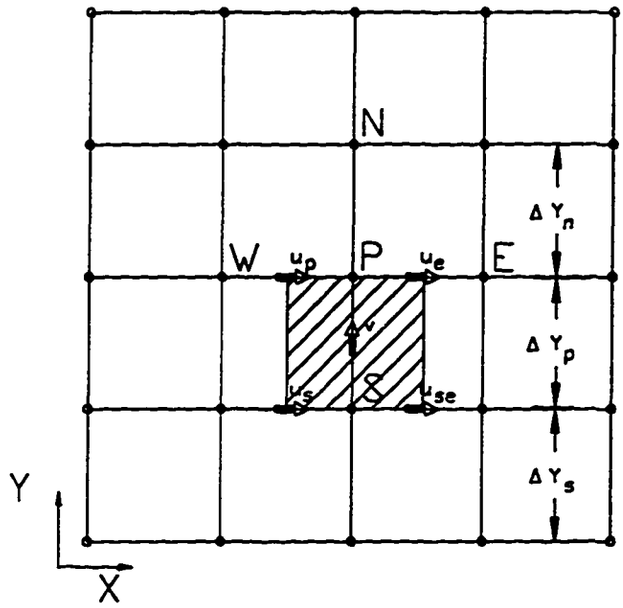

Lateral Plane (i.e., X - Y Plane)
Control Volume for V Velocity

Figure 5.2–5

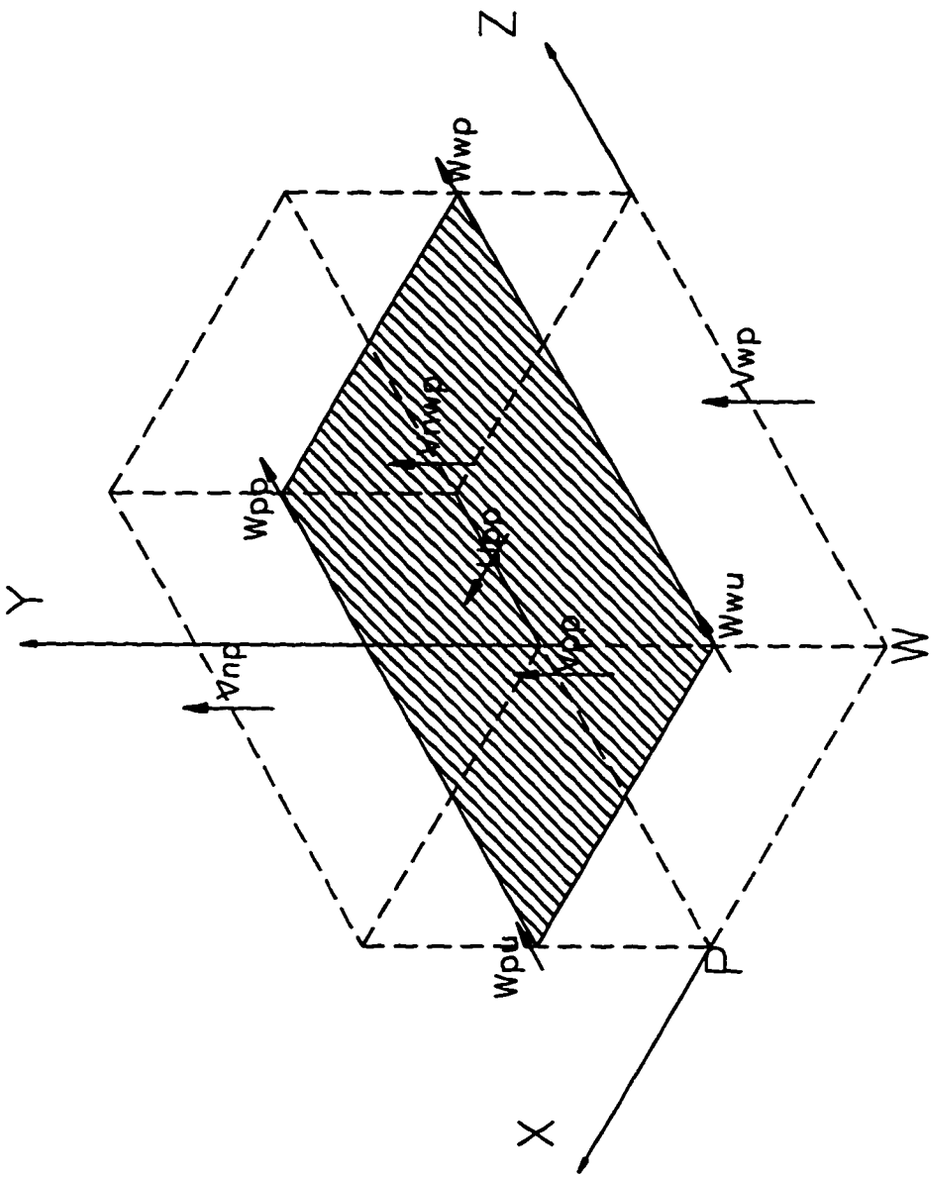

Figure 5.2-6 Control Volume for U Velocity

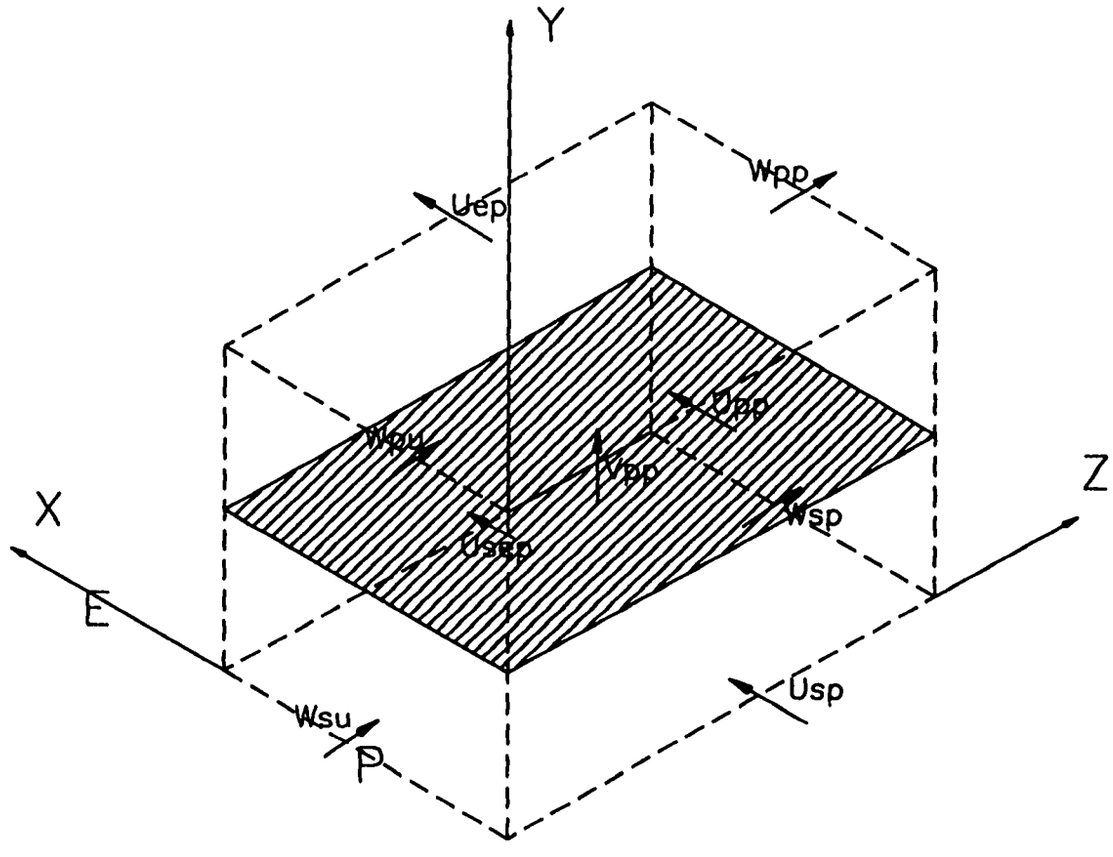

Figure 5.2–7 Control Volume
for V Velocity

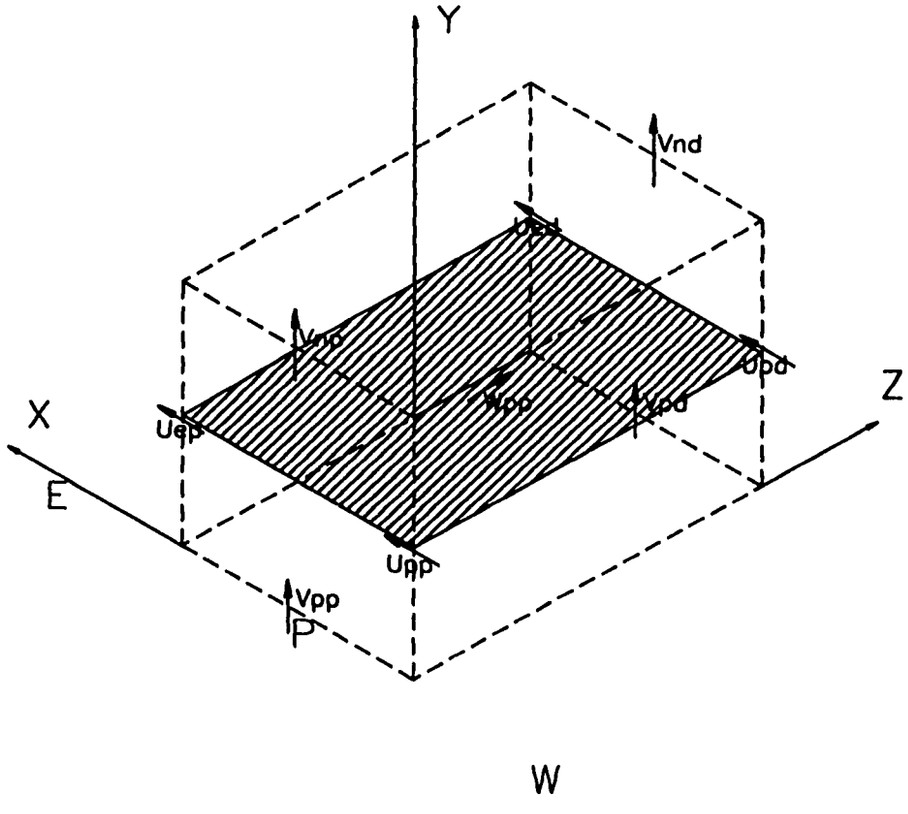

Figure 5.2–8 Control Volume
for W Velocity

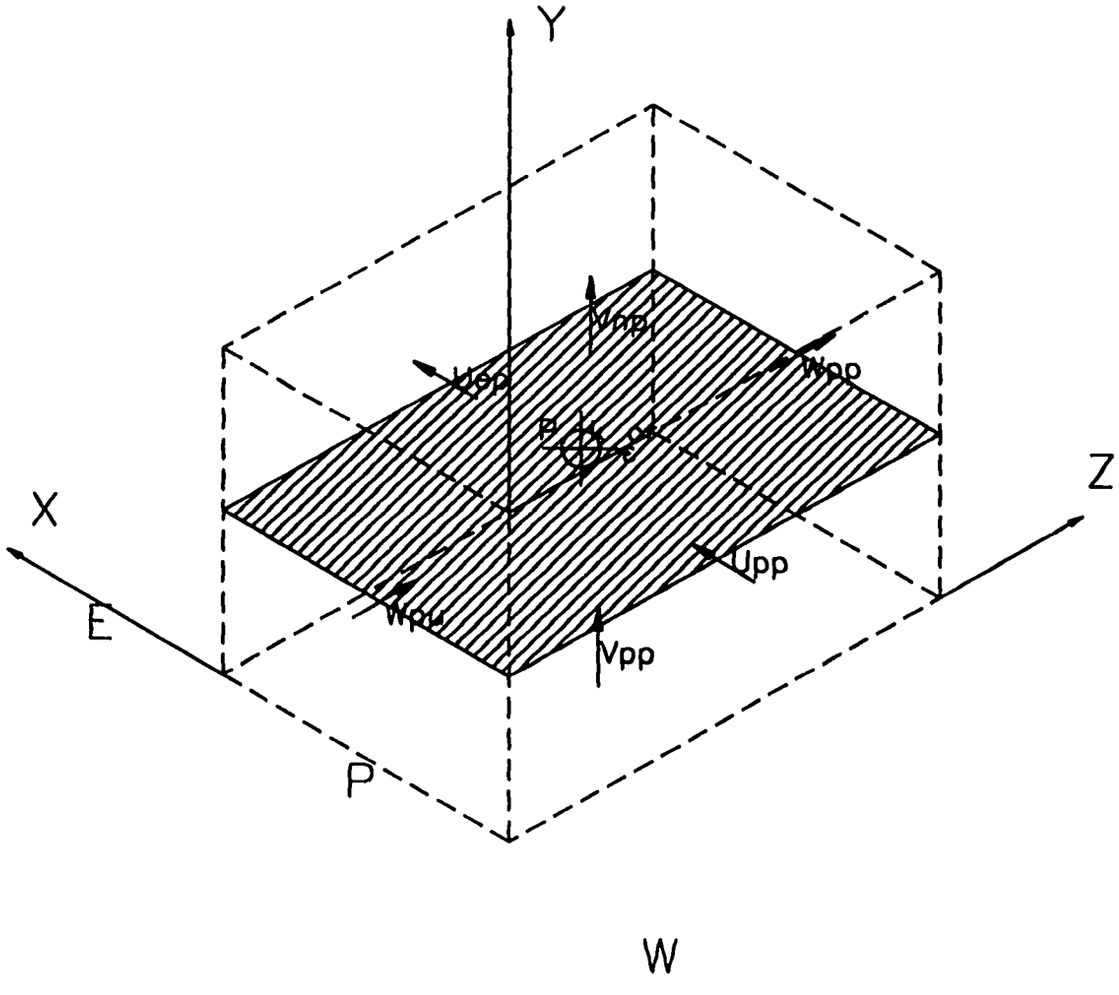

Figure 5.2–9 Control Volume
for P , k and ε

5.3 Discretizing the Governing Partial Differential Equations

The governing differential equations have a recurring structure that allows them to be cast into a generic form that equates the convective fluxes to the diffusive fluxes plus any source terms:

$$\underbrace{\frac{\partial(\rho u\phi)}{\partial x}+\frac{\partial(\rho v\phi)}{\partial y}+\frac{\partial(\rho w\phi)}{\partial z}}_{\substack{Convective\\ Flux}} = \underbrace{\frac{\partial\left(\Gamma_\phi \frac{\partial\phi}{\partial x}\right)}{\partial x}+\frac{\partial\left(\Gamma_\phi \frac{\partial\phi}{\partial y}\right)}{\partial y}+\frac{\partial\left(\Gamma_\phi \frac{\partial\phi}{\partial z}\right)}{\partial z}}_{\substack{Diffusive\\ Flux}} + \underbrace{S_\phi}_{Source} \qquad [5.3\text{-}1]$$

where ϕ is a general transport variable; u, v and w are the components of velocity along the x,y,z directions and Γ_ϕ is the diffusion coefficient.

The above equation is multiplied by the appropriate cell volume, $\Delta x\ \Delta y\ \Delta z$, and integrated. Gauss's divergence theorem can be used to relate volume integrals to fluxes:

$$\iiint div\,\overline{F}\,dV = \iint \overline{F}\bullet d\overline{S} \qquad [5.3\text{-}2]$$

The source term, S_ϕ , is linearized as a constant component, $S_{\phi,U}$, and a linearly varying component, $S_{\phi,P}\,\phi$.

Then the discretized form of the transport equations can be written:

$$F_e^x\phi_e - F_w^x\phi_w + F_n^y\phi_n - F_s^y\phi_s + F_p^z\phi_p - F_u^z\phi_u = D_e^x(\phi_e-\phi_p) - D_w^x(\phi_p-\phi_w) + D_n^y(\phi_n-\phi_p) - D_s^y(\phi_p-\phi_s) + S_{\phi,U}\Delta x\Delta y\Delta z + S_{\phi,P}\phi_p\Delta x\Delta y\Delta z \qquad [5.3\text{-}3]$$

where:

The D's represent diffusion coefficients and the F's are convective fluxes.

$$F_e^x = (\Delta y \Delta z)(\rho u)_e \qquad [5.3-4]$$

$$F_w^x = (\Delta y \Delta z)(\rho u)_w \qquad [5.3-5]$$

$$F_n^y = (\Delta x \Delta z)(\rho v)_n \qquad [5.3-6]$$

$$F_s^y = (\Delta x \Delta z)(\rho v)_s \qquad [5.3-7]$$

$$F_u^z = (\rho w)_u \Delta x \Delta y \qquad [5.3-8]$$

$$F_p^z = (\rho w)_p \Delta x \Delta y \qquad [5.3-9]$$

$$D_e^x = \Gamma_e \left(\frac{\Delta y \Delta z}{\Delta x} \right) \qquad [5.3-10]$$

$$D_w^x = \Gamma_w \left(\frac{\Delta y \Delta z}{\Delta x} \right) \qquad [5.3-11]$$

$$D_n^y = \Gamma_n \left(\frac{\Delta x \Delta z}{\Delta y} \right) \qquad [5.3-12]$$

$$D_s^y = \Gamma_s \left(\frac{\Delta x \Delta z}{\Delta y} \right) \qquad [5.3-13]$$

The unknowns: $\phi_e, \phi_w, \phi_n, \phi_s, \phi_p$ *and* ϕ_u are values between primary nodes. For example, ϕ_e, is the value of ϕ evaluated at "e" which is midway between primary nodes E and P. Values at "e" need to be determined from the values at the primary nodes. If the problem were purely diffusive, then the values at "E" and "P" would be averaged to determine the value at "e" (central differencing). If the transport were purely convective and the local flow direction was out of the

west, then the value at "P" would be used (up-wind differencing). Typically neither of these two extreme cases exists but rather some combination of the two.

5.3.1 Hybrid Scheme

The convection and diffusion terms are treated by a scheme developed by Spalding (1980) called the hybrid scheme or high-lateral-flux modification. The strength of convection relative to diffusion is measured by the local Peclet number: $P_E = \frac{\rho u \Delta x}{\Gamma}$. In the limit, when the Peclet number is zero the problem is purely diffusion driven. When the Peclet number is high the flow is convection dominated. An exact solution for one-dimensional flow indicates that the proper value to use for ϕ_e is an exponential function of the Peclet number. Since computing exponentials is compute expensive, an approximate scheme called the Hybrid scheme is used in the present algorithm. Let the exact solution be plotted for a node at "E" in the form of a_E/D_E versus Peclet number. The exponential curve can be approximated by three straight lines:

$$\text{for } P_E<-2 \qquad a_E/D_E = -P_E \qquad [5.3.1\text{-}1]$$

$$\text{for } -2<P_E<2 \qquad a_E/D_E = 1-P_E/2 \qquad [5.3.1\text{-}2]$$

$$\text{for } P_E>2 \qquad a_E/D_E = 0 \qquad [5.3.1\text{-}3]$$

5.3.2 The Final Discretized Form

An equation can now be written for the node (i,j), here denoted as P:

$$A_P\phi_P = A_E\phi_E + A_W\phi_W + A_n\phi_N + A_S\phi_S + B \qquad [5.3.2-1]$$

where: $A_P = A_E + A_W + A_N + A_S - S_{\phi,P}\Delta x\Delta y$

and $B = S_{\phi,U}$

An equation of this form is written at every node on the lateral plane. Thus there is a system of equations of size (IMAX-2) X (JMAX-2) which are implicitly coupled since each node requires the value of ϕ at its neighbors.

5.4 Solution of the Set of Algebraic Equations

5.4.1 Single Phase

The general approach to solving the equations that govern many fluid mechanics and heat transfer problems has been reviewed above. Things are actually a bit more complex than given in equation [5.3.2-1]. The coefficients A_P, A_N, A_S, A_E and A_W are not constants but rather functions of the unknowns u, v and w. This makes the equations non-linear and thus an iterative solution will be required. The coefficient terms A_P, A_N, A_S, A_E and A_W when written for one momentum equation contain not only velocities for that component but also for the other two components. That means that the equations are coupled so an outer iteration is to feed in information from the better estimates of the other variables. Another problem is that while the three momentum equations can be easily seen to fit the form of the standard equation [5.3.2-1] the

continuity equation does not explicitly contain the primitive variable pressure. It is not obvious how the pressure will be determined.

5.4.1.1 Solution Method: 'SIMPLE'

A method for the solution of the type of equation set that needs to be solved presently was given by Patankar and Spalding (1972). The method is called 'SIMPLE', which is an acronym for Semi-Implicit Method for Pressure-Linked Equations. Let us write the momentum equation for the u component velocity at the location between primary nodes"E" and "P". This will be the velocity u_e. See Figure 5.2-4. This equation has the form:

$$A_e u_e = \Sigma a_{nb} u_{nb} + b + (p_p - p_e)\Delta y\, \Delta z \qquad [5.4.1.1\text{-}1]$$

where the subscript "nb" refers to the neighboring nodes

A guess is now made for the pressure field. This will allow the solution of the three momentum equations for the velocity components. However, when these velocities are substituted into the continuity equation, there will be a mass imbalance unless the pressure field has been guessed correctly. Those velocity components determined by the guesses pressure field will be denoted as: u*, v* and w*. The guessed pressure field is denoted by p*.

The thrust of the SIMPLE algorithm is to determine a pressure correction field p', which will correct the original guess, p*, back to the correct level of pressure, p. Any pressure correction will also result in a correction to the velocity components. Thus the final sought after primitive variables (u, v, w and p) can be related to the original values (the"starred" variables) by the correction terms (u', v', w' and p'):

$$p = p^* + p' \qquad [5.4.1.1\text{-}2]$$

$$u=u^*+u' \qquad [5.4.1.1\text{-}3]$$

$$v=v^*+v' \qquad [5.4.1.1\text{-}4]$$

$$w=w^*+w' \qquad [5.4.1.1\text{-}5]$$

Equation [5.4.1.1-1] is written in terms of the final solution variables: u, v, w and p. A companion equation can be written which denotes the status of the equation before a fully converged solution has been obtained:

$$A_e u^*_e = \Sigma a_{nb} u^*_{nb} + b + (p^*_p - p^*_e)\Delta y\, \Delta z \qquad [5.4.1.1\text{-}6]$$

The difference of equations [5.4.1.1-1] and [5.4.1.1-6] is:

$$A_e u'_e = \Sigma a_{nb} u'_{nb} + (p'_p - p'_e)\Delta y\, \Delta z \qquad [5.4.1.1\text{-}7]$$

In the SIMPLE algorithm the terms $\Sigma A_{nb} u'_{nb}$ are neglected. This is done to simplify the resultant pressure correction equation and to put in a format similar to the momentum equations. This does not impose any major penalties since the solution will be iterated until the continuity equation is satisfied. The question then is how this assumption would affect the convergence rate. It will be seen below (in the discussion on SIMPLEC) that a severe computational inefficiency results because of this assumption. The words semi-implicit in the acronym SIMPLE are there to acknowledge the omission of these terms.

With the deletion of the a_{nb} terms, equation [5.4.1.1-7] can be written as:

$$A_e u'_e = (p'_p - p'_e)\Delta y\, \Delta z \quad \text{or} \qquad [5.4.1.1\text{-}8]$$

$$u'_e = d_e (p'_p - p'_e) \qquad [5.4.1.1\text{-}9]$$

where $d_e = \Delta y\, \Delta z / A_e$

Equation [5.4.1.1-9] is a velocity correction formula which was derived from the momentum equations. The corrected velocity has the form:

$$u_e = u^*_e + d_e (p'_p - p'_e)$$

At this point a method of obtaining the pressure corrections has not been given yet. If all the velocity components are written in the form of equation [5.4.1.1-9] and substituted into the continuity equation, an equation in terms of the pressure corrections (p') only will result. (Note: equation [5.4.1.1-6] will be employed to eliminate the "starred" terms.):

$$A_P p'_P = A_E p'_E + A_W p'_W + A_n p'_N + A_S p'_S + A_U p'_U + A_D p'_D + SMP \quad [5.4.1.1-10]$$

Here SMP is a mass source, or a mass imbalance, which the pressure correction must annihilate.

5.4.1.2 Solution Method: 'SIMPLEC'

An improvement to the basic SIMPLE algorithm was offered by Van Doormaal and Raithby in 1984 called SIMPLEC, with the added "C" denoting *Consistent*. The major feature of this method is to remove the approximation introduced by neglecting the terms $\Sigma a_{nb} u_{nb}$. This is done by subtracting the term $\Sigma a_{nb} u'_e$ from both sides of equation [5.4.1.1-1]. This results in the following equation:

$$(A_b - \Sigma a_{nb)} u'_e = \Sigma a_{nb} (u'_{nb} - u'_e) + b + (p_p - p_e)\Delta y\, \Delta z \quad [5.4.1.2-1]$$

Now the term $\Sigma a_{nb} (u'_{nb} - u'_e)$ which is smaller in magnitude than $\Sigma a_{nb} u_{nb}$' is neglected. This is the "consistent" approximation that yields a better estimate for u_e'.

This is a fairly simple change and is quite easy to implement in terms of coding. The value of d_e is redefined as:

$$d_e = \Delta y\, \Delta z / A_e \qquad \text{SIMPLE} \qquad [5.4.1.2\text{-}2]$$

$$d_e = \Delta y\, \Delta z / (A_e - \Sigma a_{nb}) \qquad \text{SIMPLEC} \qquad [5.4.1.2\text{-}3]$$

Adoption of the SIMPLEC algorithm over the SIMPLE algorithm resulted in a decrease in run times by a **factor of 6** and is used in the present work.

5.4.2 Two-Phase Flow Algorithm

The major difference between the single and two-phase calculations is that the local void fraction must be computed for two-phase flow. The construction of a numerically stable and robust algorithm for the void fraction was one of the more difficult challenges of this work. The difficulties in constructing such an algorithm along with the resulting numerical stability problems of a deficient algorithm are probably the cause of various problems reported in other two-phase computations. As noted in section 2.2 of the two-phase *Literature Review* above, some algorithms would only converge for density ratios between the phases close to unity.

5.4.2.1 Details of the Present Void Fraction Algorithm

The formulation of the void fraction algorithm is carried out in some detail in the appendix. The present algorithm is able to compute water/air flows where the density ratio is nearly 1000:1. The algorithm is also stable even when the flow becomes locally stratified and local void fractions approach zero or unity. This section covers several approaches successfully used in the present algorithm which have not been reported elsewhere in the literature and reviews the techniques first introduced by others and how they are presently implemented.

To derive the equation for the void fraction (as shown in Appendix V), the continuity equations for the two phases are subtracted from one another. The volume fraction of the continuous phase, denoted as phase 1, is eliminated by the relation:

$$\alpha_1 = 1 - \alpha_2 \qquad [5.4.2.1\text{-}1]$$

This straightforward approach was not stable. It violated the criterion that [Patankar (1980)]:

$$A_p = \Sigma A_{nb} \qquad [5.4.2.1\text{-}2]$$

The general form of the equation being solved for the local void fraction, α_2 is:

$$\alpha_p A_p = \alpha_e A_e + \alpha_e A_e + \alpha_e A_e + \alpha_e A_e + \alpha_e A_e + S_{\alpha_1} \qquad [5.4.2.1\text{-}3]$$

The coefficient of A_p originally did not meet the criterion above. It was necessary to subtract from the terms of A_p the sum of the two continuity equations with each normalized by its reference density in a somewhat modified form. The continuity equation itself contains the local void fraction. So introducing it directly would bring the void fraction at N, S, E, W, U and D into the coefficient for the void fraction at P. This would not readily permit the solution of the equation set at each node. A simplifying assumption was made that (for this term only) the local void fraction at the neighbors of P are all equal to the value at P. This is similar in logic to the approximations made in the SIMPLE and SIMPLEC algorithm. With this addition, the criterion for the coefficient of A_p described above is met.

Another difficulty that led to unrealistically high or low void fractions in some regions which were not physically realistic was caused by the fact that local mass conservation, i.e., the mass conservation around a single control volume, was only accurate to within some required tolerance. Since the void fraction algorithm was dependent on the local mass imbalance to yield a required change in the local void fraction, sometimes unrealistic changes to the local void

fraction were being made. This was especially serious in regions where there was little flow. Even small mass residuals resulted in very large void fraction changes. (This is one of the reasons why the two-dimensional driven cavity problem was a good test case for evaluating such phenomenon. In that problem, the flows entering and leaving cells at the core of the vortex were very small.) The solution to this was to add an effective mass residual term to S_P (which is the portion resulting from the linearization of the source term). The mass flow entering and leaving each node for both phases was added to S_P. This stabilized the procedure since now mass residuals were not large enough to destabilize the void fraction calculations.

Because the void fraction equation is developed solely from the continuity equations it had no diffusion terms. Thus the concept of hybrid discretization based on the local Peclet number was not used. Upwind differencing was used. The direction of the flux at each face of the control volume was checked for both phases. If the flow was found to be entering the control volume then the flux would be based on the appropriate neighboring void fraction. If the flow were leaving the control volume then the flux would be based on the void fraction at the center of the cell (i.e., node P).

The void fraction is physically limited to the range $0< \alpha_2 <1$. The void fraction is implicitly kept inside this range by adopting two suggestions from Carver (1982).

The void fraction level is kept above zero by a technique based on the source linearization used in SIMPLE and SIMPLEC. The components of the source term in the void fraction are each checked for sign. If they are detected to be negative then that portion of the source term S_U is artificially brought into S_P by dividing it by the old value of the void fraction. That is, if a component of S_U, say S_{U3} is found to be less than zero, then A_P is adjusted as follows:

S_{U3}/ α_{old} is subtracted from A_P and S_{U3} is excluded from S_U.

The void fraction level is kept below unity by locally under-relaxing each node by an amount dependent on the local level of the void fraction. Thus if a node has a void fraction too close to unity, a strong measure of underrelaxation is employed and little more is added to it in the next iteration. The method employed if the local void fraction exceeded 0.95. It was then underrelaxed by the amount: the larger of $1-\alpha_2$ or $1x10^{-10}$. This was implemented by a change to the source terms and to A_P.

The above discussion describes in general terms what elements went into the present void fraction algorithm. The equation development and discretization are given in Appendix V.

5.4.2.2 Details of the Partially Parabolic Pressure Correction Algorithm

The present computational algorithm used a partially parabolic formulation to determine the pressure on a lateral plane. This approach is different from that used in the parabolic procedure where separate pressure fields are employed for the lateral and longitudinal momentum equations. (*See Section 4.4 Classification of Flow Problem Solution* for further discussion .) In the present approach, the longitudinal momentum equation incorporates the use of a pressure gradient, $\frac{\partial p}{\partial z}$, which will vary across the duct cross section. In the fully parabolic approach this term is constant (based on conservation of mass across a lateral plane) on the lateral plane.

The velocity corrections are related to the pressure corrections as (see details in Appendix IV):

$$u'_{P_P} = -\frac{(\alpha_P + \alpha_W)}{2} D_u \left\{ p'_{P_P} - p'_{W_P} \right\} \qquad [5.4.2.2 - 1]$$

$$u'_{E_P} = -\frac{(\alpha_P + \alpha_E)}{2} D_u \left\{ p'_{E_P} - p'_{P_P} \right\} \qquad [5.4.2.2 - 2]$$

$$v'_{N_P} = -\frac{(\alpha_P + \alpha_W)}{2} D_v \left\{ p'_{N_P} - p'_{P_P} \right\} \qquad [5.4.2.2 - 3]$$

$$v'_{P_P} = -\frac{(\alpha_P + \alpha_S)}{2} D_v \left\{ p'_{P_P} - p'_{S_P} \right\} \qquad [5.4.2.2 - 4]$$

$$w'_{P_P} = +\alpha_P D_W p'_P \qquad [5.4.2.2 - 5]$$

$$w'_{P_U} = -\frac{(\alpha_P + \alpha_U)}{2} D_W p'_P \qquad [5.4.2.2 - 6]$$

Note that in the last two equations, (i.e., the pressure correction-velocity correction correlations for W), that $\dot{p_D} = \dot{p_U} = 0$. Also, even though W_U is not calculated along with U_P, V_P and W_P it is affected by a change in the pressure at P. The equation for the pressure correction p' at the node P can be derived with the above substitutions into the combined continuity equations.

5.4.3 The Tridiagonal Matrix Algorithm

As mentioned earlier, the solution technique is to solve the momentum equations in succession; that is while the u momentum equation is being solved the latest available velocity components for v and w are used. This means that after the set of momentum equations have been solved that the loop must be repeated to upgrade the other velocity components. This section considers the numerical procedure used to solve one such momentum equation.

If the equation set can be cast so that the A matrix in the matrix equation: Ax = B has elements only on the diagonal or at elements one off of the diagonal (all other elements are zero) a very efficient solver can be used. This is the Tridiagonal Matrix Algorithm. This scheme is very efficient since after reordering a back substitution suffices to determine the unknowns. For multi-dimensional problems a line-by-line TDMA is used in an iterative fashion [Pratap and Spalding (1975)].

The original equation set is not tridiagonal. But a strategy that can be used to solve two successive tridiagonal systems iteratively in place of solving the full general equation. The first step would be to solve for nodes along a line of constant I, starting with I=2. The old value of the unknown variable is used if a value is needed from a node other than I=2. This means that we start by calculating a temporary value ϕ^I at each node along the line I=2:

$$\phi_p^I = A_n\phi_n^I + A_s\phi_s^I + \underbrace{\left(A_e\phi_{e,old} + A_w\phi_{w,old} + S_\phi\right)}_{\text{held Constant}} \qquad [5.4.3\text{-}1]$$

The above equation can be solved for all the values along I=2 using the tridiagonal matrix algorithm (i.e., TDMA). This process is next repeated for I=3, and so on through I=IMAX-1. Thus the domain has been swept by solving along vertical lines.

Now the process is repeated but along horizontal lines. First a solution will be obtained for nodes along J=2. Following the philosophy of the first step, an old value will be used for any node not along the line J=2. Thus the equation set to be solved is:

$$\phi_p^{II} = A_e\phi_e^{II} + A_w\phi_w^{II} + \underbrace{\left(A_n\phi_n^{I} + A_s\phi_s^{I} + S_\phi\right)}_{\text{held Constant}} \qquad [5.4.3\text{-}2]$$

This equation can be solved by TDMA also. Then horizontal sweeps are made for J=3 and on until J=JMAX-1 has been solved.

The entire two step process is now repeated. Usually the above process is looped through four times to improve the accuracy of the solution.

Much of the computational effort is spent with the equation solver which solves the set of linear equations. The TDMA is used to solve all equations: momentum, pressure correction and void fraction. Effort has been made to cast all equations, including the void fraction equation, into a form that could be solved by TDMA.

5.5 Determination of Mesh Spacing to Obtain Grid Independent Solutions

Any numerical procedure which obtains the solution to an engineering or science problem by modeling a continuous phenomenon by means of a finite number of points in the domain needs to be repeated for various mesh densities to establish the coarsest grid that can be employed and still get accurate solutions. It is desirable to use the fewest number of nodes necessary so as to minimize run times. Grid independence can depend on the particular problem

and flow regime being modeled. Thus a laminar and turbulent flow in the same flow domain may require different mesh densities to obtain grid independent solutions.

Results for the single phase driven cavity problem were somewhat closer to Burggraf's solution with a 32x32 mesh instead of a 20x20 mesh. The 42x42 mesh showed no further improvement. For the three dimensional problems, the explicit step size in the flow (marching) direction was established by the stability criterion. Grid sensitivity studies for the two-phase water/air straight/curved/straight duct were performed for meshes of size: 16x16; 20x20; 24x24; 28x28 and 32x32 in the lateral plane. These meshes all had uniform grid spacing in both the x and the y directions. There was about a four fold increase in compute time between the coarsest and finest meshes. Figures 5.5-1 through 5.5-10 show typical results of the grid sensitivity study for two-phase flow predictions in a curved duct. A plot of the distributed phase velocity vectors is followed by a contour plot of the distributed phase's volume fraction at 45° in the bend. These two plots are repeated for the five grid sizes, starting with the coarsest and proceeding to the finest. Even the coarsest mesh, the 16x16, is able to capture the primary details of the flow. Various other quantitative measurements were also examined to decide what mesh resolution required. Overall pressure drop through the bend, local friction factor at various locations in the bend and other parameters were considered. These parameters all led to a similar conclusion. A typical study is shown in Figure 5.5-11. Here the pressure gradient across the bend at 45° is plotted for the various mesh sizes studied. A constant level is being approached for mesh densities of 20x20 to 24x24, but then the normalized gradient begins to decrease for finer meshes. The drop in the pressure gradients is due to the fact that the first node off the wall for the finest meshes has a y^{+} value which is too low and violates the assumptions used for the log-law wall functions and the transport equations for k and ε. Thus the first node must be located such that the

application of the transport equations for the turbulent quantities is valid--thus it is necessary to locate all of the grid nodes in the fully-turbulent region. The value of y^+ for the continuous phase is plotted for the different mesh densities in Figure 5.5-12. The wall value of y^+ is less than 50 for the 28x28 and the 32x32 meshes.

The above studies indicated that a mesh density in the range of 20x20 to 24x24 should be used. The 20x20 mesh was used for the two-phase runs since it appeared to represent the best trade-off between accuracy and maintaining the local value of y^+ above 50 throughout all of the duct for various flow conditions.

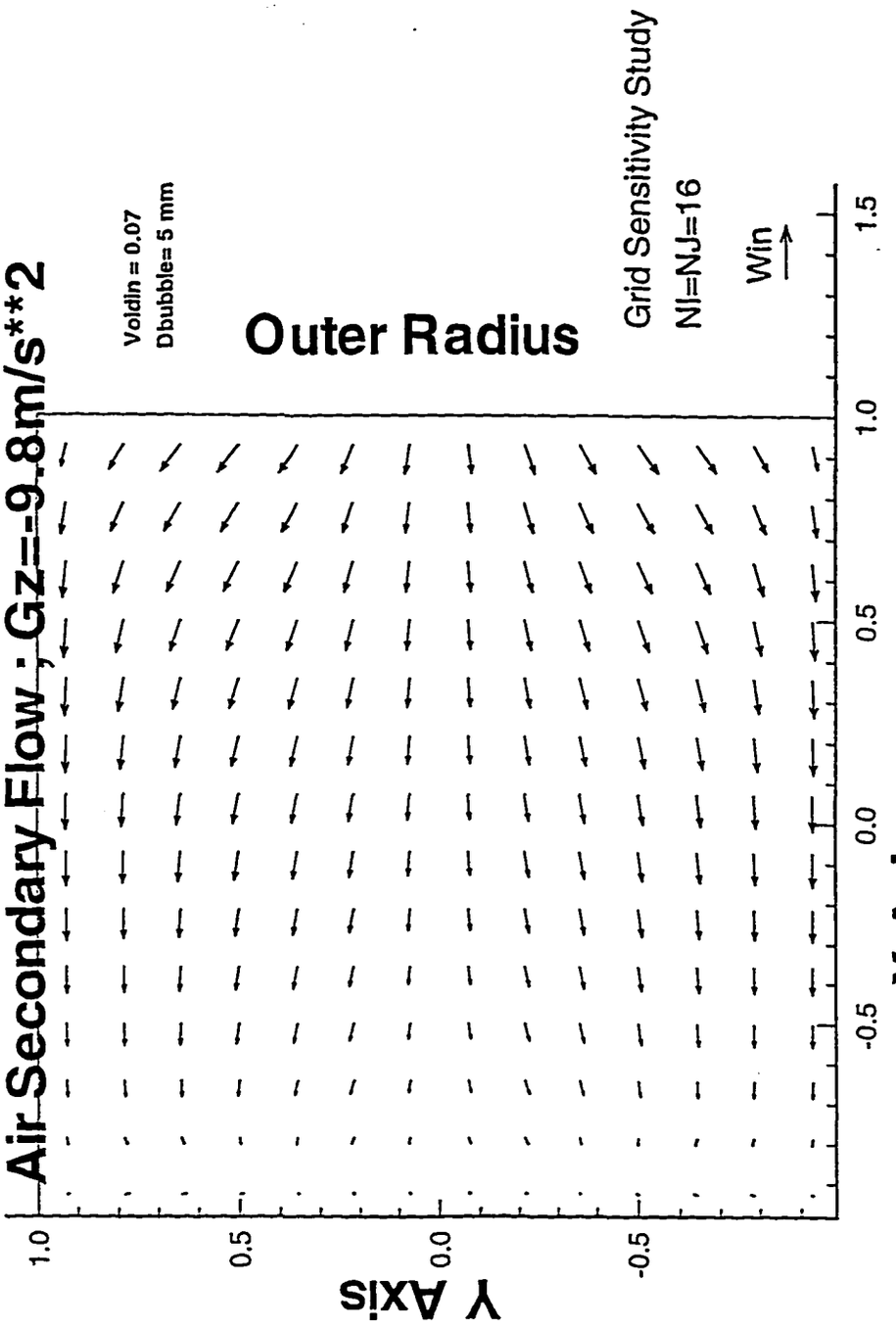

Figure 5.5-1 Two-Phase Water/Air Flow; Air Velocity Vectors in Curved Duct At 45°
NI=NJ=16 Grid Sensitivity Study

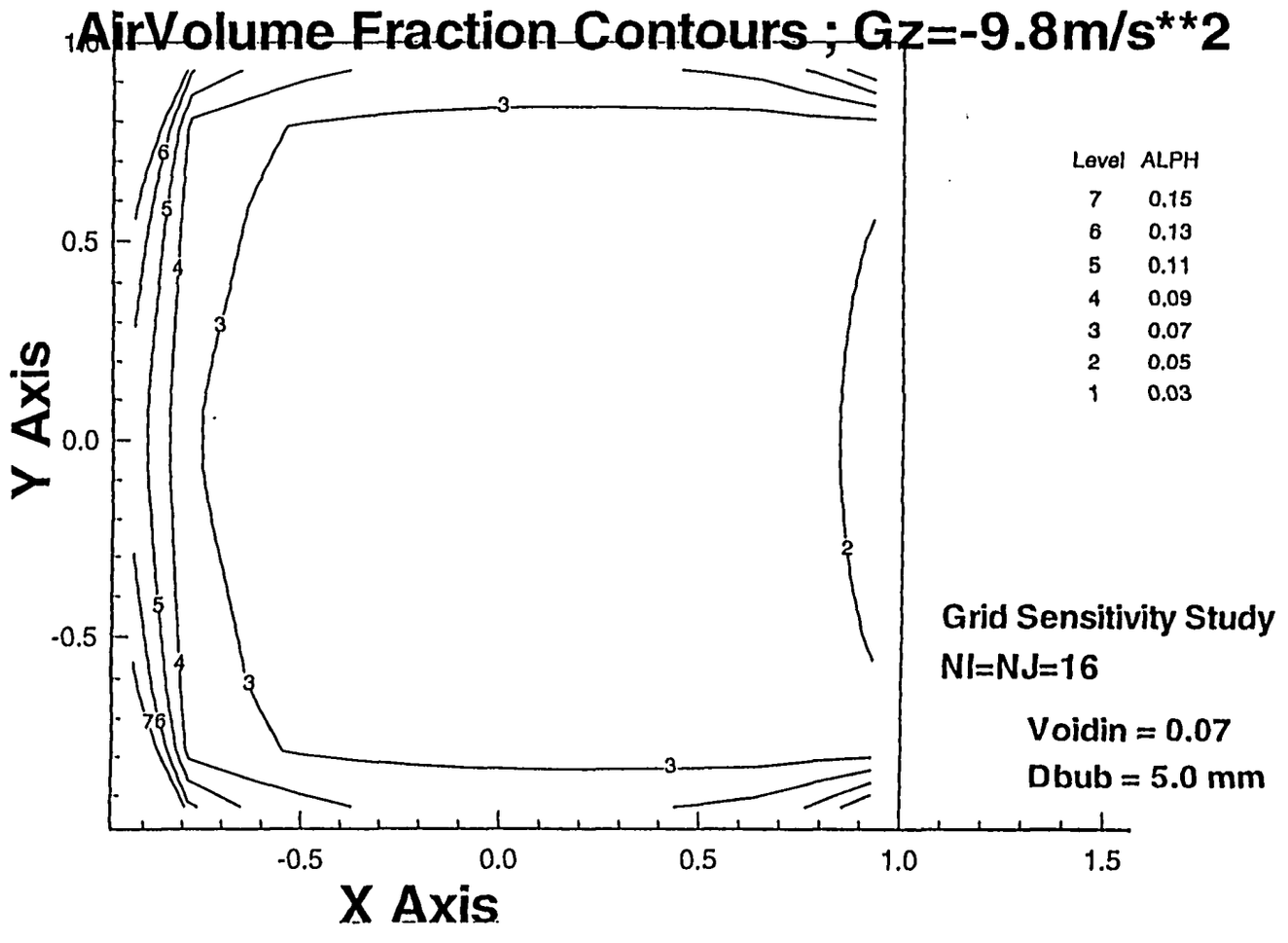

Figure 5.5-2 Two-Phase Water/Air Flow; Void Fraction Contours in Curved Duct at 45°
NI=NJ=16 Grid Sensitivity Study

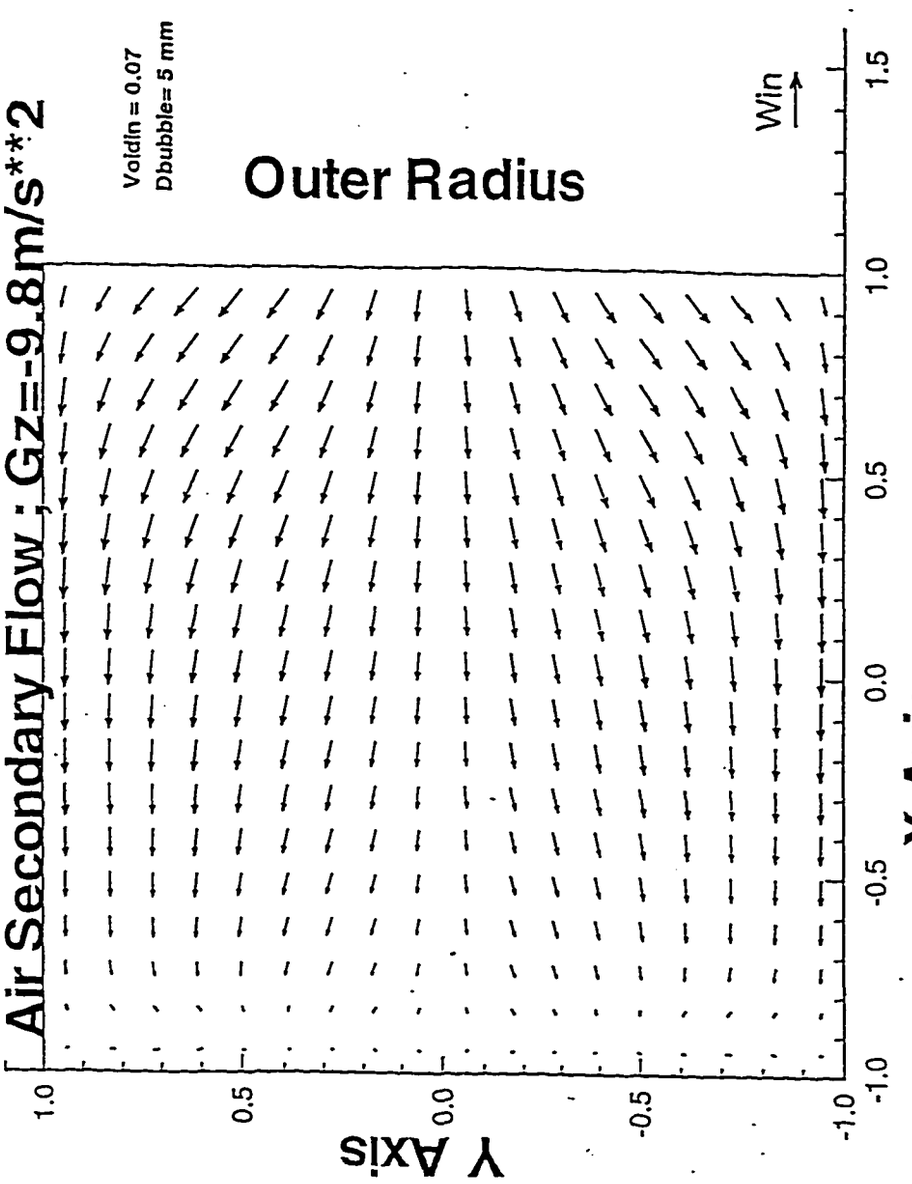

Figure 5.5-3 Two-Phase Water/Air Flow; Air Velocity Vectors in Curved Duct At 45°
NI=NJ=20 Grid Sensitivity Study

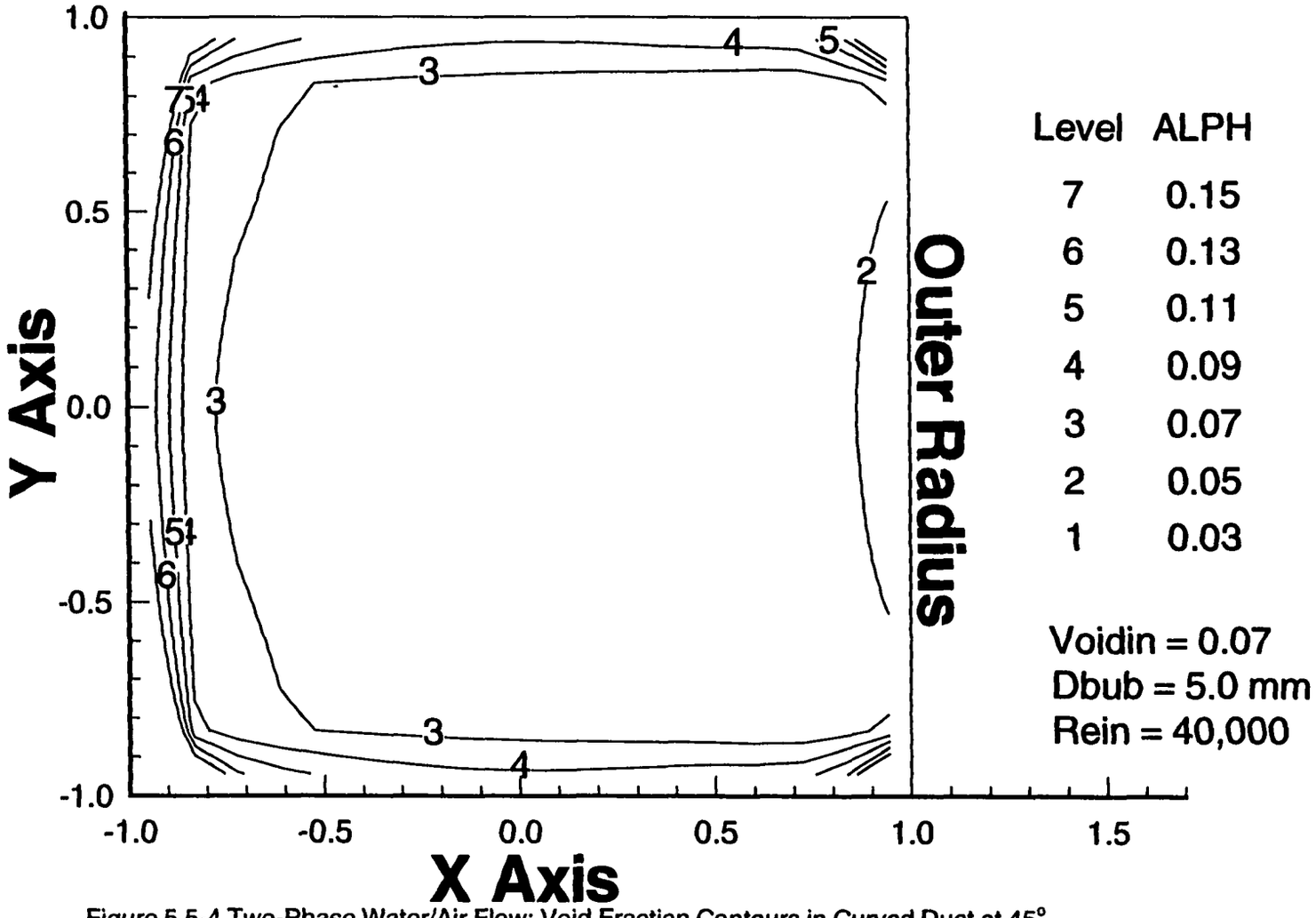

Figure 5.5-4 Two-Phase Water/Air Flow; Void Fraction Contours in Curved Duct at 45°
NI=NJ=20 Grid Sensitivity Study

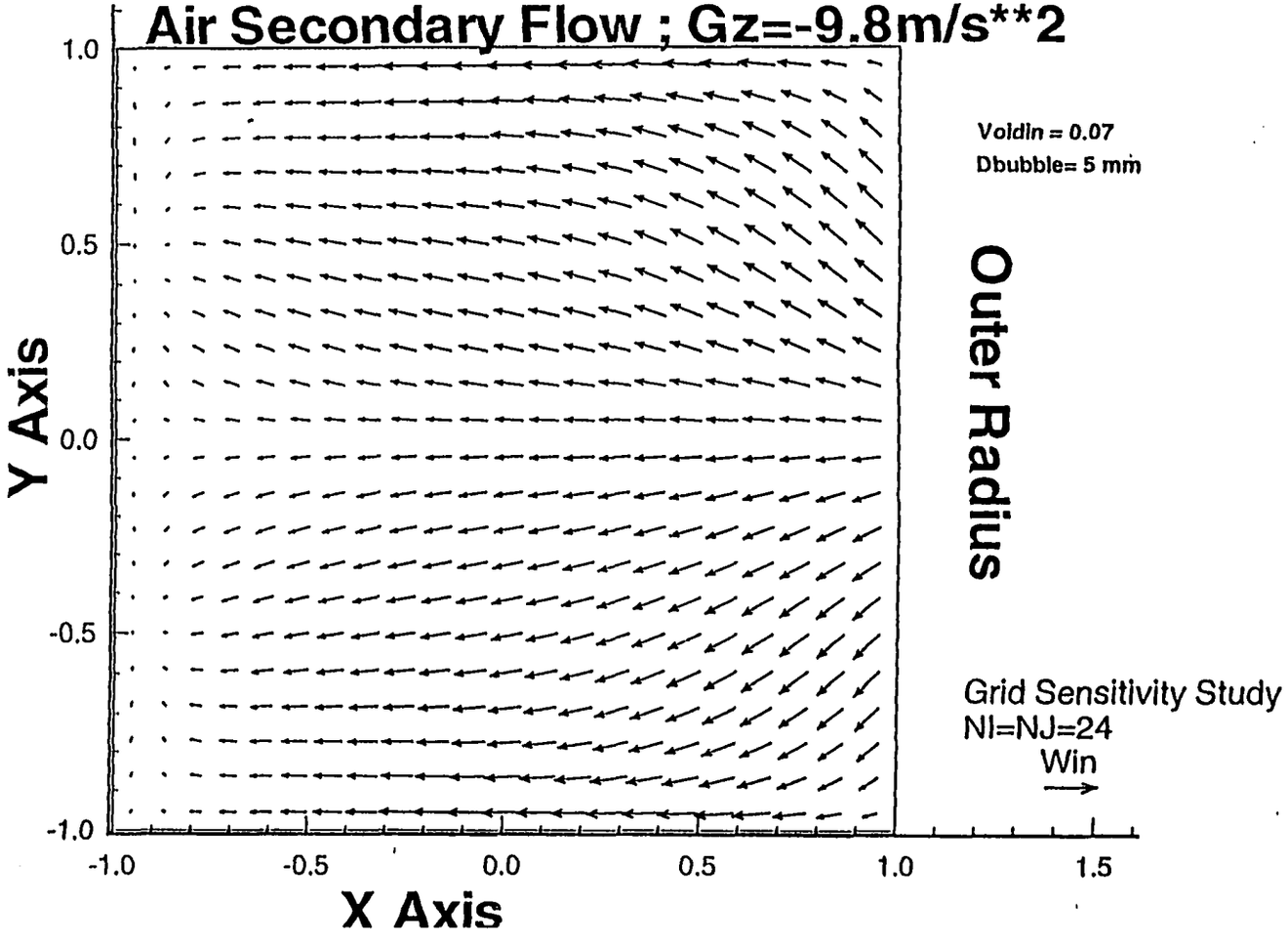

Figure 5.5-5 Two-Phase Water/Air Flow; Air Velocity Vectors in Curved Duct At 45°
NI=NJ=24 Grid Sensitivity Study

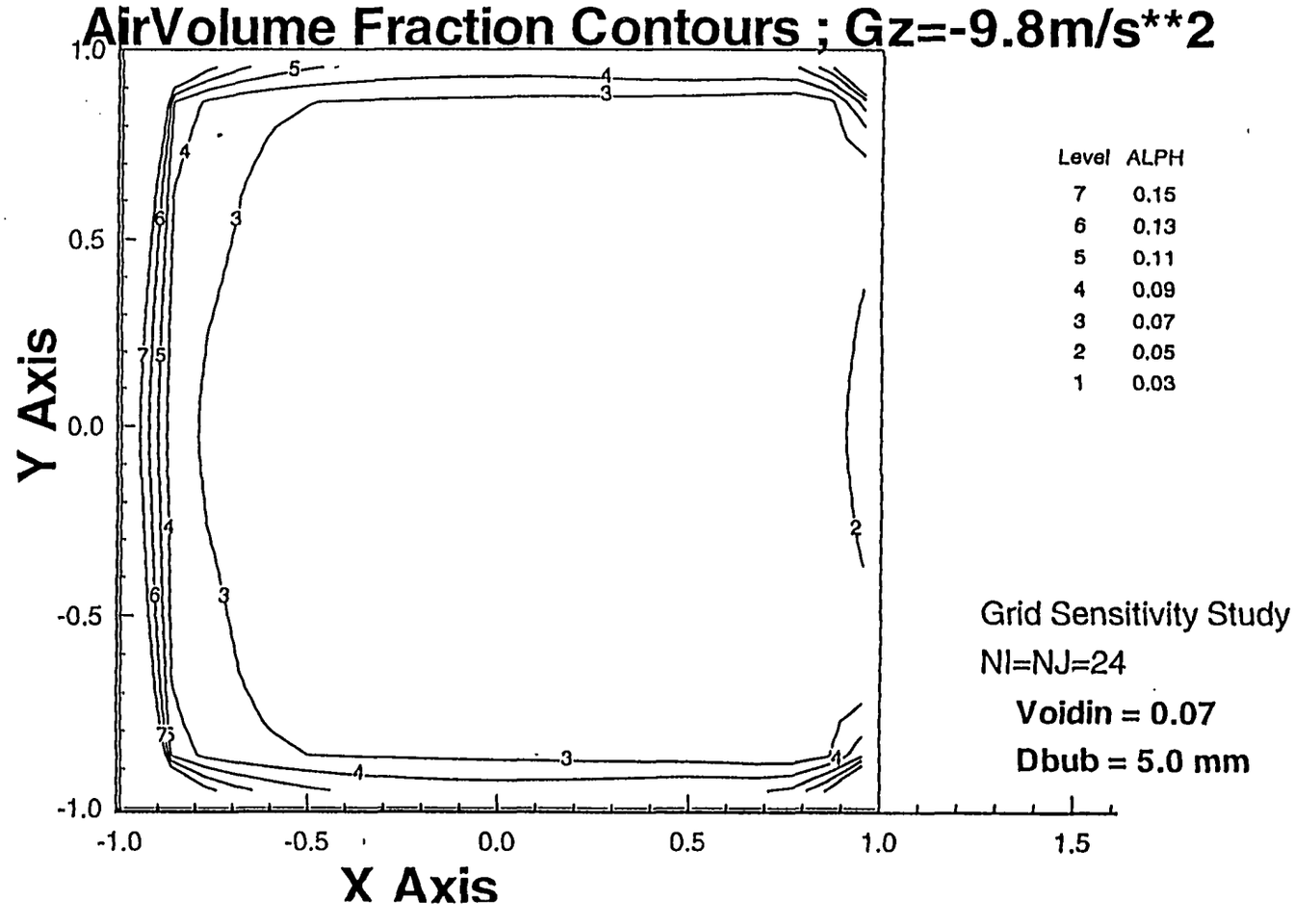

Figure 5.5-6 Two-Phase Water/Air Flow; Void Fraction Contours in Curved Duct at 45°
NI=NJ=24 Grid Sensitivity Study

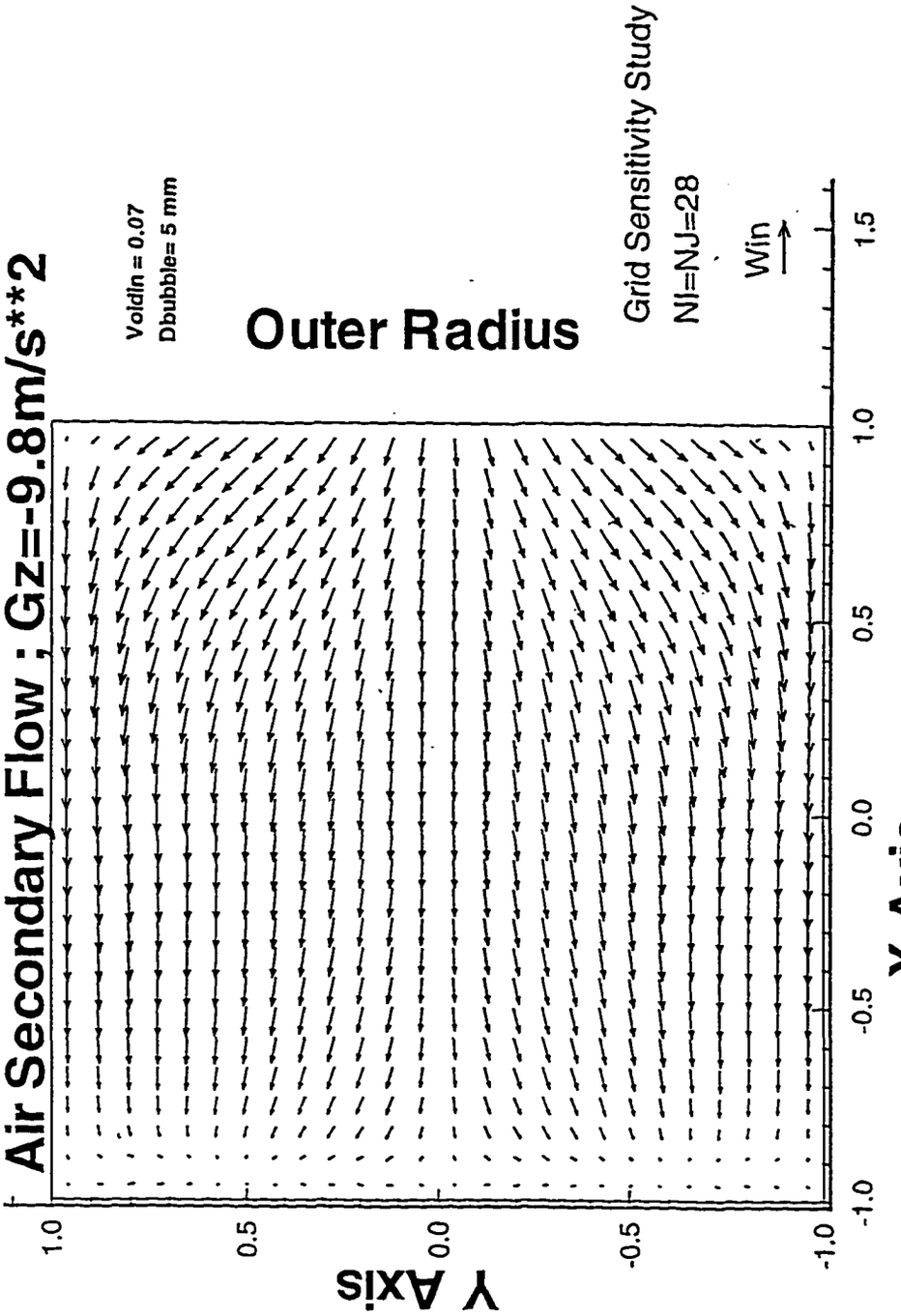

Figure 5.5-7 Two-Phase Water/Air Flow; Air Velocity Vectors in Curved Duct At 45°
NI=NJ=28 Grid Sensitivity Study

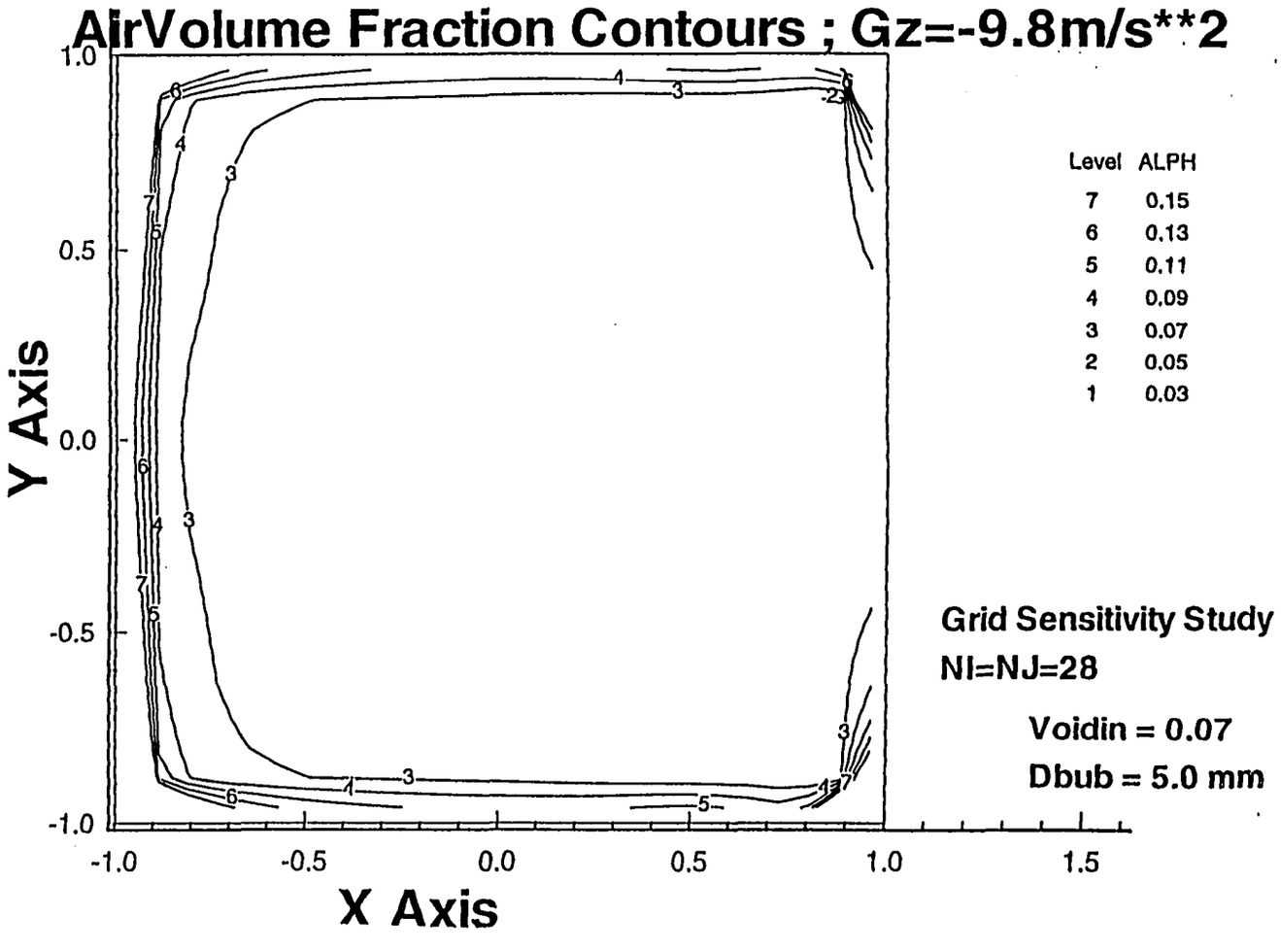

Figure 5.5-8 Two-Phase Water/Air Flow; Void Fraction Contours in Curved Duct at 45°
NI=NJ=28 Grid Sensitivity Study

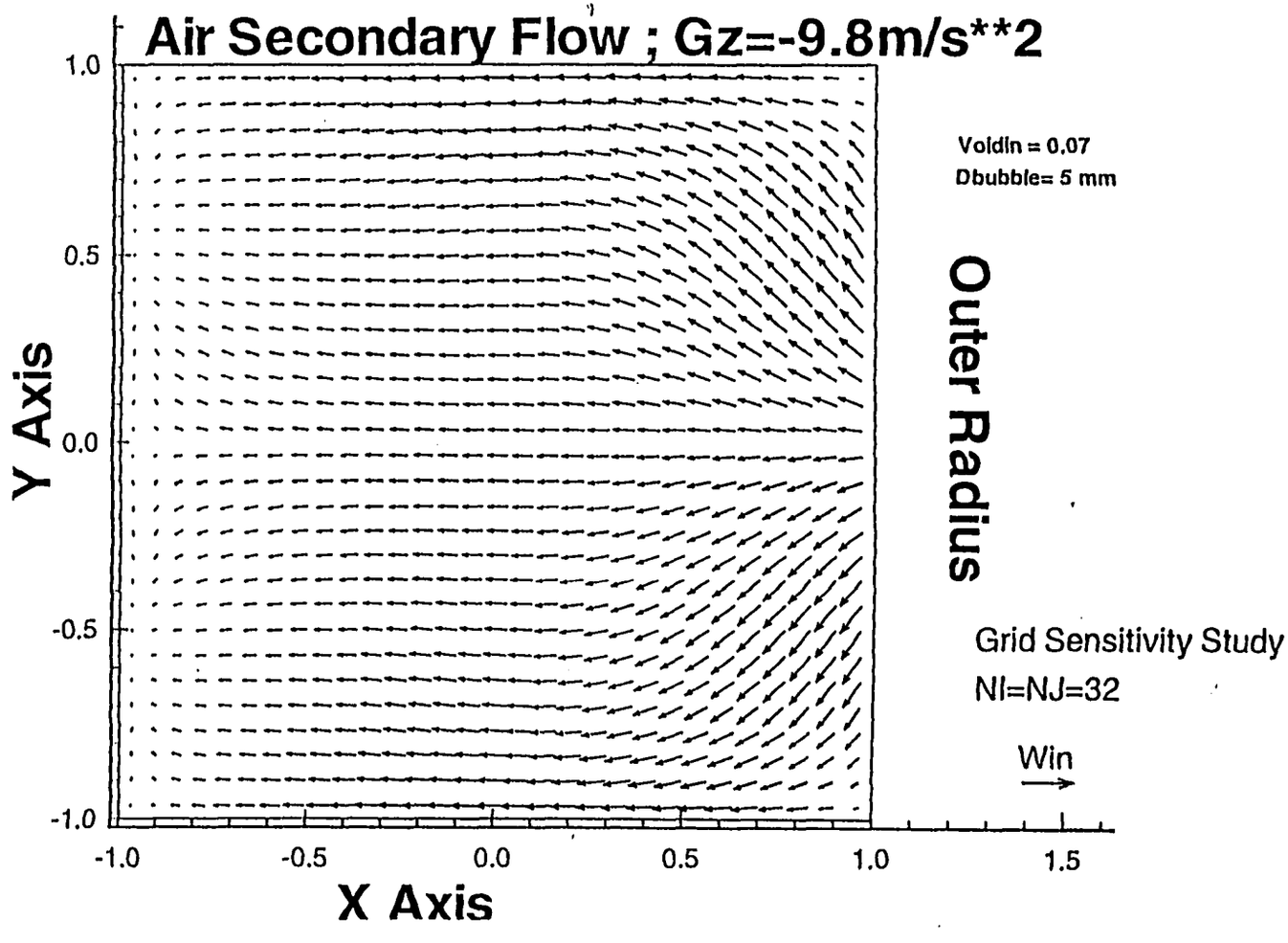

Figure 5.5-9 Two-Phase Water/Air Flow; Air Velocity Vectors in Curved Duct at 45°
NI=NJ=32 Grid Sensitivity Study

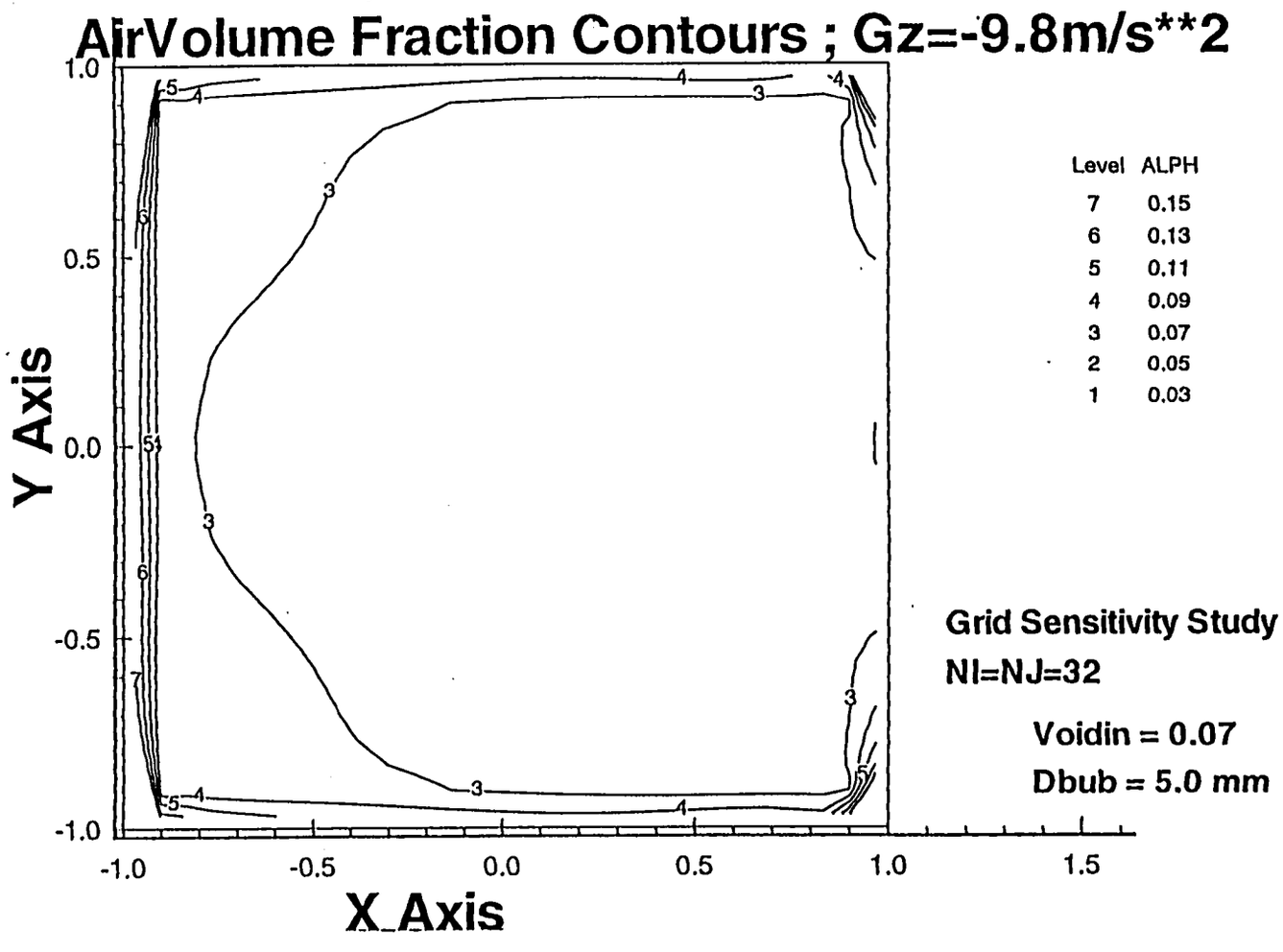

Figure 5.5-10 Two-Phase Water/Air Flow; Void Fraction Contours in Curved Duct at 45°
NI=NJ=32 Grid Sensitivity Study

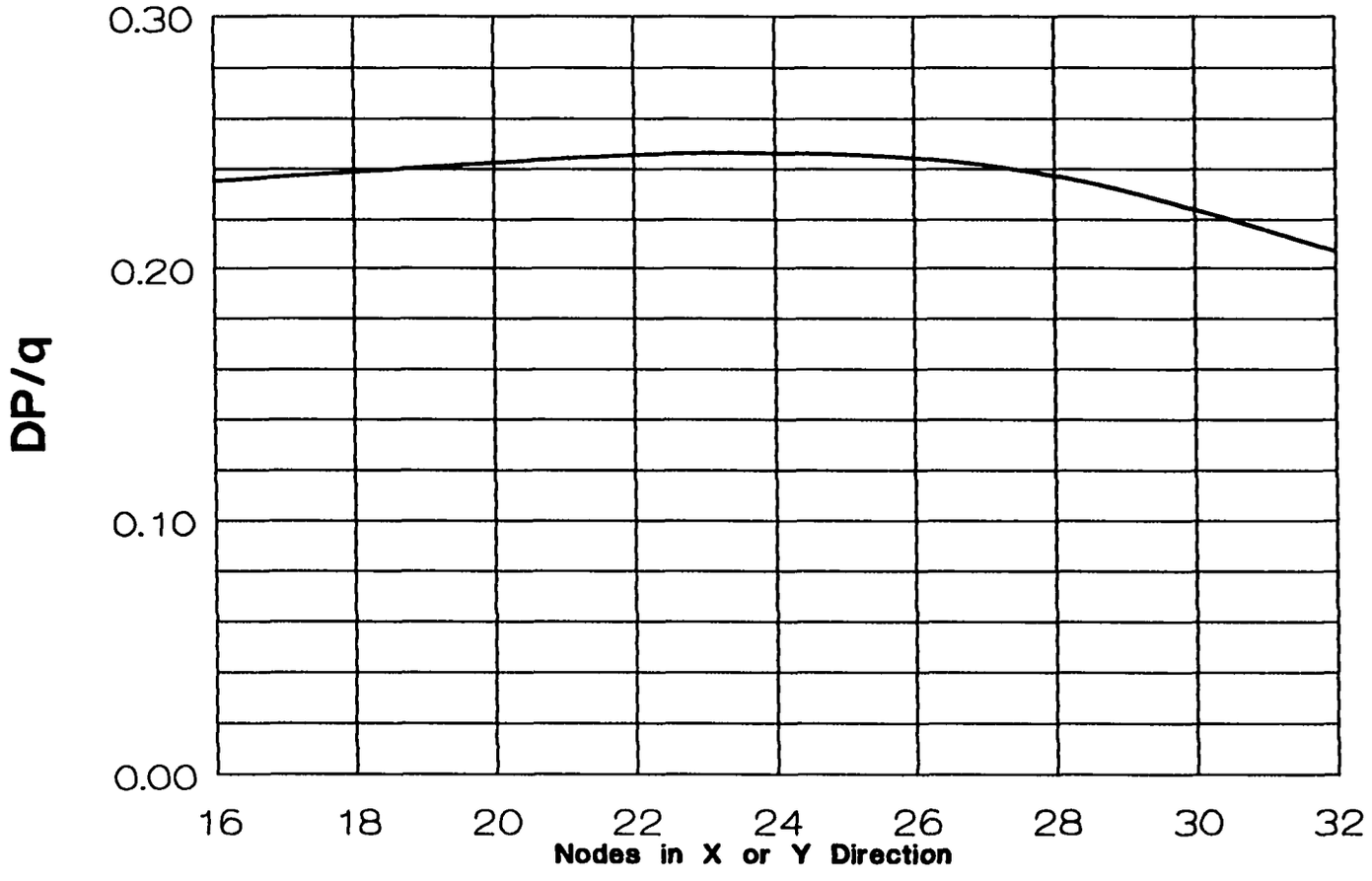

Figure 5.5-11 Pressure Gradient Across Duct at 45°
Grid Sensitivity Study

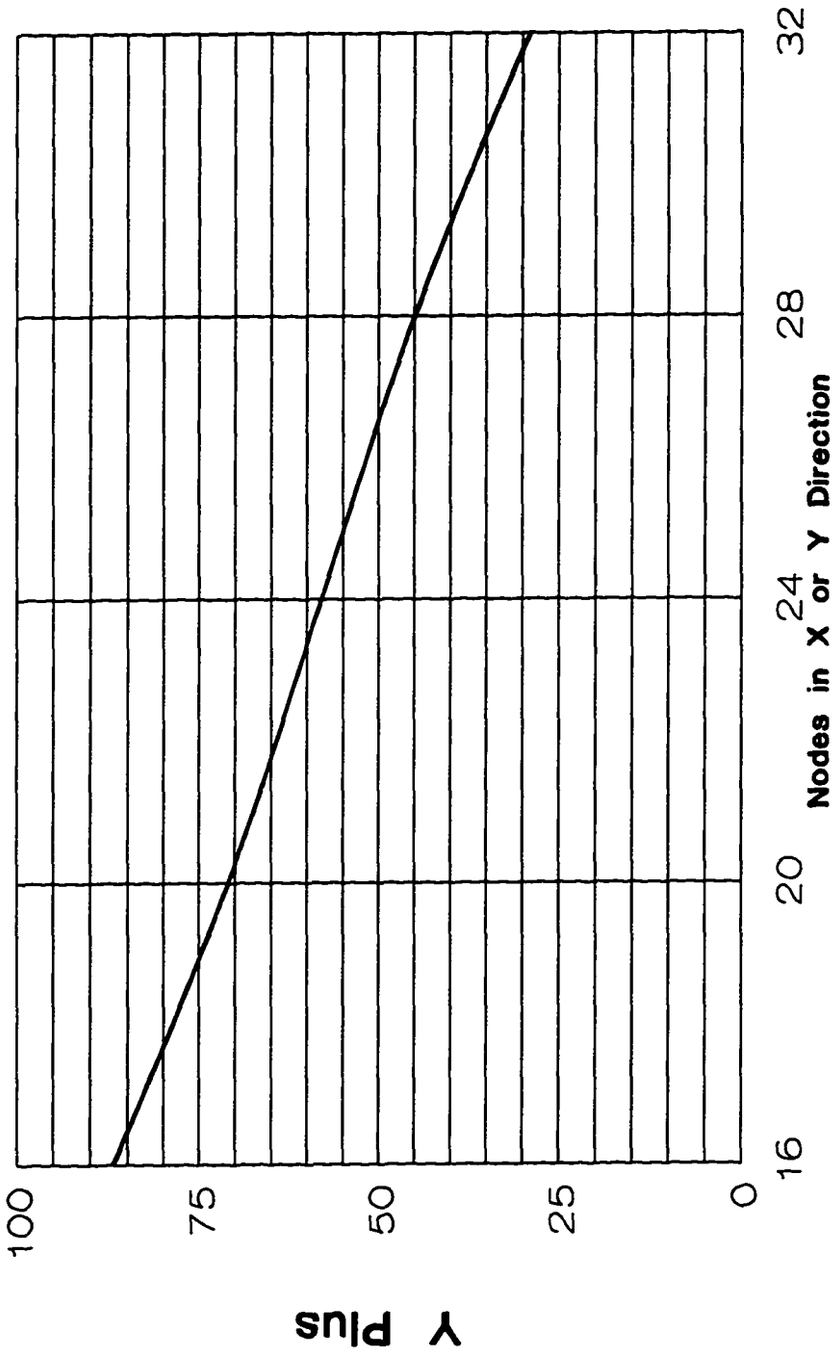

Figure 5.5-12 y^+ Study; Curved Duct at 45°
Grid Sensitivity Study

5.6 Program Logic

The general program flow chart is shown in Figure 5.6-1.

The main routine is DUCTMN.

The u, v and w momentum equations are solved in CALCU, CALCV and CALCW subroutines respectively.

The void fraction subroutine is CALCALPH.

The pressure correction subroutine is CALCP.

A global average pressure is calculated in CALCPGLB.

Other subroutines including those used for initialization, input, output, turbulent property calculations and graphical output are also required.

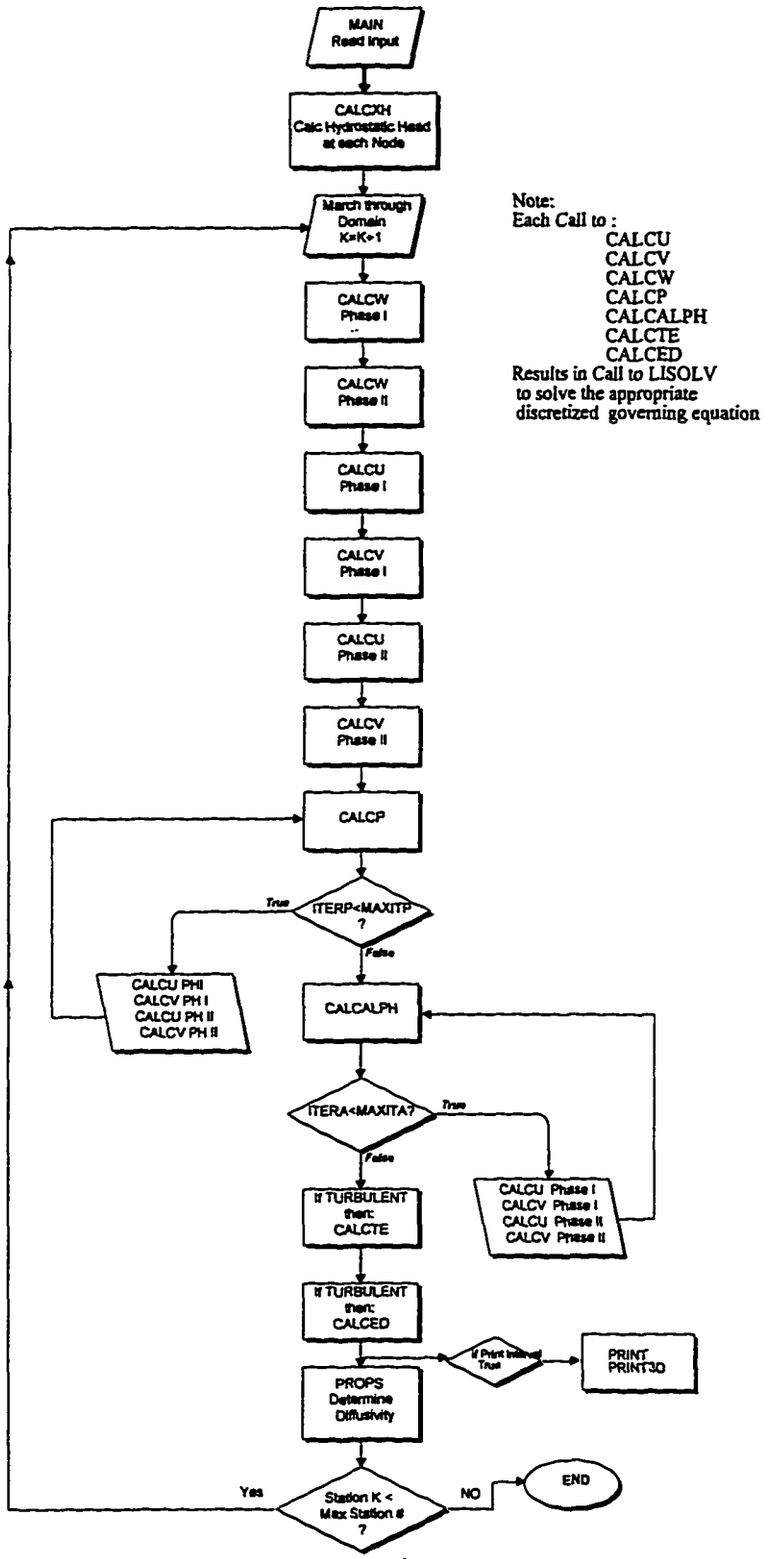

Figure 5.6-1 Flow Chart for the Present Computer Code, 'DUCT'

5.7 Run Times

Run times for the turbulent two-phase water and air problem in a configuration with straight (i.e., 45 hydraulic diameters) /curved (90^{o} bend) /straight (22.5 hydraulic diameters) duct with the two-phase modified isotropic k-ε turbulence model for a 20x20 mesh size were approximately:

1 hour and 45 minutes on a Silicon Graphic Inc. Indigo^{2} workstation (equipped with the MIPS R8000 processor);

12 hours on an IBM compatible 486/66 PC. (with a minimum of 16 Mbyte RAM).

6. COMPUTATIONAL RESULTS

6.1 Single Phase

6.1.1. Laminar

Two-Dimensional Driven Cavity (Single Phase)

Analysis of steady flow in a two-dimensional driven cavity is one of the classic problems of fluid mechanics. It could be used as a benchmark for a new numerical algorithms. It is also of interest since its basic fluid mechanics can be instructive in the study of recirculating flows since it can serve as a model for the viscous structure of a separated flow eddy. Burggraf (1966) used the streamfunction-vorticity formulation of the governing equations to solve the driven cavity problem. Steady-state two-phase solutions of the flow field inside a cavity with stationary side and bottom walls with the top wall moving at a constant velocity U_{wall} were calculated for laminar and turbulent flow conditions. The laminar solutions were verified by comparison to previous solutions, namely Burggraf (1966). The laminar single phase flow pattern in the cavity, shown in Figure 6.1.1-1, shows a primary vortex with its center approximately midway between the vertical side-walls and approximately 40 percent of the cavity's length down from the moving wall. The location of the vortex center is strongly dependent on the strength of the computed secondary vortices which appear in the bottom corners. A magnified view of the vortex in the bottom right corner is shown in Figure 6.1.1-2. The uniform vorticity theory of Batchelor (1956) fails to predict such secondary vortices. Figure 6.1.1-3 compares normalized local velocities in the x direction (with the top wall of the cavity moving in the positive x direction)

along the vertical centerline. The local velocity is zero at the bottom stationary wall and equal to the prescribed top wall velocity at the moving wall. The comparison is very favorable when it is recognized that the slightest shift in the location of the center of the vortex changes the u distribution drastically.

Three-Dimensional Flows

Straight Duct

Computed results for developing laminar flow in a square duct are presented in this section. The inlet longitudinal velocity profile is assumed to be uniform. The centerline longitudinal velocity in the square duct is shown in Figure 6.1.1-4 at increasing axial distances from the inlet. The axial distances, Δz, are normalized as $\Delta z/(D_H Re)$. The profile is rather flat at small distances from the inlet and eventually grows into a parabolic profile with a peak value of 2.075. This peak value agrees well with the theoretical value of 2.096. These profiles change very little at normalized distances of 0.06, 0.09 and 0.1. The calculated hydraulic entry length of 0.075 is in agreement with Kays' (1966) value of 0.075. For the fully developed flow the only non-zero velocity component is the longitudinal velocity, with zero lateral velocities u and v. For the fully developed conditions the computed lateral velocities are approximately $1x10^{-6}$ of the throughflow velocity.

The longitudinal velocities are non-zero during the developmental stage while the velocity profile changes from the inlet uniform profile to the parabolic profile. Fluid is transported from the edges towards the center as the boundary layers develop so as to establish the profile with the peak velocity at the duct center. Figure 6.1.1-5 shows the lateral velocities at a normalized axial distance of 0.0128. The value of u at node (5,4) and v at the node (4,5) on a 20x20 mesh are plotted in Figure 6.1.1-6 from the inlet to a normalized distance of 0.105. These velocities show a maximum at a distance of 0.004 which then drops to zero as the flow becomes fully developed. [Due to symmetry, u(5,4) should equal v(4,5).]

The local friction factor times Reynolds number is plotted in Figure 6.1.1-7 as a function of normalized duct axial length. The computed value of (f*Re) for fully developed condition is 14.25 which is in exact agreement with the theoretical value (Kays, 1966). Initially the friction factor reaches a level of 75 as the velocity profile starts to develop. This trend is in agreement with experimental data.

Curved Duct

Computations were performed for developing laminar flow in a curved duct of square cross section at the same conditions as those used by Ghia and Sokhey (1977). Two problems have been studied, which are referred to as Ghia I and Ghia II:

	R/D_H	Re	Dean Number, K_D
Ghia I	14	206	55
Ghia II	100	2100	210

The Ghia II problem has a Dean number above the critical Dean number (which is approximately 143), while the Dean number for the Ghia I problem is below the critical value. Experimentally, above the critical Dean number such flows have been shown to have an extra pair of counter-rotating vortices.

The longitudinal velocity profile develops from the uniform inlet flow to a fully developed profile by about 103°. The symmetric inlet velocity profile develops into a profile with a peak velocity biased towards the outer radius at approximately 0.8 of the duct width away from the inner radius. The present predictions for the Ghia I problem are compared with the Ghia (1976) solution in Figure 6.1.1-8. A nondimensionalized peak velocity of 1.94 is predicted by Ghia and 1.88 in the present work. The agreement is generally good for both the peak value and the radial location of the peak. Secondary flows in lateral planes at 31° and 175° are shown in Figures 6.1.1-9 and 6.1.1-10. Peak secondary flow velocities are approximately 0.2 times the average through-flow velocity at 31° and 0.175 at 175°. Only a single pair of counter-rotating vortices are predicted at all locations in the curved duct, in agreement with experimental data [Dean (1928), Humphrey (1981), Akiyama(1988), Cheng (1992)].

The flow patterns, centerline longitudinal velocity distribution as well as the secondary flows, are much more complex and interesting above the critical Dean number. The centerline longitudinal velocity distributions for the Ghia II problem are similar to those for subcritical flows for angular locations up to about 30°; the peak axial flow velocity occurs at approximately 80 percent of the distance from the outer wall (see Figure 6.1.1-11) and has peak values approaching 1.65. At larger angles the imbalance between the centrifugal force and the pressure gradient at the outer wall causes the generation of a second pair of counter-rotating vortices. At this point (approximately 60°) in the duct, the centerline longitudinal velocity distribution changes

drastically. The peak velocity begins to shift back towards the center of the duct. The present computed results agree very well with those predicted by Ghia et. al. (1976); the fully developed longitudinal velocity distributions are compared with Ghia's in Figure 6.1.1-12. Both Ghia's work and the present work show a peak velocity of 1.4 occurring very close to the duct center. For the fully developed flow secondary flows on a lateral plane at 72^{o} is shown in Figure 6.1.1-13 and compared with the secondary flow streamfunction as computed by Cheng, et. al. (1976). The prediction of the extra pair of counter-rotating vortices agrees well with experimental data [Dean (1928), Humphrey (1981), Akiyama (1988), Cheng (1992)] and the Cheng (1976) computational results.

Overall Losses for Curved Ducts

The pressure drop in the duct becomes constant after an initial normalized development length of about 0.01 (much shorter than the 0.075 value for a straight duct due to the strong radial pressure gradient) There in the initial developmental length, the pressure changes are much more rapid in the curved duct. The pressure change along the duct is shown in Figure 6.1.1-14. The present prediction for the high Dean number agrees well with Ghia albeit with a somewhat higher gradient.

A comparison between computed friction factor for curved ducts normalized by the friction factor for a straight duct is shown along with experimental data in Figure 6.1.1-15. Results shown for friction factor for fully developed flow cover a wide range of Dean number. As might be expected, friction factor is seen to increase with increasing Dean number and the

present numerical predictions agree extremely well with the empirical data of Ito (1960 and 1970).

Results of present laminar flow computations for two-dimensional and three-dimensional geometries have been presented. Velocity distributions in a driven cavity and developing flows in straight and curved ducts have been presented. Laminar flow predictions presented agree quite favorably with results presented in the literature.

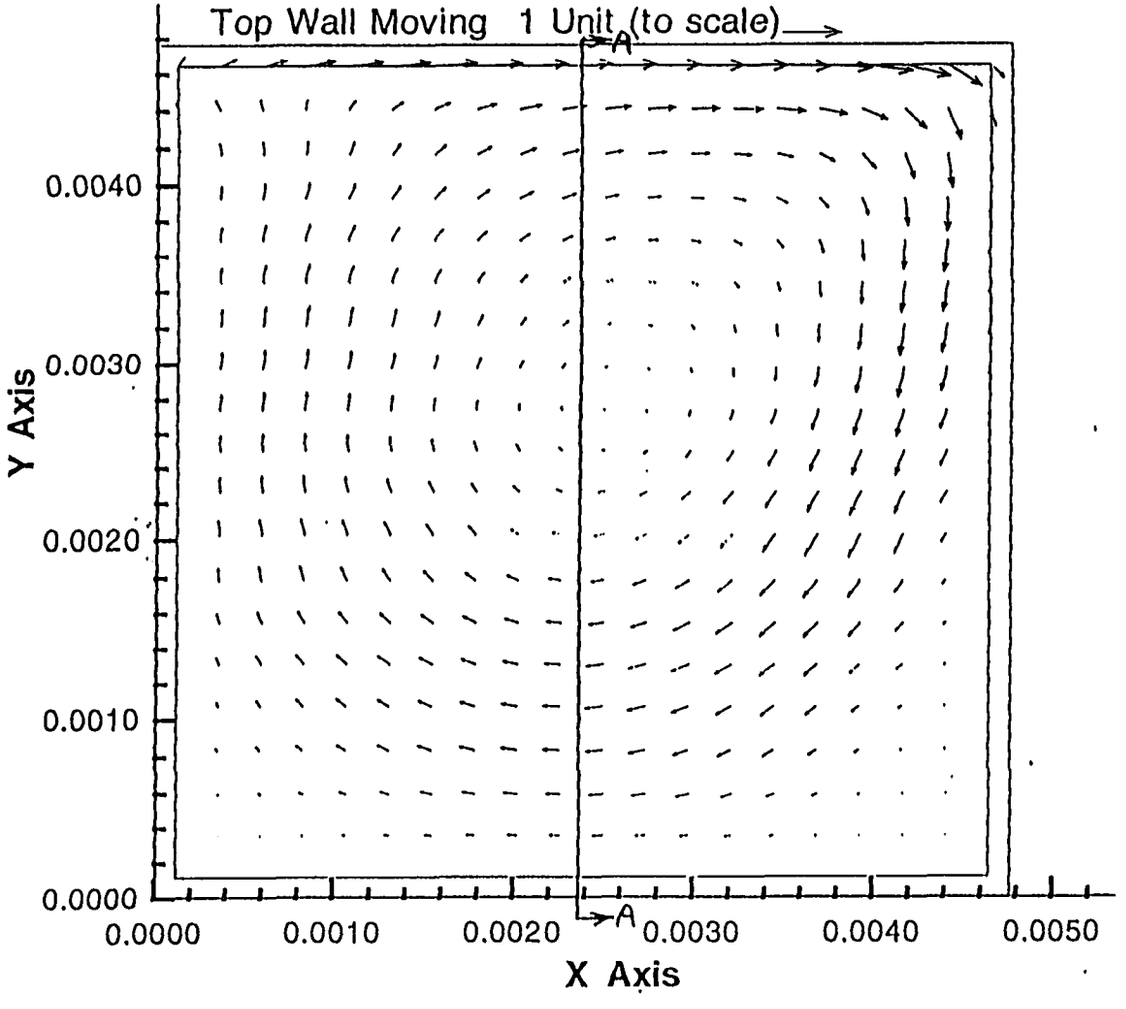

Figure 6.1.1-1 Velocity Vectors for the Driiven Cavity Problem; Re =400

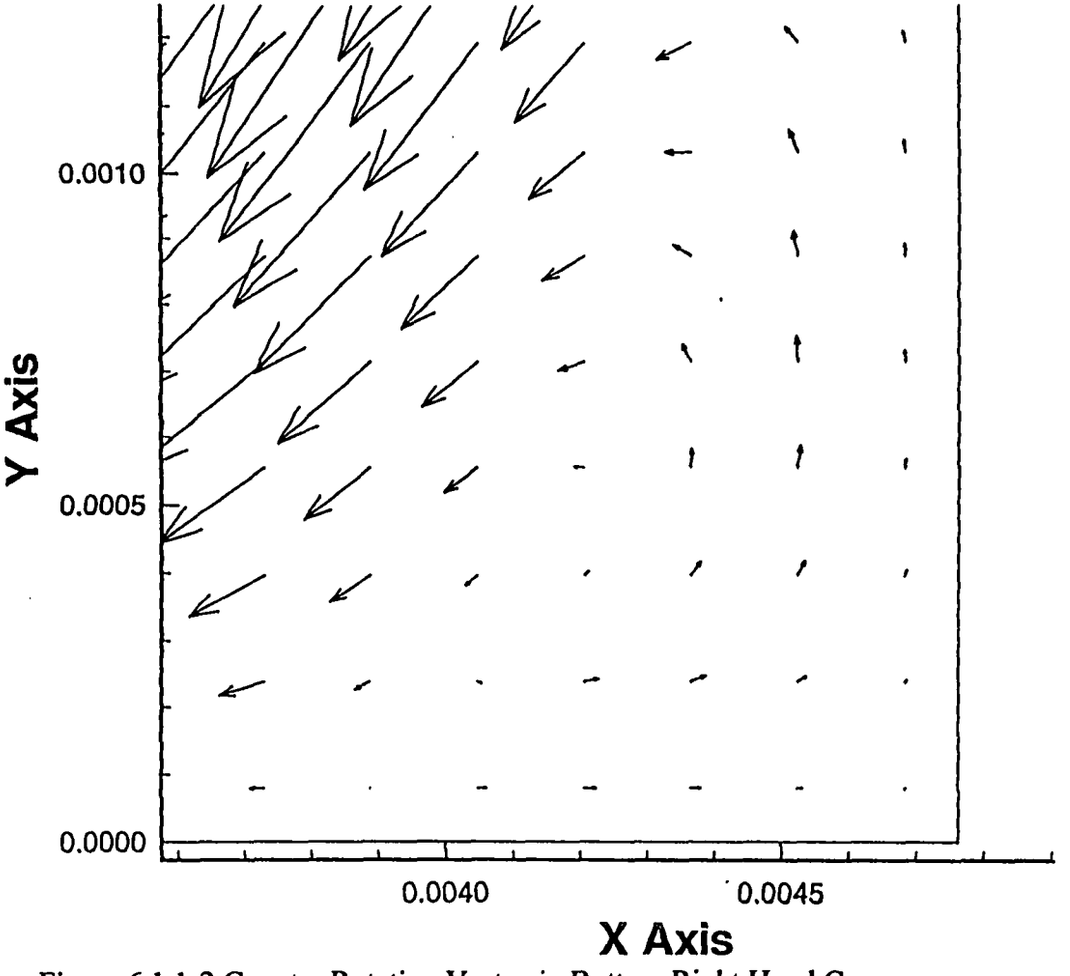

Figure 6.1.1-2 Counter Rotating Vortex in Bottom Right Hand Corner
Driven Cavity Problem; Re =400

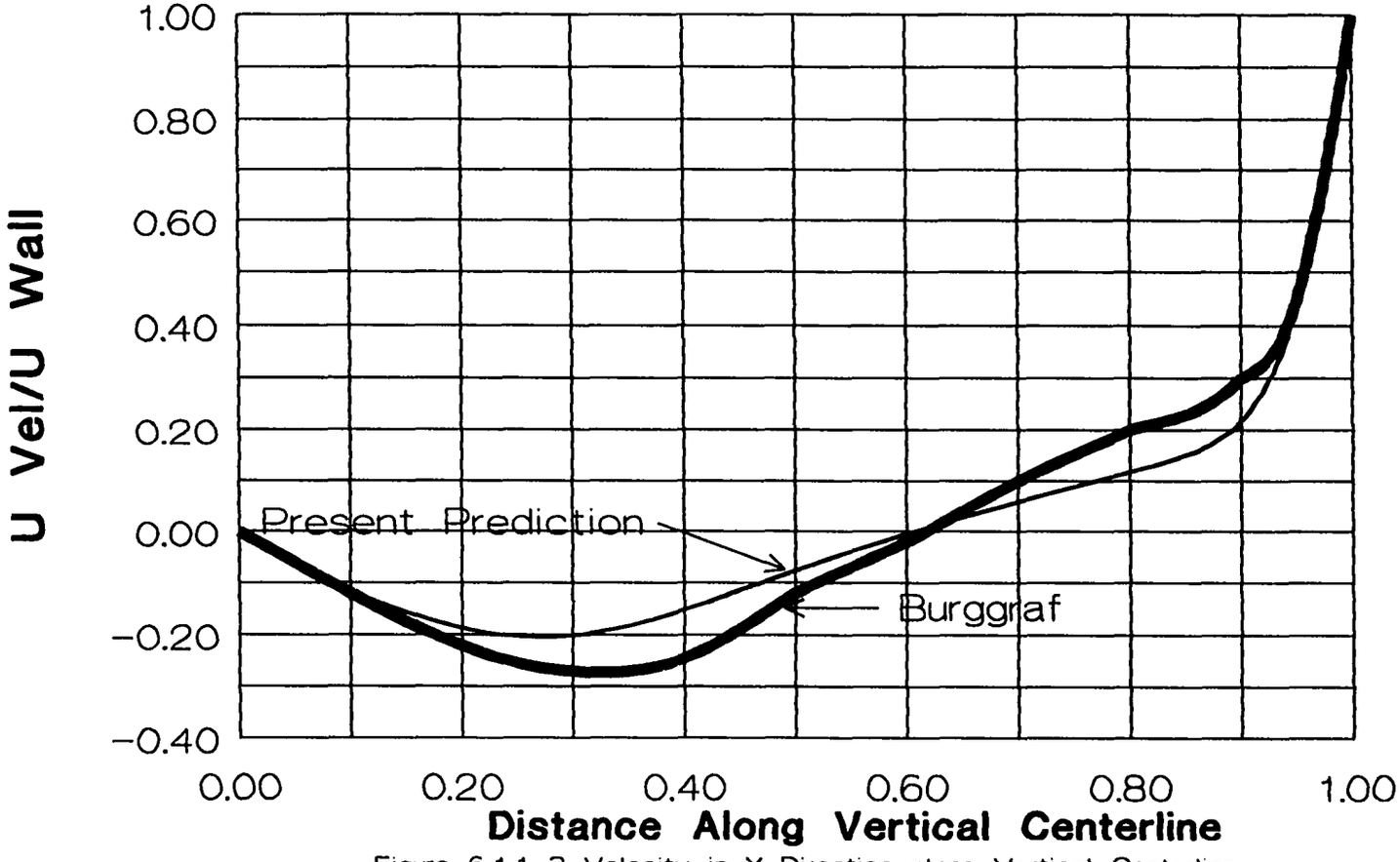

Figure 6.1.1-3 Velocity in X Direction along Vertical Centerline compared to Burggraf's for the Driven Cavity Problem; Re = 400

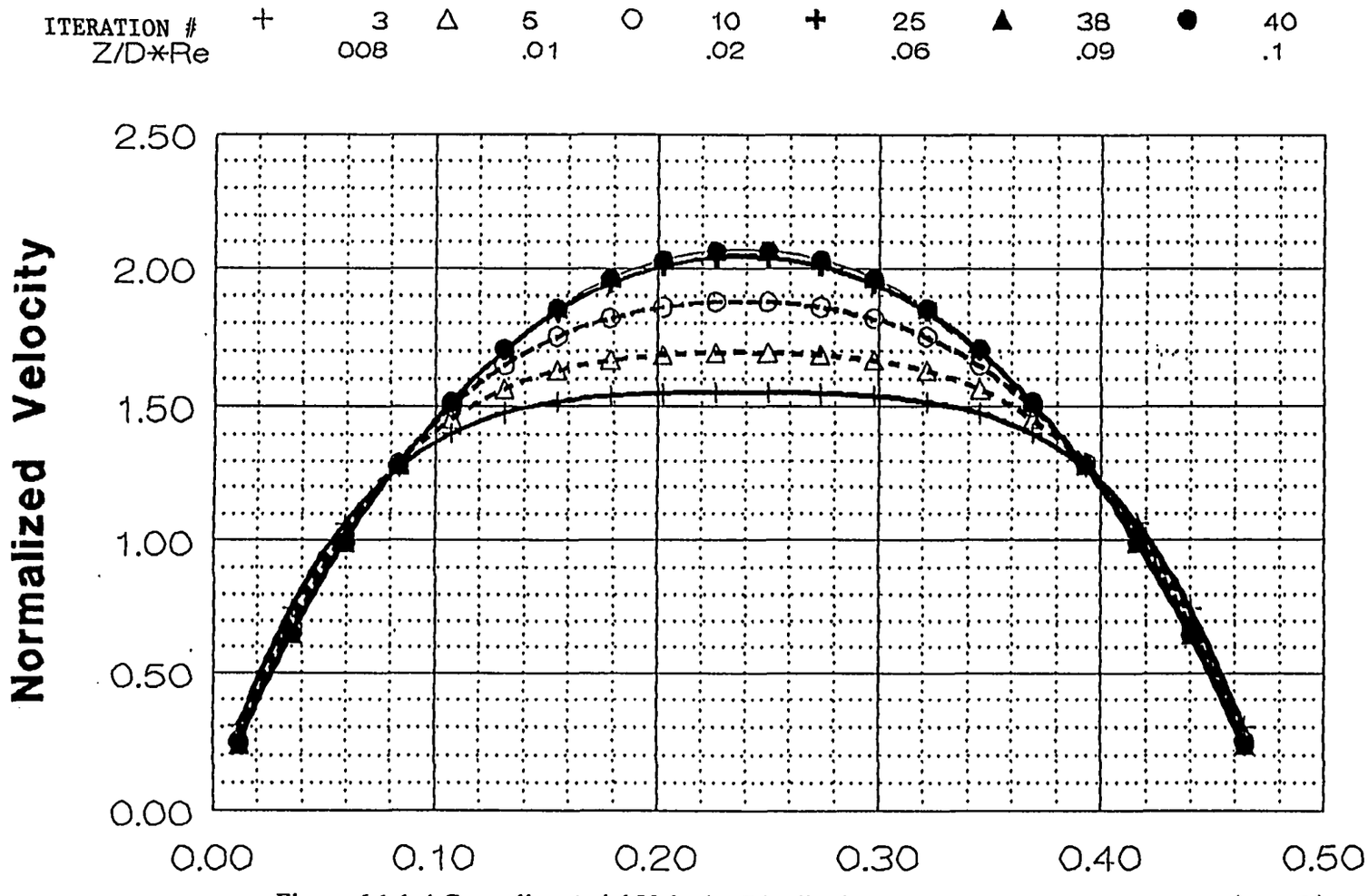

Figure 6.1.1-4 Centerline Axial Velocity Distribution Development in a Straight Duct with Laminar Flow

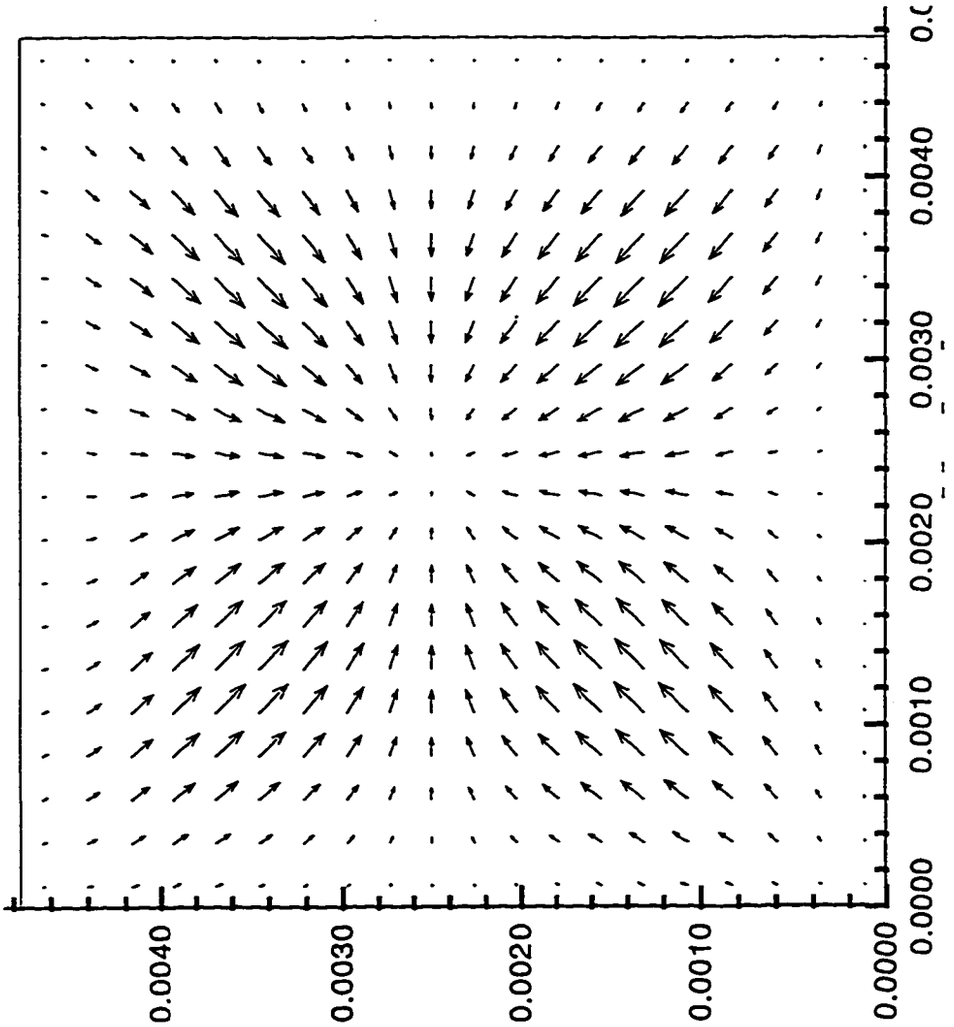

Figure 6.1.1-5 Lateral Velocities--Developing Laminar Flow in a Straight Duct with Laminar Flow at Z/D*Re=0.0128

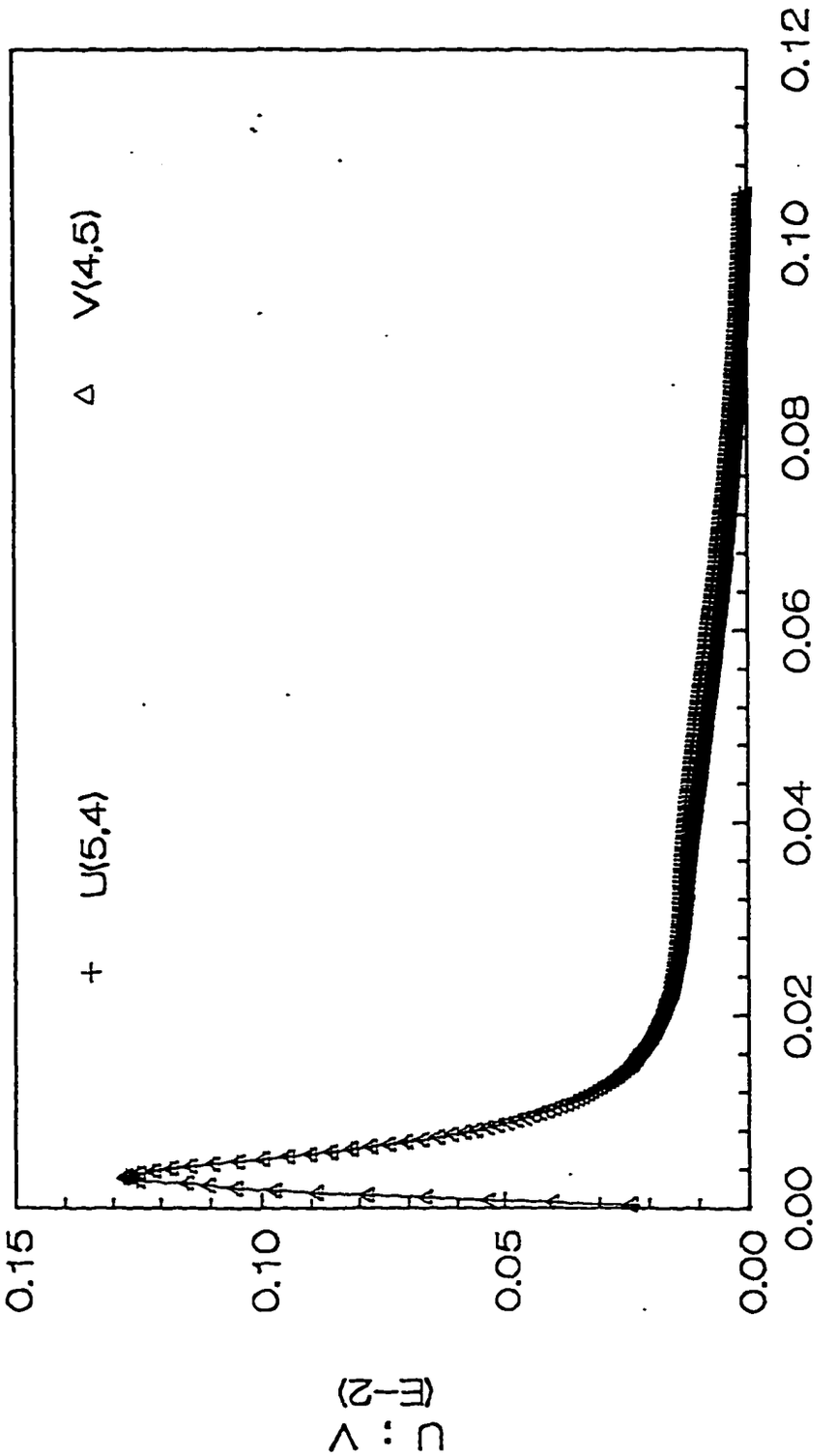

Figure 6.1.1-6 Lateral Velocities vs Normalized Distance; in a Straight Duct with Laminar Flow on a 20 X 20 Grid

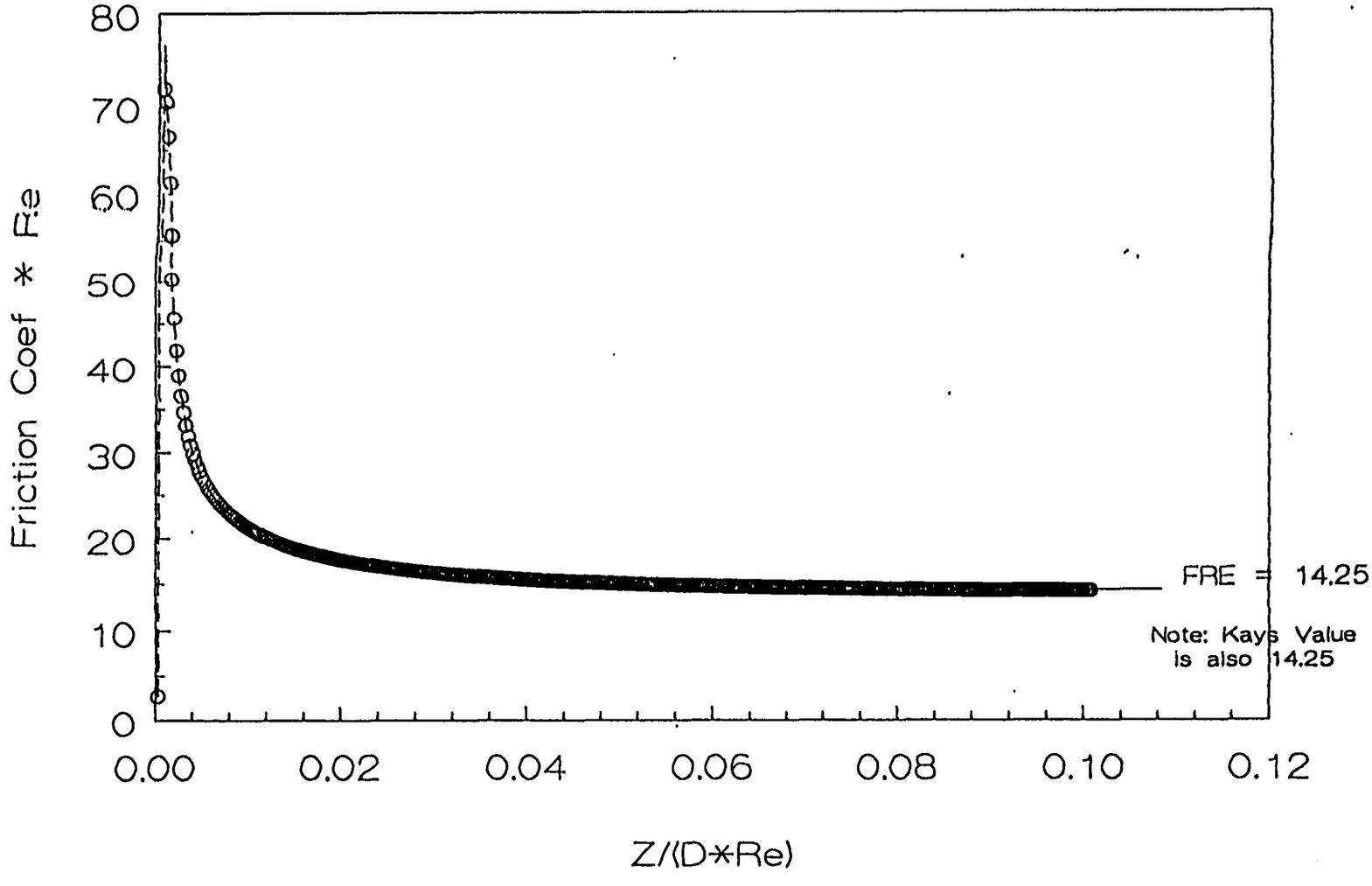

Figure 6.1.1-7 Friction Coeff*Re Number vs Normalized Distance; in a Straight Duct with Laminar Flow

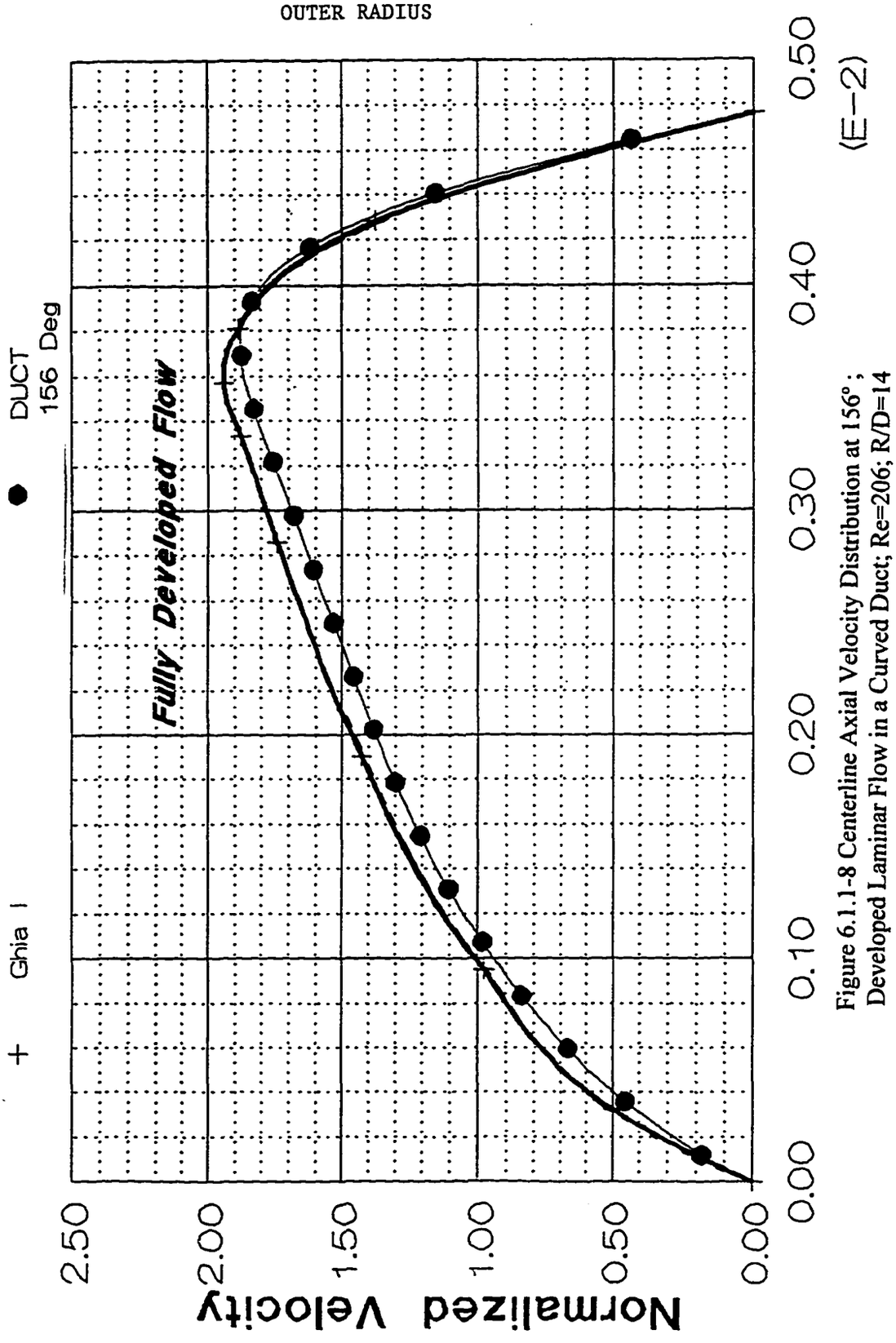

Figure 6.1.1-8 Centerline Axial Velocity Distribution at 156°; Developed Laminar Flow in a Curved Duct; Re=206; R/D=14

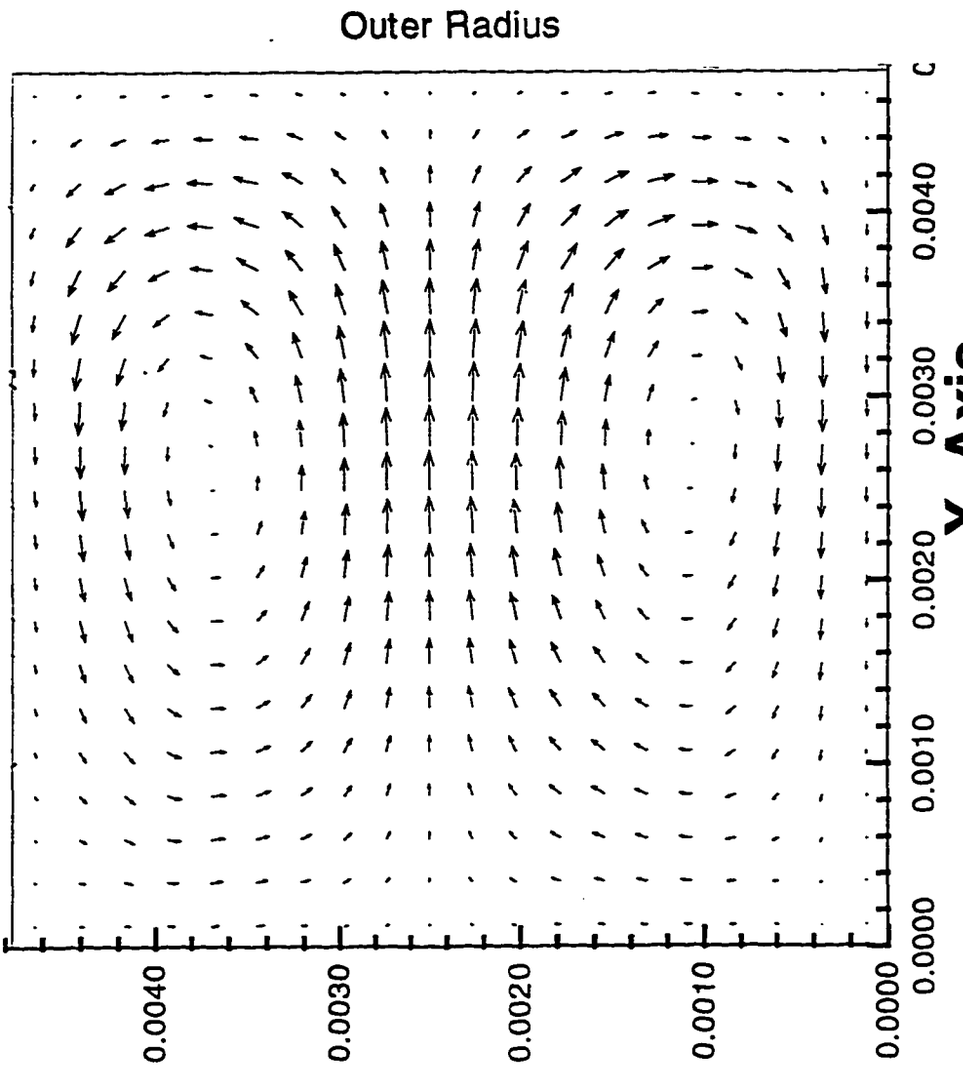

Figure 6.1.1-9 Lateral Velocities at 31°;
Laminar Flow in a Curved Duct; Re=206; R/D=14

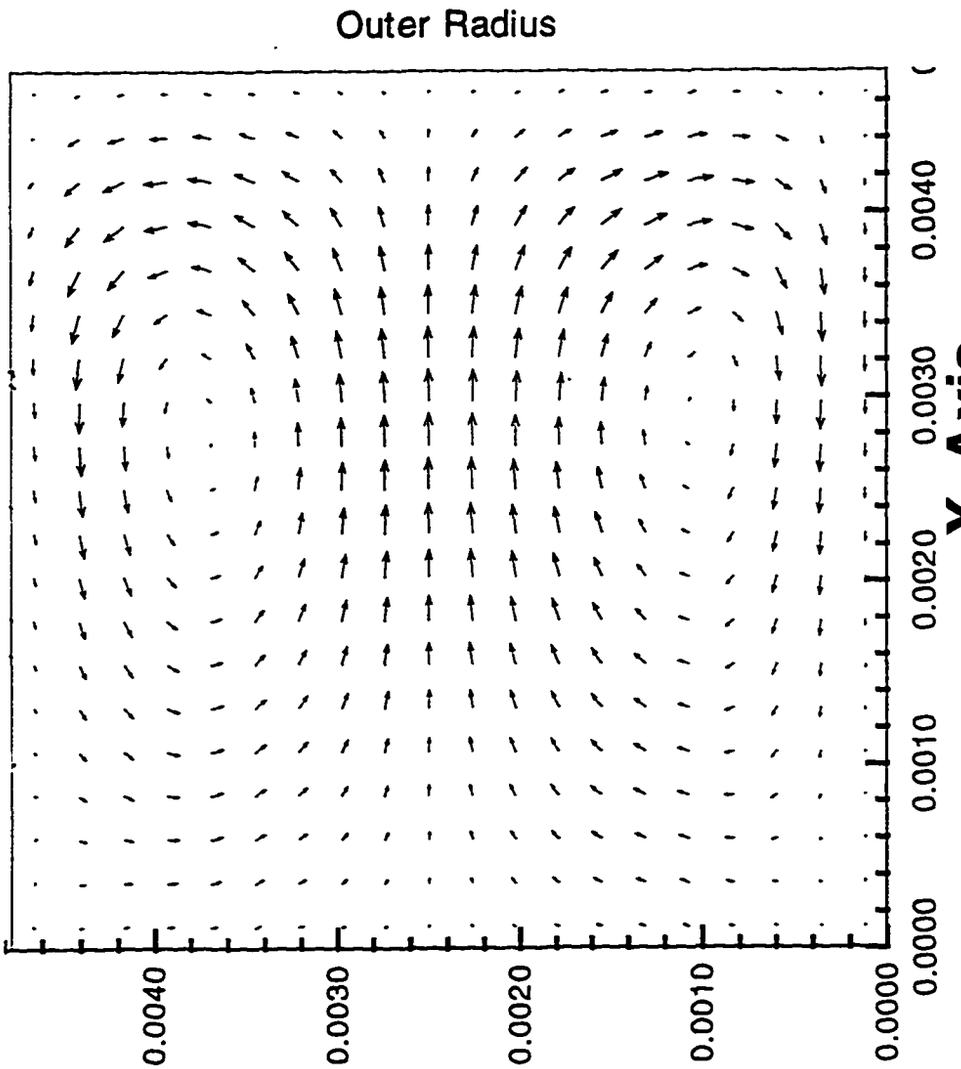

Figure 6.1.1-10 Lateral Velocities at 175° ;
Developed Laminar Flow in a Curved Duct; Re=206; R/D=14

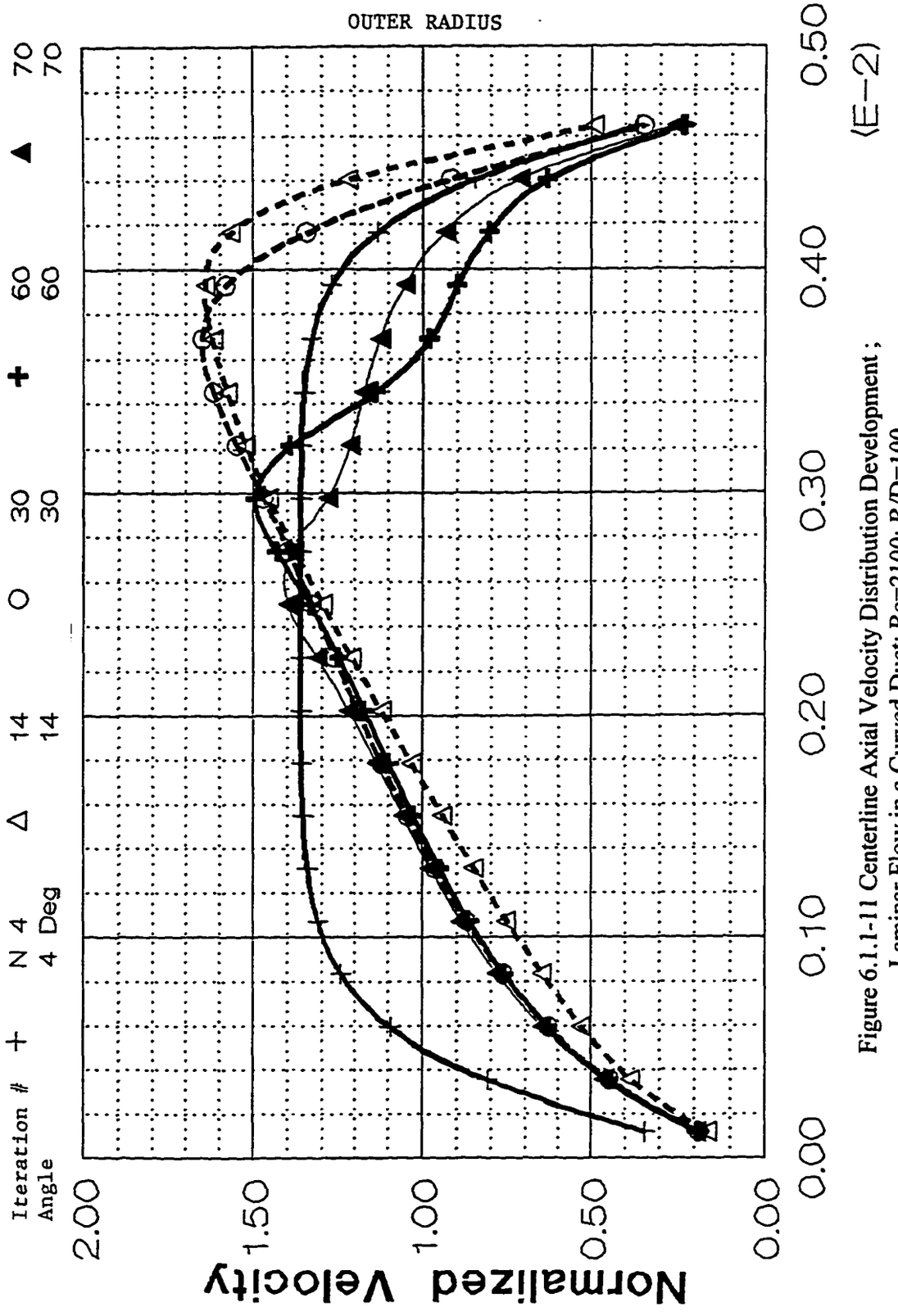

Figure 6.1.1-11 Centerline Axial Velocity Distribution Development ; Laminar Flow in a Curved Duct; Re=2100; R/D=100

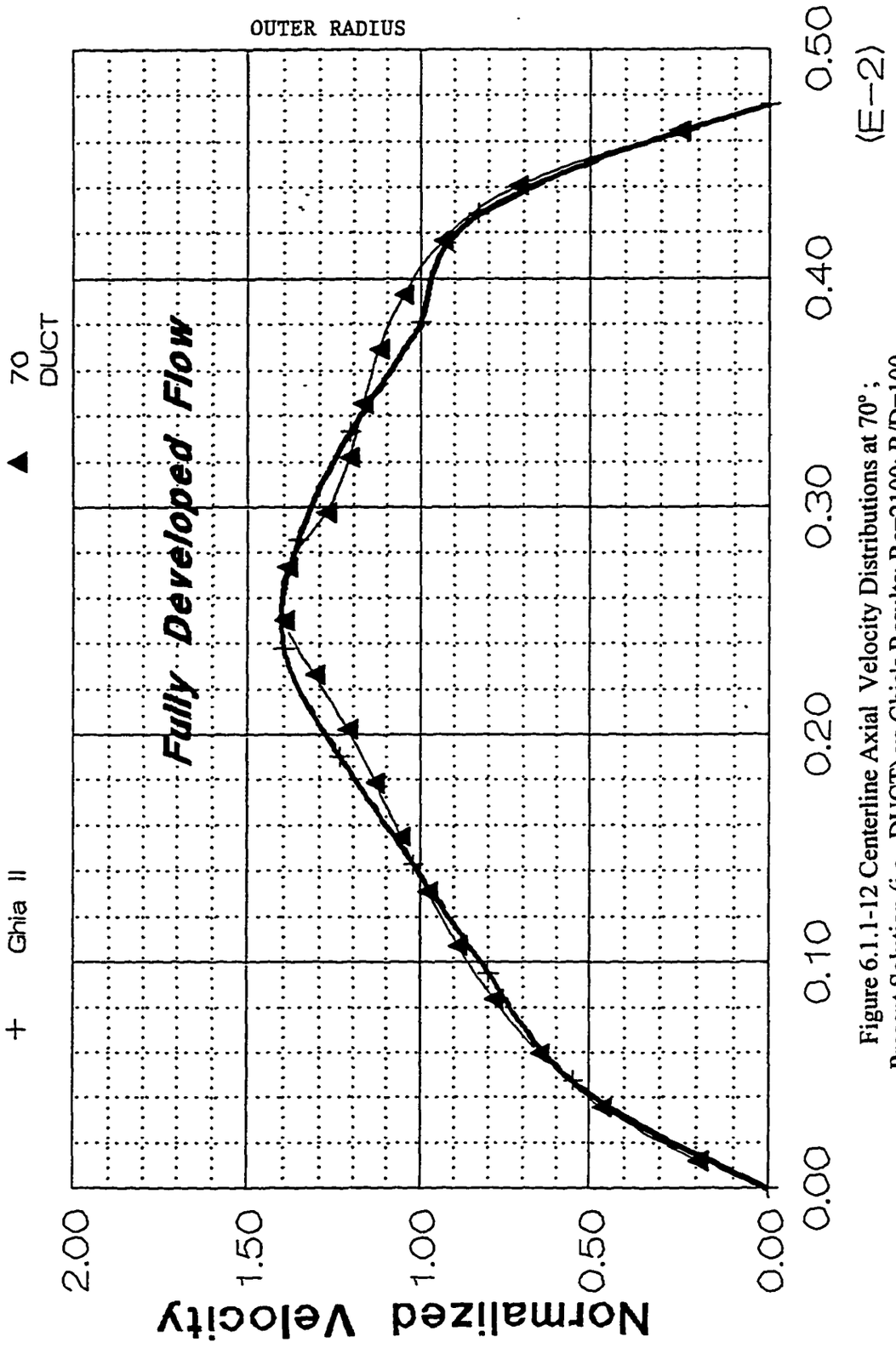

Figure 6.1.1-12 Centerline Axial Velocity Distributions at 70°; Present Solution (i.e., DUCT) vs Ghia's Results; Re=2100; R/D=100

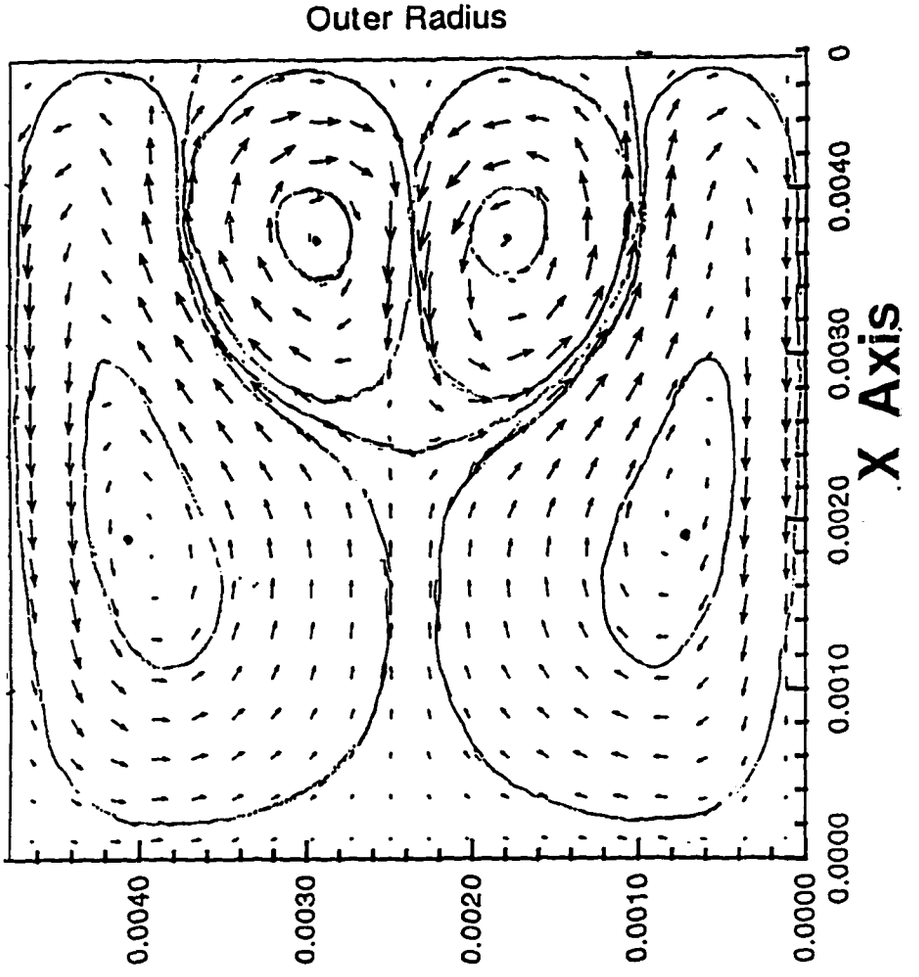

Figure 6.1.1-13 Lateral Velocities at 70°;
Present Solution (i.e., DUCT) vs Cheng's Results; Re=2100; R/D=100

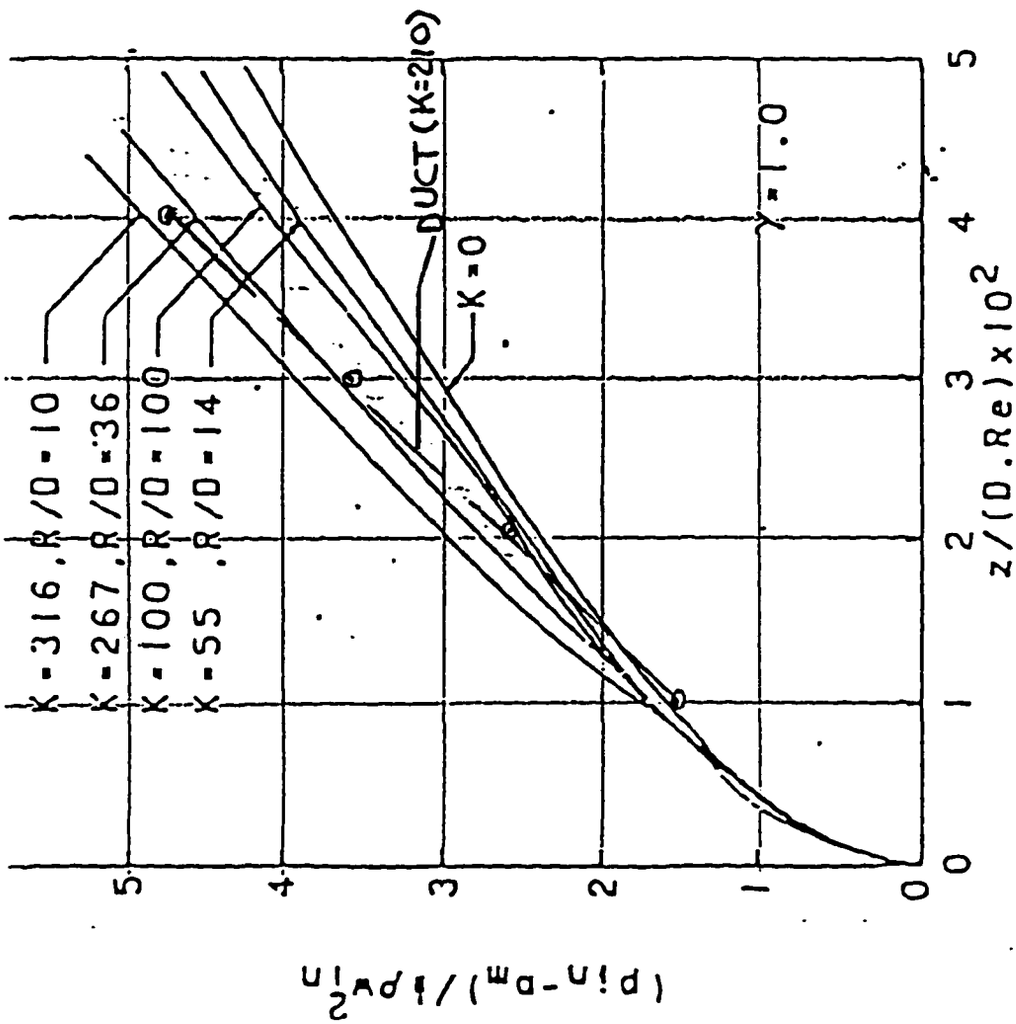

Figure 6.1.1-14 Axial Pressure Drop vs Normalized Distance for Curved Ducts; Present Solution (i.e., DUCT) vs Ghia's Results

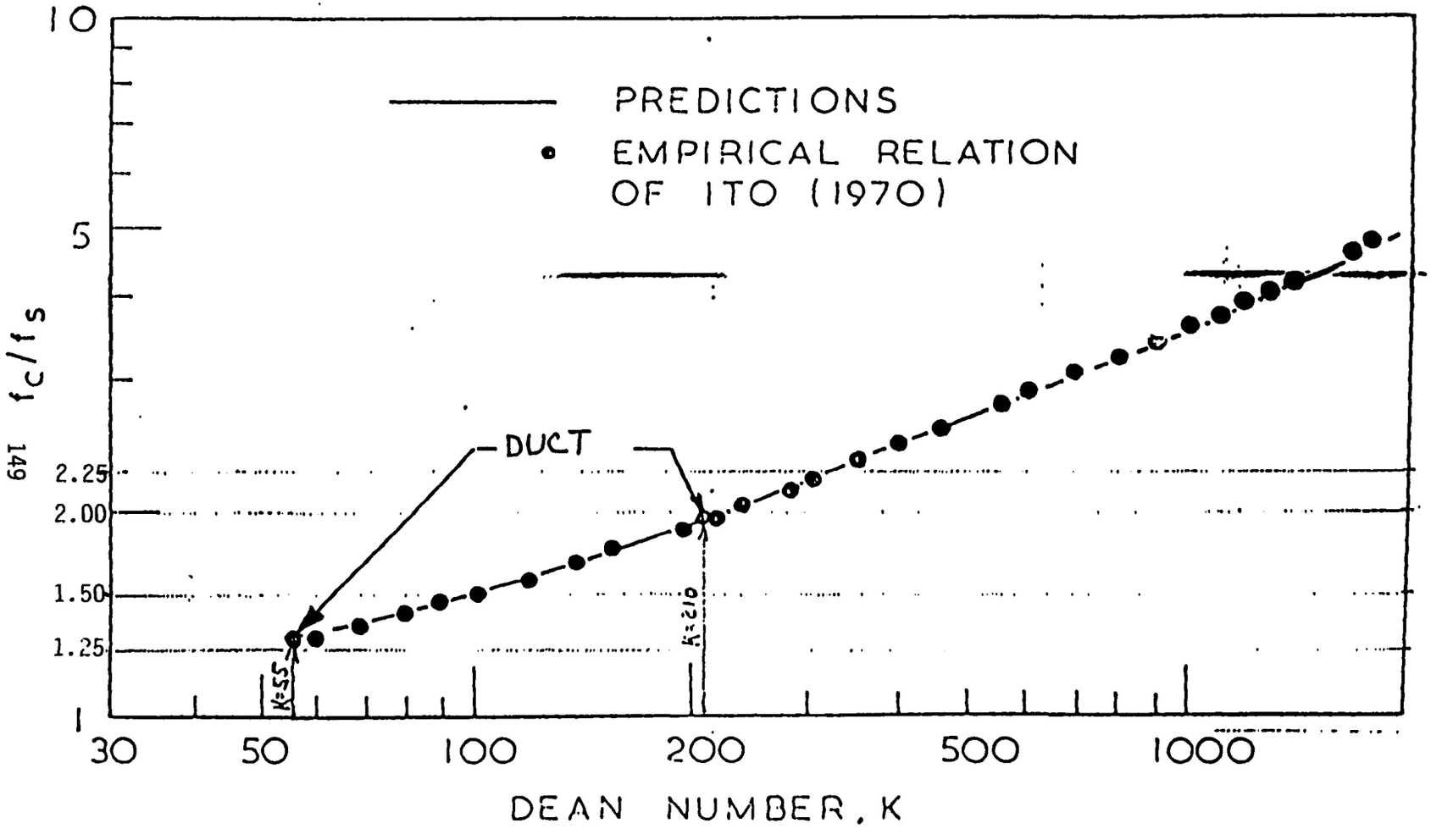

Figure 6.1.1-15 Fully Developed Flow Friction Factor vs Dean Number for Curved Ducts; Present Solution (i.e., DUCT) vs Ito's Empirical Data

6.1.2 Single Phase Turbulent Flow Predictions

This section presents the results for the turbulent flows in various geometries. As will be seen, isotropic as well as nonisotropic turbulent viscosity models have been used for some of the developing flows.

Flows in Straight Ducts

For flows in straight ducts turbulent centerline longitudinal velocity distributions are much flatter than their laminar flow counterparts. These distributions as calculated by the present procedure are given in Figure 6.1.2-1. The peak normalized velocity occurs in the duct's center at 25 hydraulic diameters downstream from the inlet where a uniform velocity distribution was assumed. The velocity distributions at 50 and 62.5 hydraulic diameter are essentially the same as at 25, indicating that fully developed flow is reached at this distance from the inlet. The velocity peak calculated with the present procedure is about 1.32. The experimentally measured peak value is 1.295 according to Ahmed and Brundrett (1971) and 1.275 according to Melling's measurements (1975).

The variation of the peak value of the longitudinal velocity with distance from the inlet is shown in Figure 6.1.2-2. The peak value is predicted to occur at 25 hydraulic diameters from the inlet by the present computations. The final asymptotic value is reached after about 40 hydraulic diameters and is approximately 1.23. The experimental data of Melling showed that the peak velocity occurred at approximately 30 hydraulic diameters from the inlet. Computations of Emery that used an elaborate length scale model showed a peak value very close to that calculated herein (i.e., 1.32) but at approximately 37.5 hydraulic diameters from the inlet.

While the secondary flow velocities approach zero for fully developed laminar flow, the existence of nonzero secondary flows in fully developed turbulent flows have been known for over 75 years. In such turbulent flows the secondary flows tended to transport flow towards the corners. As a result of this transport, the contours of axial velocity tend to bulge out toward the corners. The secondary flows into the corner are called secondary flows of the second type. The driving mechanism for these flows are the gradients in the normal Reynolds stresses. A standard k-ε turbulence model with its isotropic turbulent viscosity would be incapable of resolving these motions. A anisotropic Algebraic Reynolds Stress Model [Neti and Eichorn(1979)] was used to compute the turbulent straight duct. The predicted secondary flow vectors at 37.5 hydraulic diameters are shown in Figure 6.1.2-3. Four pairs of counter-rotating vortices are predicted to occur, one pair near each corner. The maximum secondary flow velocity is approximately 3 percent of the through-flow. The predicted axial velocity contours, (Figure 6.1.2-4), show bulges into the corners and have been confirmed by experiments [Melling (1975)].

Because of these secondary flows the wall shear stress is not uniform across the duct side but has been found to have two maximums which are located between the corner and the mid-point of a side wall. The present numerical prediction of wall shear stress distribution is compared with data from Leutheusser (1963) in Figure 6.1.2-5. The qualitative trend described above is predicted well. The predicted maximum wall shear stress is predicted to be 1.08 of the average shear stress, which agrees well with the experimentally measured value of 1.075.

Contours of normalized turbulent kinetic energy ($\frac{\rho k}{\tau_w}$) are shown in Figure 6.1.2-6. The predicted contours are very similar to those measured by Brundrett and Baines (1964), with the highest level close to the wall and the lowest levels near the duct's center. The currently

predicted highest level is approximately 3.4 compared to the experimental data of 4.5; the lower levels are predicted to be 1.65 compared to those in experiments of 2.5.

Turbulent Flows in Curved Duct

The present 'DUCT' computer code was validated for single phase turbulent flow in curved ducts also. Various geometries were computed for which experimental data existed in the open literature. Humphrey (1977, 1981) presented results, both experimental and computational, for fully developed flow in a curved duct of square cross section with mean radius of $2.3\ D_H$ at a Reynolds number of 40,000. A straight inlet section of 45 hydraulic diameters ahead of the curved duct was used to insure that the inlet flow was fully developed. Humphrey (1977) used the same configuration for laminar flow conditions and found flow separation along the outer wall at planes up to 12°. This region of separation was not evident in the centerline longitudinal velocity distributions but at the two locations 6 percent off of the endwalls. This implies that a bend R/D_H of 2.3 is too small to avoid separation *when the flow is laminar.* Due to the anticipated separation this laminar flow case could not be computed with the present partially parabolic procedure. However, for turbulent flow in a similarly curved duct, Humphrey's data does not show any such separation and reverse flow. Thus turbulent flow in the tight duct was used for validating the present computational algorithm.

The present computational predictions capture the trends of the longitudinal turbulent centerline velocity development measured by Humphrey. These are distinctly different from those seen in the laminar flow case. In the turbulent flow case, the maximum velocity position is close to the mean radius until about 60° where it begins to move toward the outer wall; whereas for laminar flow in a curved duct the maximum velocity location moved rapidly toward the outer

wall and remained there. The predicted longitudinal centerline velocity distributions at various locations throughout the duct are shown in Figure 6.1.2-7 for a uniform inlet velocity distribution (see profile close to the inlet). This develops into the fully developed condition at about 45 hydraulic diameters downstream of the inlet. This longitudinal velocity profile has a peak at the center of the duct and the peak slowly moves toward the outer wall further along in the 90° curved section. Figure 6.1.2-7 shows the centerline axial velocity distribution across the x direction, i.e., from inner to outer radius. This distribution is nearly maintained for all y values. This three-dimensional nature of the flow allows mass to be conserved even though the centerline distributions shown in Figure 6.1.2-7 might seem to indicate that the curved duct has more mass at the end of the straight duct than at the inlet. The present predictions are compared with Humphrey's experimental data as well as Humphrey's computational predictions (1981) at the 45° plane in the curved duct (Figure 6.1.2-8). The present prediction also captures the measured slight shift in location of the maximum towards the outer walls better, but both predictions yield peak velocities smaller than seen in the experiment. A comparison of the longitudinal velocity predictions of the present work and Humphrey's at the exit (90°) of the curved duct is shown in Figure 6.1.2-9. The presently predicted values are somewhat lower and shifted more towards the outer radius than Humphrey's prediction.

The predicted secondary flow patterns are shown in Figure 6.1.2-10. The cross plane flow consists of a single pair of counter rotating vortices with maximum secondary velocities of approximately 30 percent of the through flow velocity. This velocity level is higher than that for the laminar duct flow case. The contours of the u component of velocity (i.e., the component in the x or radial direction) at the exit of the duct are shown in Figure 6.1.2-11 from the present

predictions as well as that of Humphrey. Both predictions show maximum velocities of about 30 percent of the longitudinal velocity in the negative x direction, i.e., towards the inner radius.

The predictions of the turbulent curved duct flow compared reasonably well with Humphrey's data in most areas but still showed indications that improvements in modeling were needed to match the existing data. The present calculations (and Humphrey's) were carried out with a standard k-ε turbulence model. In complex flows where significant anisotropic rate-of-strain components might be present (due to streamline curvature or rotation or separation, etc.) the present turbulence model with its assumption of isotropic turbulent eddy viscosity may not be able to capture the flow details accurately. Various algebraic curvature correction models were tried. In general these models resulted in some areas of improvement while degrading the results elsewhere. The most promising was the theory of Leschziner and Rodi (1981), which modifies the eddy viscosity to include local curvature effects based on the a Richardson number. This modified turbulence model was applied to the Humphrey problem. The computed centerline velocity distributions are shown in Figure 6.1.2-12. These can be compared with those given in Figure 6.1.2-7 which used the standard k-ε turbulence model. The peak velocities are somewhat higher here in the areas where the isotropic model underpredicted the level compared to experimental data. The velocity gradient near the outer wall is steeper. The velocity distributions at 45° (Figure 6.1.2-8) shows that the peak velocity is now 1.15 instead 1.13 but is still less than the experimental level of 1.30.

The results of using an algebraic modification to the standard k-ε turbulence model are not very encouraging and suggest that a higher level of sophistication is required. This conclusion based on several trials of various algebraic curvature correction methods in the present algorithm is consistent with the general observations expressed by Tamamidis and Assanis

(1993). Pourahmadi and Humphrey (1983) extended the Algebraic Reynolds Stress model (ARSM) to include curvature effects. This seemed to improve the predictive capabilities of their code. However, based on the present work and their work done with ARSM for modeling strongly curved ducts, it appears the full Reynolds Stress transport equations will be necessary for the proper prediction of these flows. For more gently curved ducts (the duct configuration used in this work has a mean radius of 5.5) it is expected that the standard k-ε model will yield results which are more reasonable.

Pratap (1976) has presented experimental turbulent curved duct data for a rectangular cross section curved duct of aspect ratio 0.25 (the height is 0.25 time the base, where the base dimension is the difference between the outer and inner radii). The present program was run to simulate the geometry tested by Pratap. Unfortunately the duct had a very short straight inlet section (2.5 hydraulic diameters) so that the inlet boundary condition to the curved section is not fully developed and not easily specified. Additionally, due to inlet screens, the inlet velocity profile had a low velocity region near the center which tended to persist throughout the curved section. To predict the flow in that configuration, the measured inlet velocity profile was used as the initial velocity profile in the computations. Most of the reported measurements were made close to the end-walls (approximately 13 percent from the walls) rather than the centerline, due perhaps to the large size of their test duct which made cantilevering a probe into the duct difficult. A comparison of the present computations and Pratap's measurements are shown in Figure 6.1.2-13, for the flow at 56 degrees. Despite all the shortcomings mentioned above the comparison is generally good.

Overall Losses for Turbulent Flow in Curved Ducts

Predictions of the local flow features of turbulent flows in straight andcurved ducts have been given in the previous sections. These include secondary flow patterns, longitudinal velocity profiles and distribution of shear stress. These calculations helped in the development of the computational algorithm and served to validate the results. The designer is often not so concerned about local features as much as how these features affect overall parameters such as the pressure loss between different stations. The present section discusses the computed overall pressure losses for turbulent flow in curved ducts and compares these results to data available in the literature.

There appears to be a large variability in the experimentally measured values for pressure loss in pipe bends due mainly to the methods used for the measurements. An experimental method used by Ito (1960) and also reported by Blevins (1984) in which long tangents or straight sections are used both upstream and downstream of the bend seems to be the best way of measuring the overall head losses. Such a geometry was numerically simulated to compute the numerical pressure loss data. This procedure insured geometric consistency between the experimental data used and the numerical computations. The approach used here is physically more realistic since it accounts for all the losses including the recovery phase of the bend. The proposed method for finding the loss due to a pipe bend uses the pressure difference between two stations--one inside the long straight section preceding the bend which is far enough from the inlet so that the flow is fully developed and the other at the exit of the long straight section following the bend. This pressure loss is then reduced by the fully developed loss for a straight duct of length equal to the sum of the inlet and exit sections. Thus the method yields the total loss

due to the bend alone. Measuring pressure loss just across the bend itself underestimates the losses since it does not account for the mixing (recovery) loss associated with the distorted profile at the exit of the bend.

The overall loss coefficient for a square cross section curved duct (90^{o} bend) was predicted for single phase flow at a Reynolds number of 40,000 and compared to test data from Blevins (1984). The results are shown in Figure 6.1.2-14. Also shown on the figure is the mean value of the loss coefficient for single phase flow measured in a square cross section 90^{o} bend as part of this work but a lower Reynolds number. The data from the present experiments are at a Reynolds number of 24,140. The measured loss coefficient has been adjusted for Reynolds number (proportional to $Re^{-0.2}$). The resultant loss coefficient falls very close to the experimental data quoted in Blevins. The loss coefficient is plotted as a function of bend radius ratio (i.e., mean radius normalized by the hydraulic diameter of the duct). The loss increases with radius ratio in the range of 2 to 7. The present numerical scheme appears to somewhat underestimate the loss for R/D_H =2.3 and overestimated the loss for R/D_H above 3.5. The overall agreement over such a wide range of radius ratios is encouraging when we recognize the spread in the data presented in the literature and the wide parametric range of the physics of the flow considered here. At the lowest radius ratio numerically computed (i.e., 2.3) the losses are dominated by diffusion losses and the problem requires an elliptic algorithm with an anisotropic turbulence model, while at the largest ratio computed (i.e., 7) the losses are dominated by wall skin friction.

The present computational algorithm was used to analyze the overall loss in 90^{o} curved ducts with rectangular cross sections. These computations were compared to loss data as reported by Idelchik (1976). Both the analytical predictions and the data show that the pressure loss for rectangular cross section ducts of aspect ratio greater than unity (i.e., height is greater

than the dimension in the radial direction) is less than that for a square cross section duct. Similarly, the loss for rectangular cross section duct of aspect ratio less than unity is larger than that in a square duct. The existence of counter-rotating vortices in curved ducts means that the flow is subjected to large shear when the aspect ratio is less than unity. Thus it is not surprising that the pressure losses are greater for these low aspect ratio cross sections. Figure 6.1.2-15 shows the pressure loss comparison between data and the present prediction method. The test data indicates that the minimum loss occurs for an aspect ratio of 1.85. The 'DUCT' code predicts this minimum at an aspect ratio of 2.0. The last two figures indicate that the overall pressure loss for a curved duct of square or rectangular cross section can be predicted very well with the present algorithm.

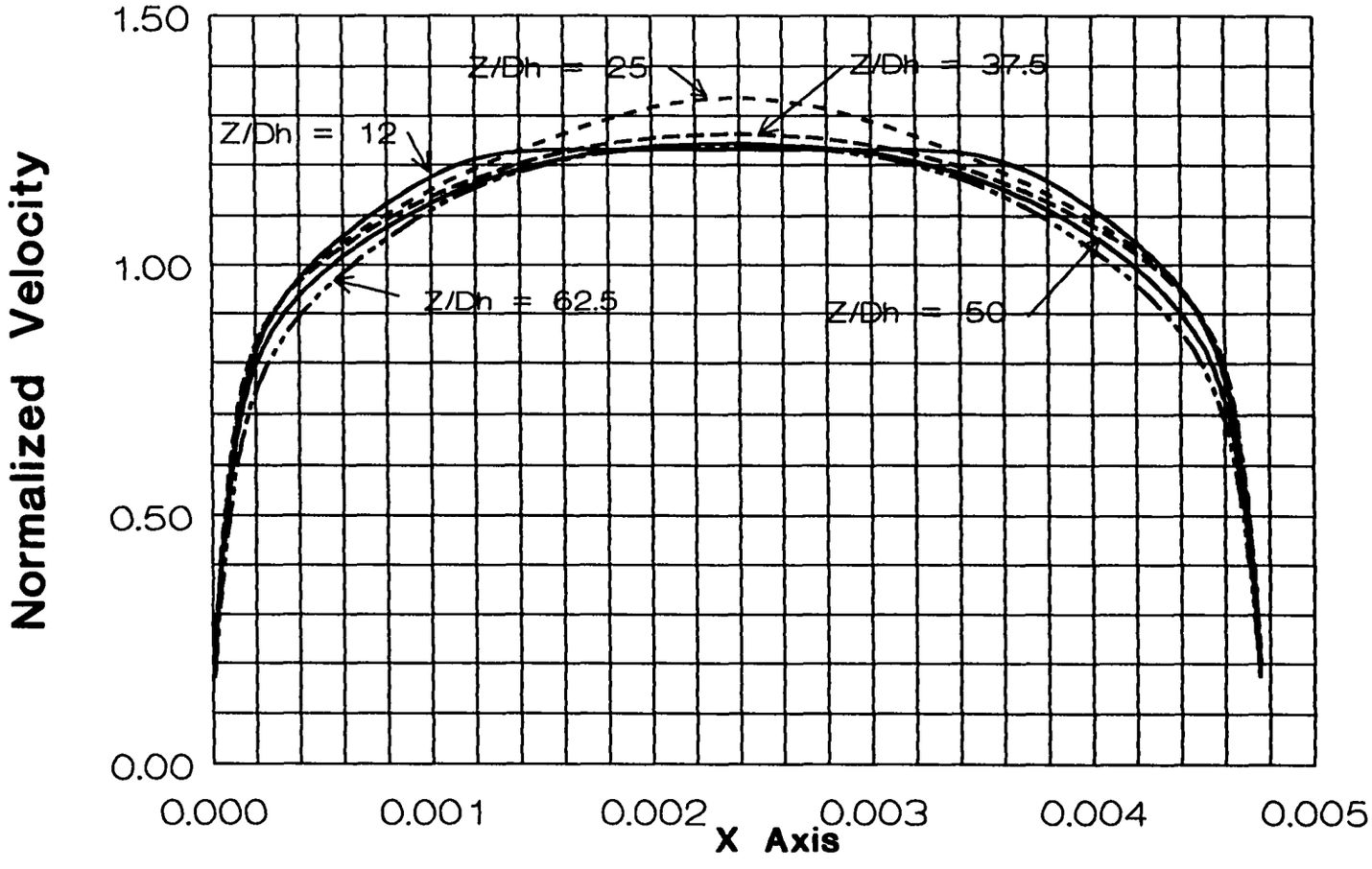

Figure 6.1.2-1 Centerline Normalized Axial Velocity Distributions for Turbulent Flow in a Straight Duct with Square Cross-Section vs Normalized Distance

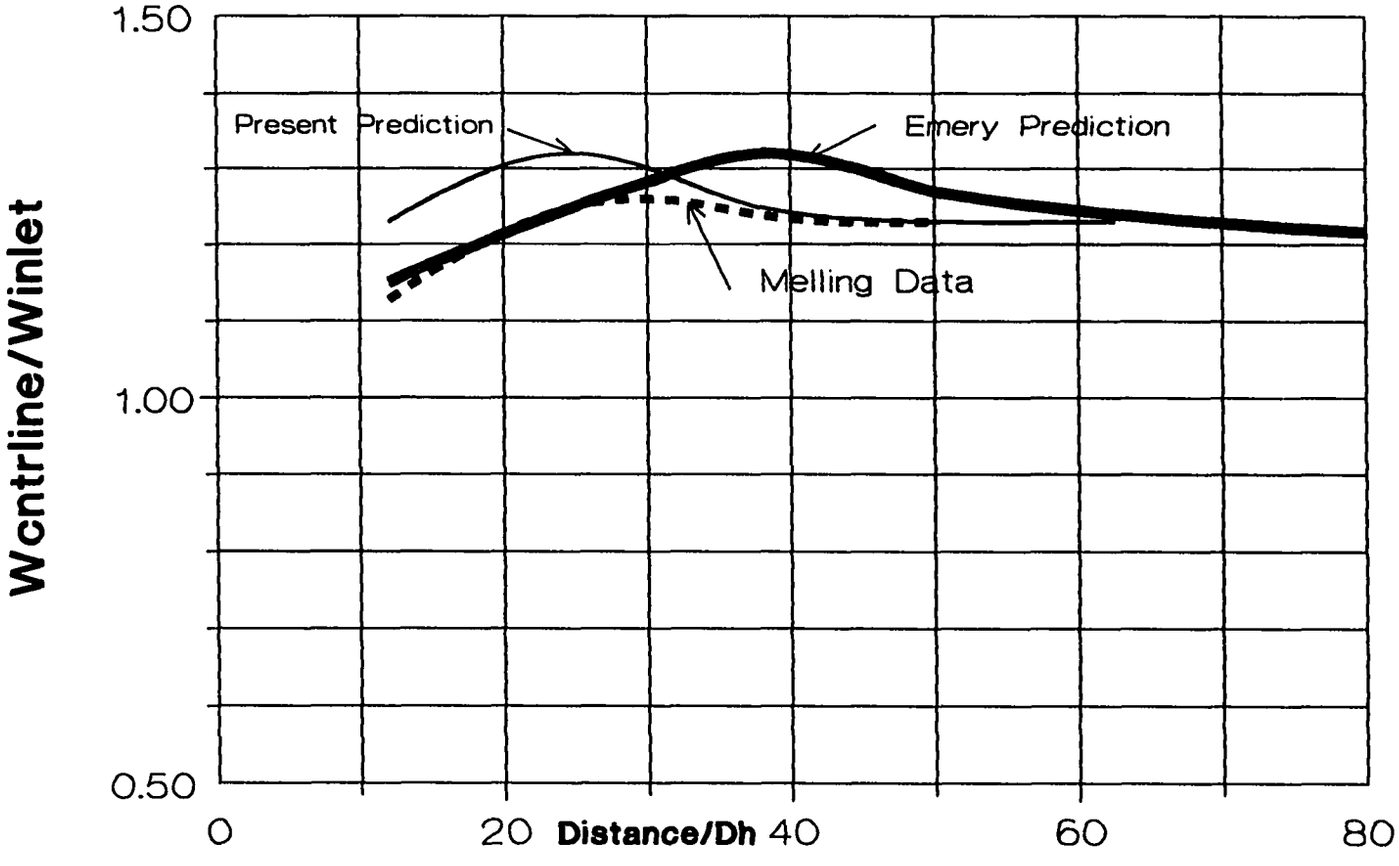

Figure 6.1.2-2 Centerline Normalized Axial Maximum Velocity for Turbulent Flow in a Straight Duct with Square Cross-Section vs Normalized Distance

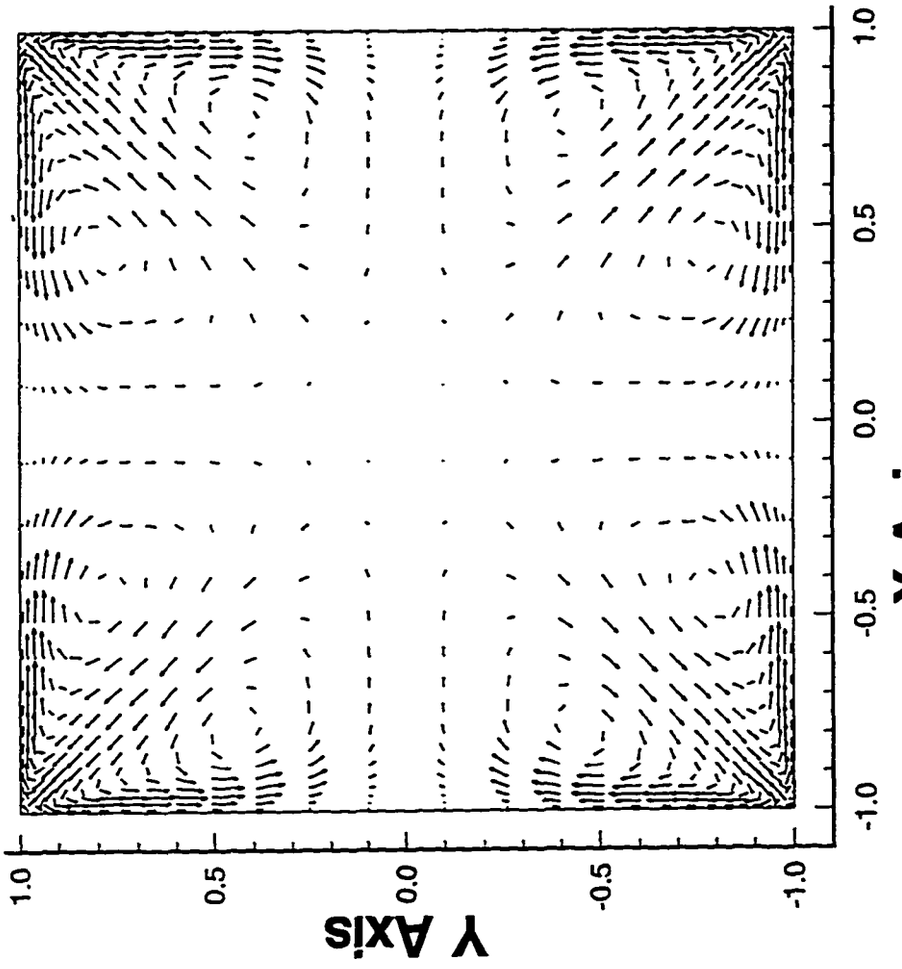

Figure 6.1.2-3 Secondary Flow Velocity Vectors for Turbulent Flow;
in a Straight Duct at a downstream distance equal to 37.5 hydraulic diameters

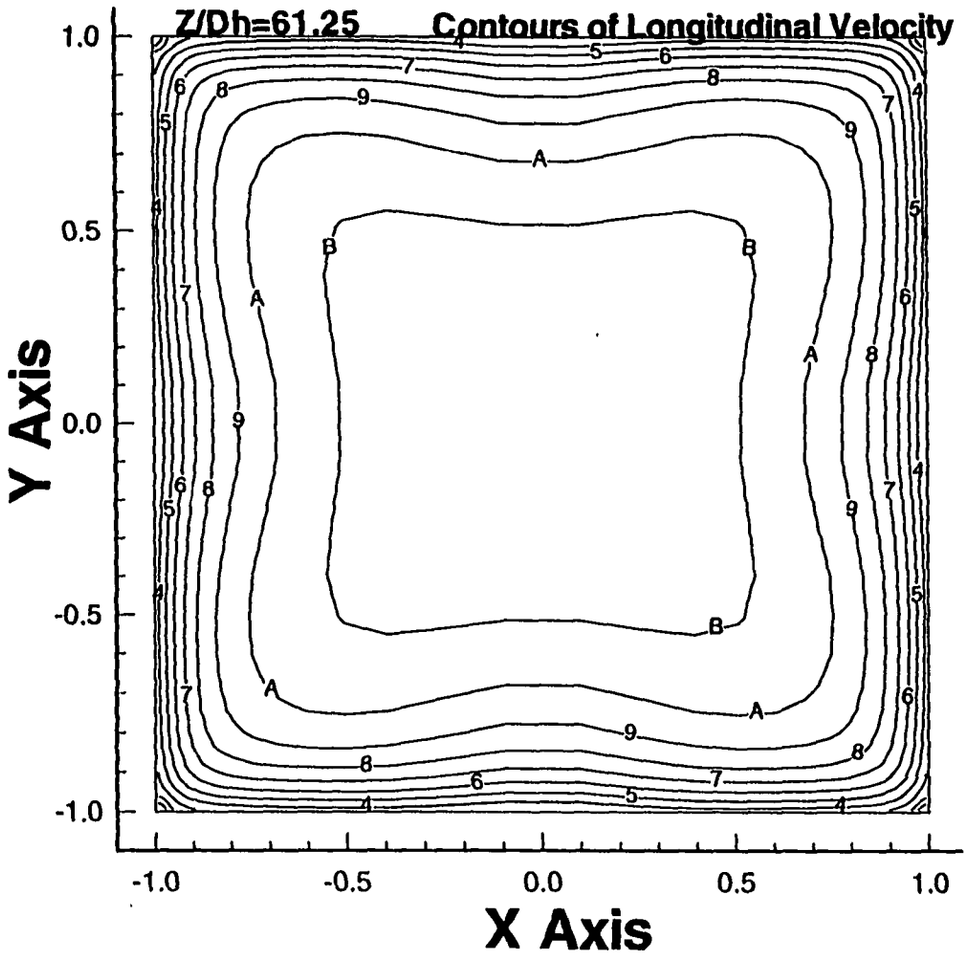

Figure 6.1.2-4 Contour Plot of Axial Velocity Vectors for Fully Developed Turbulent Flow in a Straight Duct with Square Cross-Section

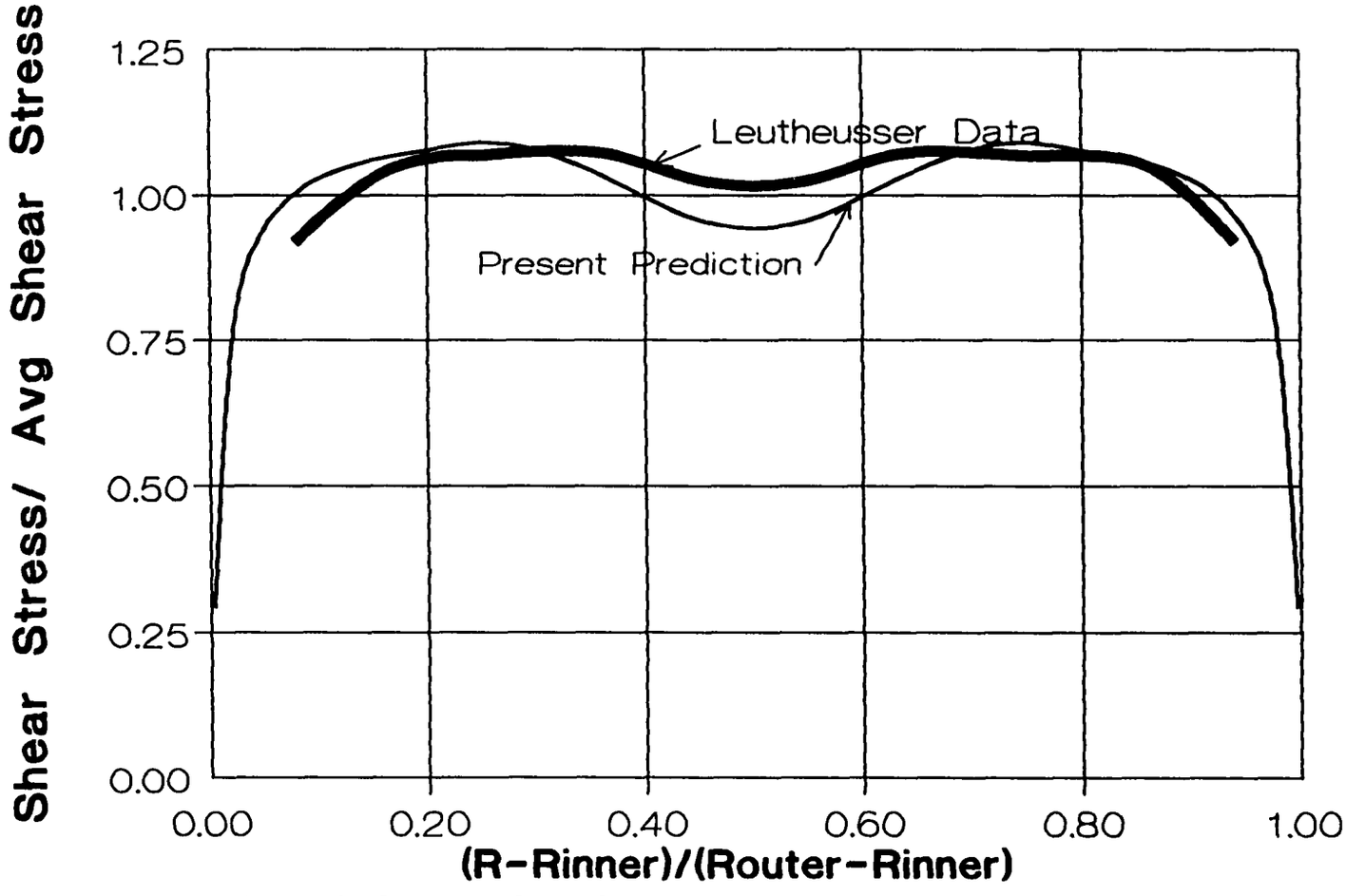

Figure 6.1.2-5 Wall Shear Stress Distribution for Developed Turbulent Flow in a Straight Duct; Present Predictions compared to Leutheusser's Data

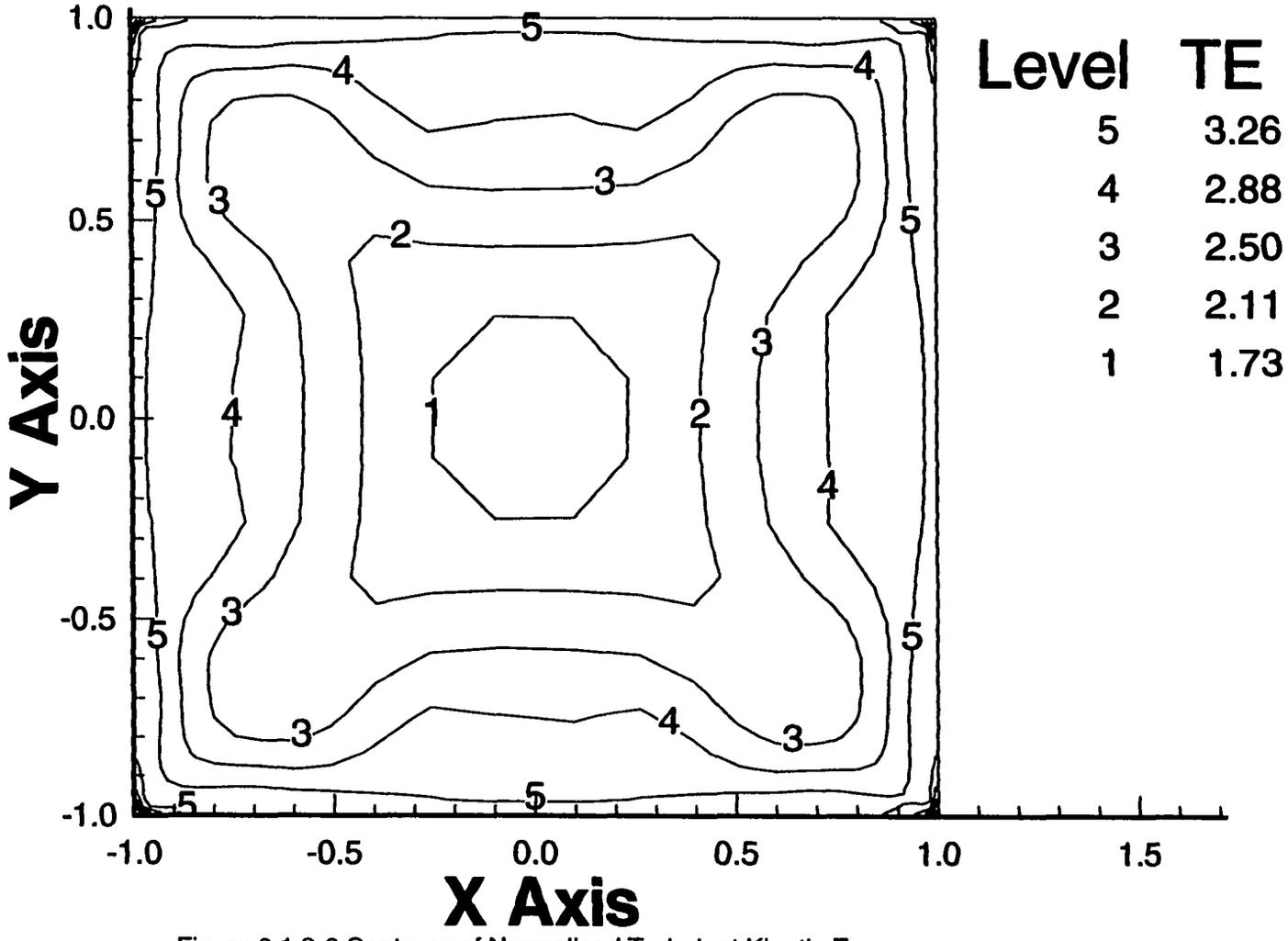

Figure 6.1.2-6 Contours of Normalized Turbulent Kinetic Energy for Turbulent Flow in a Straight Duct; $Z/D_H = 37.5$

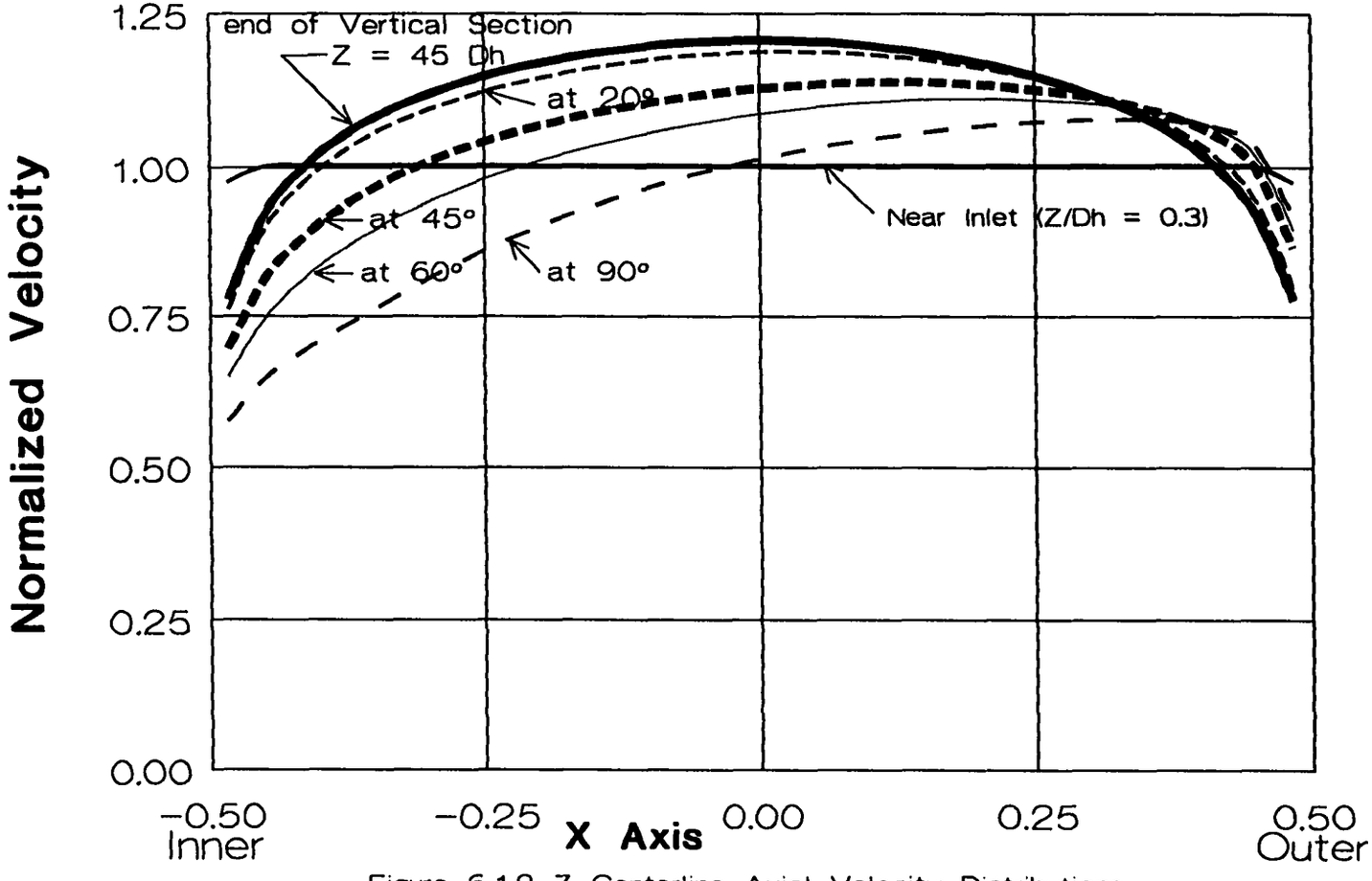

Figure 6.1.2-7 Centerline Axial Velocity Distributions for Turbulent Flow in a Straight then Curved Duct; R/Dh = 2.3

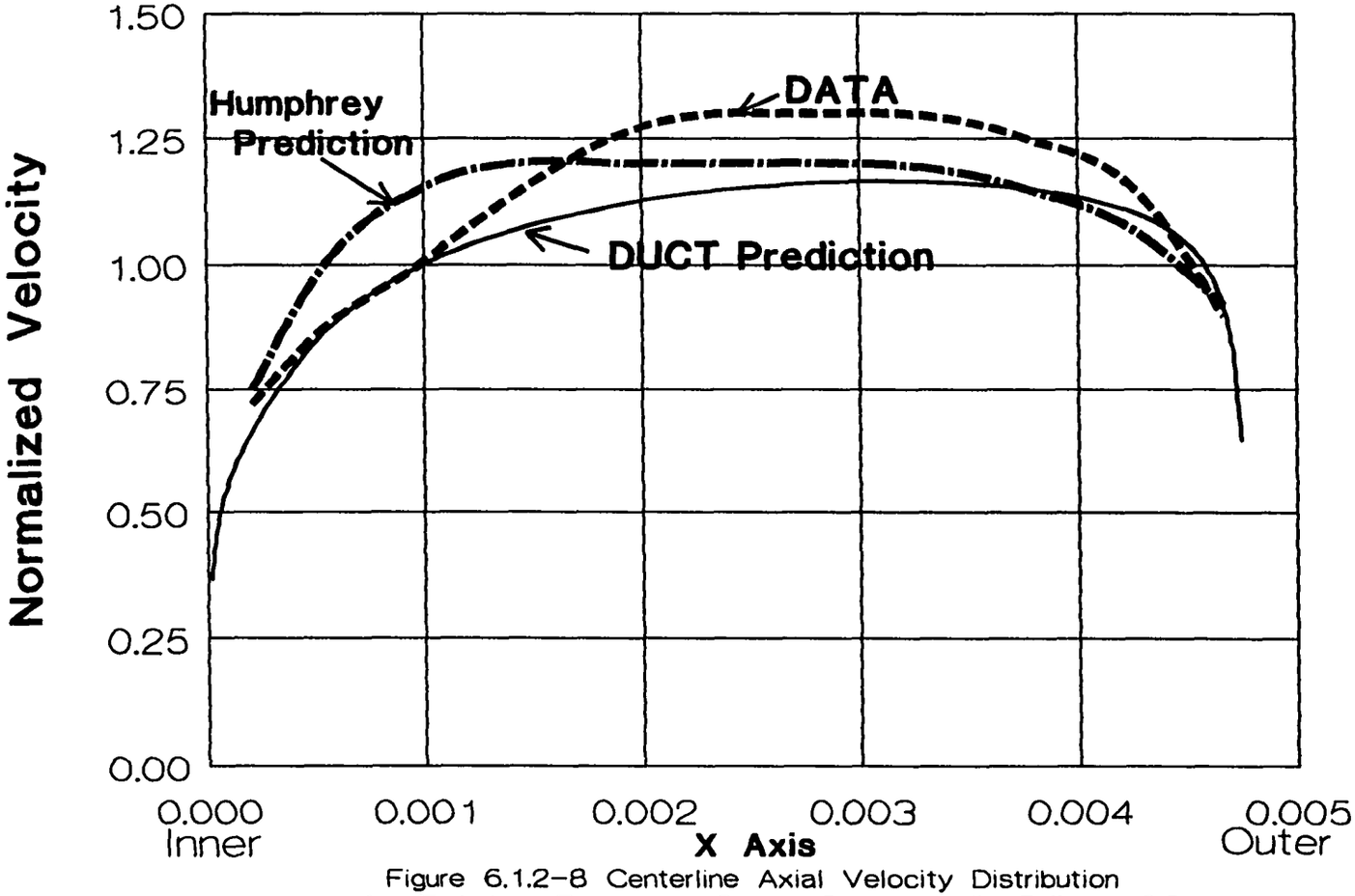

Figure 6.1.2-8 Centerline Axial Velocity Distribution for Turbulent Flow in a Curved Duct at 45°; R/Dh = 2.3

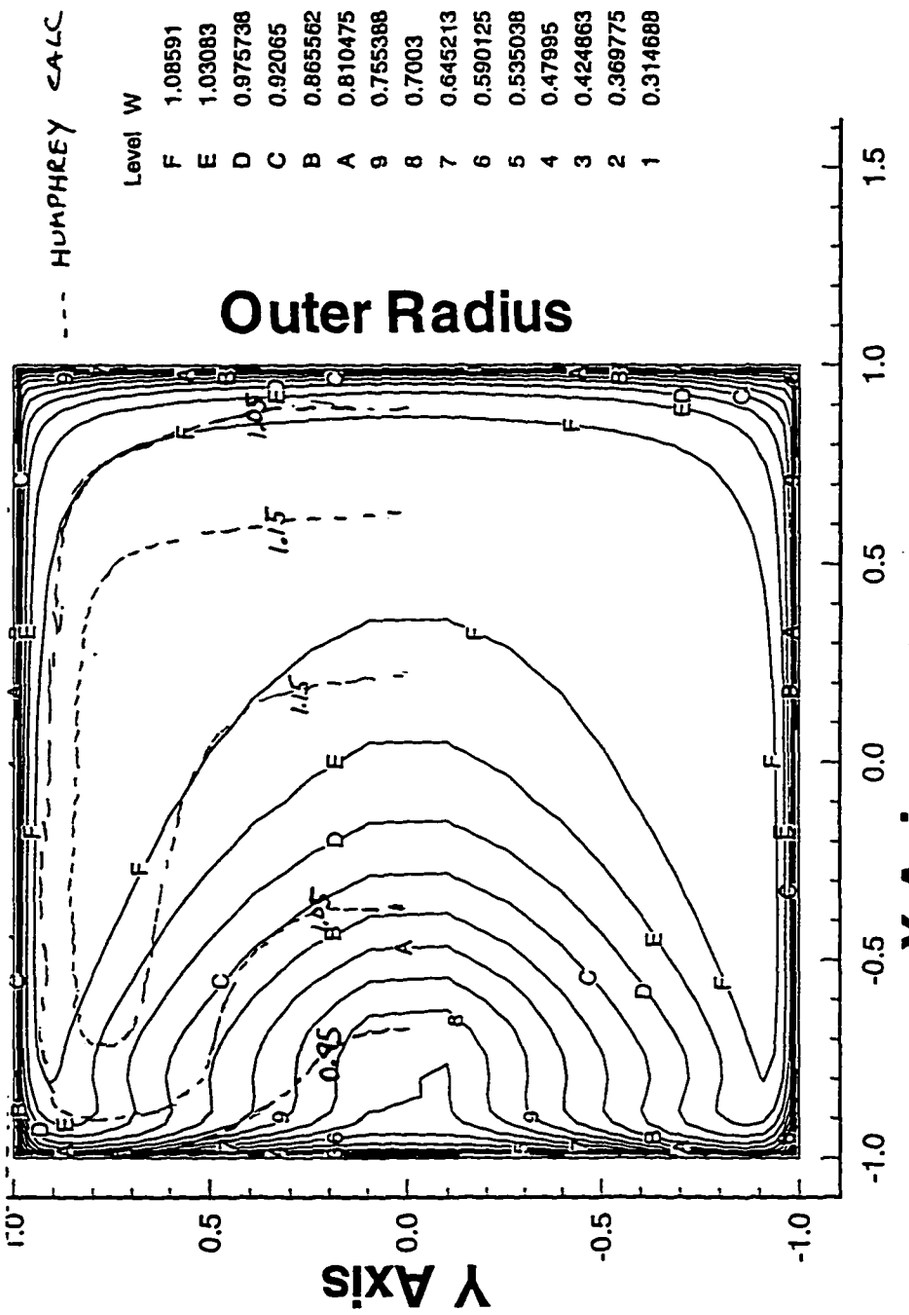

Figure 6.1.2-9 Contours of Longitudinal Velocity for Turbulent Flow in a Curved Duct at 90°;R/D=2.3

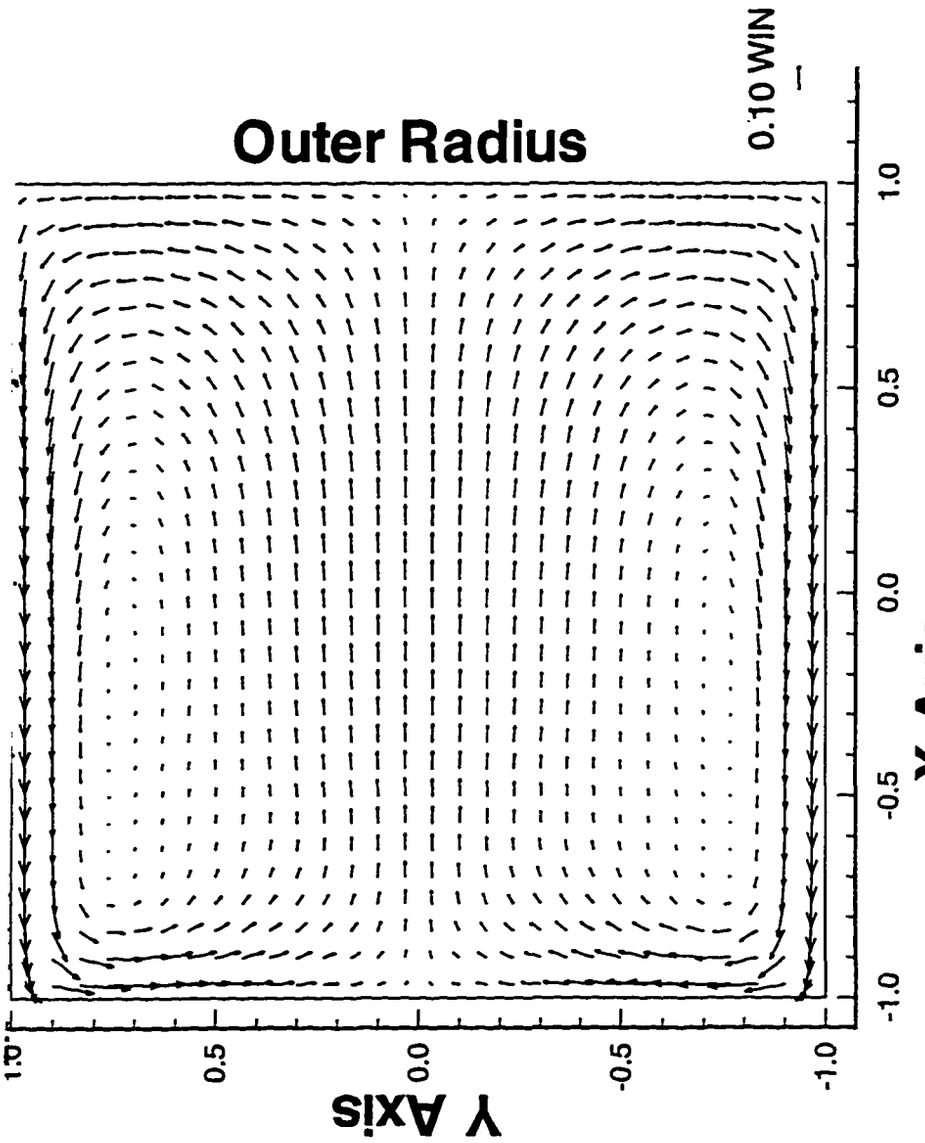

Figure 6.1.2-10 Secondary Flow Velocity Vectors for Turbulent Flow in a Curved Duct at 90°;R/D=2.3

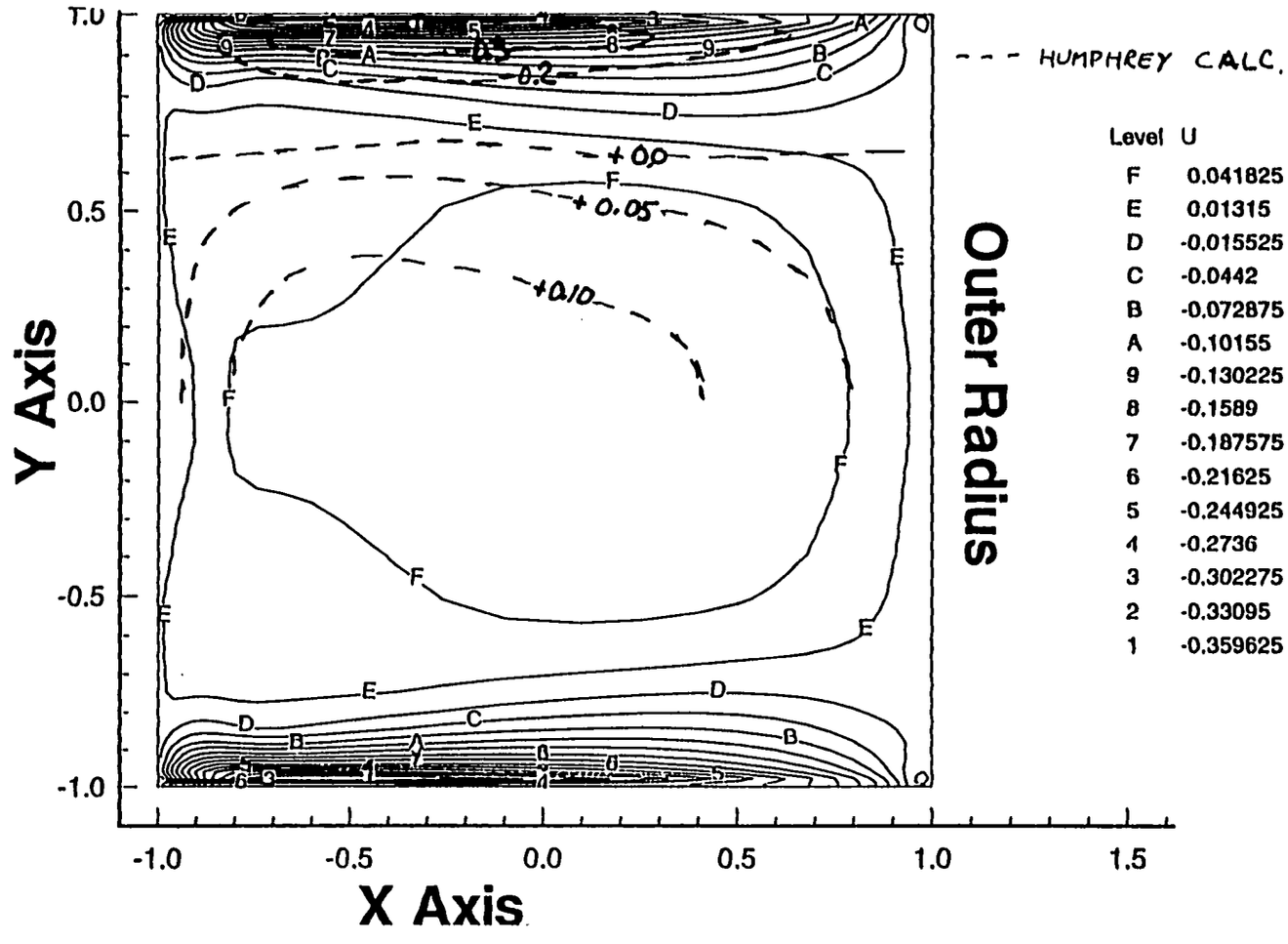

Figure 6.1.2-11 Contours of U Component of Velocity for Turbulent Flow in a Curved Duct at 90°;R/D=2.3

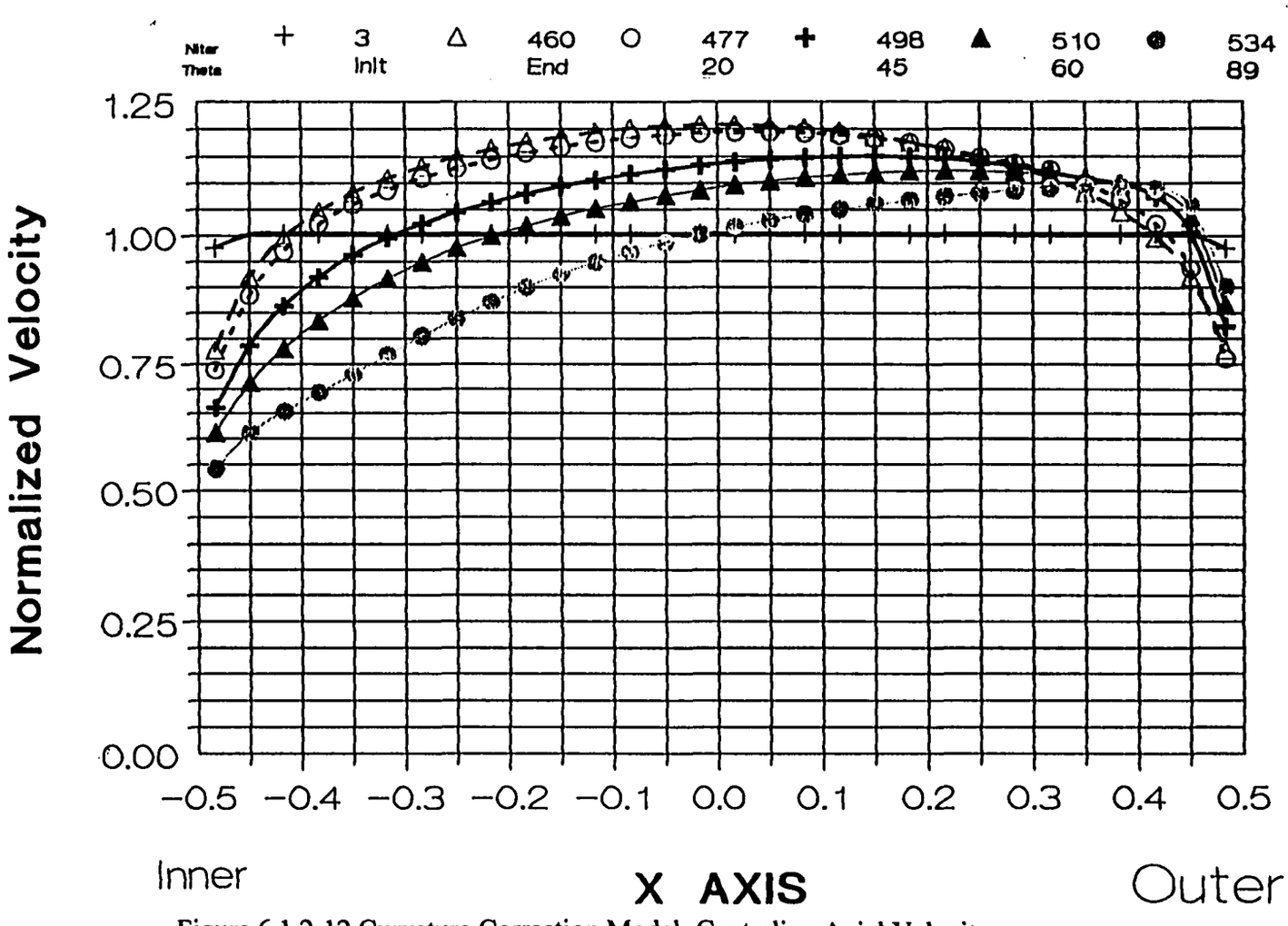

Figure 6.1.2-12 Curvature Correction Model: Centerline Axial Velocity Distributions for Turbulent Flow in a Straight then Curved Duct ;R/D=2.3

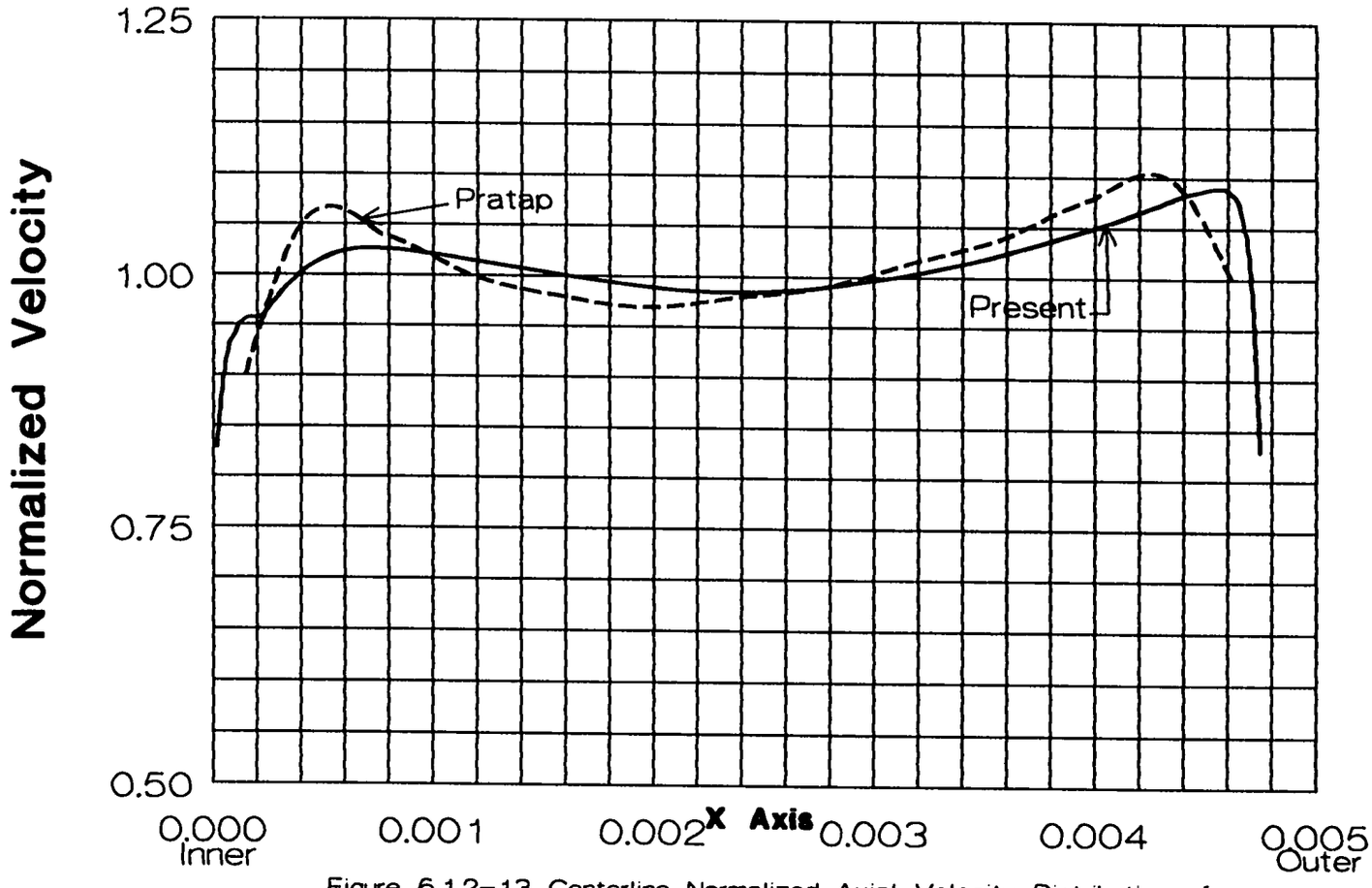

Figure 6.1.2-13 Centerline Normalized Axial Velocity Distributions for Turbulent Flow in a Curved Duct with 4:1 Rectangular Cross-Section

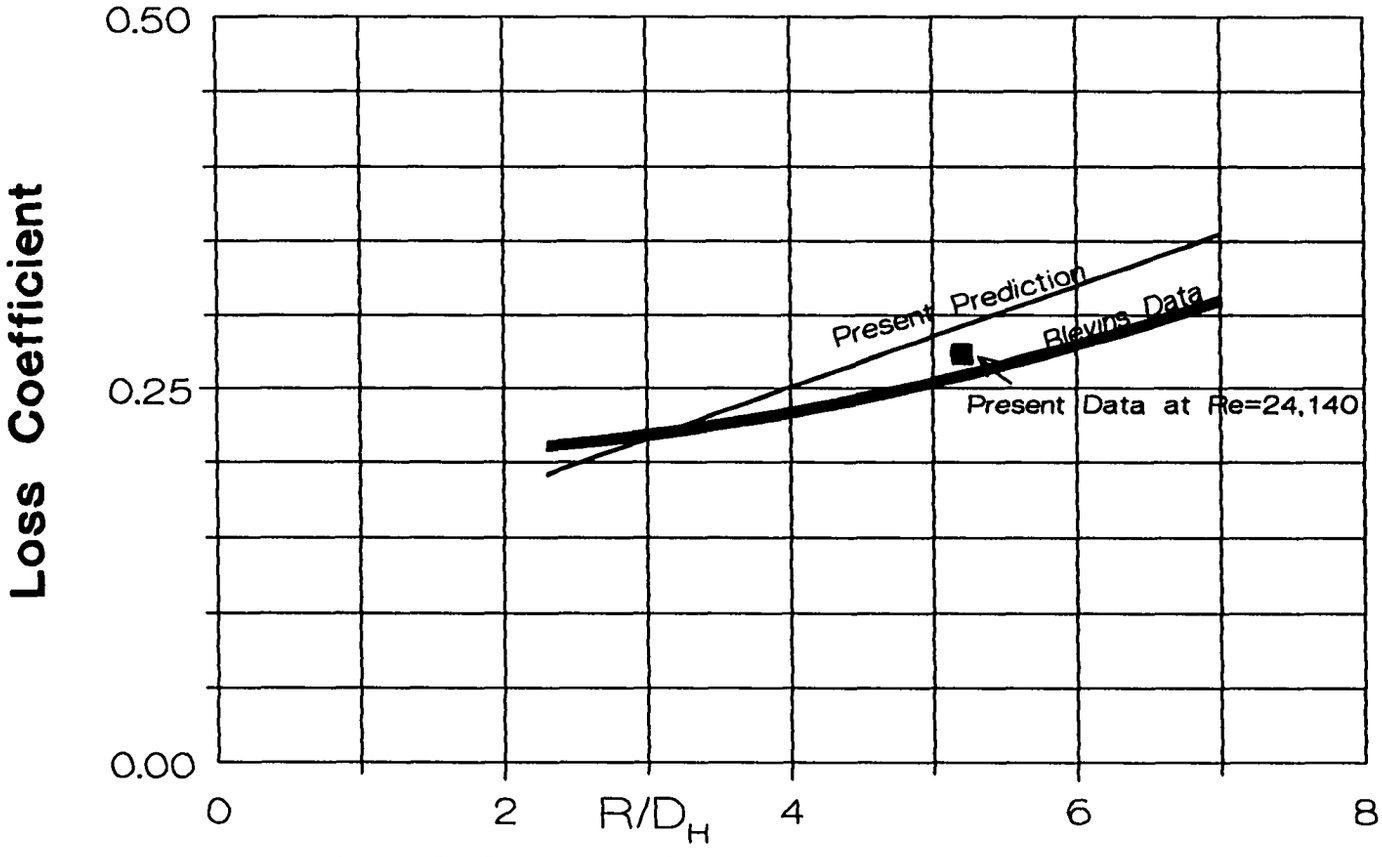

Figure 6.1.2-14 Loss Coefficient vs. Curved Duct Mean Radius
Comparison of Predictions with Experimental Data

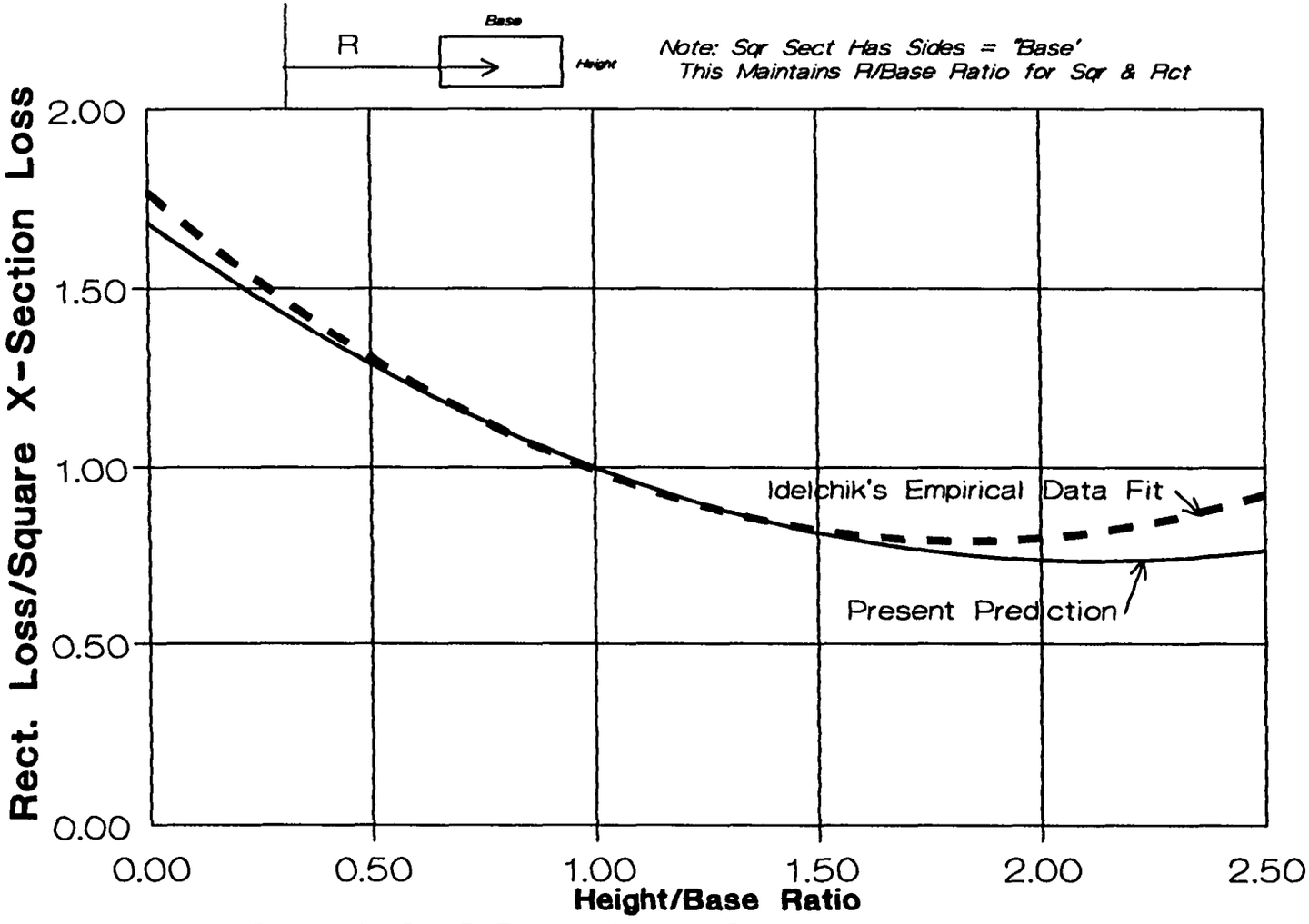

Figure 6.1.2-15 Ratio of Loss Coefficient for Curved Duct with Rectangular Cross-Section to Square Cross-Section

6.2 Two-Phase

6.2.1 Two Phase Flow in a Driven Cavity

The driven cavity problem for laminar and turbulent flow conditions for a two-phase medium was investigated next. This problem, as discussed in Section 5, "NUMERICAL SOLUTION ALGORITHM" , is an excellent means of verifying the robustness of the void fraction algorithm. This problem is also of practical interest for simulating two-phase flows in machinery components operating both under micro-gravity (associated with low-earth orbit) as well as normal earth gravity. Rectangular cavities of various aspect ratios considered and the methods used here are suitable for predicting two-phase flow in labyrinth seals. Figure 6.2.1-1 shows a schematic of a labyrinth seal and LDA measurements made in it by Morrison (1963). The resemblance to the driven cavity problem is clear. The presence of vapor negatively affects the critical heat flux in nuclear reactors and the gas degrades the performance of pump components, resulting in impeller cavitation damage, bearing and seal cavity overheating due to a decrease in the heat transfer.

The vast majority of the existing two-phase flow experimental data has been obtained at earth gravity conditions. Two-phase flow patterns are strongly influenced by the gravity body force. Performing the experiments at micro-gravity on earth requires flying the experiment in a parabolic flight profile or using a drop facility. These tests are limited to seconds in duration and are very expensive. In general it is not easy to perform such low gravity experiments in an earth bound laboratory. Thus the benefit of accurately modeling these flows computationally is clear.

The two-phase medium considered is a mixture of water and oil with water being the continuum (primary) phase and the oil being the secondary phase occupying the smaller volume. The initial condition for the problem is a uniform distribution of the two fluids at rest in the cavity with a prescribed volume fraction of the second phase (oil). A steady state solution for the flow field is computed by successive better approximations (iterations) of the flow field. For the case considered here, the lighter fluid (oil) rises and the terminal rise velocity can be estimated. For the water and oil emulsion, density ratio ($\rho_{oil} / \rho_{water} \cong 1$) being almost unity, the quasi-steady process of momentum adjustment that includes the effects of U_{wall}, the interfacial forces between the two phases and the oil rise phenomenon is considered. For larger bubbles (oil drops) with larger density ratios at higher values of acceleration the eventual stratification of the lighter fluid may be inevitable due to gravity. The solutions presented here are those prior to that, during the quasi-steady readjustment process when the changes are slow or negligible. For turbulent flows, the isotropic viscosity for the continuum phase is calculated using the k-ε model modified to accommodate the effects of the second phase. Turbulence of the second phase is calculated with one of the two methods discussed earlier. The results are presented with linear dimensions normalized with the cavity hydraulic diameter and the velocities normalized by the top wall velocity. The boundary condition on the top wall is set to the prescribed U_{wall} with no slip and the other three wall velocity boundary conditions are set to zero also due to no slip. The problem is isothermal in nature since viscous dissipation is small at these low velocities and viscosities considered. The independent variables considered are Reynolds number based on the wall velocity, cavity hydraulic diameter and the continuum fluid viscosity which determines the nature of the flow (laminar or turbulent), the void fraction (volume fraction of second phase - oil), oil

drop (bubble) diameter, acceleration due to gravity and the aspect ratio of the cavity. Results are presented for two values of Reynolds number: 400 and 40,000, corresponding to laminar and turbulent flow regimes. Average (initial) void fraction of the second phase used is in the range of 5 percent to 30 percent. Oil drop (assumed spherical) diameters considered are 2, 5, and 10 mm which correspond to non-dimensional values based on the cavity hydraulic diameter of .08, .2 and .39. The density ratio of the two phase (water/oil) is 997/884. Two values of acceleration due to gravity used are those corresponding to that on earth (9.8 m/sec^2) and that at low earth orbit (space shuttle, .2 m/sec^2). Effect of the aspect ratios .5, 1 and 2 are also presented. The dependent variables are the four components of velocities, pressure, local void fraction distributions, slip ratio distributions and turbulence properties.

The phase velocity distributions for laminar flow (Re = 400) in a square cavity with an average oil volume fraction of 30 percent in the form of droplets (bubbles) are shown in Figures 6.2.1-2 to -6. The first two of these figures represent water (continuum phase) velocity distributions at two different gravity levels, and the second two figures present the same for the oil. The water velocity distributions look very similar to patterns seen in single phase solutions for this problem. At earth gravity, the buoyancy effects and the rise velocity are higher for the lighter phase (oil). The effect of this rise velocity on the water velocity distribution is seen in the left third of the cavity. The vertical velocities (up) are more uniformly distributed with a larger inactive cell in the middle for the low gravity case. At earth gravity, the oil rise velocity is of the same order of magnitude as the wall velocity, whereas at low gravity values, with lower rise velocity, the oil is influenced more by top plate velocity. The effect of the water momentum is clear at the bottom of the cavity (Figure 6.2.1-5). The strong water velocity ($\cong U_{wall}$) toward the left is seen to move the oil to the left also. The void fraction (oil volume fraction) distributions

corresponding to the above velocity distributions are given in Figures 6.2.1-6 and -7. At earth gravity, there is substantially more oil at the top (Figure 6.2.1-6), than at lower gravity. The larger void fractions are close to about 95 percent. The ability to compute such high void fractions is testament to the robustness of the algorithm used here. The accumulation of oil to the right-hand corner is more obvious at lower gravity as the plate is influencing the oil movement just as much as the buoyancy effects.

Effect of bubble (oil droplet) size is illustrated in Figures 6.2.1-8 to -11. Oil velocity distributions at nondimensional bubble sizes of 0.08 (2 mm) and 0.4 (10 mm) are presented here. The larger bubble occupies a substantial fraction of the cavity width. At a void fraction of 0.3 in a 25 mm cube, 5 mm and 2 mm diameter bubbles would have populations of the order of 75 and 1170 respectively, but there would be only nine 10 mm bubbles. Velocity distributions of the lighter continuum phase (oil) as presented here with only nine bubbles may cause one to question whether the continuum assumption is still valid. Yet it is gratifying to note that the effect of the presence of bubbles distributed throughout the computational domain (at all computational nodes) with a 30 percent void fraction initially in each computational cell does give physically meaningful results; e.g., the vertical velocities are seen to be noticeably larger for the larger bubble size all else being the same (Figures 6.2.1-8 and -9).

Slip ratio for this 2D problem is given as : $\sqrt{(u_1 - u_2)^2 + (v_1 - v_2)^2} / U_{Wall}$

Slip ratios shown in Figures 6.2.1-10 and -11 are larger in the right-hand part of the cavity where the liquid is forced downward due to the top wall motion and the oil droplets resist this due to buoyancy. Slip values are somewhat larger for the larger bubble case and the maximums approach the wall velocity. The larger values of slip at the bottom of the cavity are a

consequence of the definition above where buoyancy driven oil velocity is larger for the large bubbles in the region where the water has a low vertical component of velocity.

Phase velocity distribution at a low (5 percent) void fraction are shown in Figures 6.2.1-9 and 6.2.1-10 with $D_{bubble}/D_{hyd} \cong 0.2$ (5 mm bubble) at low gravity. Water velocities are not unlike those at higher gravity and higher void fractions (Figure 6.1.1-1) but are affected less so by the smaller amount of buoyancy forces. Oil velocity distribution looks more like those for the smaller bubbles (2 mm, Figure 6.2.1-8) and indicates the importance of bubble size on the phenomena.

Results of computation of turbulent two-phase flow (Re=40,000) in the driven cavity are presented in Figures 6.2.1-14 to -19. As k-ε model of turbulence that includes turbulence contribution due to the second phase is used for both phases. The momentum imparted by the top wall is substantially larger here than in the laminar case and U_{wall} is larger than the oil rise velocity even at earth gravity. Thus the velocity distribution for both phases display nearly symmetrical cellular motion even at the higher earth gravity. Thus it is clear that the gross flow patterns in such cavities are governed by the ratio of wall and rise (U_{wall}/V_{rise}) velocities. Unlike some of the laminar cases described earlier, here the oil is transported well throughout the cell and has horizontal velocities comparable to the wall velocity at the top as well as the bottom of the cell.

The oil accumulates here also in the right-hand top corner as shown in the void fraction contours in Figures 6.2.1-18 and -19, but the quantities are much smaller as the oil is"churned" better and is more uniformly distributed throughout the cavity. The largest values of void fraction, approximately 0.70 are well below those in the earlier cases (≈ 0.95). The effect of gravity and buoyancy forces appears to be weak here as evidenced by the void fractions that are practically the same at both gravity values.

Results for laminar flow in the cavity at different aspect ratios is brought out in Figures 6.2.1-20 through -24. Similar computations for turbulent flows in rectangular cavities have also been computed. Results at low buoyancy forces are shown to bring out the effects of the moving wall better and thus are presented here. Not surprisingly, the taller cavity is left with a larger area of low velocities at the bottom. The water velocity distribution has slightly larger downward velocities near the right wall with the largest values comparable to U_{wall}. As seen in the earlier distributions for a square cavity, the central core for the water flow has very little motion. Void fraction distribution for the oil in the wide and tall cavities are given in Figures 6.2.1-22 and -23. Again, accumulation of the oil in the right top corner is evident. The accumulation of the lighter phase in the top half of the cavity, even for these low buoyancy forces, is noticeable for the taller cavity.

Vertical velocity variation across the cavity at the mid plane is shown for two void fractions in Figure 6.2.1-24. The velocities are larger for the higher void fraction (both positive and negative) as would be expected. The distribution is somewhat flatter for lower void fractions. Volume fraction of oil along the cavity diagonal is shown in Figure 6.2.1-25 for two different oil droplet (bubble) diameters. Smaller diameter droplets are likely to stay mixed with water (emulsify) better and thus result in a more uniform distribution of void fraction. Except for the right-hand corner where the oil tends to accumulate, the void fraction of oil is fairly constant along the cavity diagonal for the smaller diameter oil droplets. The larger diameter oil droplets do not stay at the bottom as well, as is also evident from this graph.

Results of two phase computations for a water-oil mixture have been presented above. The computational scheme appears to capture most of the expected features for phase velocity,

and void fraction distributions. Additional details pertaining to the two-phase driven cavity problem are given by Graf and Neti (1996).

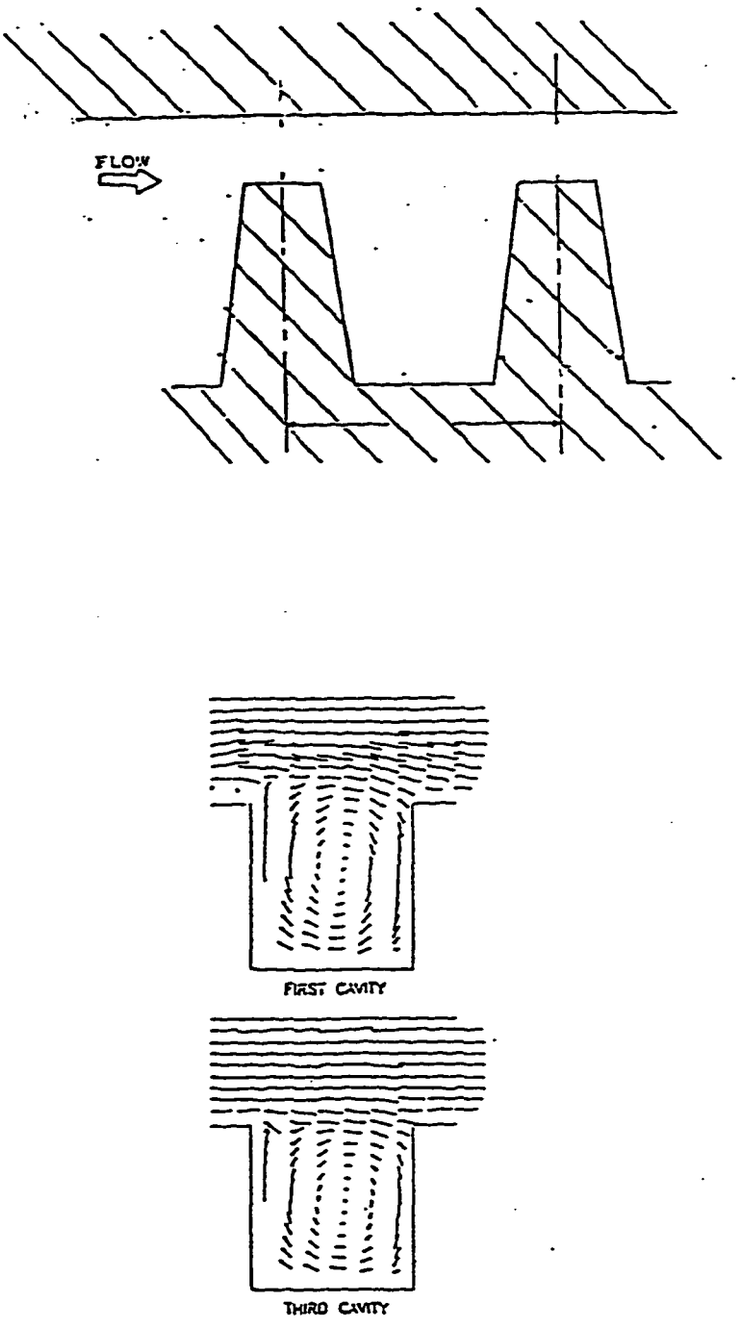

Figure 6.2.1-1 Labyrinth Seal Geometry & Measured Flow
(illustrating its closeness to the driven cavity problem)

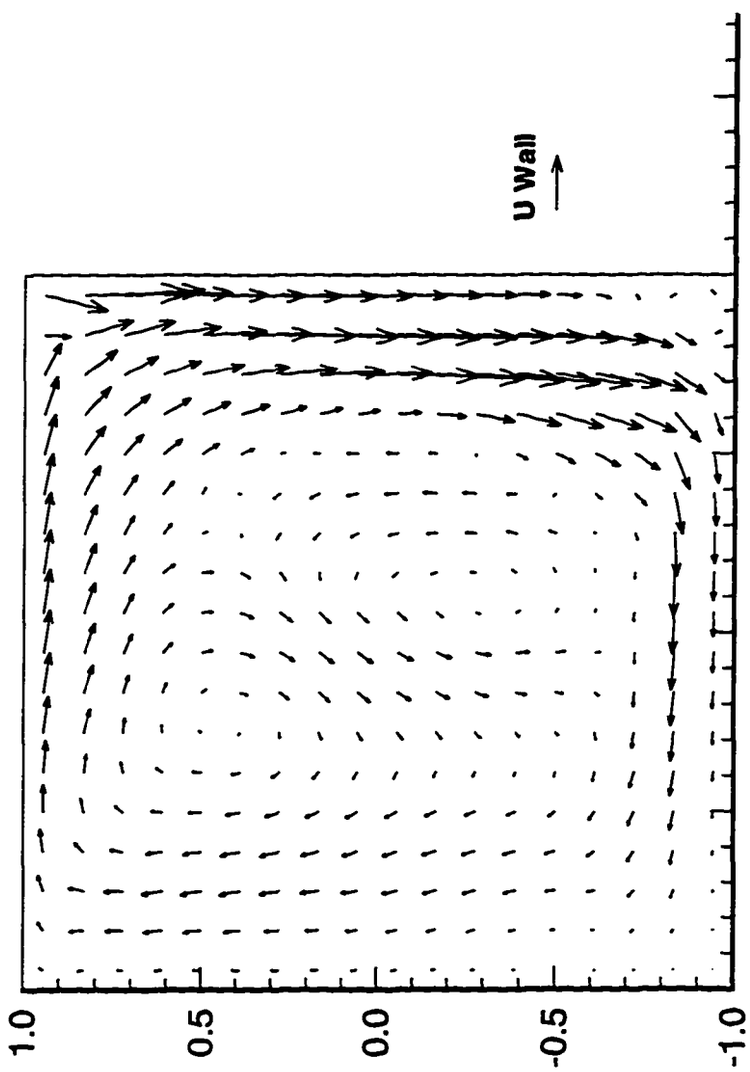

Figure 6.2.1-2 Water/Oil Laminar Flow;Water Vectors at earth gravity; Re=400;D_b/D_H=0.197;Void Fraction=0.30

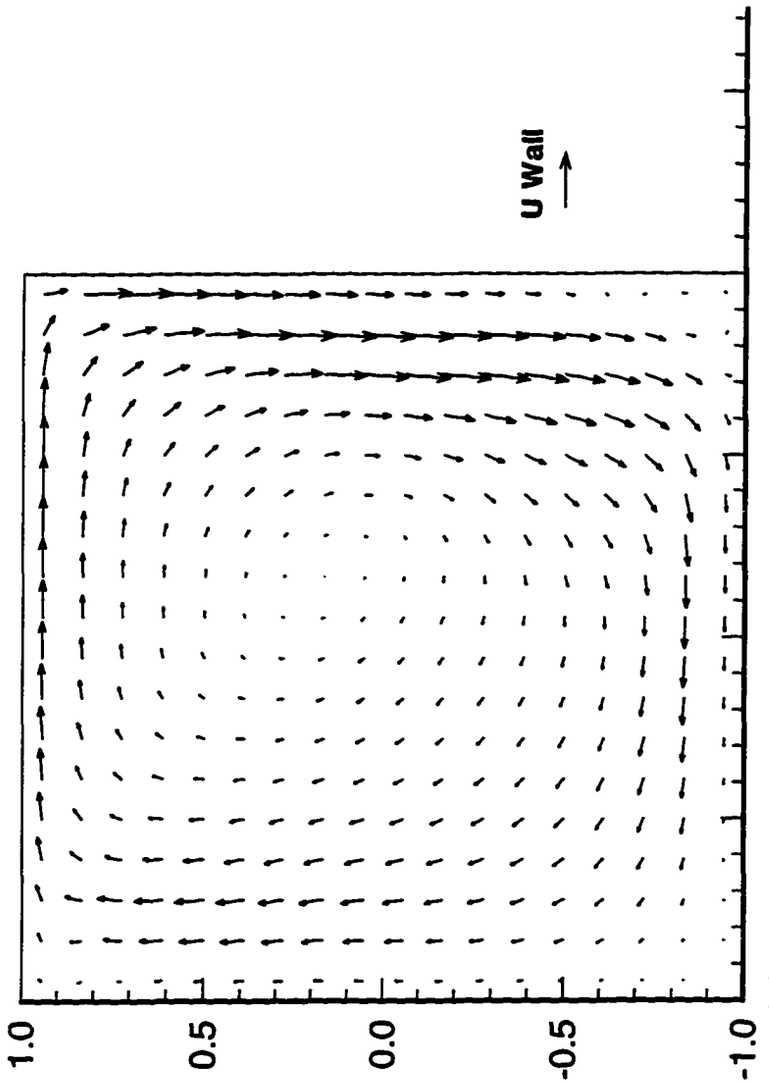

Figure 6.2.1-3 Water/Oil Laminar Flow;Water Vectors at microgravity; Re=400;D_b/D_H=0.197;Void Fraction=0.30

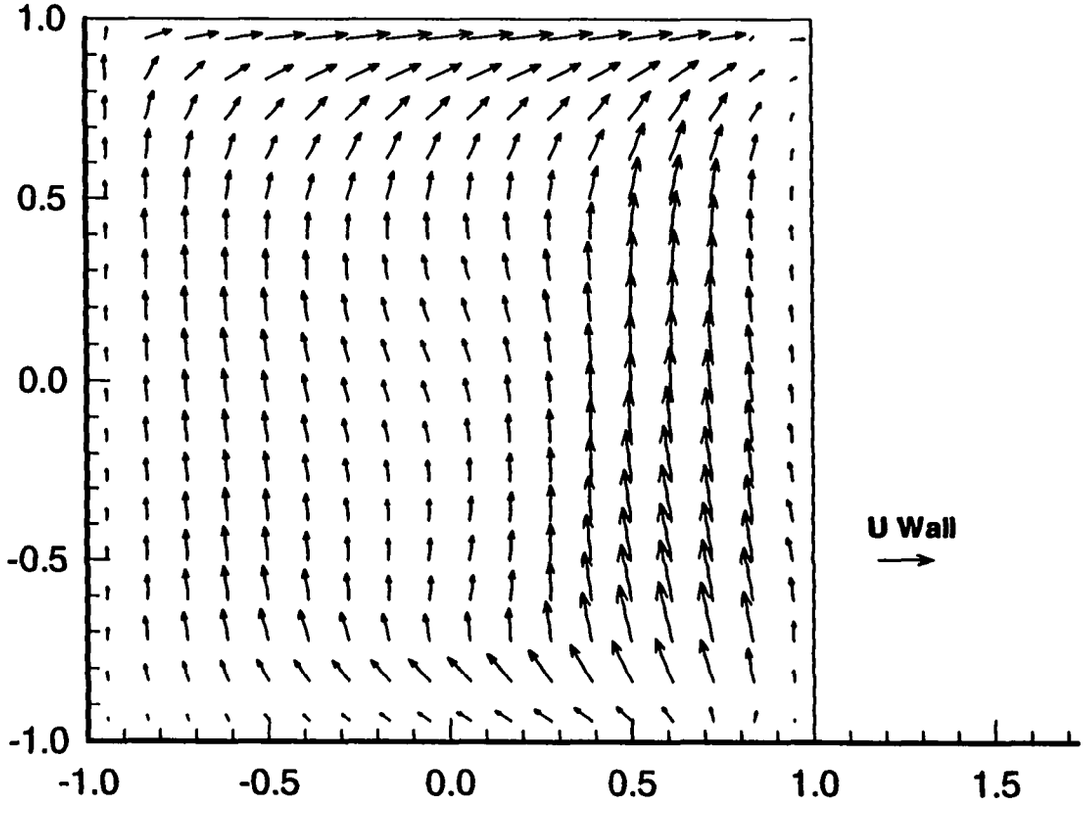

Figure 6.2.1-4 Water/Oil Laminar Flow;Oil Vectors at earth gravity; Re=400;D_b/D_H=0.197;Void Fraction=0.30

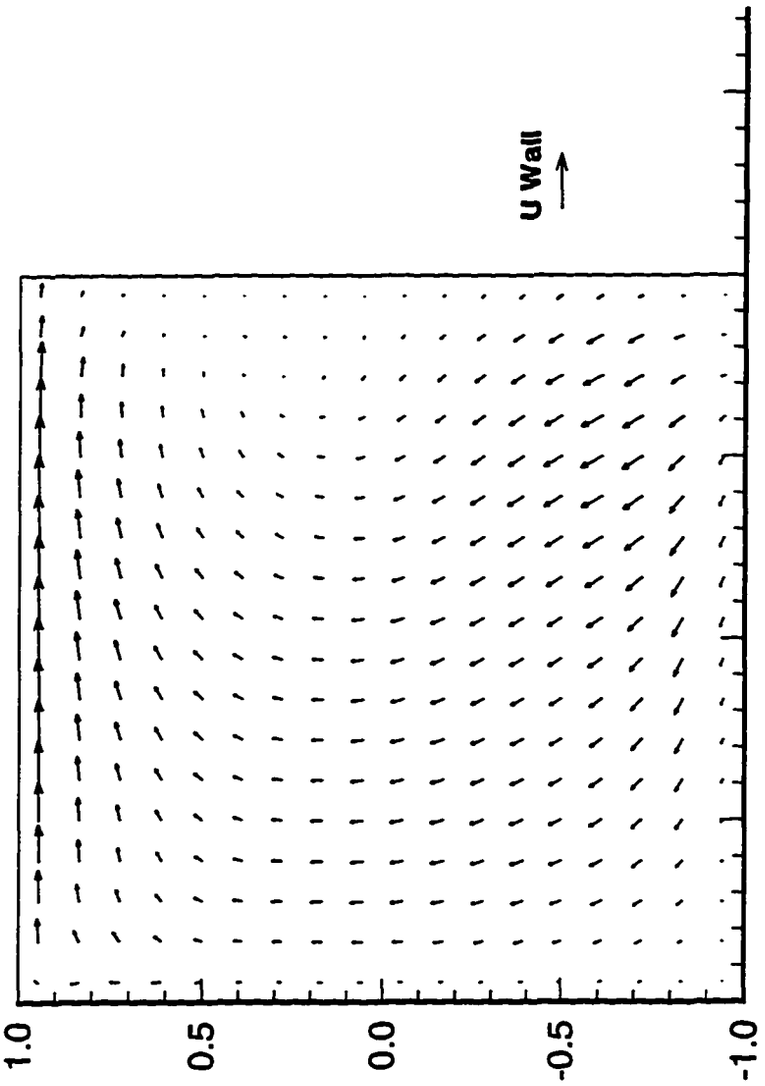

Figure 6.2.1-5 Water/Oil Laminar Flow;Oil Vectors at microgravity; Re=400;D_b/D_H=0.197;Void Fraction=0.30

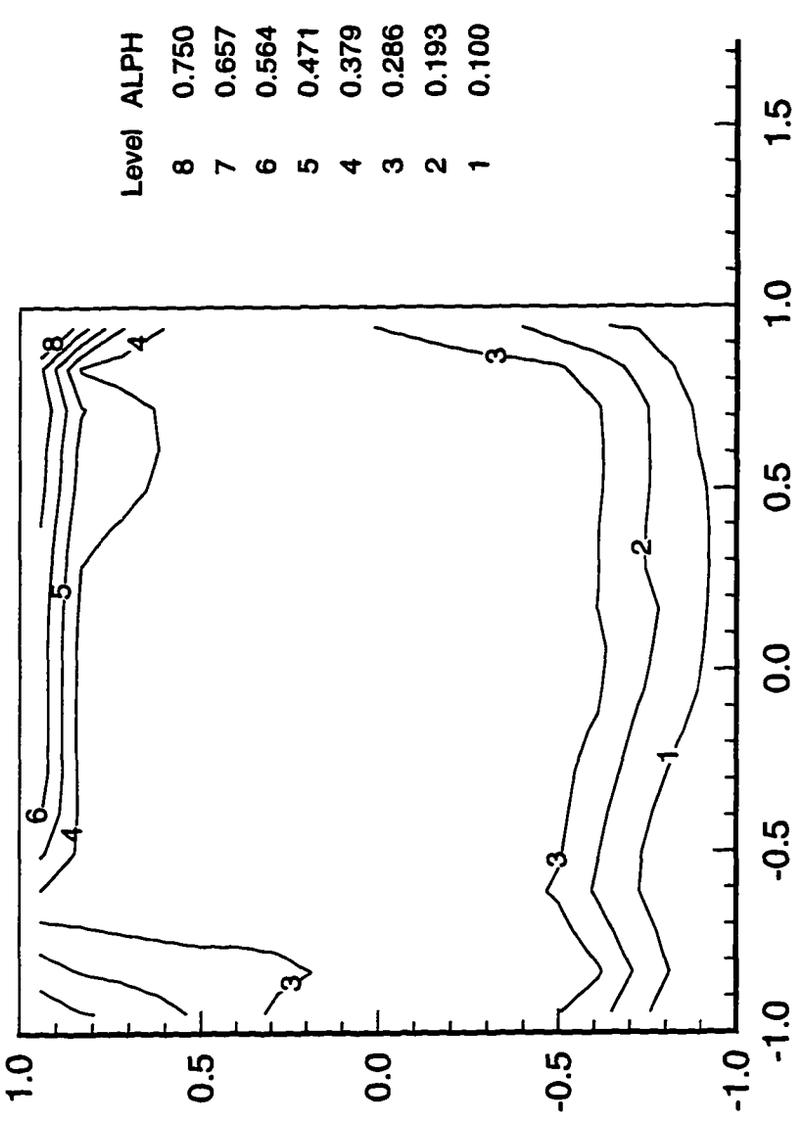

Figure 6.2.1-6 Water/Oil Laminar Flow;Oil Fraction Contours at earth gravity; Re=400;D_b/D_H=0.197;Void Fraction=0.30

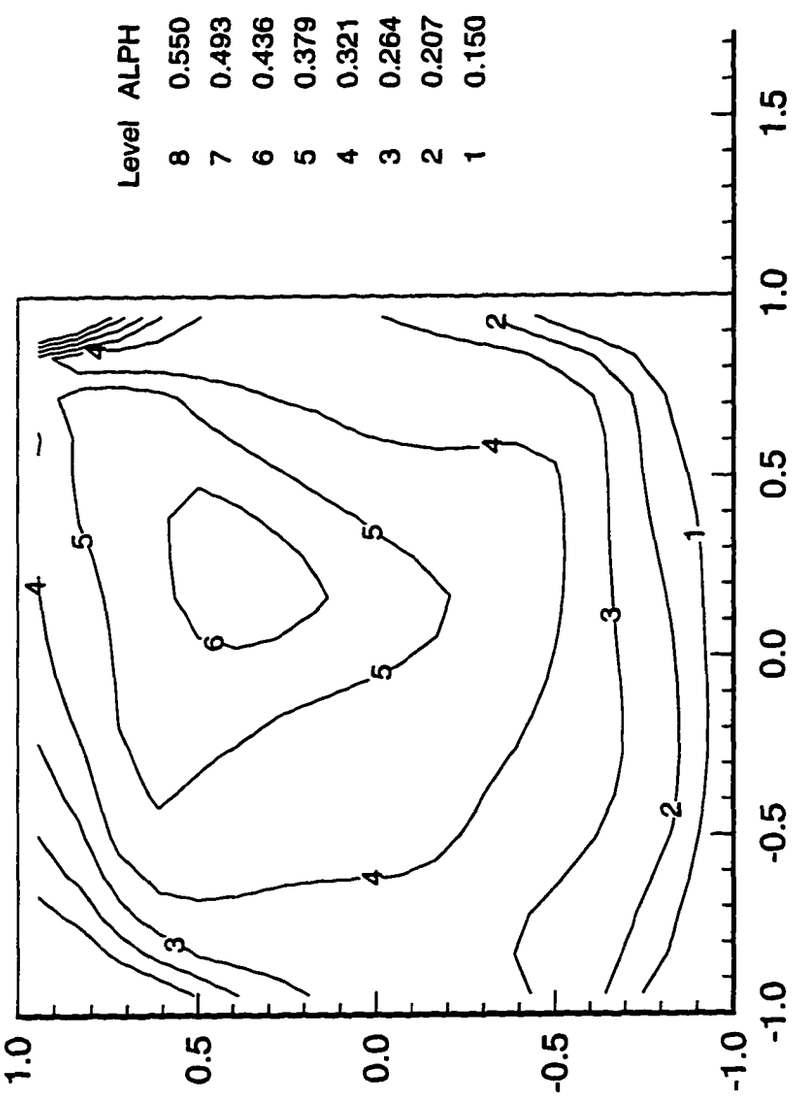

Figure 6.2.1-7 Water/Oil Laminar Flow;Oil Fraction Contours at microgravity; Re=400;D_b/D_H=0.197;Void Fraction=0.30

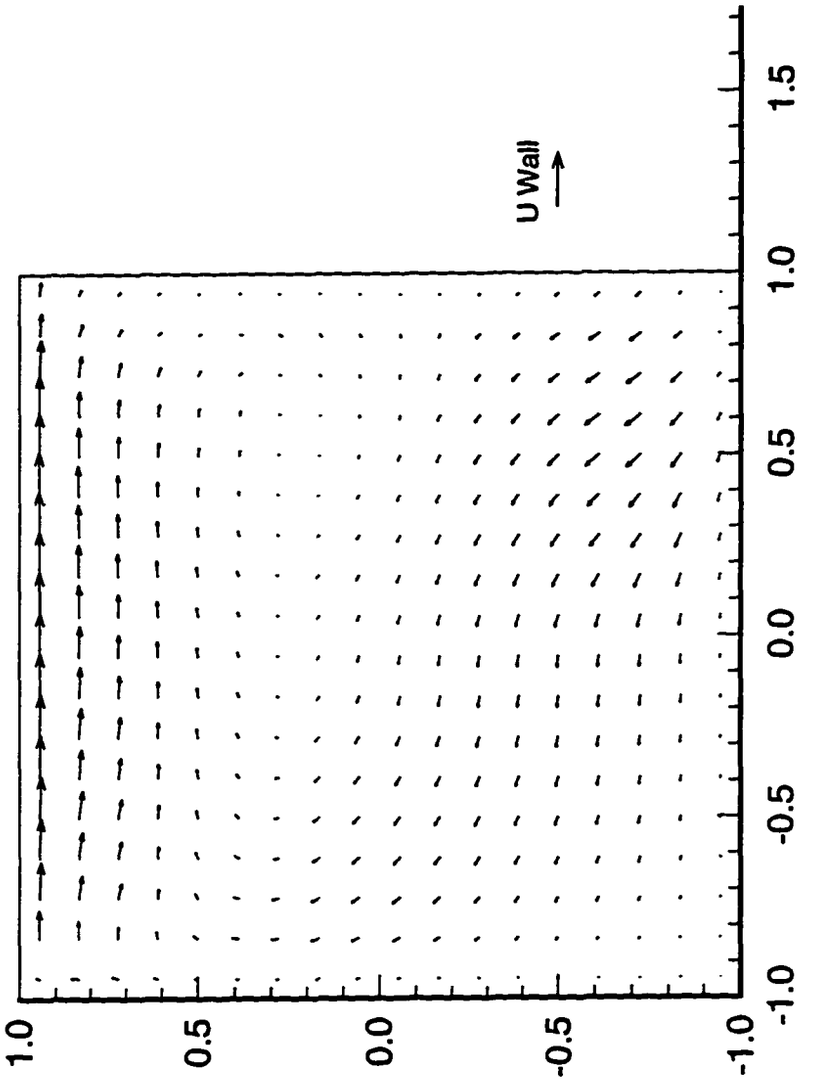

Figure 6.2.1-8 Water/Oil Laminar Flow;Oil Vectors of the smallest bubbles at microgravity; Re=400;D_b/D_H=0.079;Void Fraction=0.30

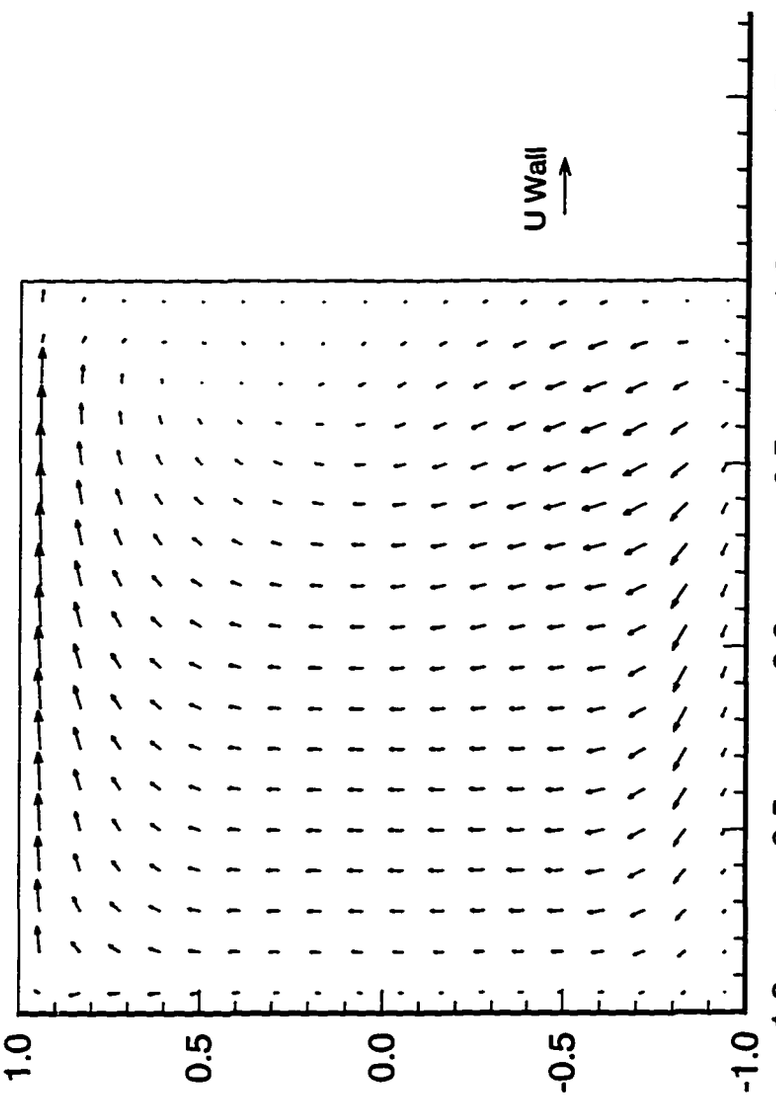

Figure 6.2.1-9 Water/Oil Laminar Flow;Oil Vectors of the largest bubbles at microgravity; Re=400;D_b/D_H=0.39;Void Fraction=0.30

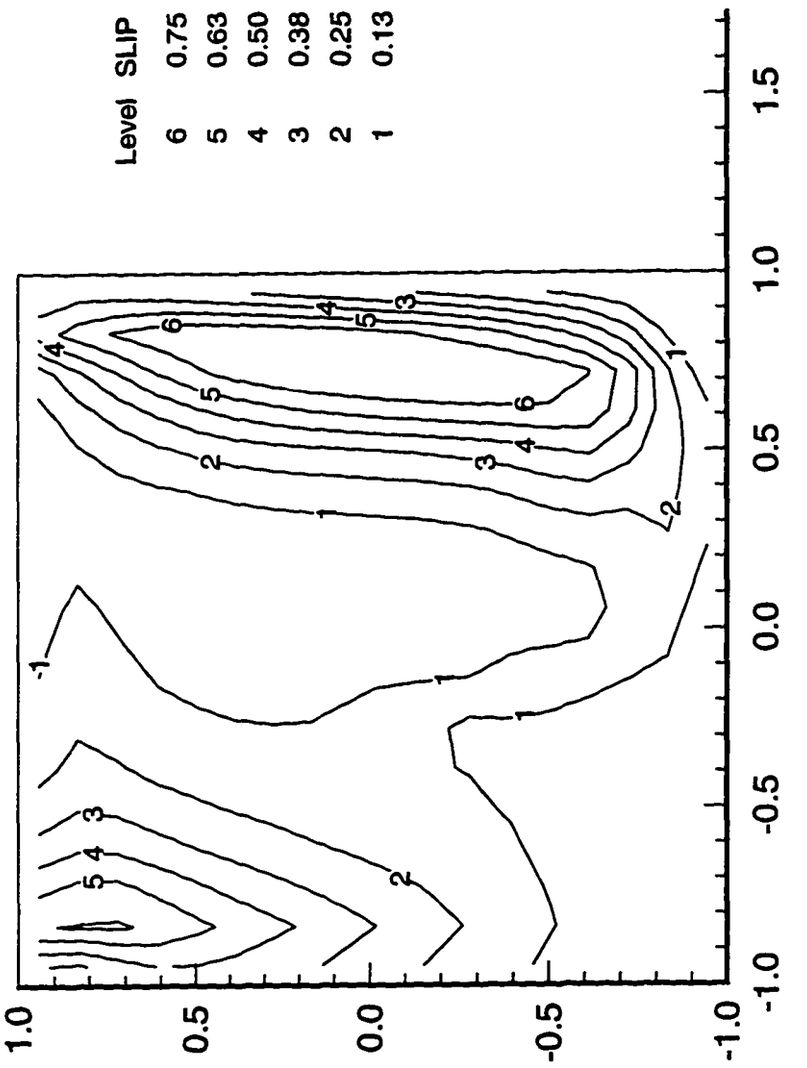

Figure 6.2.1-10 Water/Oil Laminar Flow;Slip Ratio Contours of the smallest bubbles at microgravity; Re=400;D_b/D_H=0.079;Void Fraction=0.30

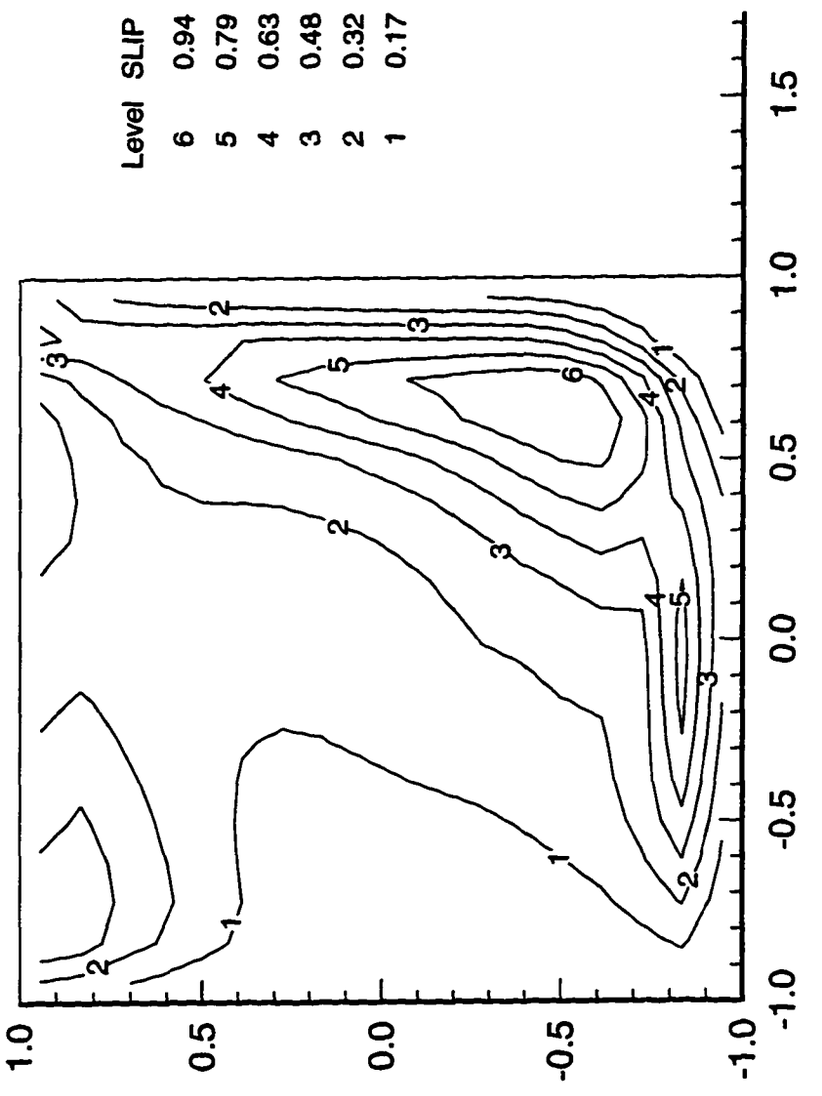

Figure 6.2.1-11 Water/Oil Laminar Flow;Slip Ratio Contours of the largest bubbles at microgravity; Re=400;D_b/D_H=0.39;Void Fraction=0.30

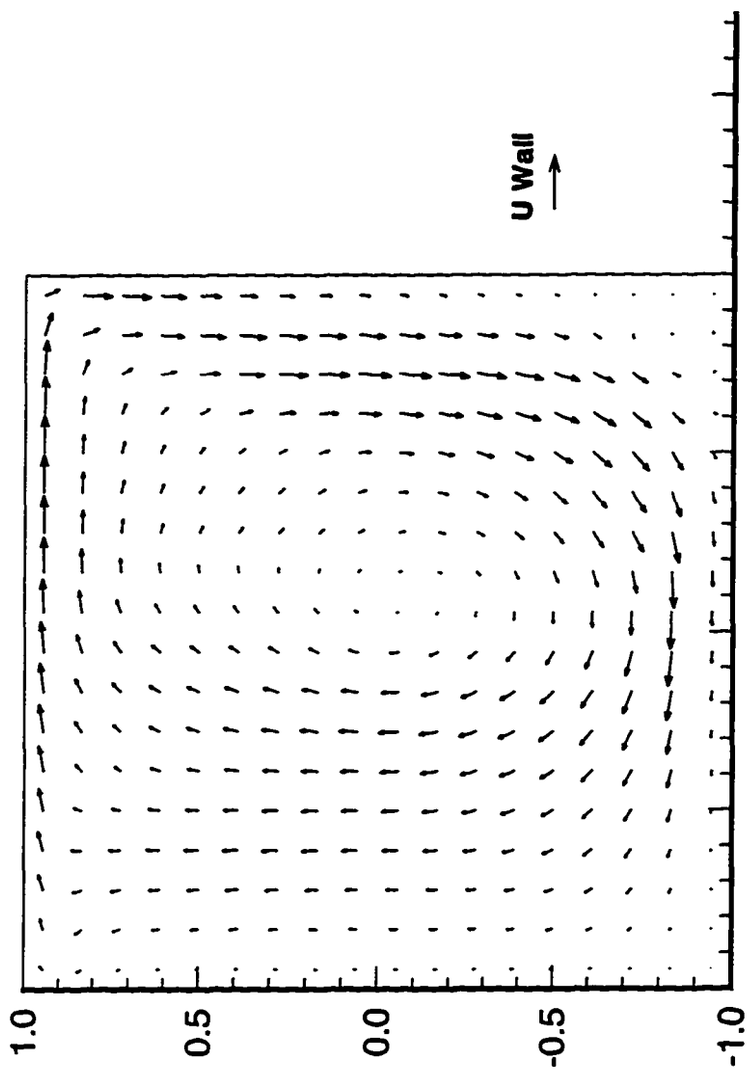

Figure 6.2.1-12 Water/Oil Laminar Flow;Water Vectors at microgravity;Lowest Initial Void Fraction; Re=400;D_b/D_H=0.197;Void Fraction=0.05

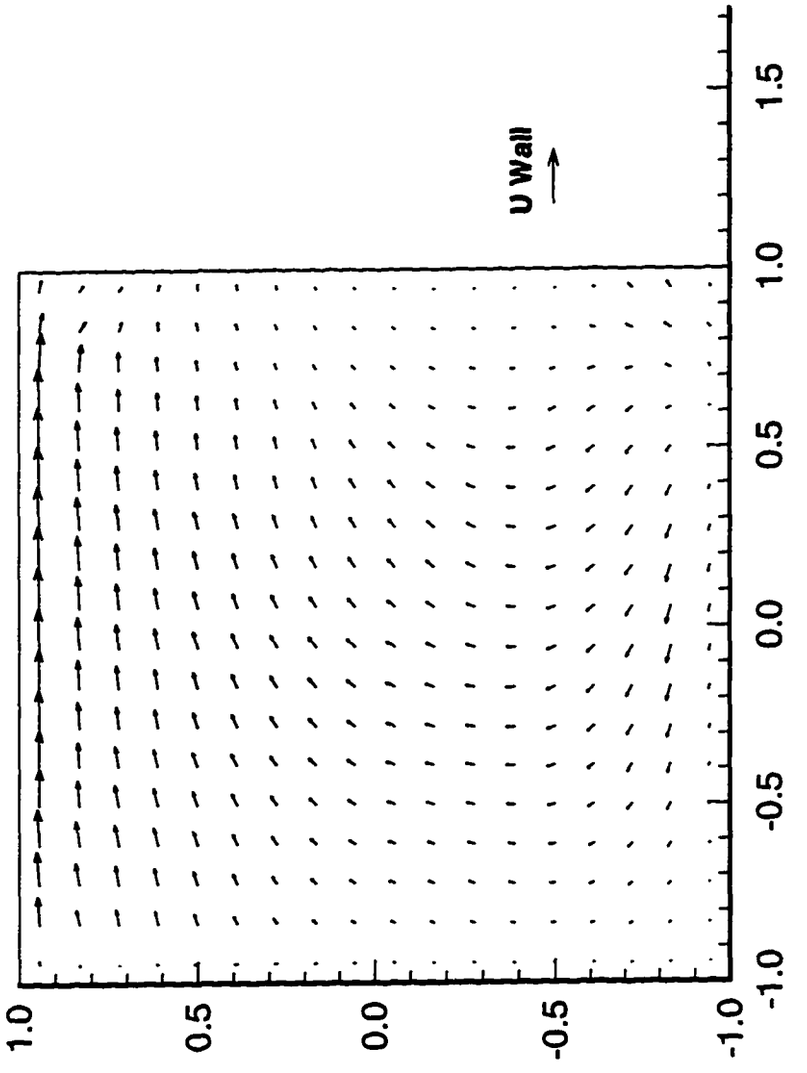

Figure 6.2.1-13 Water/Oil Laminar Flow;Oil Vectors at microgravity;Lowest Initial Void Fraction; Re=400;D_B/D_H=0.197;Void Fraction=0.05

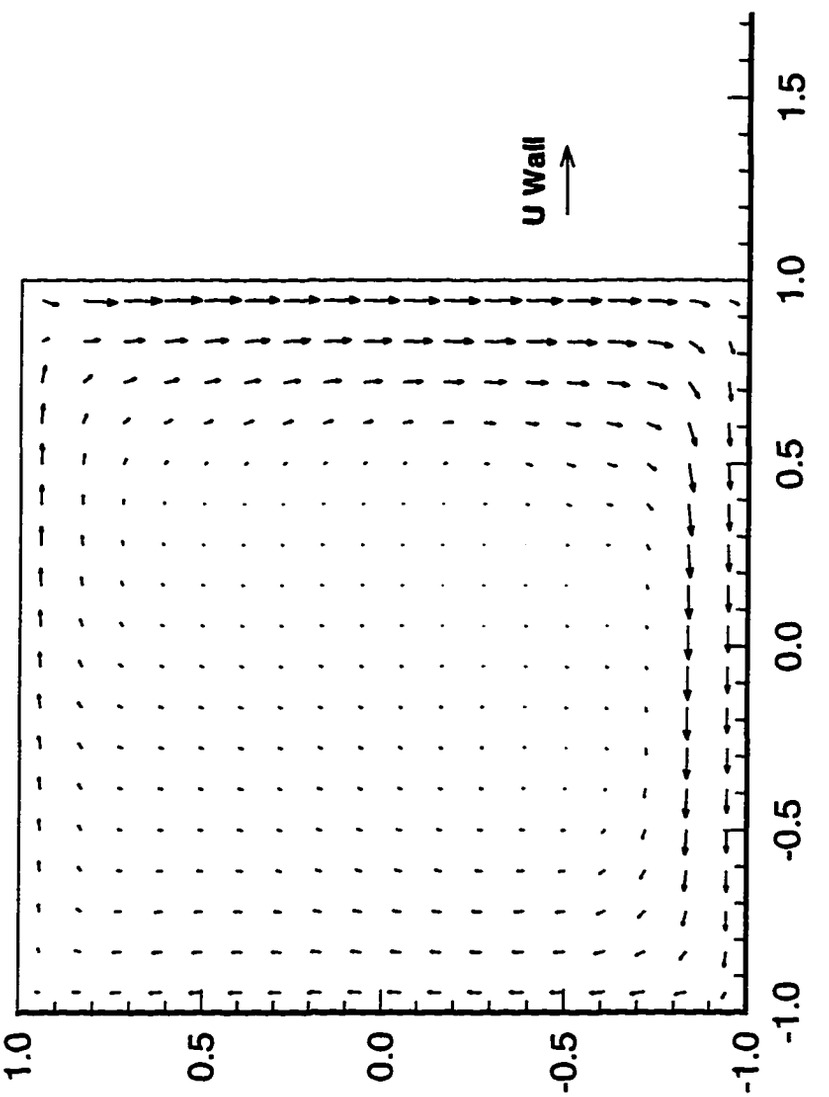

Figure 6.2.1-14 Water/Oil Turbulent Flow;Water Vectors at earth gravity; k-e for both phases;Re=40,000;D_b/D_H=0.197;Void Fraction=0.30

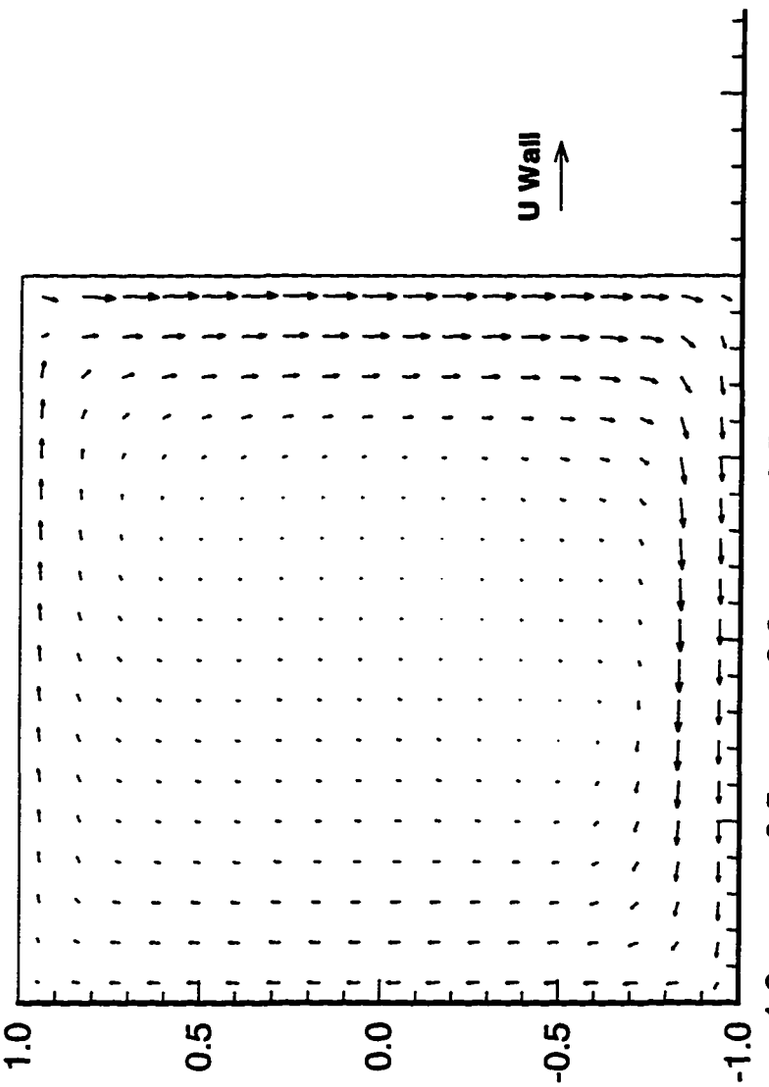

Figure 6.2.1-15 Water/Oil Turbulent Flow;Water Vectors at microgravity; k-e for both phases;Re=40,000;D_b/D_H=0.197;Void Fraction=0.30

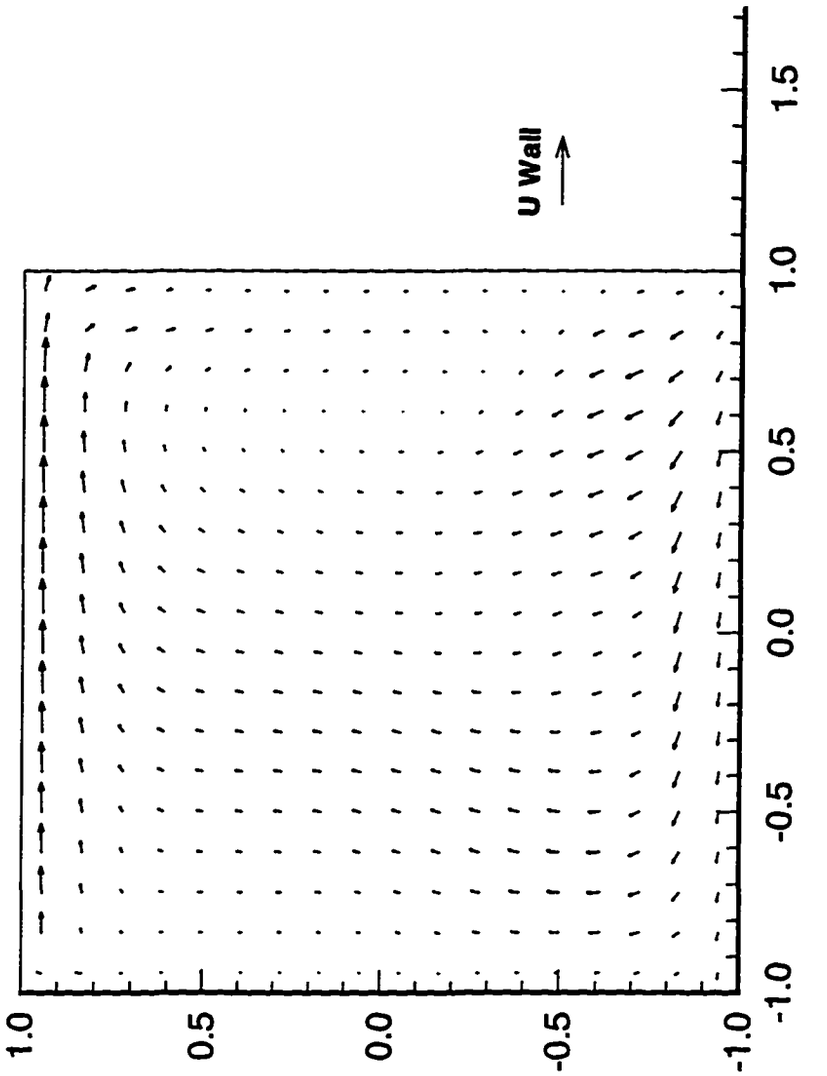

Figure 6.2.1-16 Water/Oil Turbulent Flow;Oil Vectors at earth gravity; k-e for both phases;Re=40,000;D_b/D_H=0.197;Void Fraction=0.30

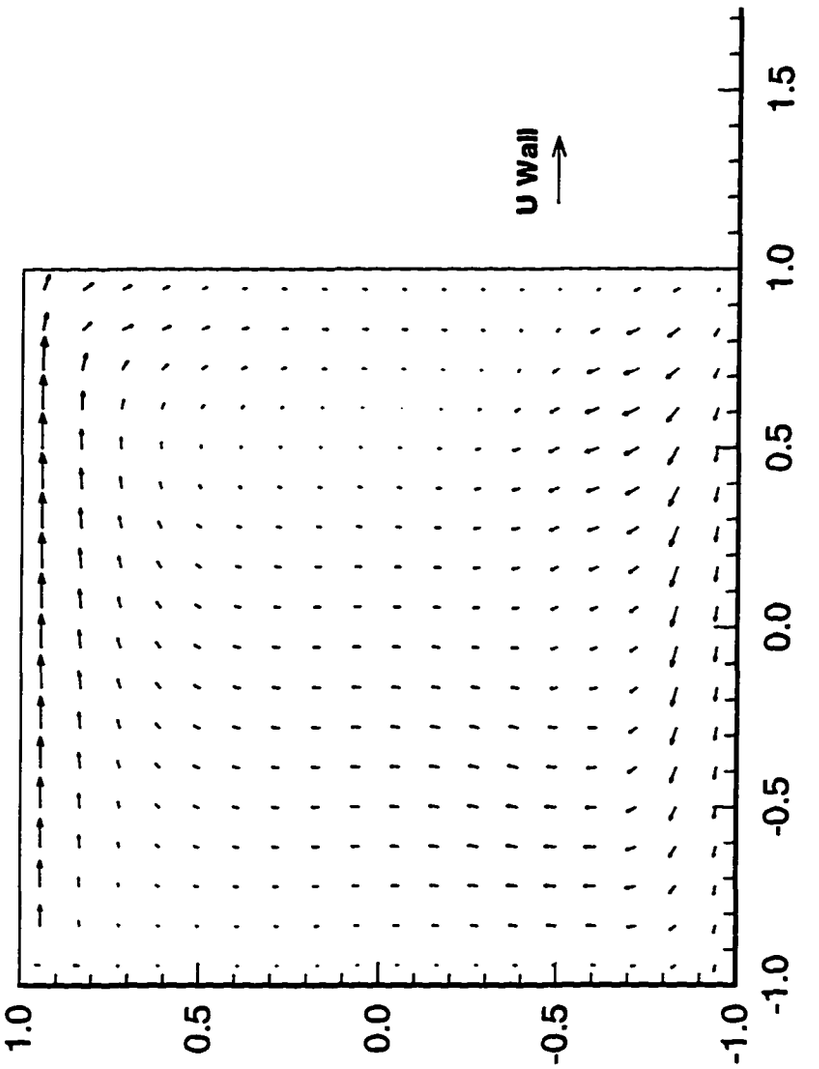

Figure 6.2.1-17 Water/Oil Turbulent Flow;Oil Vectors at microgravity; k-e for both phases;Re=40,000;D_b/D_H=0.197;Void Fraction=0.30

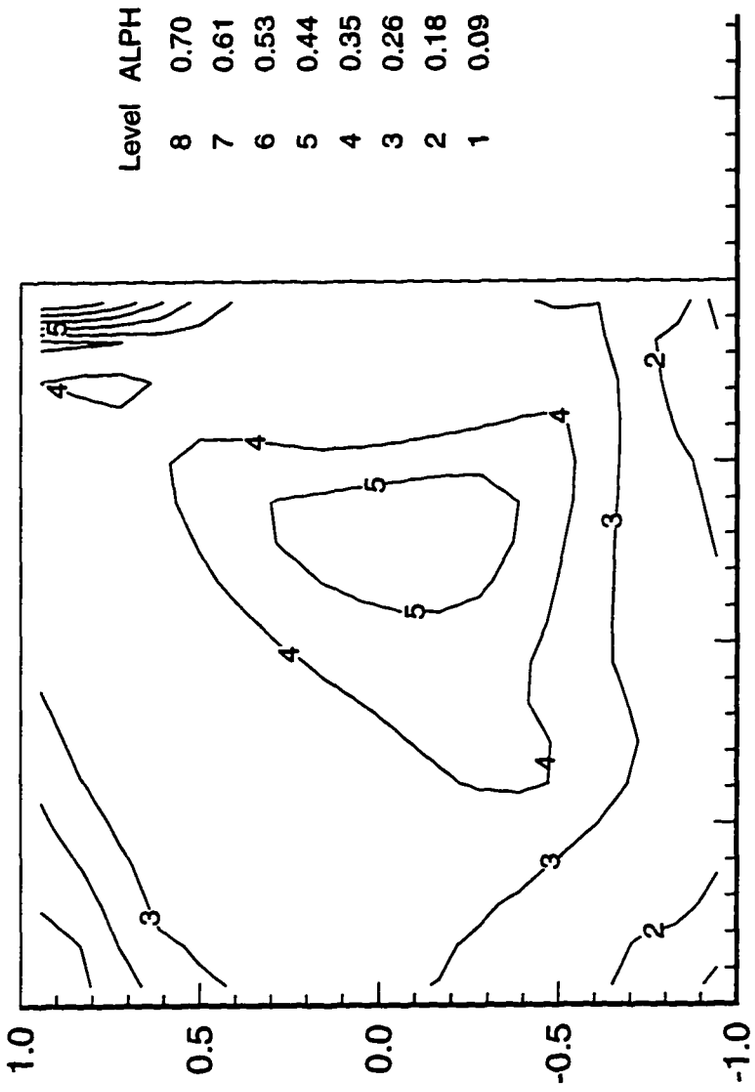

Figure 6.2.1-18 Water/Oil Turbulent Flow;Oil Fraction Contours at earth gravity; k-e for both phases; Re=40,000;D_b/D_H=0.197;Void Fraction=0.30

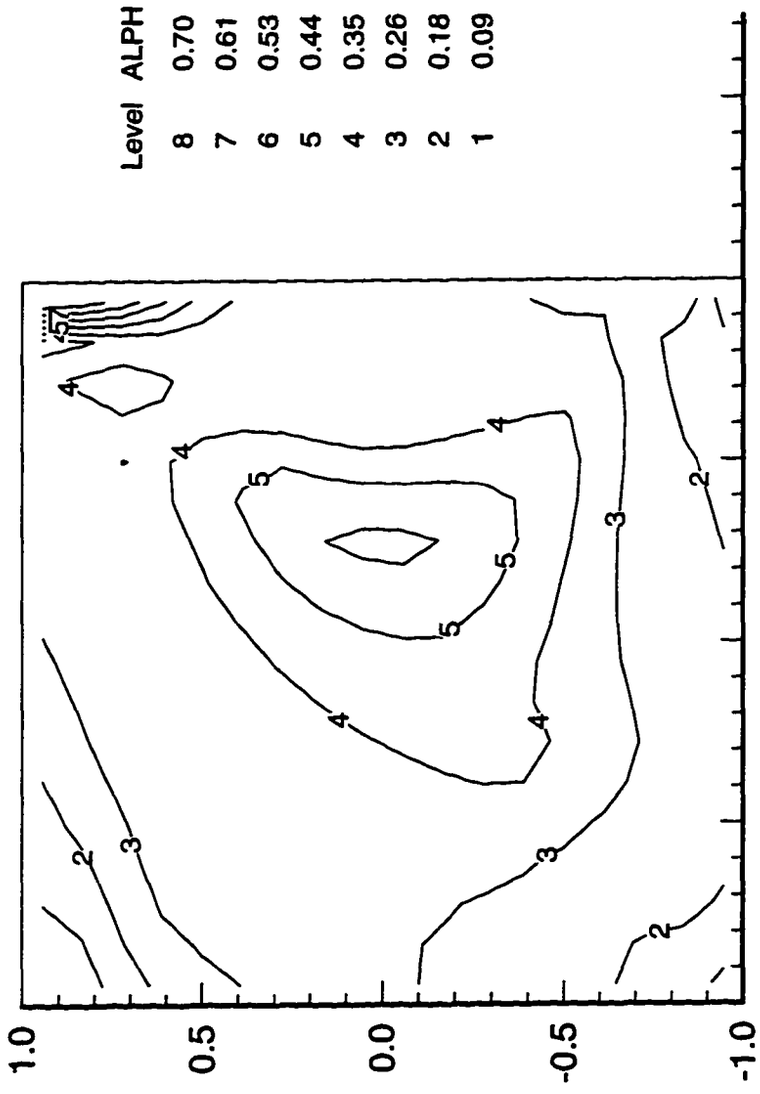

Figure 6.2.1-19 Water/Oil Turbulent Flow;Oil Fraction Contours at microgravity; k-e for both phases; Re=40,000;D_b/D_H=0.197;Void Fraction=0.30

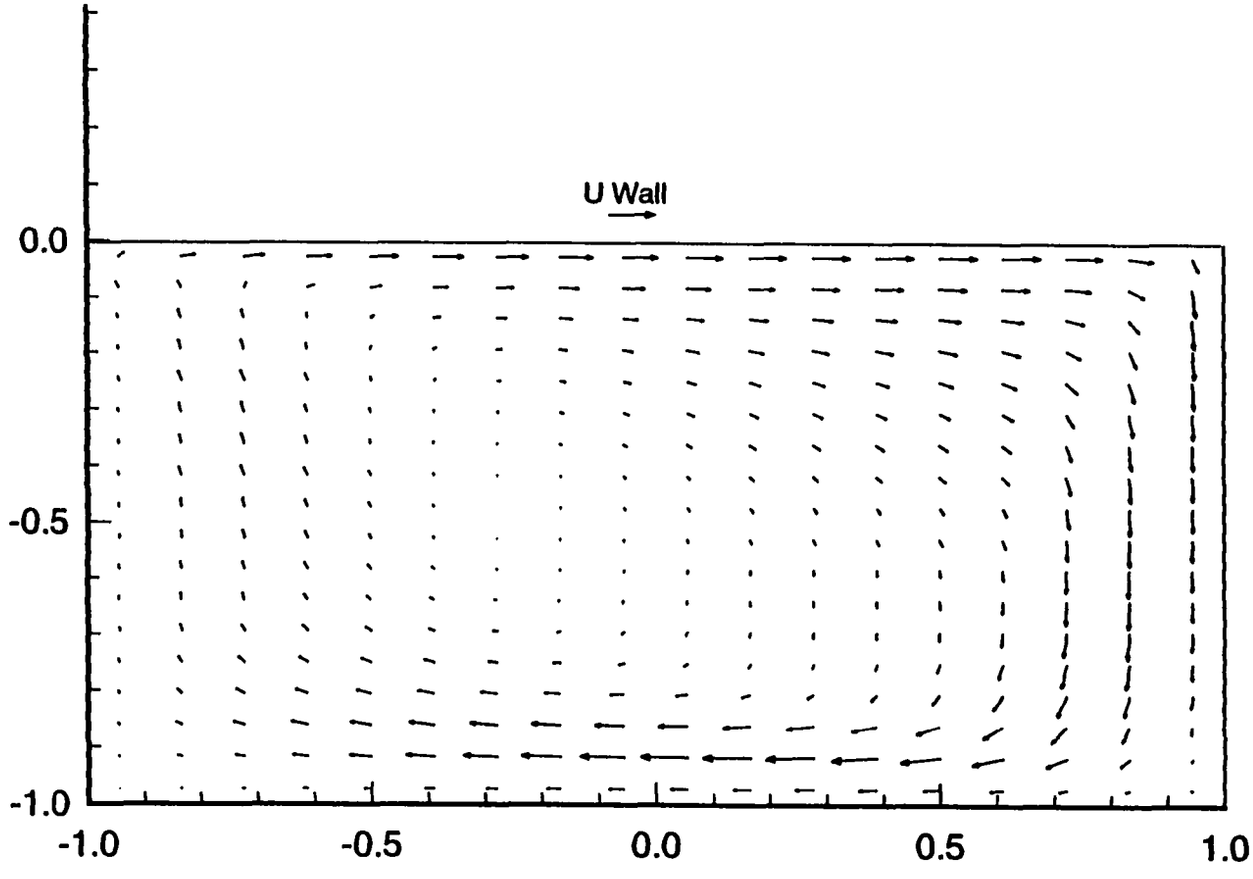

Figure 6.2.1-20 Aspect Ratio=0.5;Water Vectors at microgravity; Laminar Flow; Re=400; D_b/D_H=0.197; Initial Void Fraction = 0.3

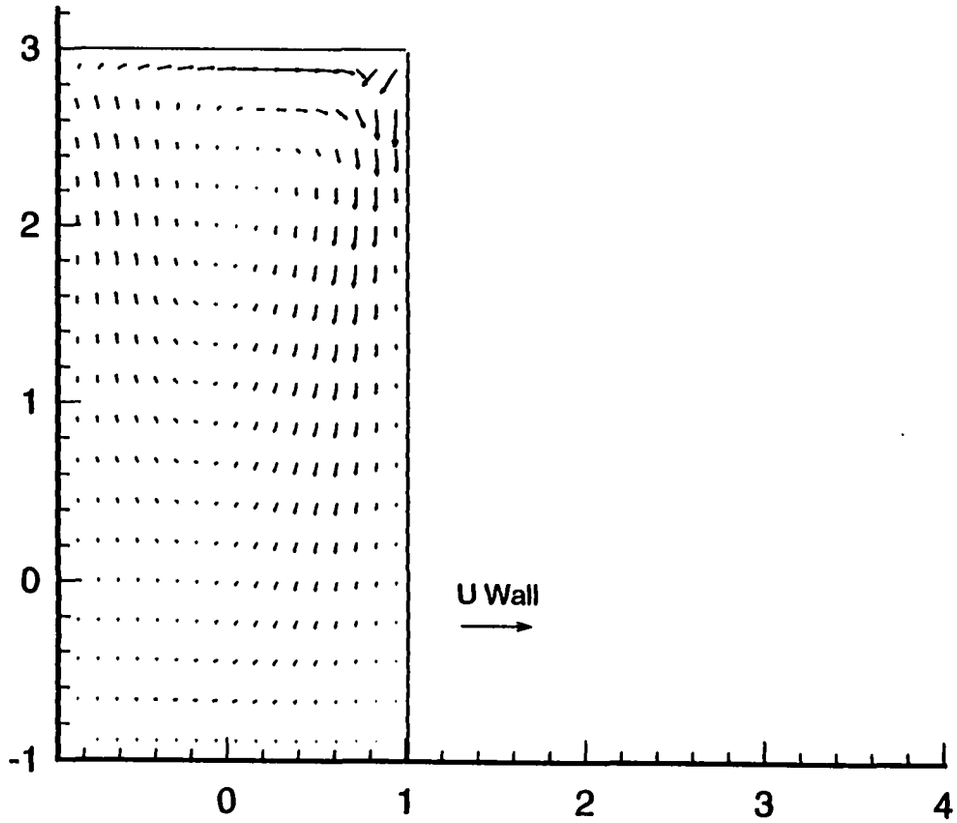

Figure 6.2.1-21 Aspect Ratio = 2.0; Water Vectors at microgravity; Laminar Flow; Re=400;D_b/D_H=0.197;Initial Void Fraction = 0.3

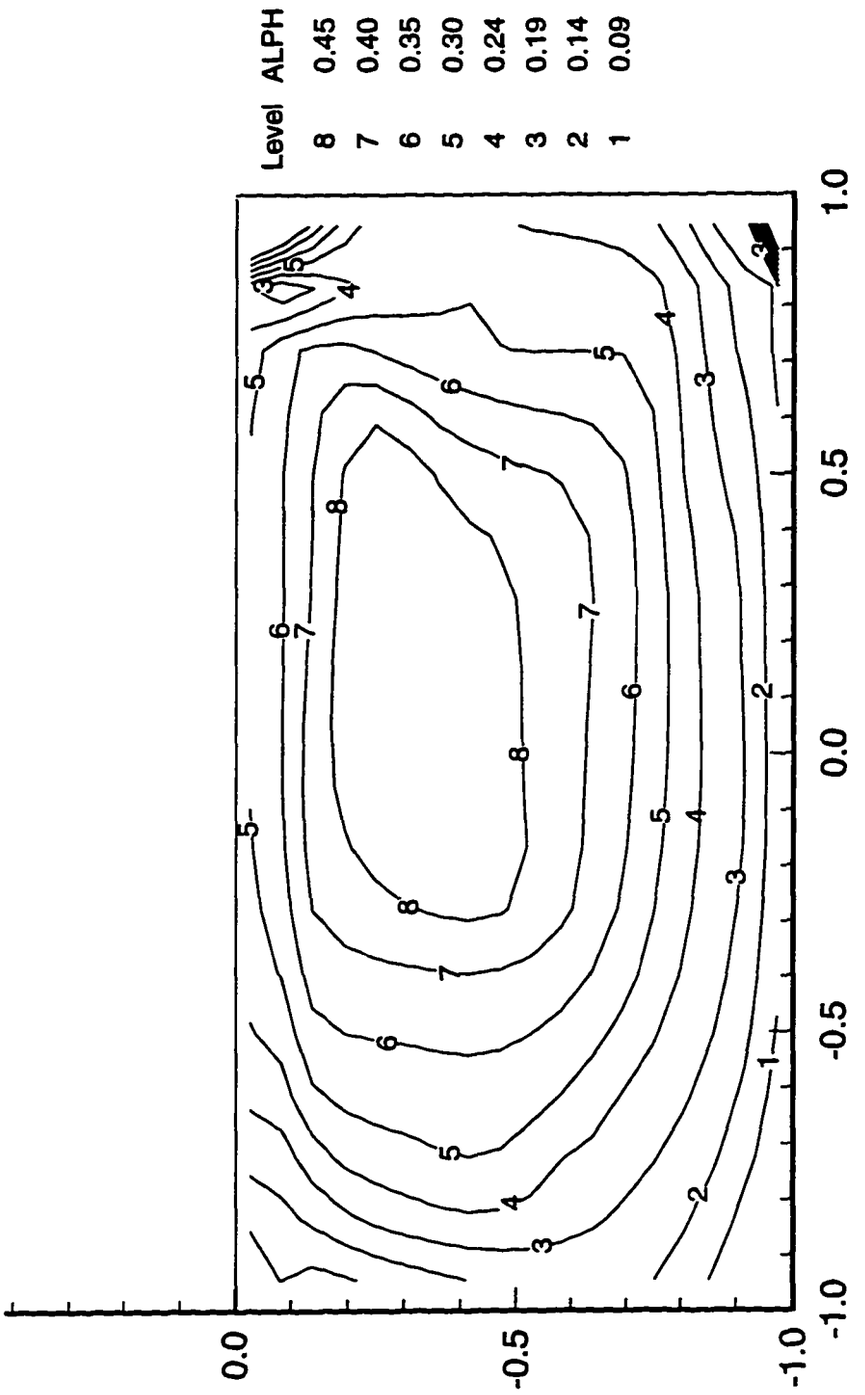

Figure 6.2.1-22 Aspect Ratio=0.5; Oil Fraction Contours at microgravity; Laminar Flow; Re=400; D_b/D_H=0.197; Initial Void Fraction = 0.3

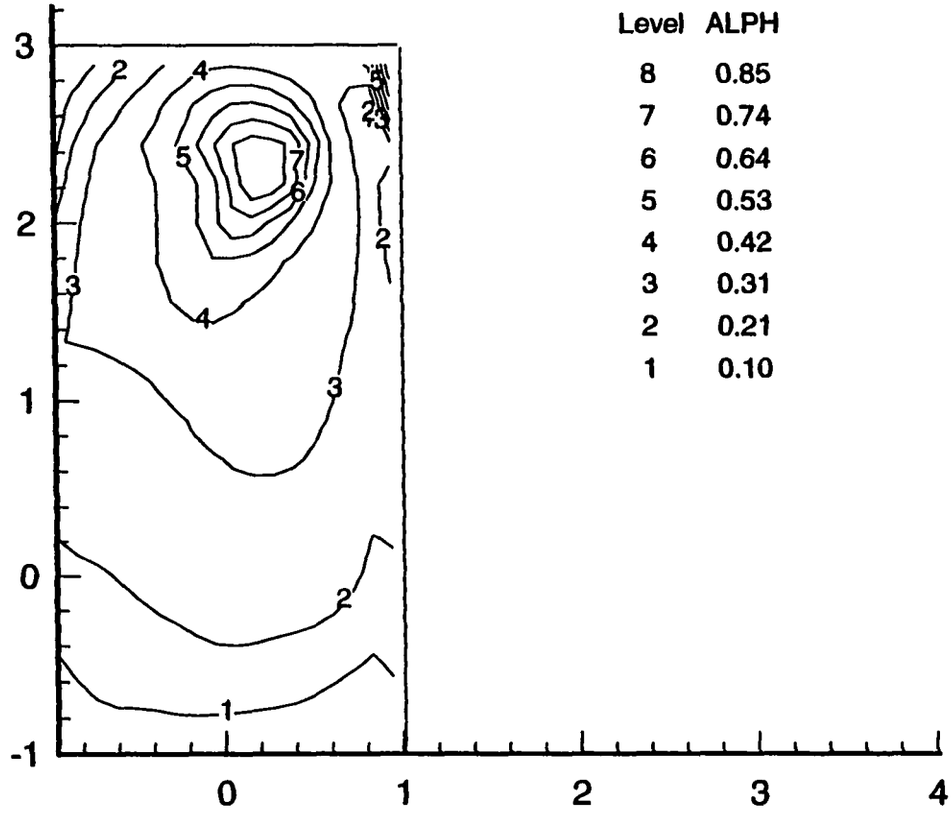

Figure 6.2.1-23 Aspect Ratio = 2.0; Oil Fraction Contours at microgravity; Laminar Flow; Re=400;D_b/D_H=0.197;Initial Void Fraction = 0.3

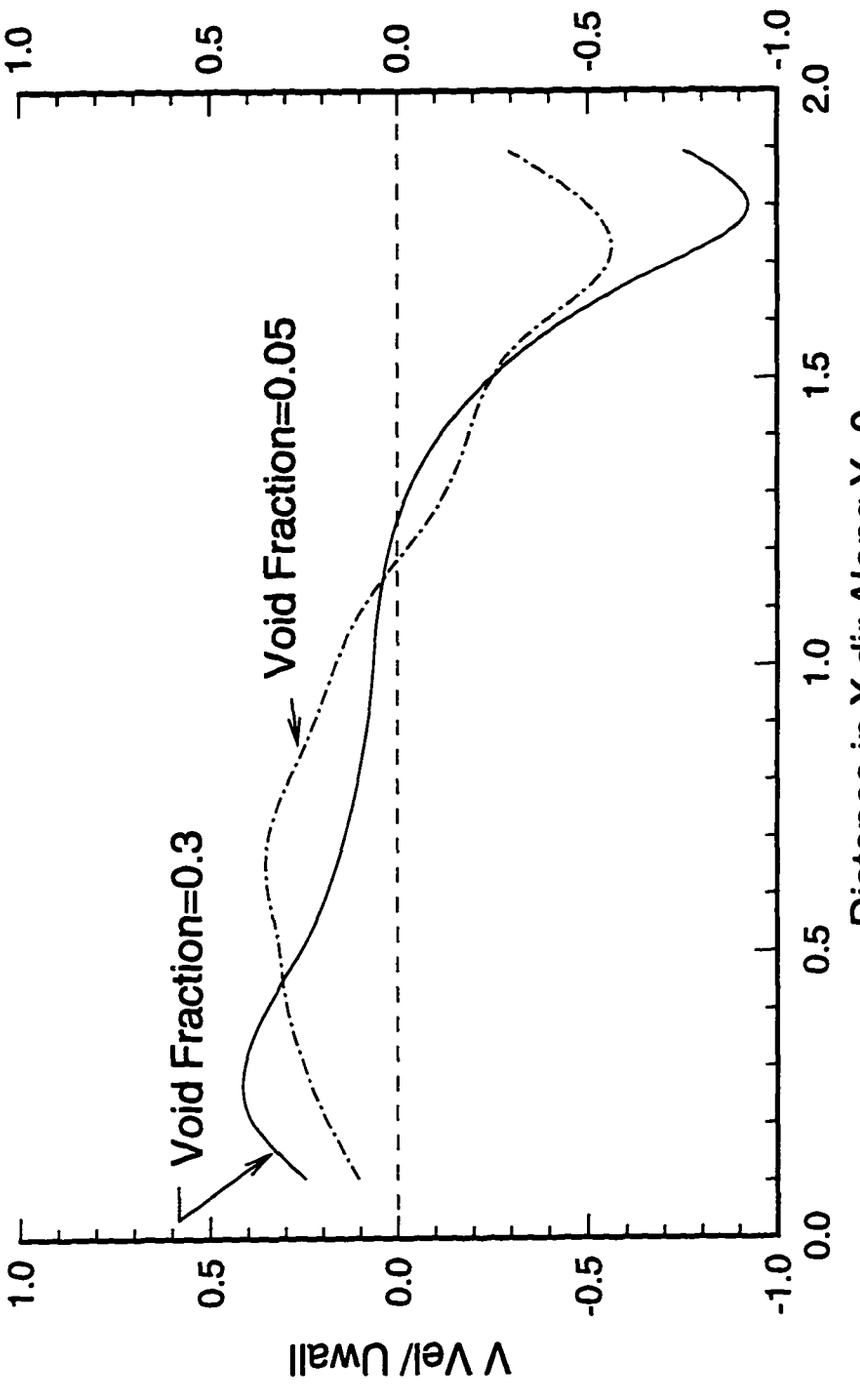

Figure 6.2.1-24 Comparison of Vertical Velocities across Y=0 (i.e.,mid-way between bottom & top walls); Laminar Flow; Re=400; Microgravity; $D_b/D_H = 0.197$

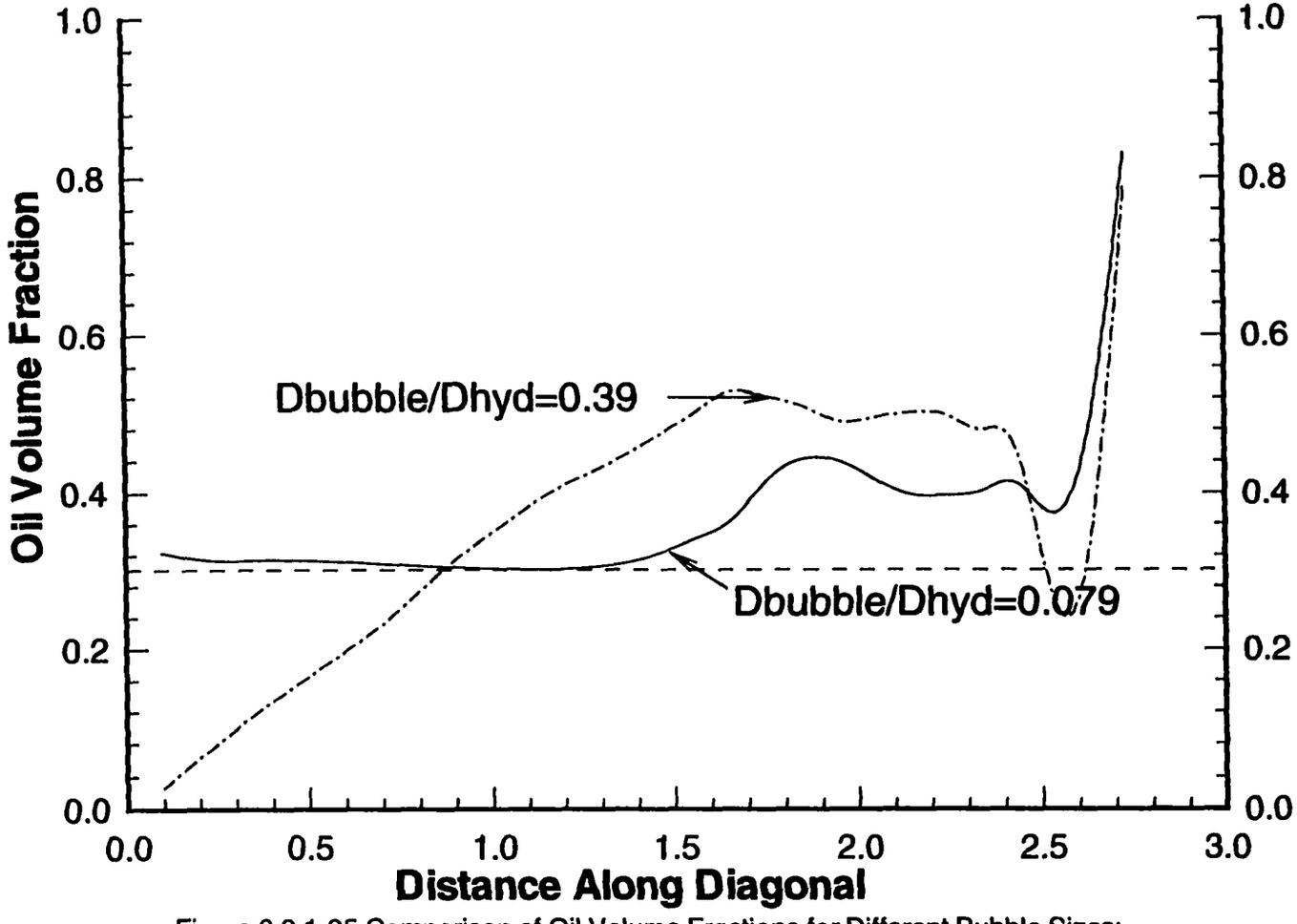

Figure 6.2.1-25 Comparison of Oil Volume Fractions for Different Bubble Sizes; Laminar Flow; Re=400; Microgravity; Initial Volume Fraction = 0.3 Throughout

6.2.2 Turbulent Two-Phase in a Straight Duct

Vertical upwards two-phase flows in circular cross section pipes have been studied analytically and experimentally by Neti and Colella (1983), Wang et. al. (1987) and Neti and Mohammed (1990). Such detailed quantitative measurements are not available for vertical up two-phase flows in square cross section ducts. The present numerical algorithm described earlier has been used to predict vertical upflows in square cross sections.

For the square duct two-phase flow predictions, for a given void fraction, the bubble distribution and the static pressure is assumed to be uniform at the inlet to the vertical section. The void fraction distribution at the end of the vertical duct, i.e., at a distance of 45 hydraulic diameters downstream (fully developed) shows a central core which has a void fraction distribution less than the average inlet value and a region of high void fraction near the walls. This peaking near the wall is the result of the bubble's tendency to be driven towards the walls which is a consequence of both the lateral lift force on the bubble due to the gradient of the axial velocity and the lower static pressure that exists along the duct's perimeter. The static pressure distribution at a distance of 45 hydraulic diameters downstream from the inlet shows a central core of higher static pressure surrounded by a region of low pressure (Figure 6.2.2-1). The pressure parameter plotted is $\frac{P_{local} - \bar{P}}{\frac{\rho W^2_{avg}}{2}}$.

The predicted water velocity profile for turbulent two-phase flow is shown on Figure 6.2.2-2 and is somewhat flatter than that predicted for single phase flow at the same vertical location (see Figure 6.1.2-7). The presence of the bubbles in the two-phase up flow distribute momentum across the section. Measurements in circular cross section pipes [Neti and Colella (1983), and Wang et. al. (1987)] show that the continuous phase velocity profile is flattened with the largest difference occurring near the wall. Close to the wall, the concentration of the lighter phase which due to gravity is moving faster than the water tends to increase the velocity of the water. This is often called the "chimney effect". The longitudinal velocities for the distributed phase (Figure 6.2.2-2) are higher than those of the continuous phase due to buoyancy effects and the near 1000:1 density ratio between water and air.

Along with the void redistribution the flow exhibits momentum adjustments that include lateral flows, boundary layer growth and axial velocity changes. The predicted void fraction contours for an average inlet void fraction of 0.07 and for 5 mm bubbles are shown in Figure 6.2.2-3 for the fully developed flow condition. There is a central core of void fraction about 0.06. The void fraction increases rapidly close to the wall and is higher in a rather small wall layer. Figure 6.2.2-4 is a line-plot of void fraction predicted across the centerline, along with the inlet average void fraction shown for reference. Figure 6.2.2-5 [Neti et. al., (1996)] presents the void fraction data measured by Wang et. al. in a circular pipe for vertical up flow. The same trend is seen there, a flat void fraction over much of the flow area with significant peaks near the walls. There is not similar experimental data in the literature for a square duct. The only non-circular pipe data available is from a high aspect ratio rectangular cross section [Moujaes and Dougall (1987)]. These measurements were made to simulate flow in a nuclear core vertical rod bundle. The cross section was 76.7 mm long and 12.7 mm wide. Average bubble size was

nearly 5 mm. Void fraction distributions presented along the long side which is made up of averages taken in the short side direction show a void peak near the wall also.

Void fraction distributions with an inlet value of 0.3 show a similar central region of void fraction less than the inlet region with a peaking of the void fraction close to the wall. Figure 6.2.2-6 shows that a central region of 0.25 void fraction with wall peak values as high as 0.6.

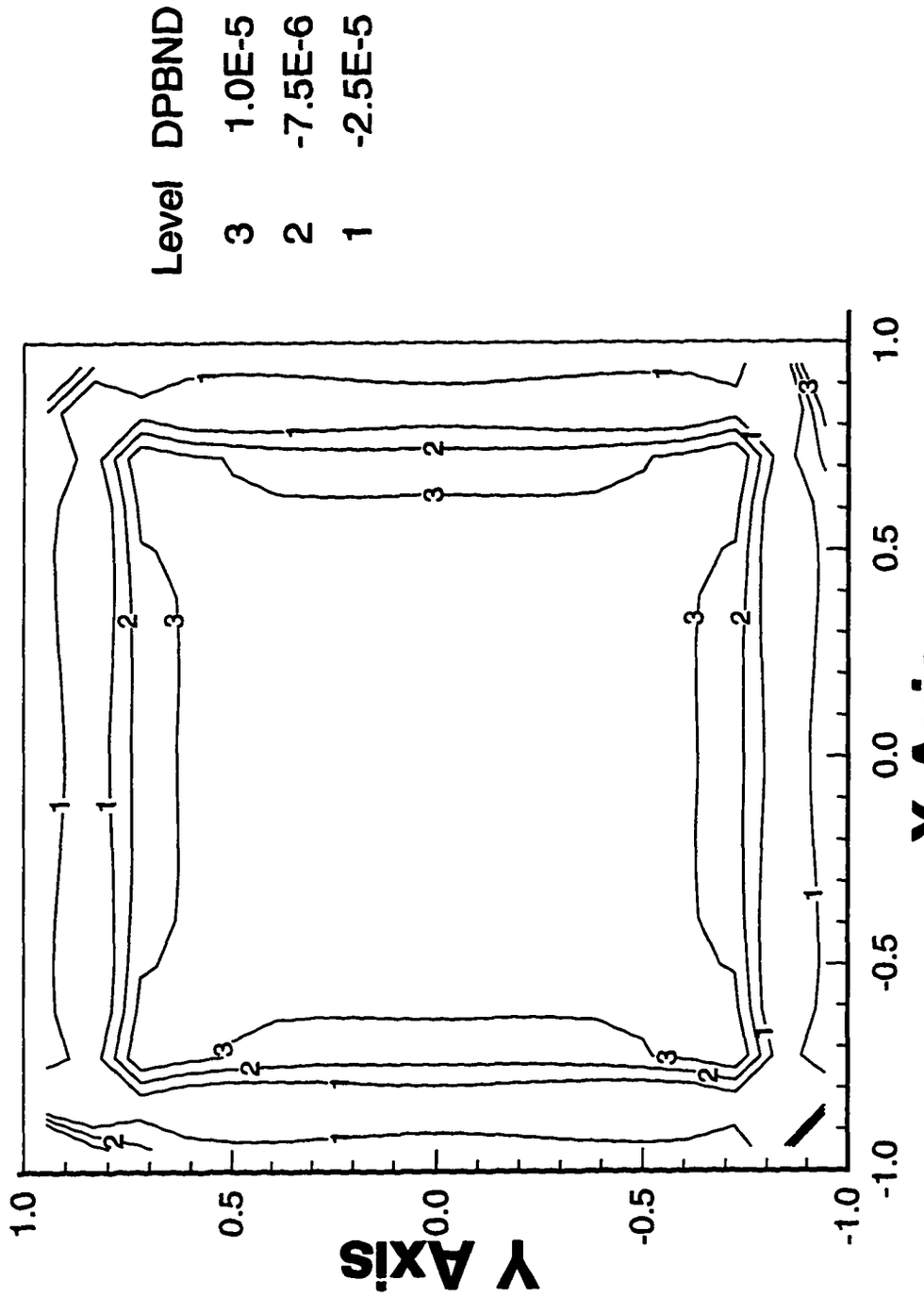

Figure 6.2.2-1 Static Pressure Contours at end of Vertical Straight Duct; Z/D_h=45; Water/Air; Re=40,000; Voidin=0.07;D_b=5 mm

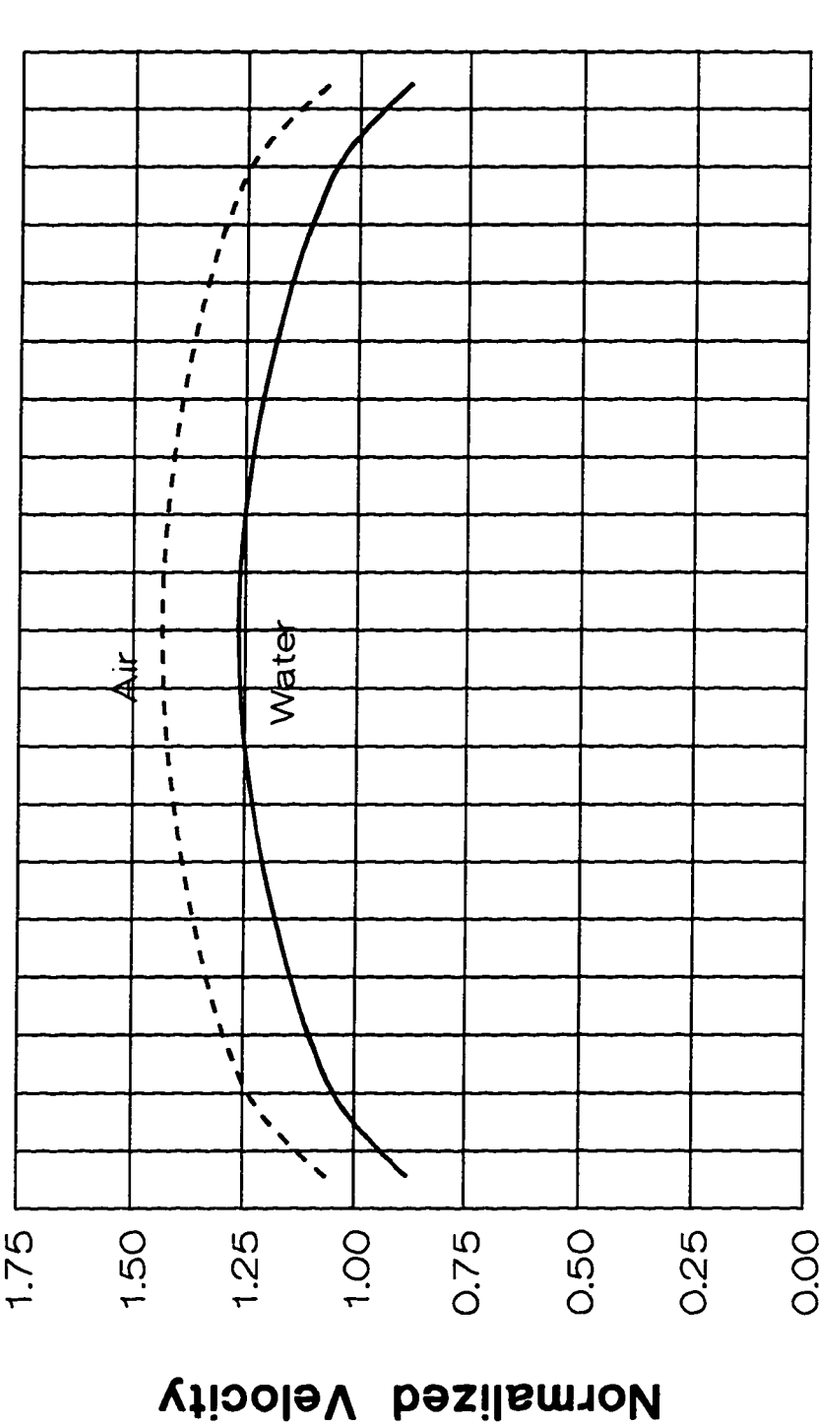

Figure 6.2.2-2 Two-Phase Water/Air Flow; Centerline Longitudinal Velocity Distributions; at end of Vertical Duct (Z/D_H = 45); Re=40,000; d_{bub} = 5 *mm*; D_H = 25.4 *mm*

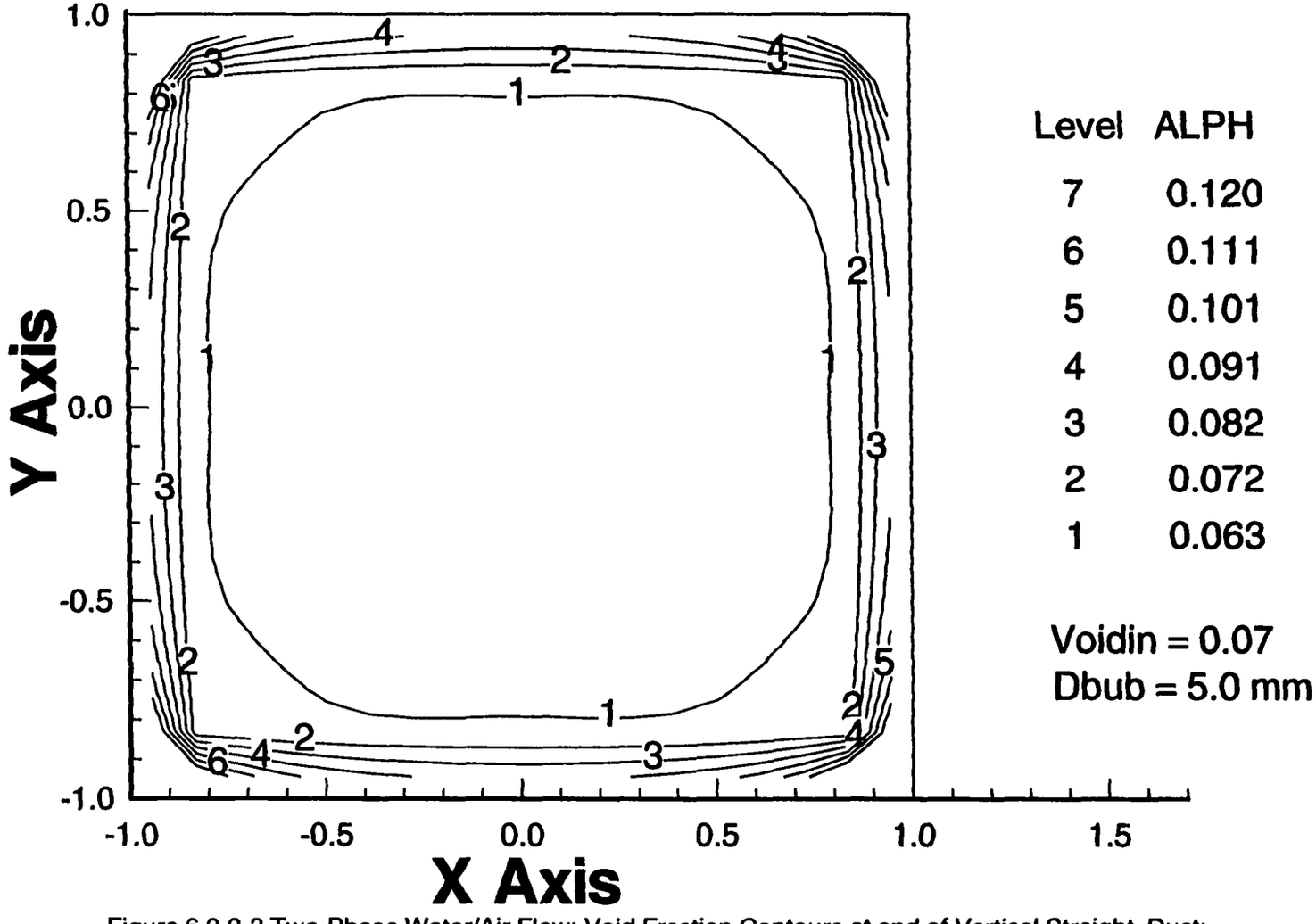

Figure 6.2.2-3 Two-Phase Water/Air Flow; Void Fraction Contours at end of Vertical Straight Duct; Z/D_H=45;Re=40,000; d_{bub} = 5 mm; D_H = 25.4 mm

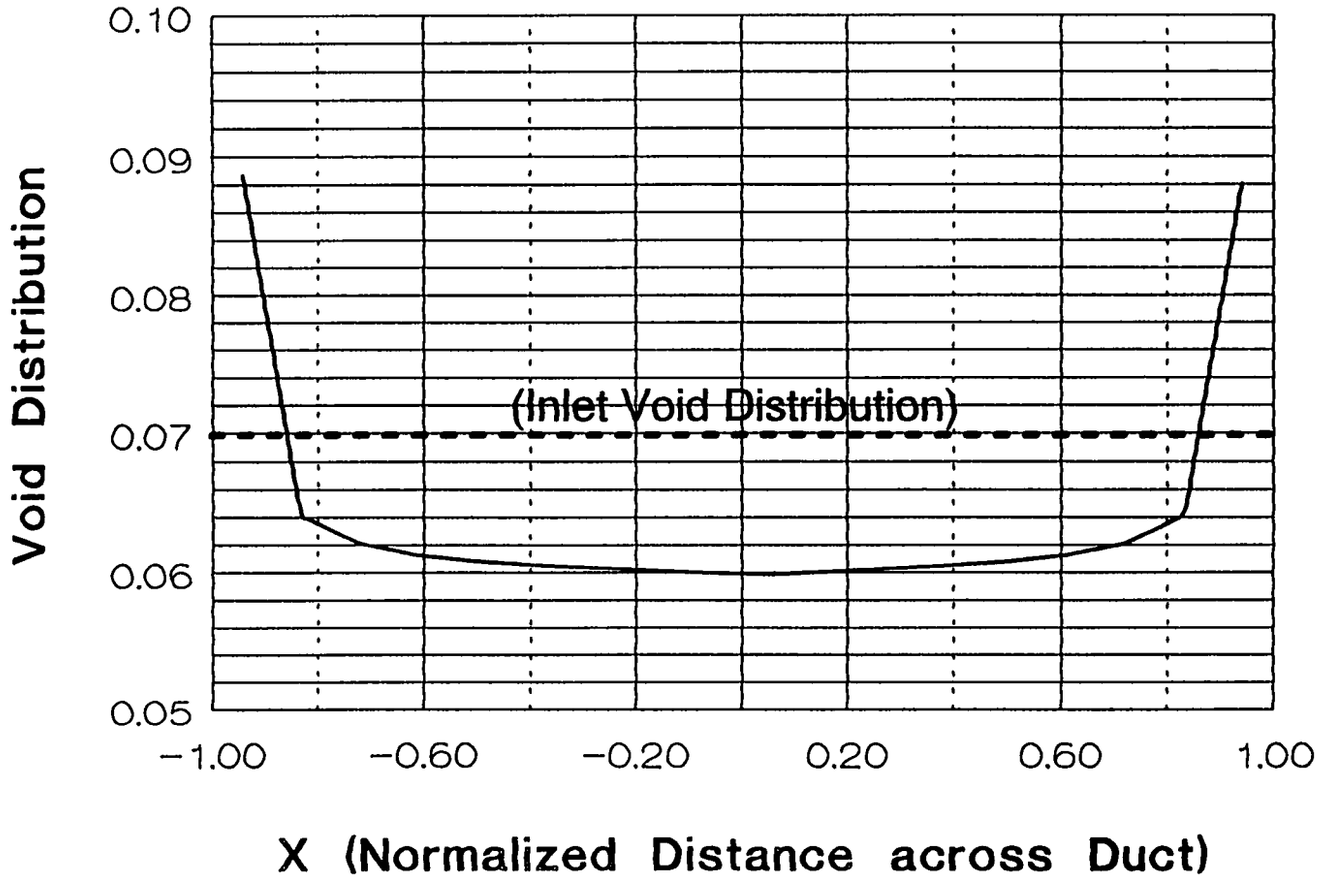

Figure 6.2.2- 4 Two-Phase Water/Air Flow; Centerline Void Fraction Distribution @ end of Vertical Straight Duct; Z/D_H=45; Re=40,000 ; d_{bub}=5 mm; D_H=25.4 mm

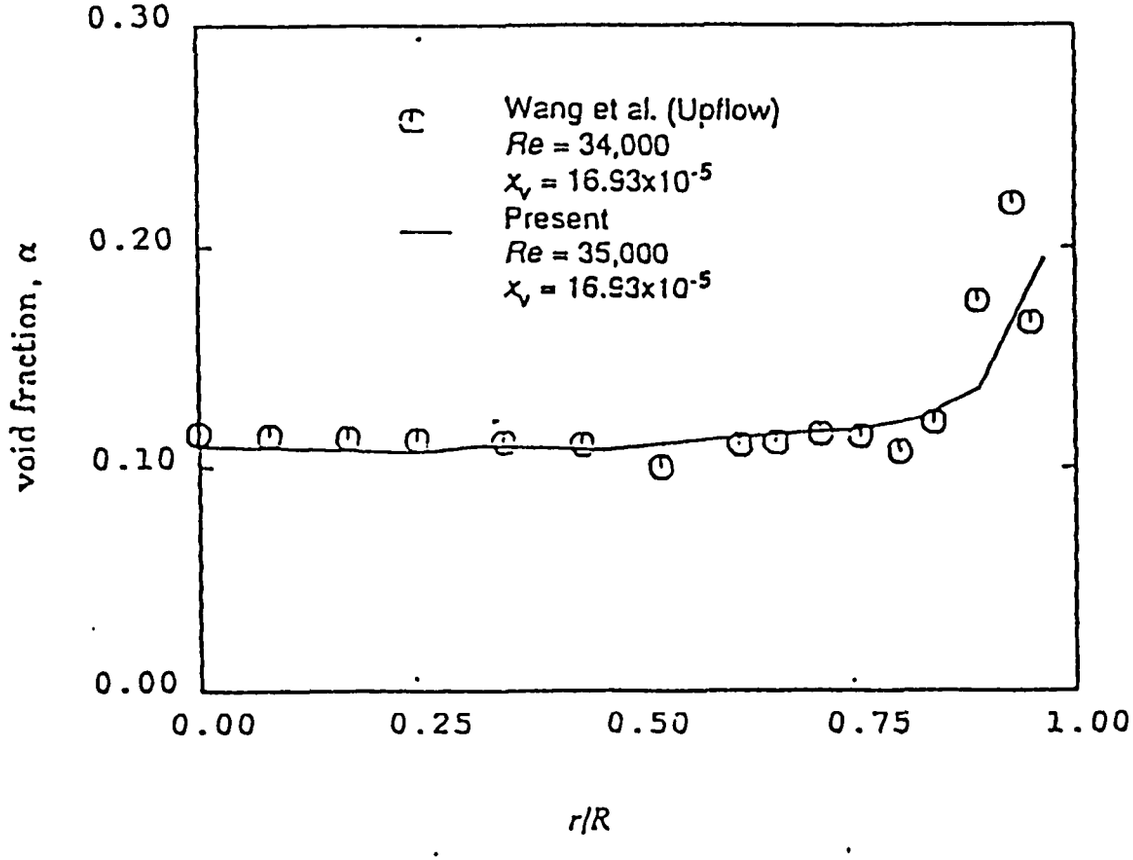

Figure 6.2.2- 5 Experimental Data of Wang et. al. in Circular Cross-Section Pipe showing Void Fraction Peaking at Walls

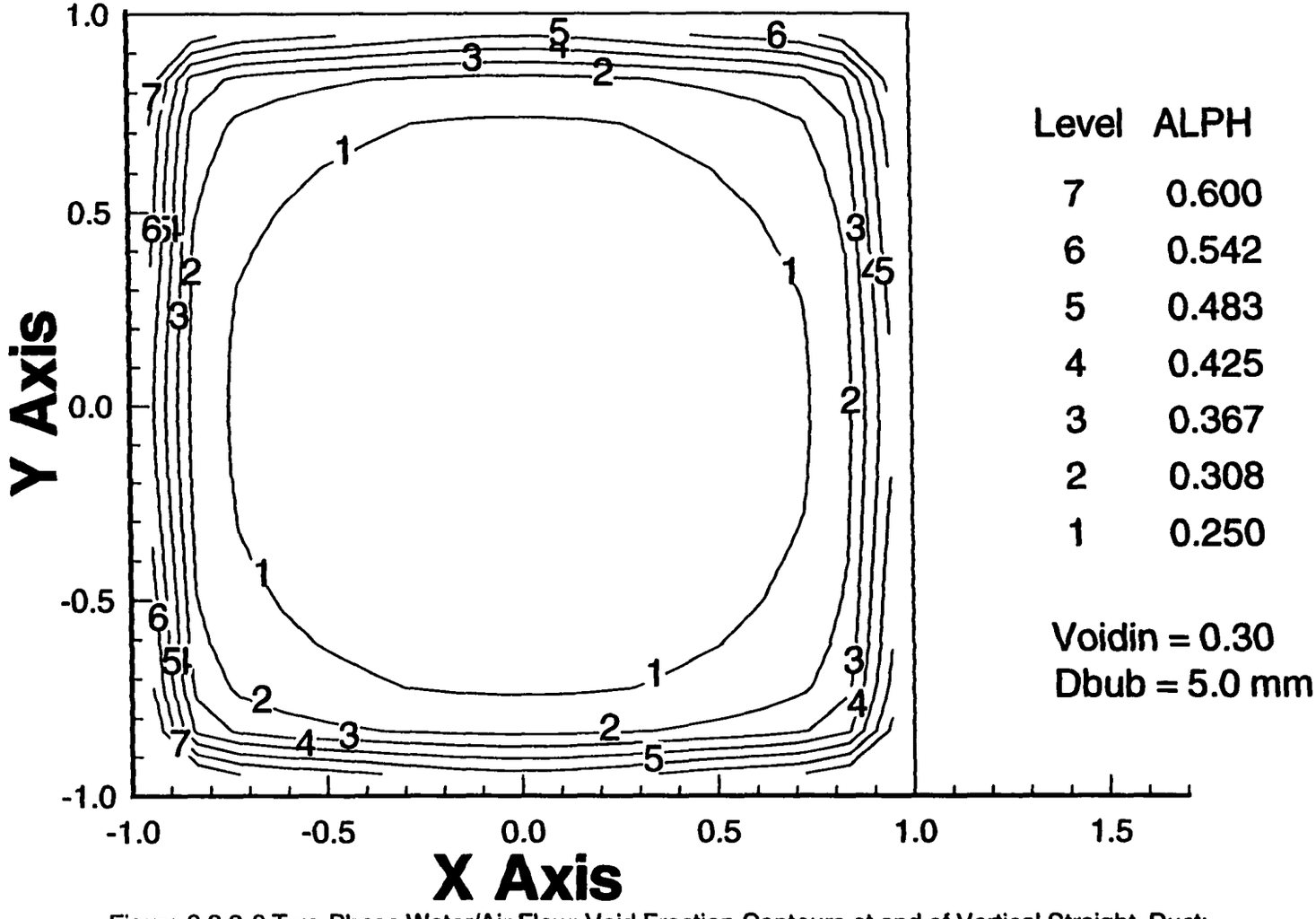

Figure 6.2.2-6 Two-Phase Water/Air Flow; Void Fraction Contours at end of Vertical Straight Duct; High Inlet Void Fraction (= 0.3); Z/D_H=45;Re=40,000; d_{bub} = 5 mm; D_H = 25.4 mm

6.2.3 Two-Phase Flow in Straight-Curved-Straight Duct with Large Bubbles (Simulating the Present Two-Phase Flow Measurements)

The present work uses a long square cross section duct ahead of the bend. The inlet void profile at the inlet to the bend is computed and is found to have the trend seen by many experimentalists, a void fraction distribution with peak values near the walls, as discussed in the previous section. Therefore, the present results for flow in bends with square cross section have physically realistic inlet void profiles, which rapidly change as the flow progresses through the 90^{o} bend and then into a horizontal section. This computational approach is preferable to starting at the duct's inlet with an assumed void fraction profile as was done by Carver (1984 and 1986) for his calculation of two-phase flow in a circular cross section curved pipe. His assumption of a sinusoidal void distribution is not correct for vertical up flow for which numerous experimentalists have found a peak in the void distribution near the walls. The bubbly flows described in this section are computed at bubble diameters of 5 mm, which simulates the bubble diameter used in the test loop.

Measurements were made in a test loop that consisted of a vertical square duct with an up flow section followed by the 90^{o} bend and then a horizontal straight duct. Computational predictions of flow were made for the same flow configuration so that the inlet and exit conditions for the bend were included naturally and not arbitrarily assigned. The inlet velocity and void fraction profiles at the start of the bend are those calculated implicitly in the forty five diameter straight square duct described in the previous section.

A qualitative description of the bubble distribution throughout the test configuration was recorded by a series of digital pictures taken to support the analytical work of this dissertation.

This series of pictures (see section 3.4 *Data and Results*) showed that the bubbles, on entering the curved section of the test loop, move quickly towards the inner bend and follow a path closer to the inner radius throughout the bend. On leaving the bend, the bubbles end up at the bottom of the horizontal straight section, but then quickly move towards the top of the horizontal section. The air and water are fairly well stratified by the end (22 diameters) of the horizontal straight section. This geometry was expected to be a challenge to the present numerical algorithm, since there was a drastic shift in void distribution with maxima near the inner radius of the curved duct followed by high void fractions near the top (i.e., equivalent to the outer radius side) in the horizontal duct. Velocity, pressure and void distributions for two-phase flow in the square cross section curved duct are discussed below.

The present predictions for the continuous phase velocity vectors on a plane located at 45° in the curved section are shown in Figure 6.2.3-1. The inlet water/air flow conditions are those at the end of the straight duct and an average void fraction of 0.07; bubble diameter of 5 mm (in the 25.4 mm square duct) and a Reynolds number of 40,000. The secondary flow velocity vectors for the continuous phase show the familiar pair of counter rotating vortices which was discussed in conjunction with both laminar and turbulent single phase flow in a curved duct. However, for the two-phase flow case, the vectors flowing towards the outer radius are much stronger than those returning towards the inner bend. This suggests that more flow is moving towards the outer radius than is required to change the longitudinal velocity profile from a symmetric one to one with a peak velocity at a radius biased towards the outer radius. The continuous phase is moving preferentially to the outer radius due to the body forces. The companion secondary flow velocity vector plot for the distributed phase, air, is shown in Figure 6.2.3-2. This indicates that the air is moving fairly strongly towards the inner radius. Peak

lateral velocities are approximately 0.75 of the average throughflow velocity. The associated void fraction (i.e., volume fraction of the distributed phase) contours are shown on Figure 6.2.3-3. While the majority of the cross section has a void fraction approximately equal to the inlet void fraction of 0.07, the void fraction at the outer radius is 0.05 and the void fraction along the inner radius is as high as 0.15.

At approximately 75° and more (depending on the Reynolds number), the centrifugal force which is driving the heavier water towards the outer radius is almost balanced by the component of gravity which is acting downwards. The present prediction for the continuous phase velocity vectors on a plane located at the end of the 90° curved section is shown on Figure 6.2.3-4. There is still a pair of counter rotating vortices visible but the vortices are very weak at this position in the duct. The peak lateral velocity is approximately 10 percent of the average through flow velocity. The distributed phase's lateral velocities are still moving towards the inner radius (see Figure 6.2.3-5) but the velocities are generally smaller than those at 45°. The associated void fraction contours at the end of the curved duct are shown in Figure 6.2.3-6. The void fraction along the outer radius (at the top of the duct) is 0.03. There is a large area for which the void fraction is between 0.03 and 0.067. The cross sectional area closest to the inner radius shows high void fractions, with a peak value of 0.25. This clearly demonstrates the dominance of the centrifugal force over gravity at these flow conditions.

The static pressure in the duct at the bend's inlet has a central core of high pressure, with low pressure along the periphery (Figure 6.2.2-1). Inside the bend the centrifugal force is balanced by a radial pressure gradient in which the highest pressure is along the outer radius. The pressure, referenced to the average pressure at the bend inlet and normalized by the dynamic head:

$$Dp_{bend} = \frac{P_{local} - \overline{P}}{\frac{\rho W^2_{avg}}{2}} \qquad [6.2.3\text{-}1]$$

develops from a fairly mild pressure gradient in the duct at 30° (Figure 6.2.3-7) to a moderate radial pressure gradient at 60° (Figure 6.2.3-8) to a strong radial pressure gradient at the bend's exit (90°) (Figure 6.2.3-9). The pressure increases with increasing radial distance for lateral planes between approximately 45° and 90°. The lateral plane pressure distribution at 30°(Figure 6.2.3-7) has a maximum pressure at the outer radius and minimum pressure close to the inner radius. However, the inner radius shows a slightly higher than minimum pressure. The rapid movement of the distributed phase towards the inner radius weakens the continuous phase's secondary flow and thus the radial pressure gradient is somewhat weakened.

Thus the present computational approach correctly predicts the redistribution of bubbles towards the inner radius as well as the pressure changes associated with turbulent flow in a bend as the flow proceeds through the curved duct.

Upon leaving the curved duct, the flow enters a horizontal straight section. The predicted water velocity vector contours in the horizontal straight duct at a distance of 22.5 hydraulic diameter downstream of the exit of the bend (see Figure 6.2.3-10) show that the heavier continuous phase is now moving in the opposite direction to the bottom of the duct. The water is moving from the top towards the bottom with maximum velocities approaching 13 percent of the average longitudinal velocity. By contrast, the lighter distributed phase is now moving towards the top (which for the curved duct would be the outer radius). The maximum lateral velocity for this upward movement is approximately 33 percent of the longitudinal velocity in Figure

6.2.3-11. The associated void fractions are shown in Figure 6.2.3-12. A maximum void fraction close to 0.25 occurs near the top; a minimum void fraction of 0.05 occurs along the bottom. Thus the void fraction distributions are totally reversed from what they were in the curved section with the peak void fraction values now occurring at largest x values (corresponding to the top) whereas inside the bend the minimum void fraction levels occurred at the largest x values (i.e., the outer radius). Further down the horizontal section, the water/air flow becomes more stratified, see Figure 6.2.3-13. Peak void fraction values occurring at the top are now 0.6 while the bottom of the section has a very low void fraction level of 0.02.

The two-phase centerline longitudinal velocities at end of the straight duct presented in a previous section (see Figure 6.2.2-2) showed that a somewhat flattened turbulent profile is established for both phases at the end of the long inlet vertical section. The centerline longitudinal velocity distribution for water in two-phase flow at 45° in the bend is similarly flattened (see Figure 6.2.3-14) compared to the single phase distribution. The maximum of the longitudinal velocity in the curved portion of the duct moves towards the outer radius. The longitudinal velocities at the end of the 90° curved duct show a slight peaking near the outer radius (see Figure 6.2.3-15); otherwise the velocity is almost uniform. At this location the gravitational force is acting against the centrifugal force and the flow patterns are in transition between those for curved duct flow and those for flow in a horizontal duct. The peak longitudinal velocity inside the horizontal duct is located close to the bottom wall, and is dictated by the heavier continuous phase.

While the above centerline longitudinal velocity distributions are indicative of the cross sectional trends, they are still two-dimensional slices of what is actually a three-dimensional distribution. Mass is conserved both locally (at each node) and globally (across any given cross

section). Comparisons of the centerline velocity distributions at the end of the long vertical inlet section and the flow at 45° in the bend may appear to violate continuity. However, the three-dimensional profiles (see Figures 6.2.3-16 for the straight duct profile and 6.2.3-17 for the curved duct profile) show that the peak in the axial velocity for the straight duct is very local and falls off in all directions. However, the peak for the bend only falls off in the radial direction and is nearly constant across the duct in the direction (y) normal to the radius. The continuous phase's longitudinal velocity distribution in the y direction at a constant x distance (midway between the inner and outer radii) shows a parabolic distribution at the end of the vertical straight duct and a rather constant distribution at 45° (Figure 6.2.3-18). The longitudinal velocity distribution in the y direction at 90° is also relatively constant (Figure 6.2.3-19). The velocity distribution in the y direction in the horizontal duct, at 22.5 hydraulic diameters downstream of the bend exit, begins to take on a parabolic distribution (Figure 6.2.3-19) similar to that in the inlet vertical straight section.

Numerical simulations were also made for very high (0.3) inlet void fractions. Void fraction distributions for the most interesting cross planes are presented in Figure 6.2.3-20 and 6.2.3-21. The void fraction distribution at the end of the vertical straight duct was shown in Figure 6.2.2-5. Peak values of 0.6 were predicted at the periphery. Figure 6.2.3-20 shows the void fraction contours at the end of the bend (90°) which indicate a high concentration of the distributed phase at the inner radius. Peak values of 0.7 are predicted at the inner wall. The void fraction in the horizontal duct at 22.5 hydraulic diameters from the bend show, in Figure 6.2.3-21, an accumulation of the gas phase at the top of the duct and at both sides of the duct. Here the flow is very stratified: a void fraction of 0.7 is predicted at the top while the void fraction at the bottom is predicted to be 0.1. The present algorithm has thus been demonstrated to

be robust and stable even as the void fraction reaches very high local levels. It is expected that the predictions for flows which are highly stratified will be improved by modifying the constitutive relations that are presently based on bubbly flow.

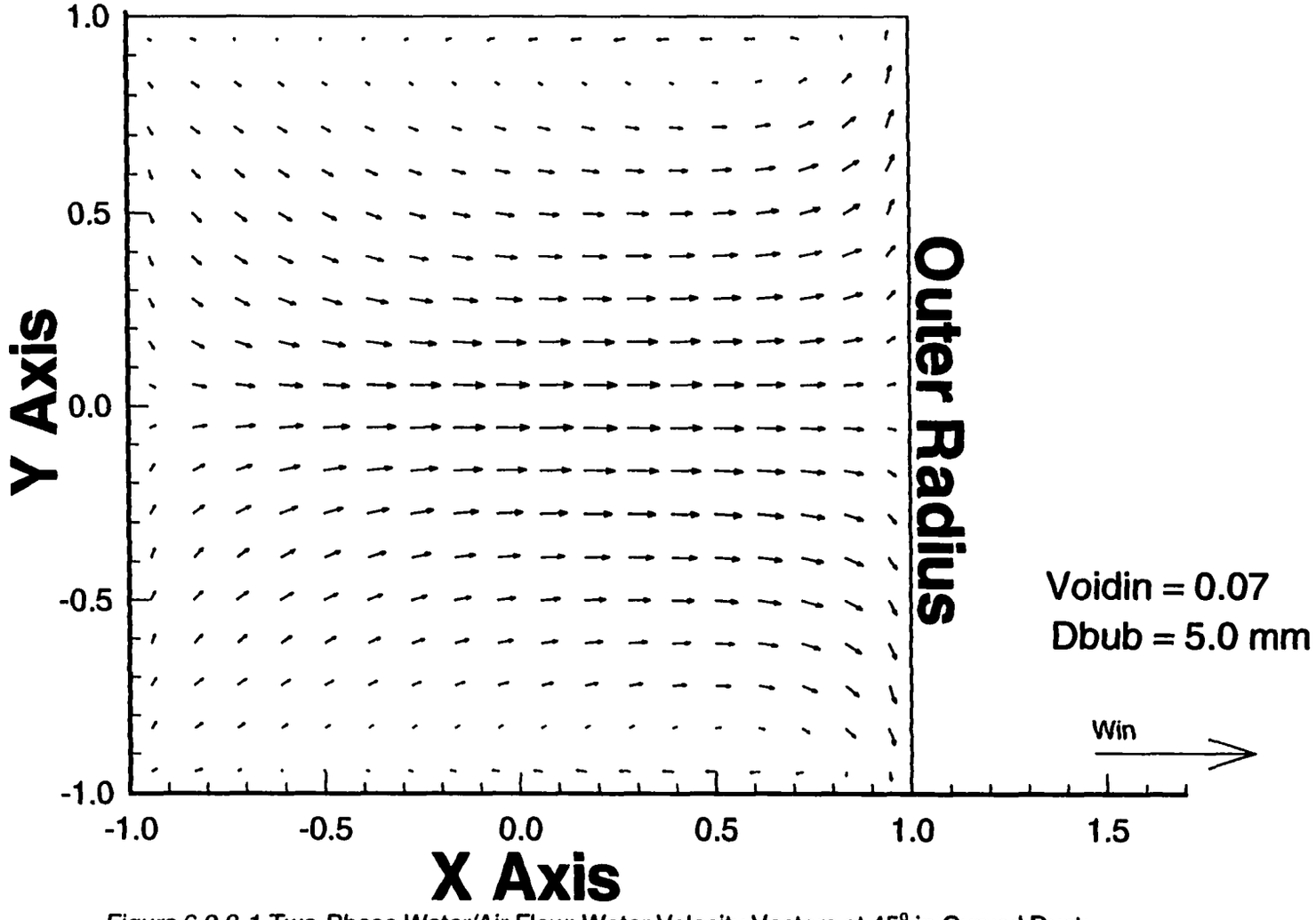

Figure 6.2.3-1 Two-Phase Water/Air Flow; Water Velocity Vectors at 45° in Curved Duct; Re=40,000; d_{bub} = 5 mm; D_H = 25.4 mm

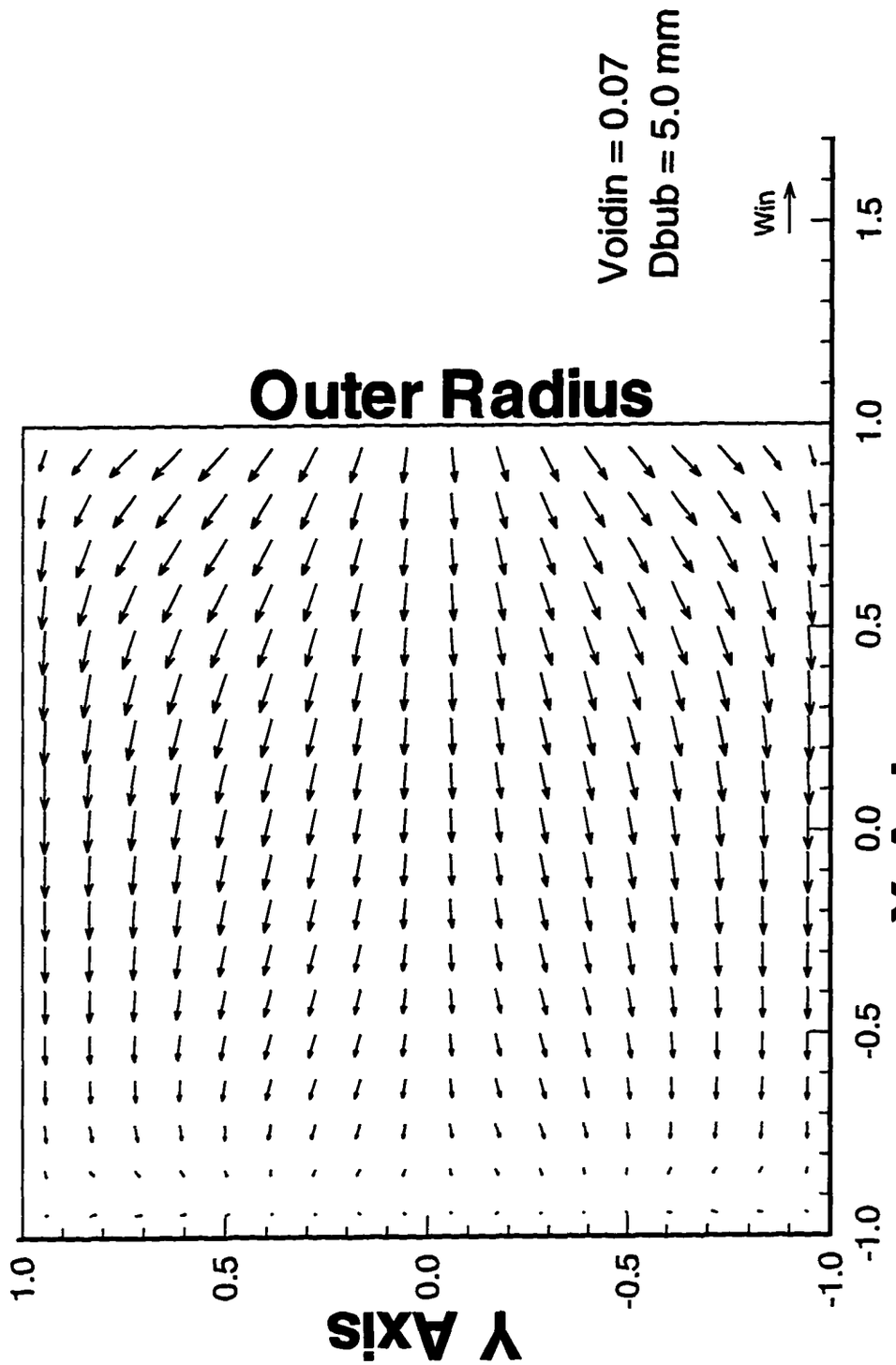

Figure 6.2.3-2 Two-Phase Water/Air Flow;Air Velocity Vectors at 45° in Curved Duct; Re=40,000; d_{bub} = 5 mm; D_H = 25.4 mm

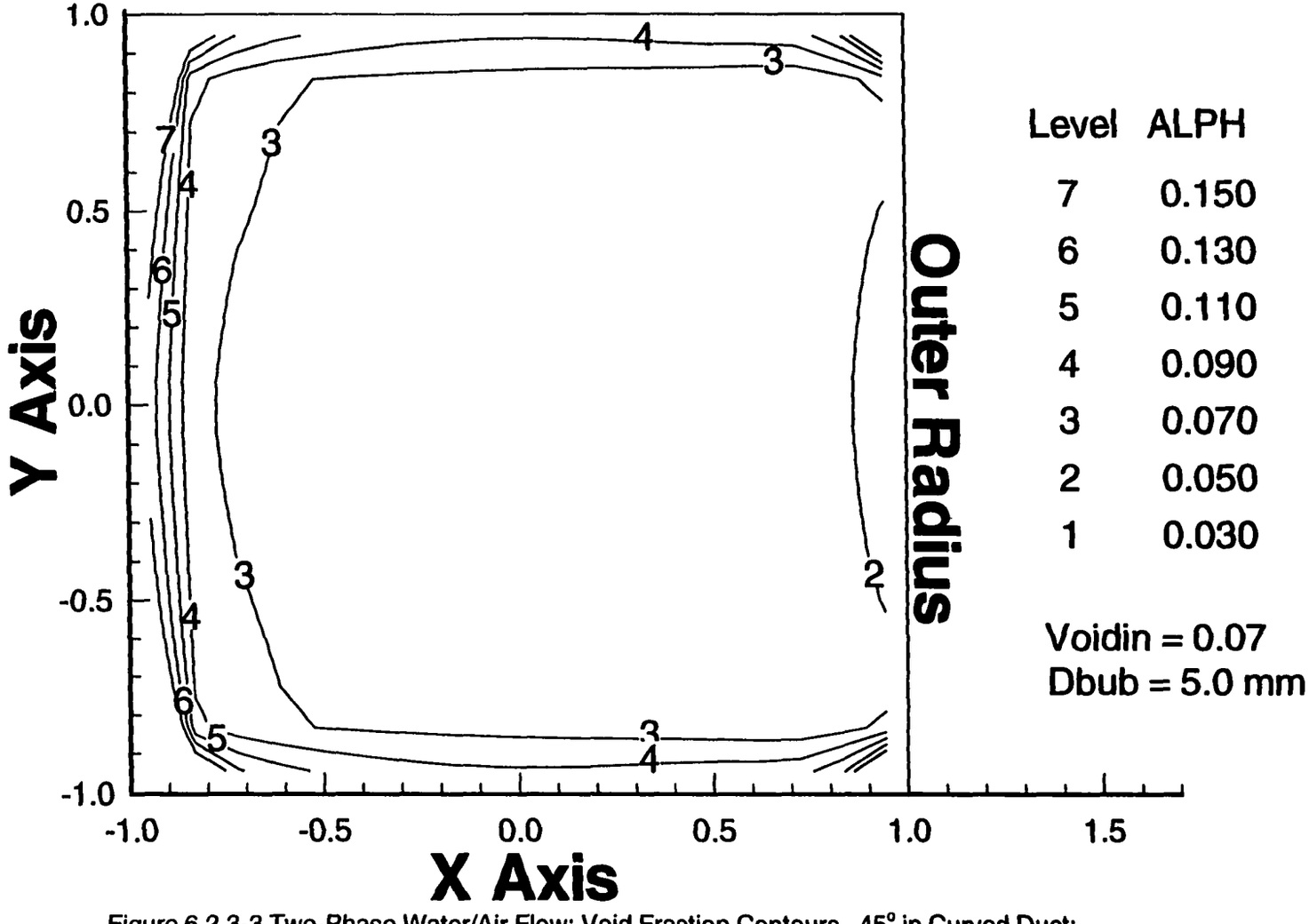

Figure 6.2.3-3 Two-Phase Water/Air Flow; Void Fraction Contours 45° in Curved Duct; Re=40,000; d_{bub} = 5 mm; D_H = 25.4 mm

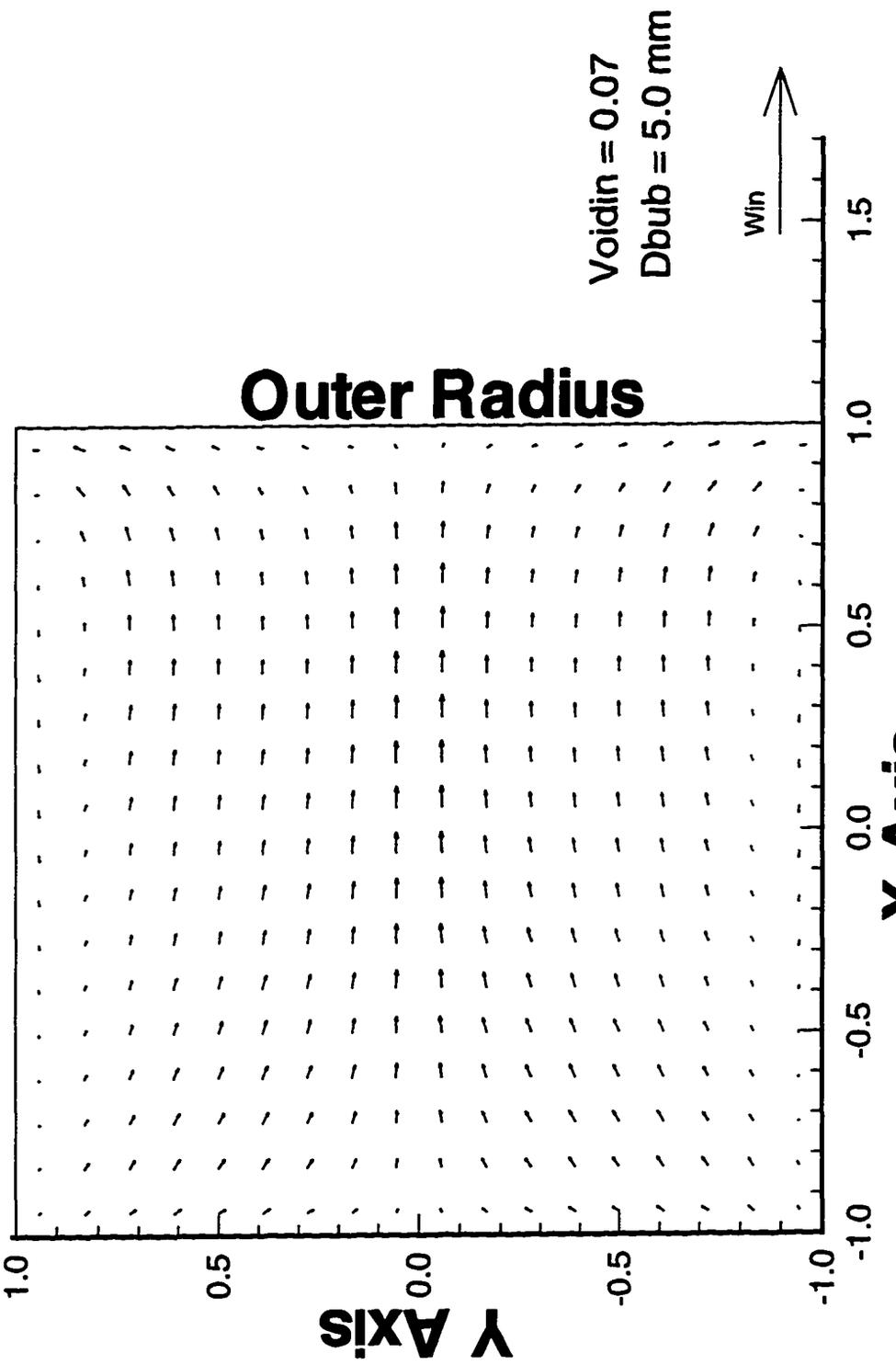

Figure 6.2.3-4 Two-Phase Water/Air Flow; Water Velocity Vectors at 90° in Curved Duct; Re=40,000; d_{bub} = 5 mm; D_H = 25.4 mm

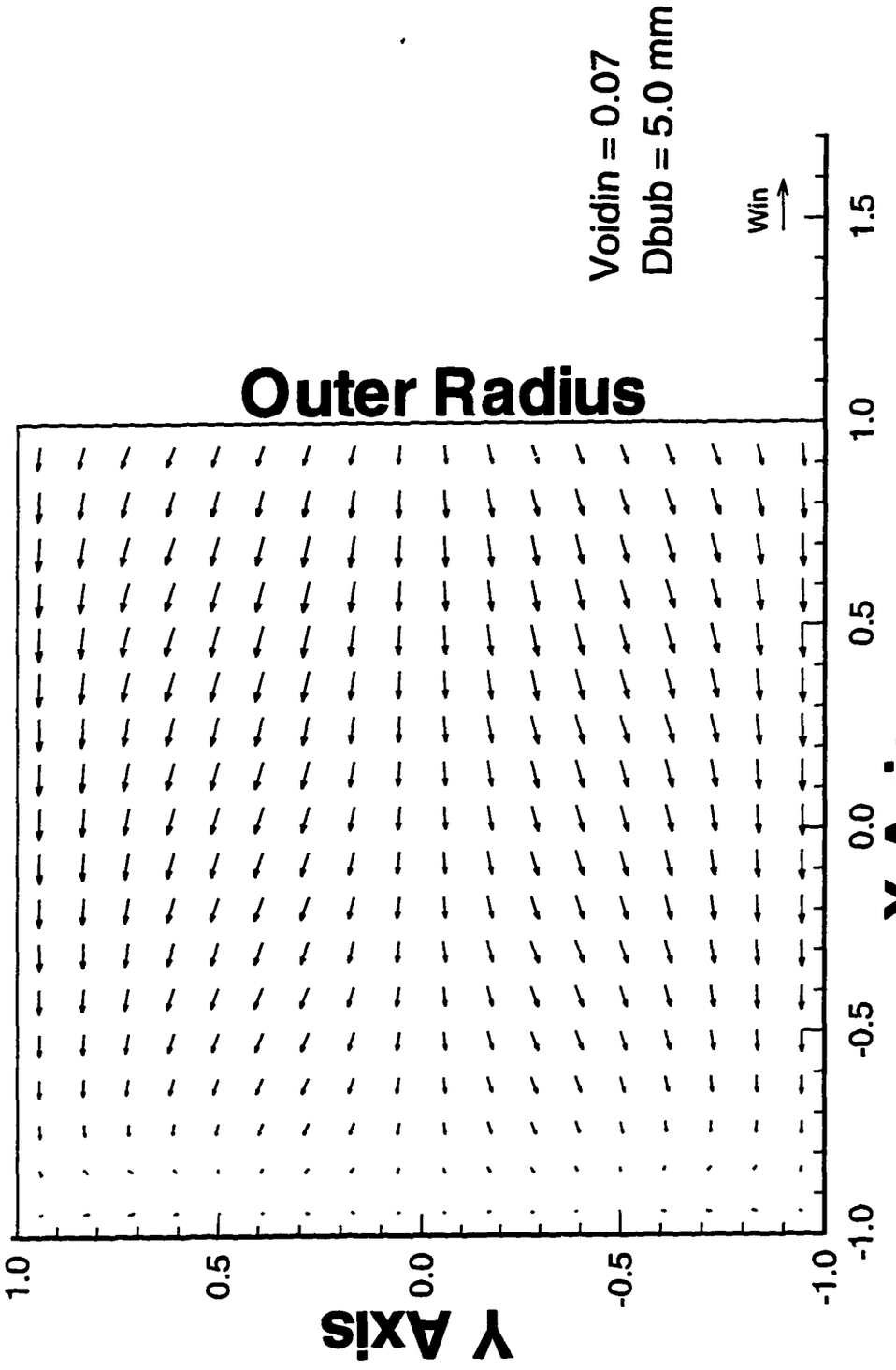

Figure 6.2.3-5 Two-Phase Water/Air Flow;Air Velocity Vectors at 90° in Curved Duct; Re=40,000; d_{bub} = 5 mm; D_H = 25.4 mm

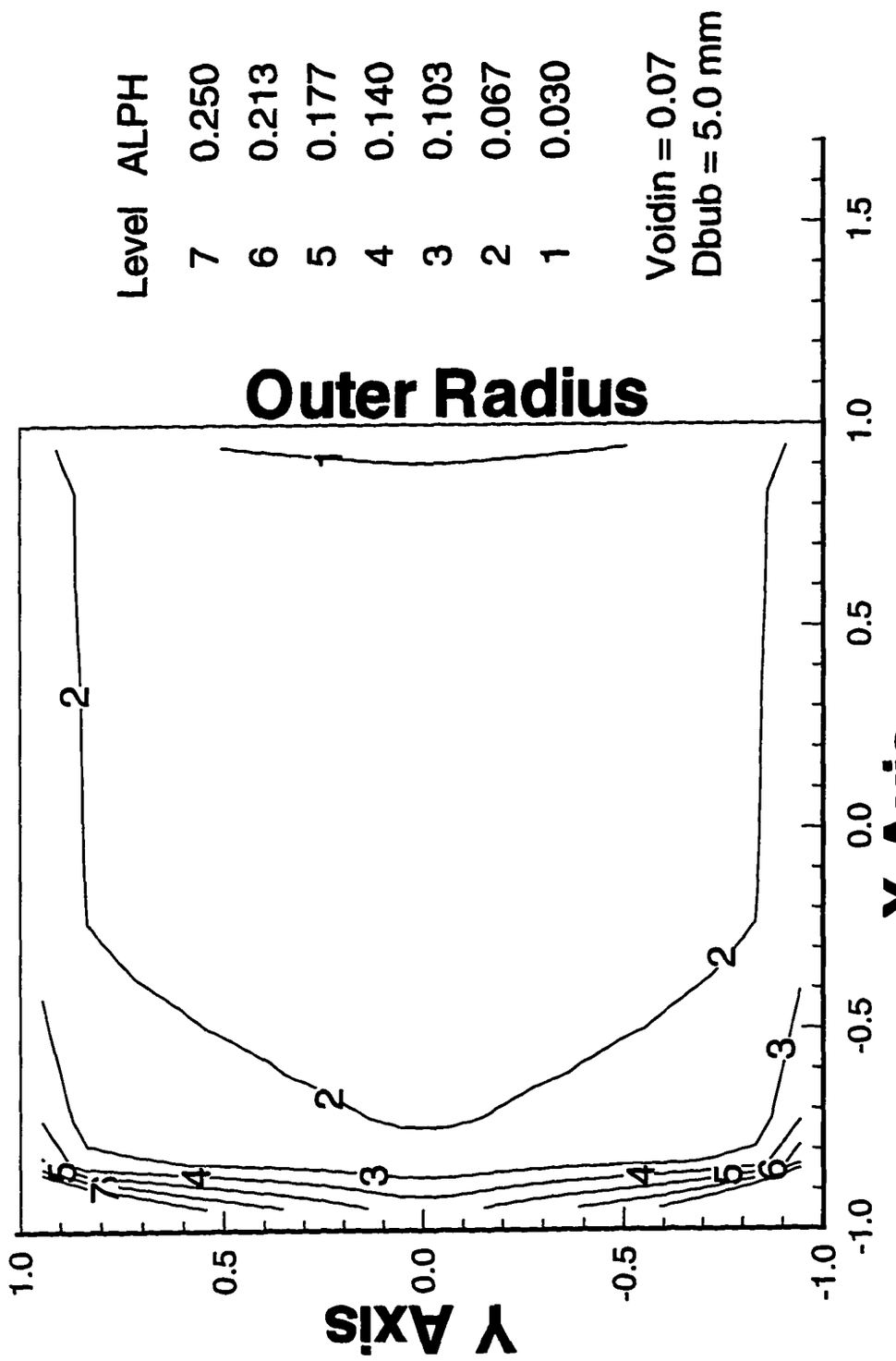

Figure 6.2.3-6 Two-Phase Water/Air Flow; Void Fraction Contours 90° in Curved Duct; Re=40,000; d_{bub} = 5 mm; D_H = 25.4 mm

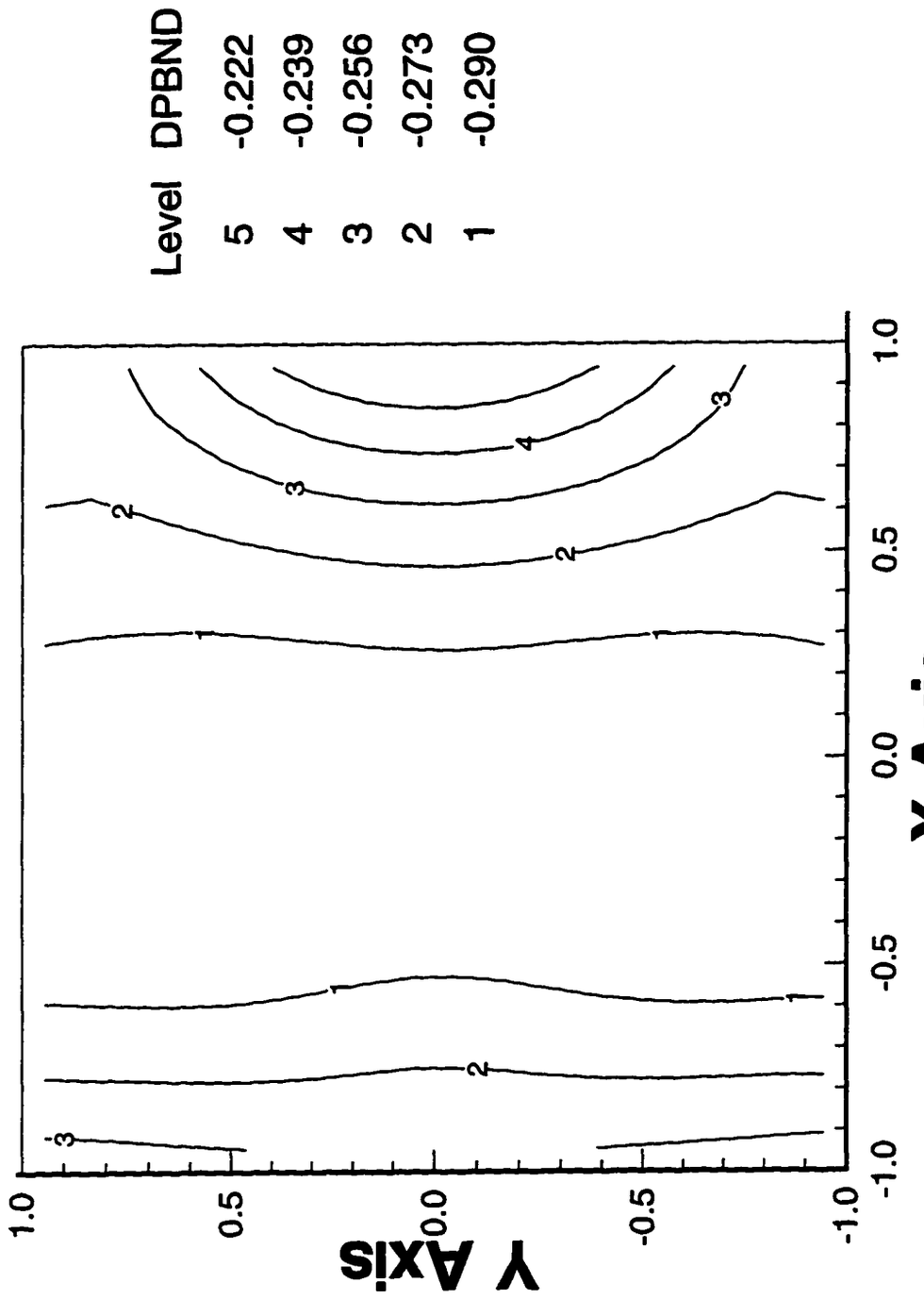

Figure 6.2.3-7 Static Pressure Contours at 30° in Curved Duct; Water/Air; Re=40,000; Voidin=0.07;D_b=5 mm

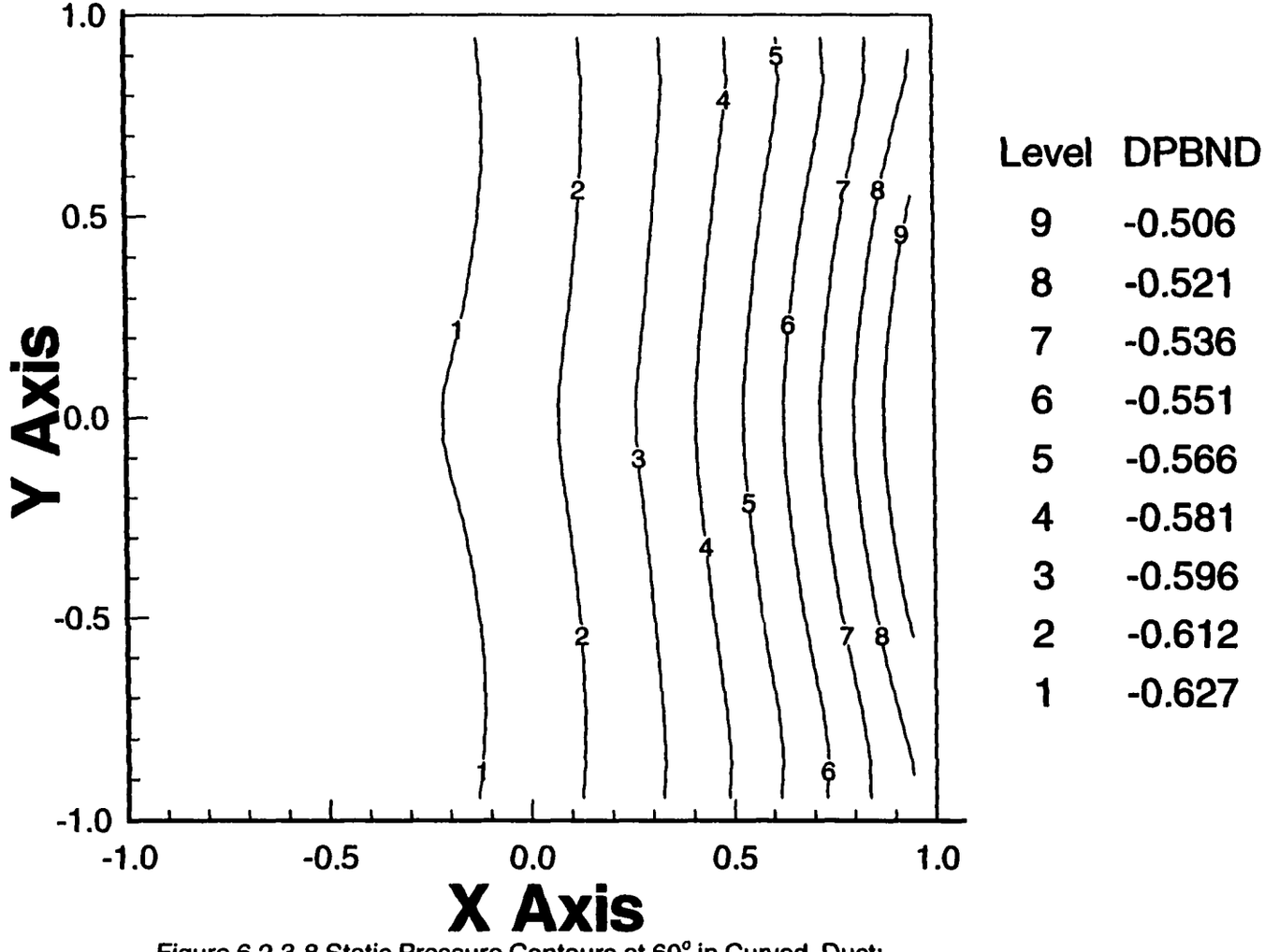

Figure 6.2.3-8 Static Pressure Contours at 60° in Curved Duct; Water/Air; Re=40,000; Voidin=0.07;D_b=5 mm

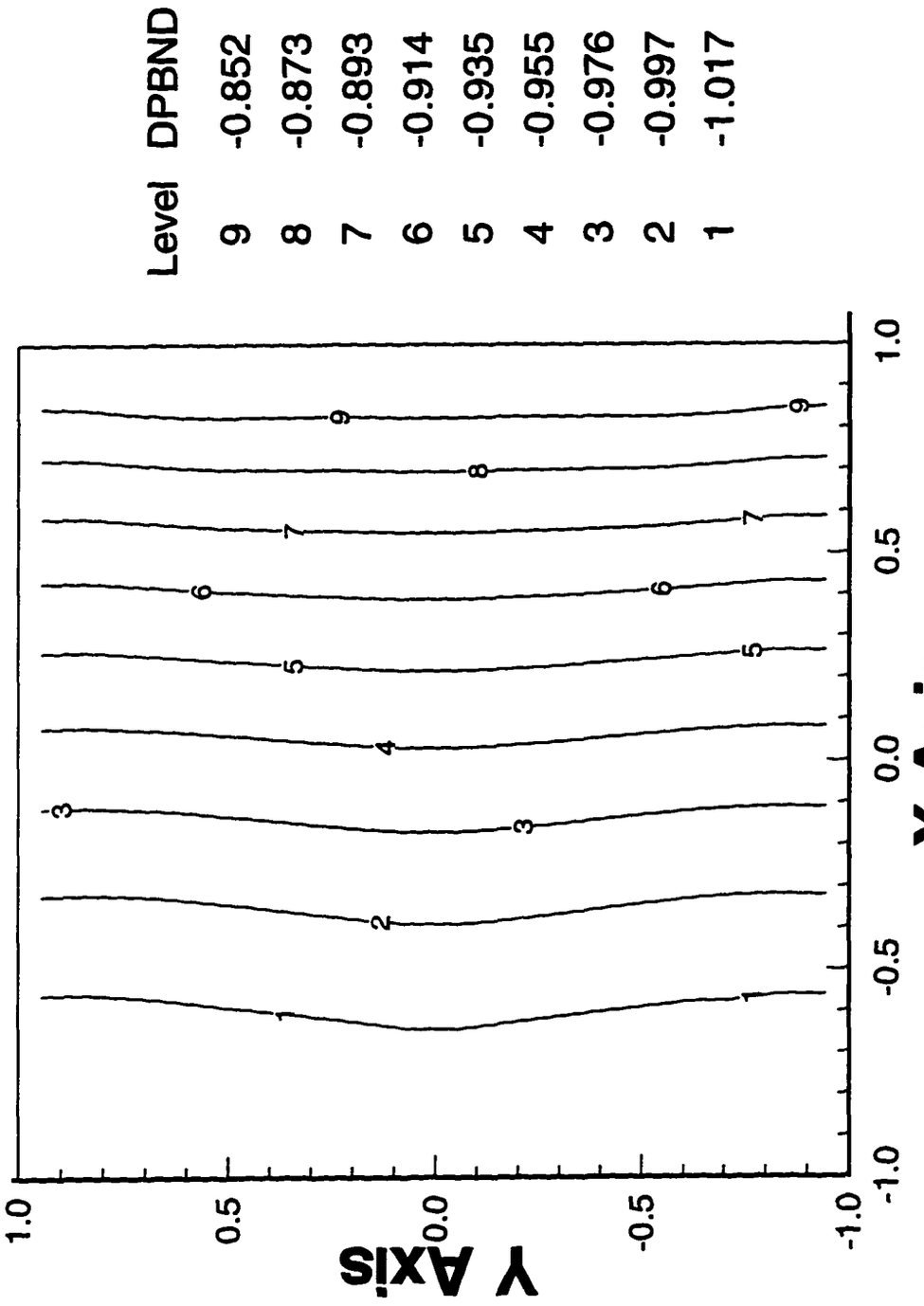

Figure 6.2.3-9 Static Pressure Contours at 90° in Curved Duct; Water/Air; Re=40,000; Voidin=0.07;D_b=5 mm

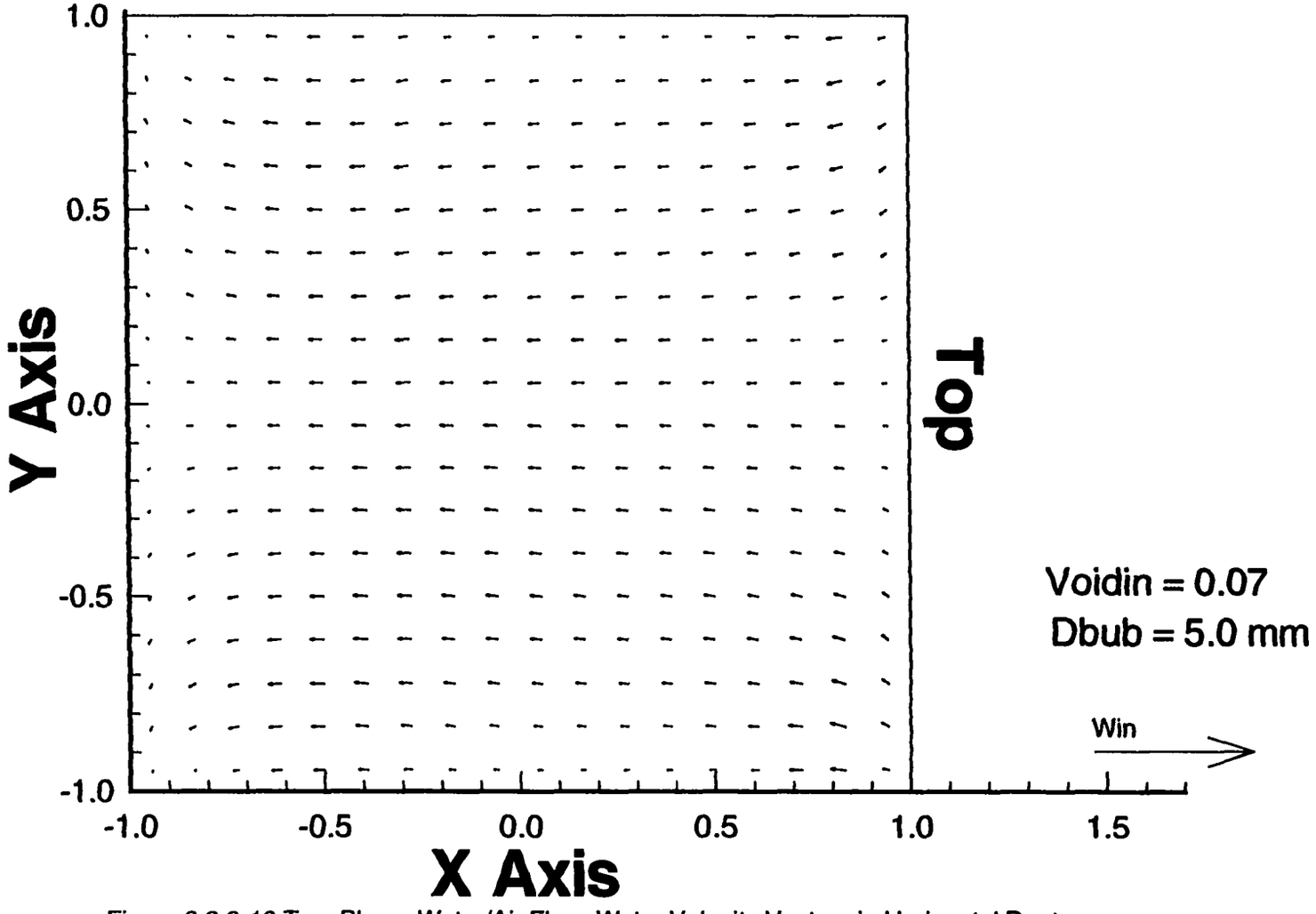

Figure 6.2.3-10 Two-Phase Water/Air Flow; Water Velocity Vectors in Horizontal Duct; Z/D_H=22.5; Re=40,000; d_{bub} = 5 mm; D_H = 25.4 mm

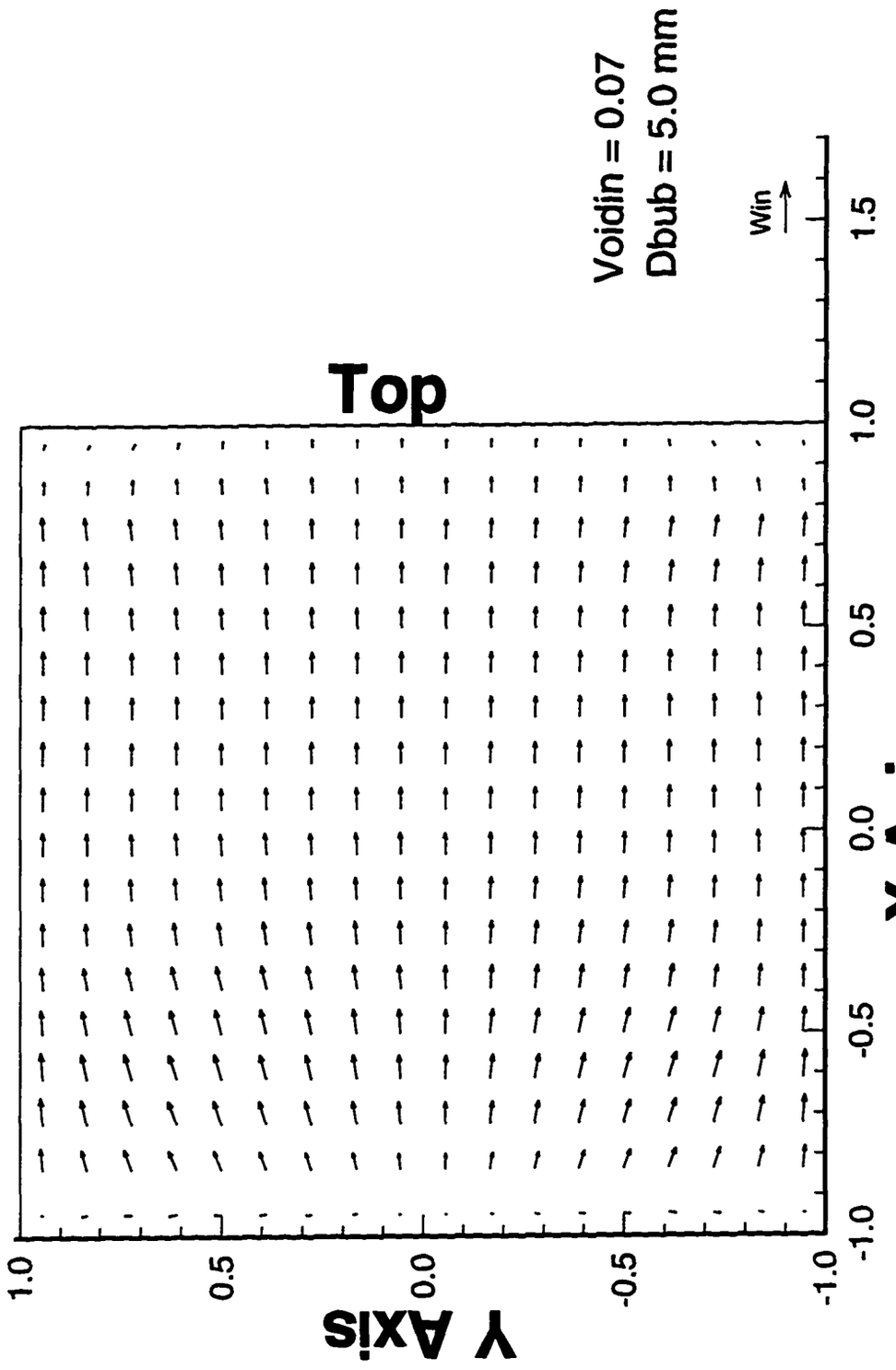

Figure 6.2.3-11 Two-Phase Water/Air Flow;Air Velocity Vectors in Horizontal Duct ; Z/D_h=22.5; Re=40,000; d_{bub} = 5 mm; D_H = 25.4 mm

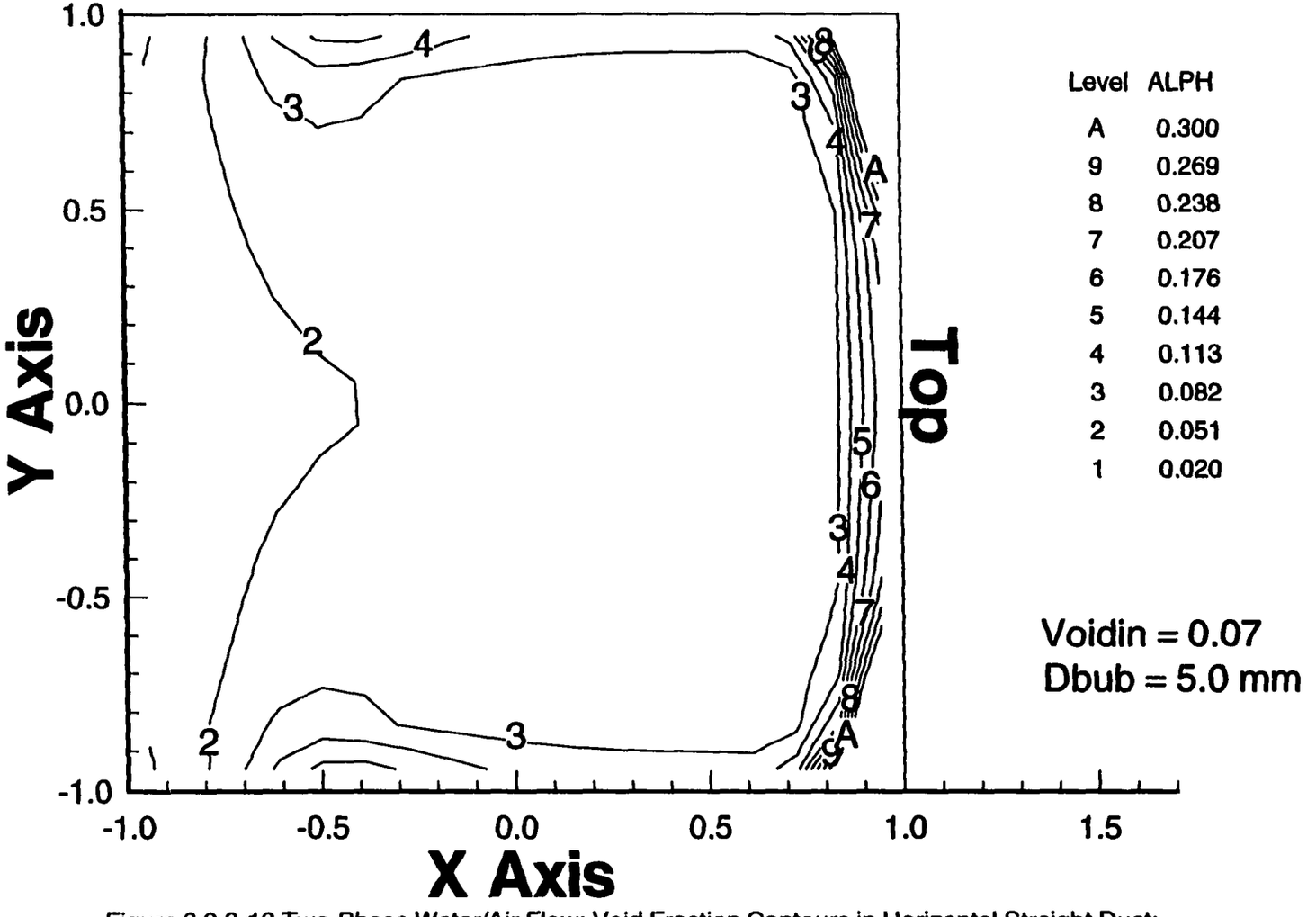

Figure 6.2.3-12 Two-Phase Water/Air Flow; Void Fraction Contours in Horizontal Straight Duct; Z/D_h=22.5 ; Re=40,000; d_{bub} = 5 mm; D_H = 25.4 mm

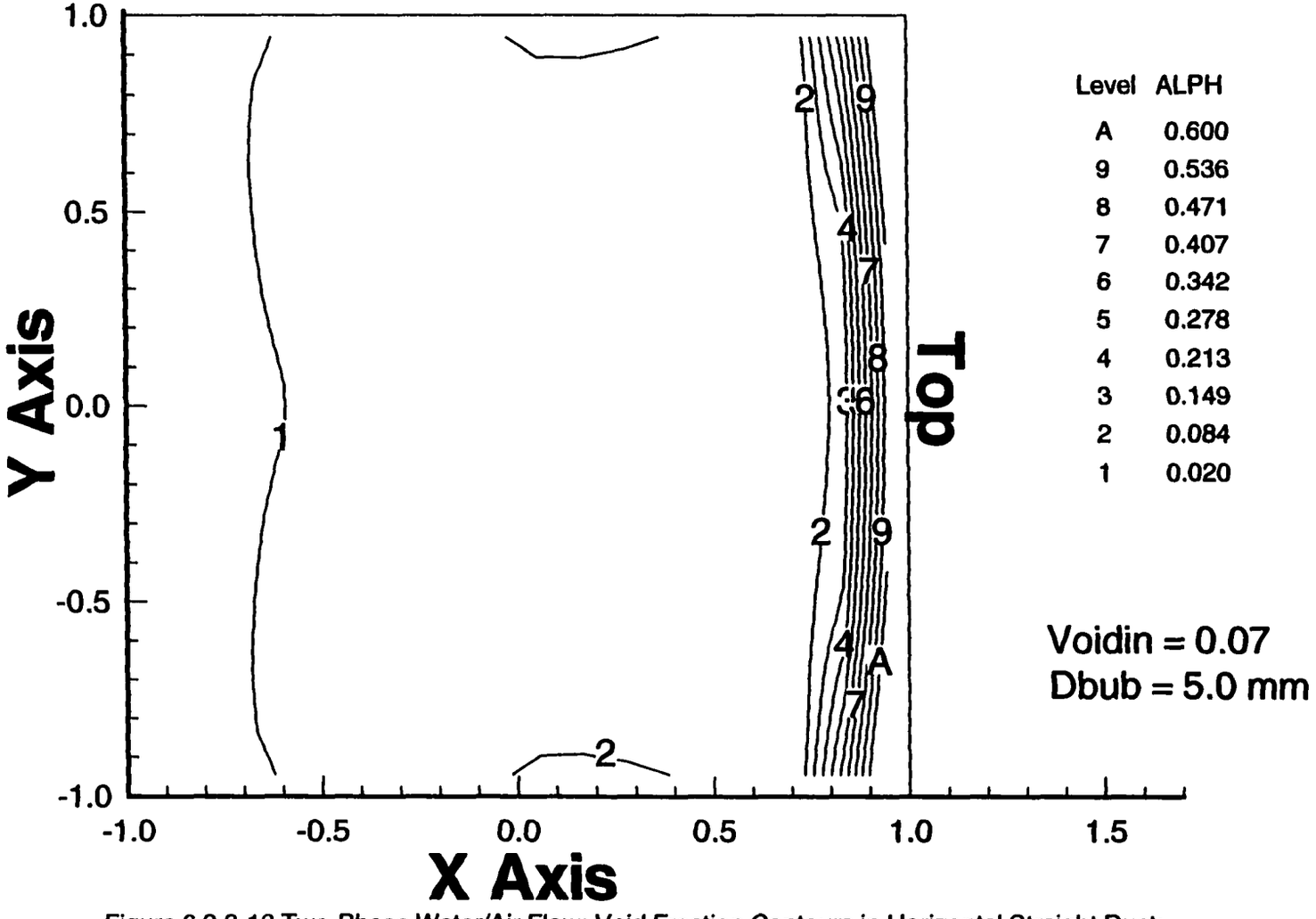

Figure 6.2.3-13 Two-Phase Water/Air Flow; Void Fraction Contours in Horizontal Straight Duct; Z/D_h=45 ; Re=40,000; d_{bub} = 5 mm; D_H = 25.4 mm

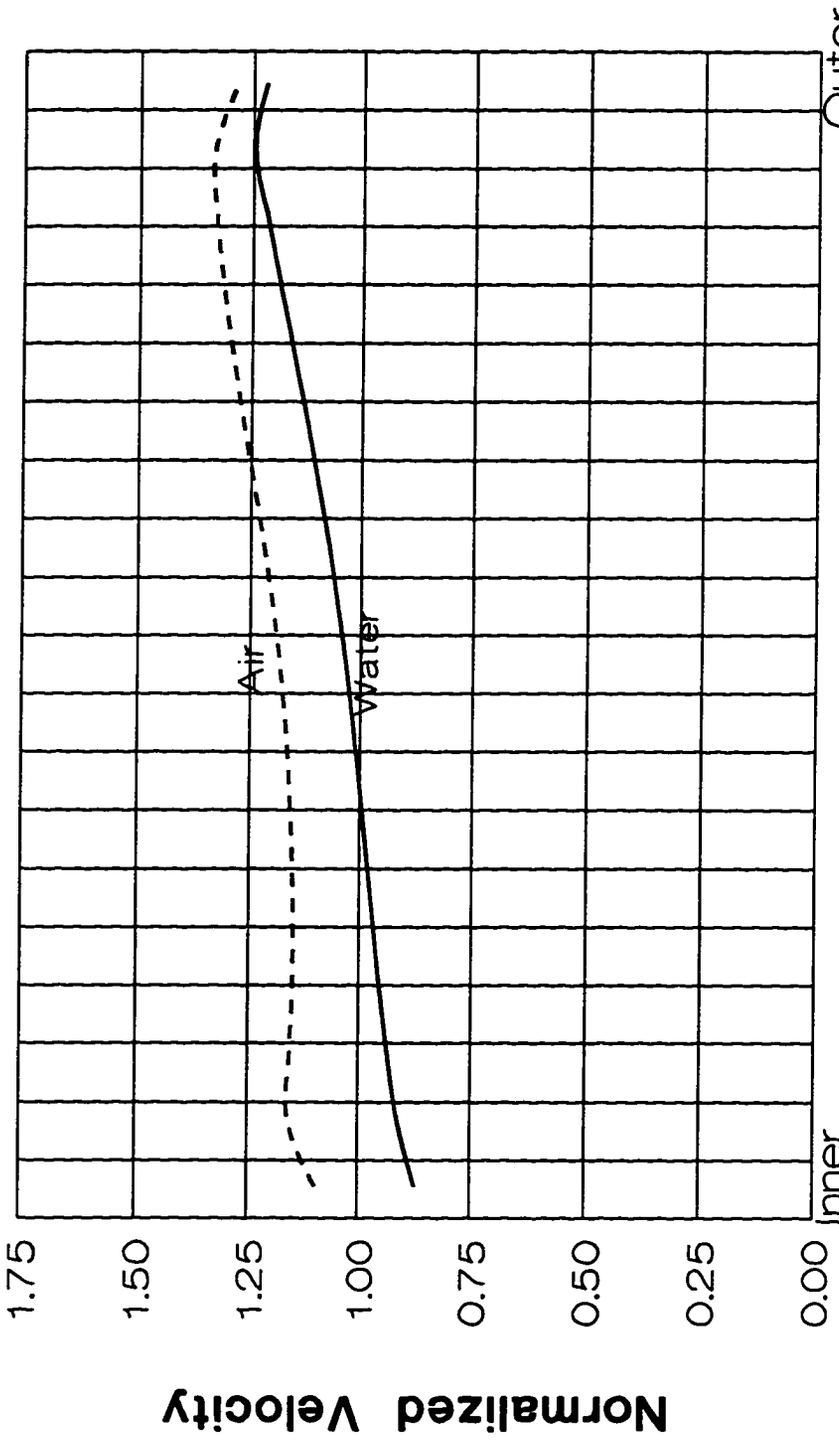

Figure 6.2.3-14 Two-Phase Water/Air Flow; Centerline Longitudinal Velocity Distributions; at 45° in Bend; Re=40,000; d_{bub} = 5 mm; D_H = 25.4 mm

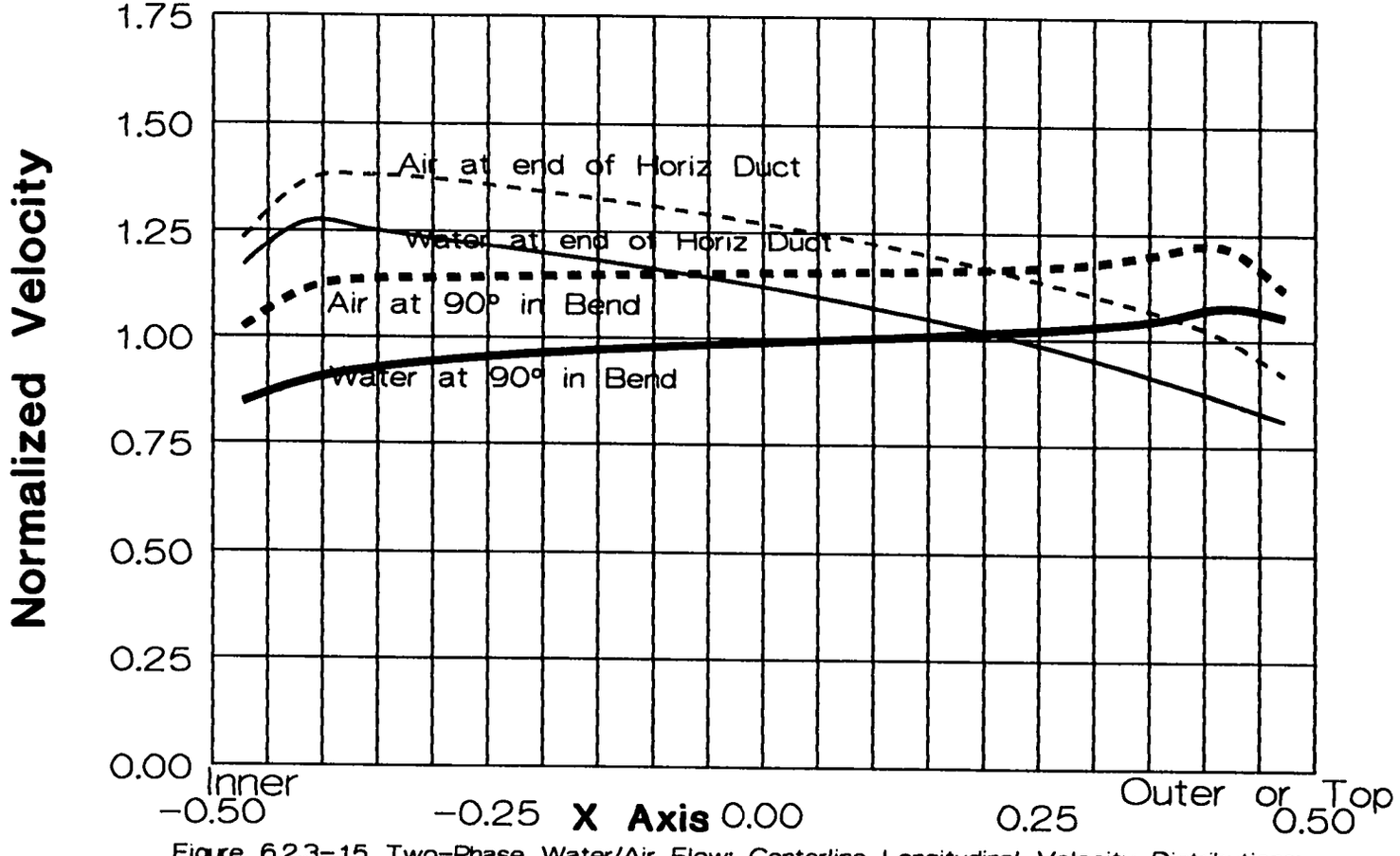

Figure 6.2.3-15 Two-Phase Water/Air Flow; Centerline Longitudinal Velocity Distributions; at 90° in Bend and End of Horiz Duct (Z/D_H =22.5); Re=40,000; d_{sub} = 5 mm; D_H = 25.4 mm

Figure 6.2.3-16 Water Normalized Longitudinal Velocity; at end of Vertical Duct (Z/D_H=45);Two-Phase Water/Air Flow

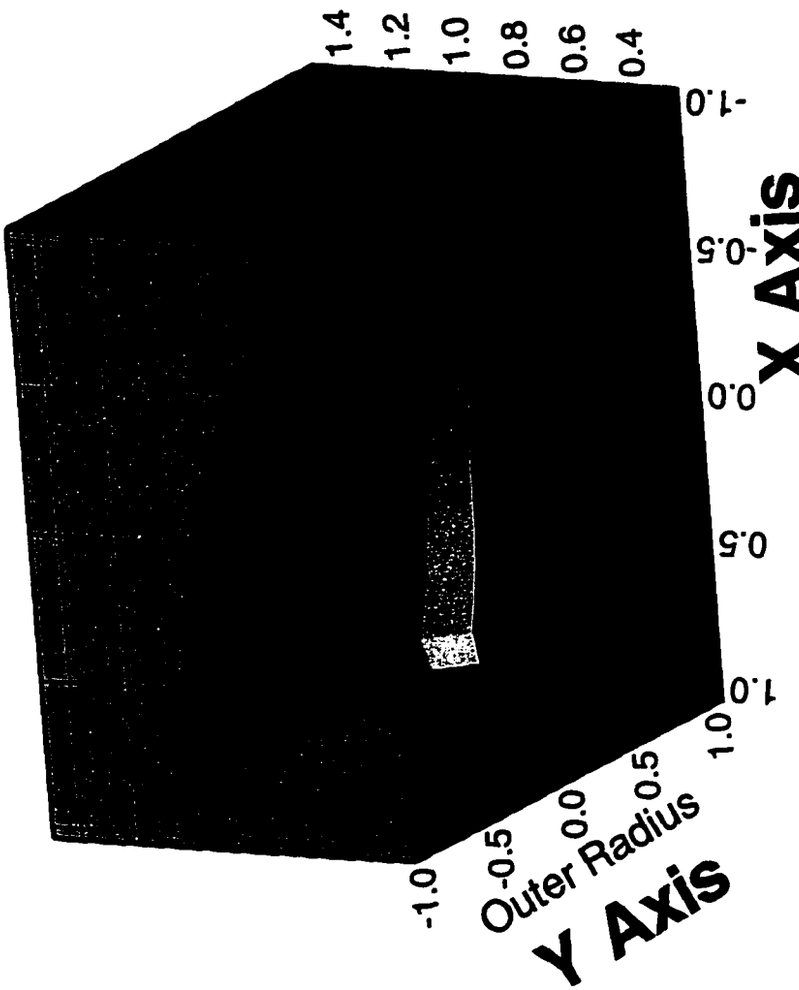

Figure 6.2.3-17 Water Normalized Longitudinal Velocity; at 45° in the Curved Duct; Two-Phase Water/Air Flow

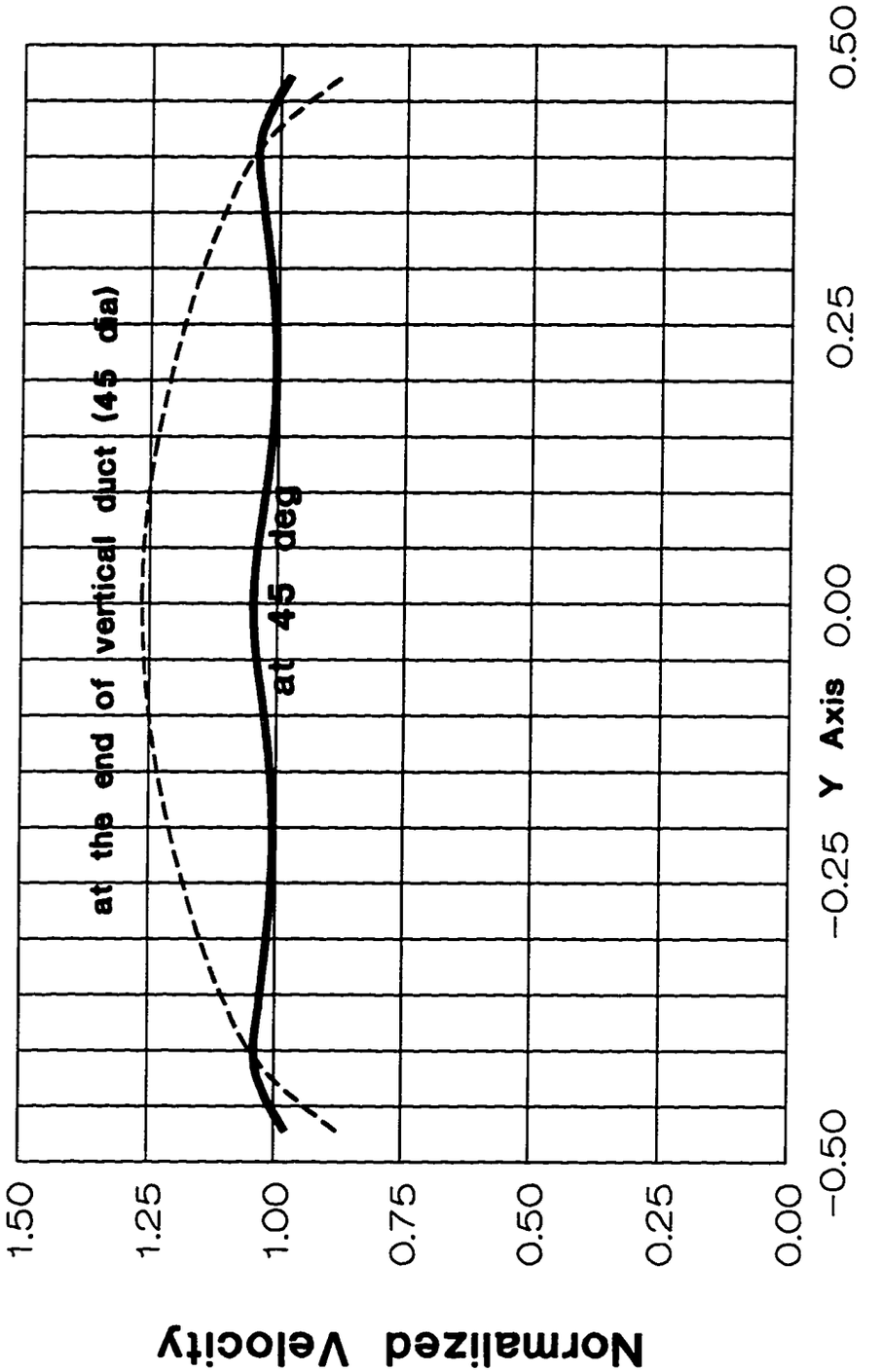

Figure 6.2.3-18 Longitudinal Velocity in Y Direction (X=Mid-Radius); at End of Vertical Duct & 45°; Re=40,000; Voidin=0.07; Db=5mm

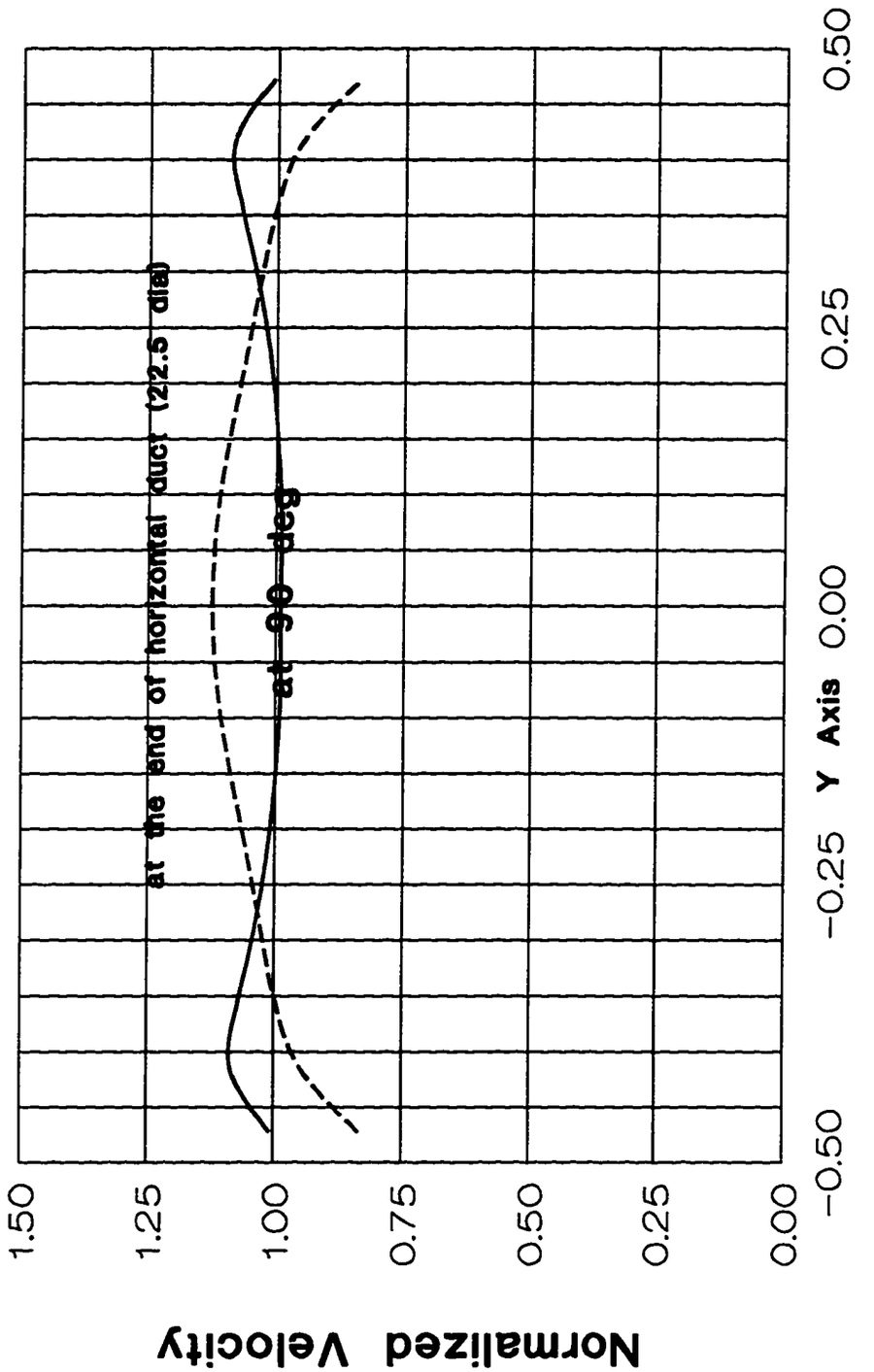

Figure 6.2.3-19 Longitudinal Velocity in Y Direction (X=Mid-Radius) at 90° & End of Horiz. Section; Re=40,000; Voidin=0.07; Db=5mm

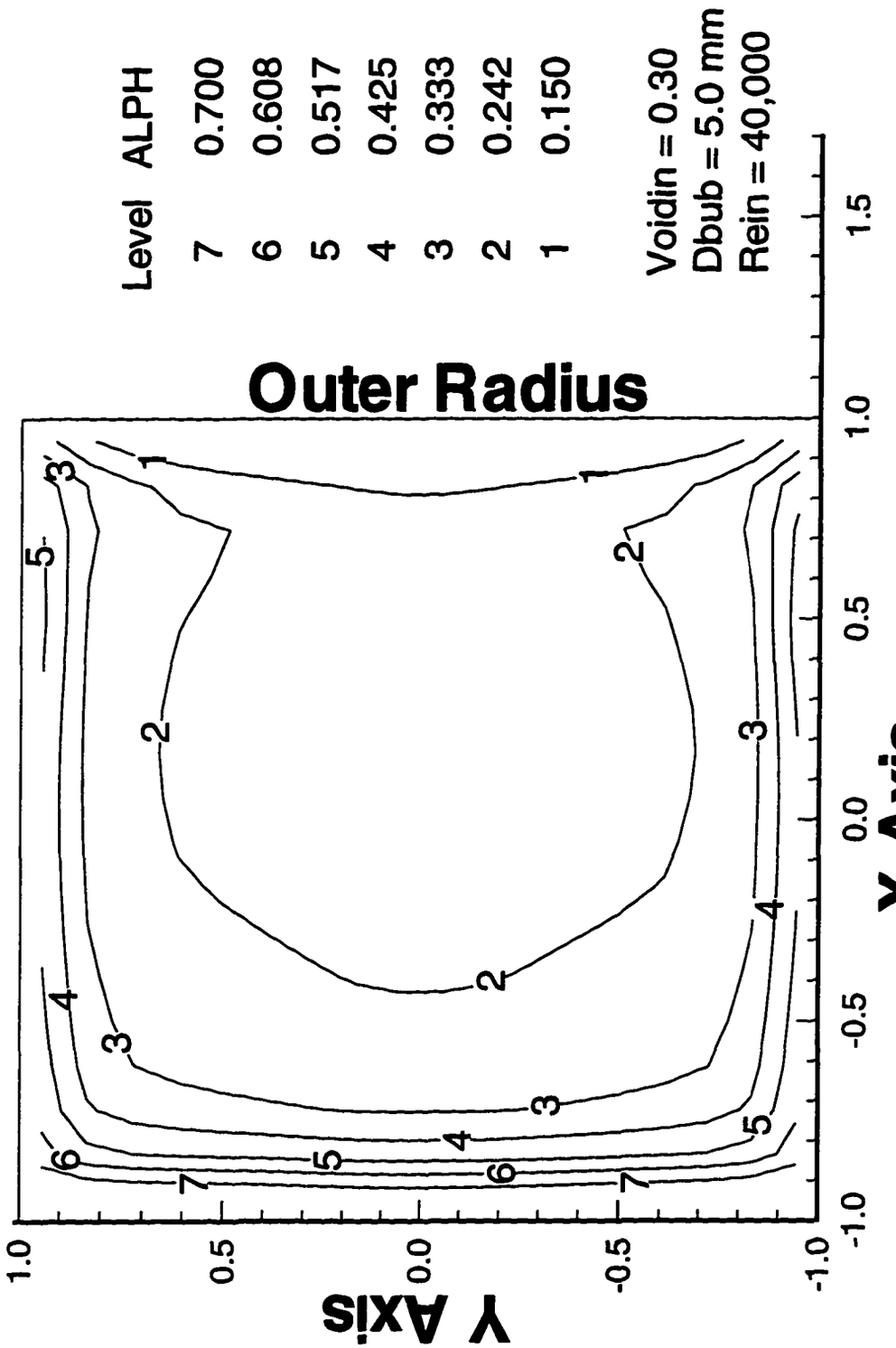

Figure 6.2.3-20 Two-Phase Water/Air Flow; Void Fraction Contours in Curved Duct at 90°; High Inlet Void Fraction (=0.3); Re=40,000; d_b=5mm; D_H=25.4 mm

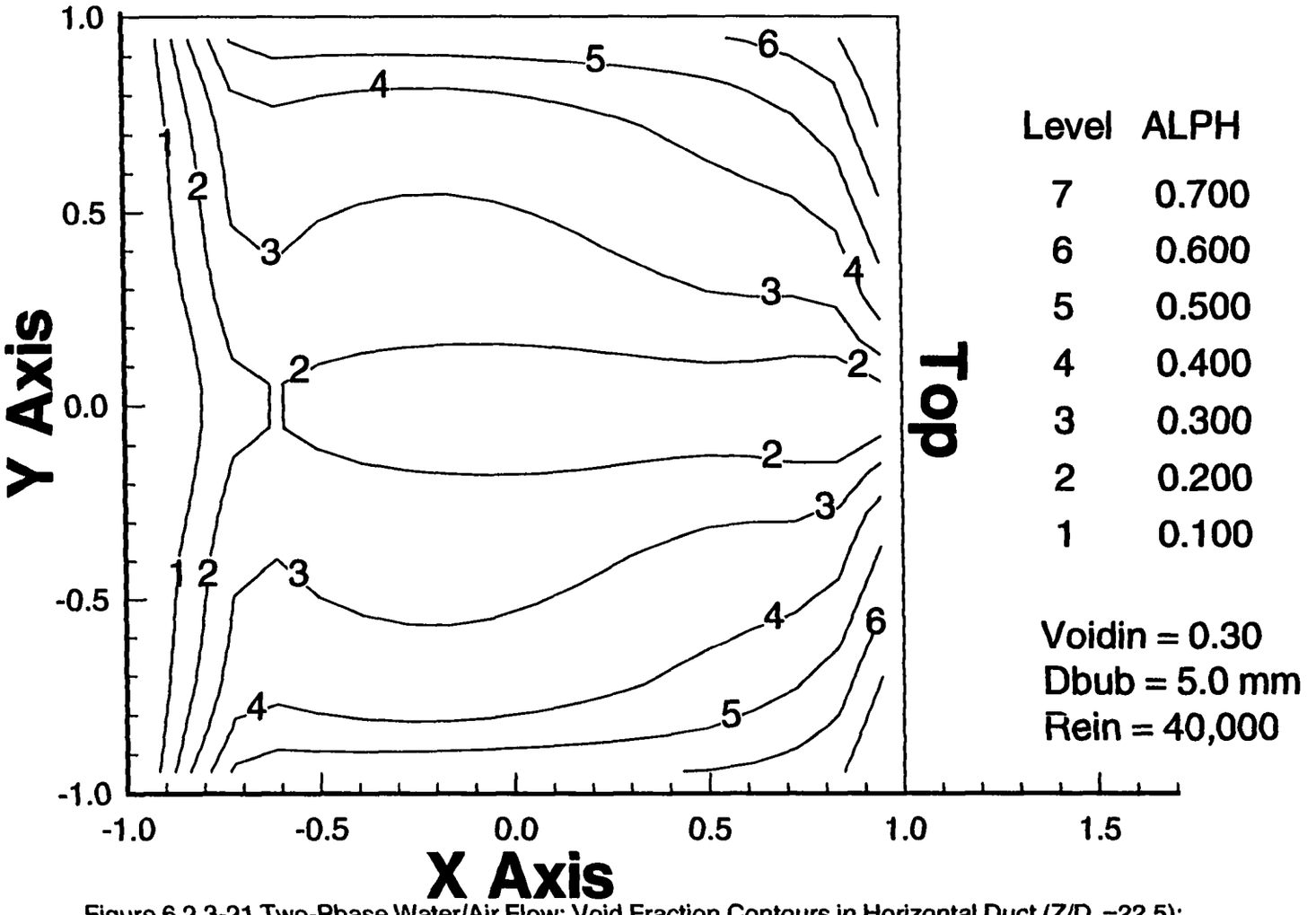

Figure 6.2.3-21 Two-Phase Water/Air Flow; Void Fraction Contours in Horizontal Duct (Z/D_H=22.5); High Inlet Void Fraction (=0.3); Re=40,000; d_b=5mm; D_H=25.4 mm

6.2.4 Two-Phase Flow in a Straight/Curved/Straight Duct with Small Bubbles

The results presented thus far for the simulation of the two-phase flow in straight/curved/straight duct setup have been with relatively large 5 mm bubbles (the side of the square cross section duct is 25.4 mm.). Results are presented here for 1 mm bubbles, much smaller than those used in the test loop. The purpose of these studies is to see if the present two-phase flow models (i.e., the constitutive equations used for the interfacial momentum exchange force and the void fraction algorithm) can accurately predict the expected flow patterns. These bubbles can almost be thought of as flow tracers since they are expected to follow the continuous phase much more faithfully than the large 5 mm bubbles did.

The void fraction distributions (for the 1 mm bubbles) throughout the duct are shown in Figures 6.2.4-1 through 6.2.4-3. The first figure shows the void fraction distribution at the end of the vertical straight section. The distribution is essentially a uniform 0.07 across the duct. The peaking at the walls does not occur for these very small bubbles. Due to larger surface area for the interphasial interactions, the drag forces overwhelm the other forces such as the Saffman force.

Figure 6.2.4-2 shows that the void distribution at 45° in the bend is essentially uniform and equal to the inlet average of 0.07. This indicates that the bubbles are following the continuous phase (in stark contrast to the situation seen in the previous section for the large (5 mm) diameter bubbles where at a similar location there was a strong gradient in void fraction across the duct in the radial (x) direction.

The void distribution at the end of the 90° bend and in the horizontal section also show a nearly uniform distribution of bubbles at a value close to the inlet void fraction(Figure 6.2.4-3).

Again, the stratification which was clearly visible for the large diameter bubbles does not occur. The small bubbles follow the continuous phase flow and do not seem to be controlled by body forces such as gravity and centrifugal forces.

The present numerical procedure predicts all the qualitative features of void fraction distributions seen in the test loop for the 3 to 5 mm bubble diameter used there (i.e., large bubbles). The small (1 mm) diameter bubbles are predicted to follow the continuous phase faithfully without being affected by body forces.

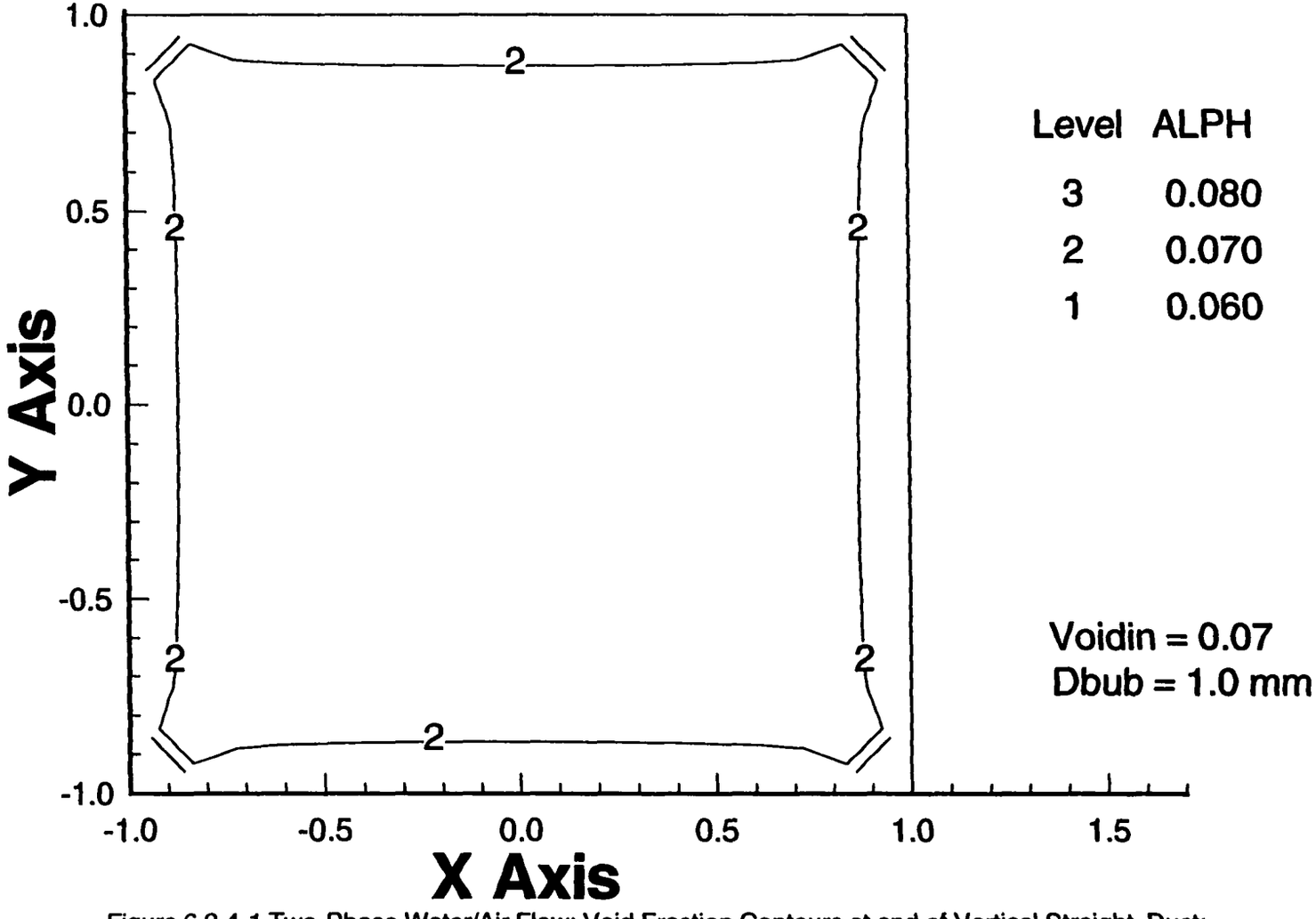

Figure 6.2.4-1 Two-Phase Water/Air Flow; Void Fraction Contours at end of Vertical Straight Duct; Small Bubble Diameter; Z/D_H=45;Re=40,000; d_{bub} = 1 mm; D_H = 25.4 mm

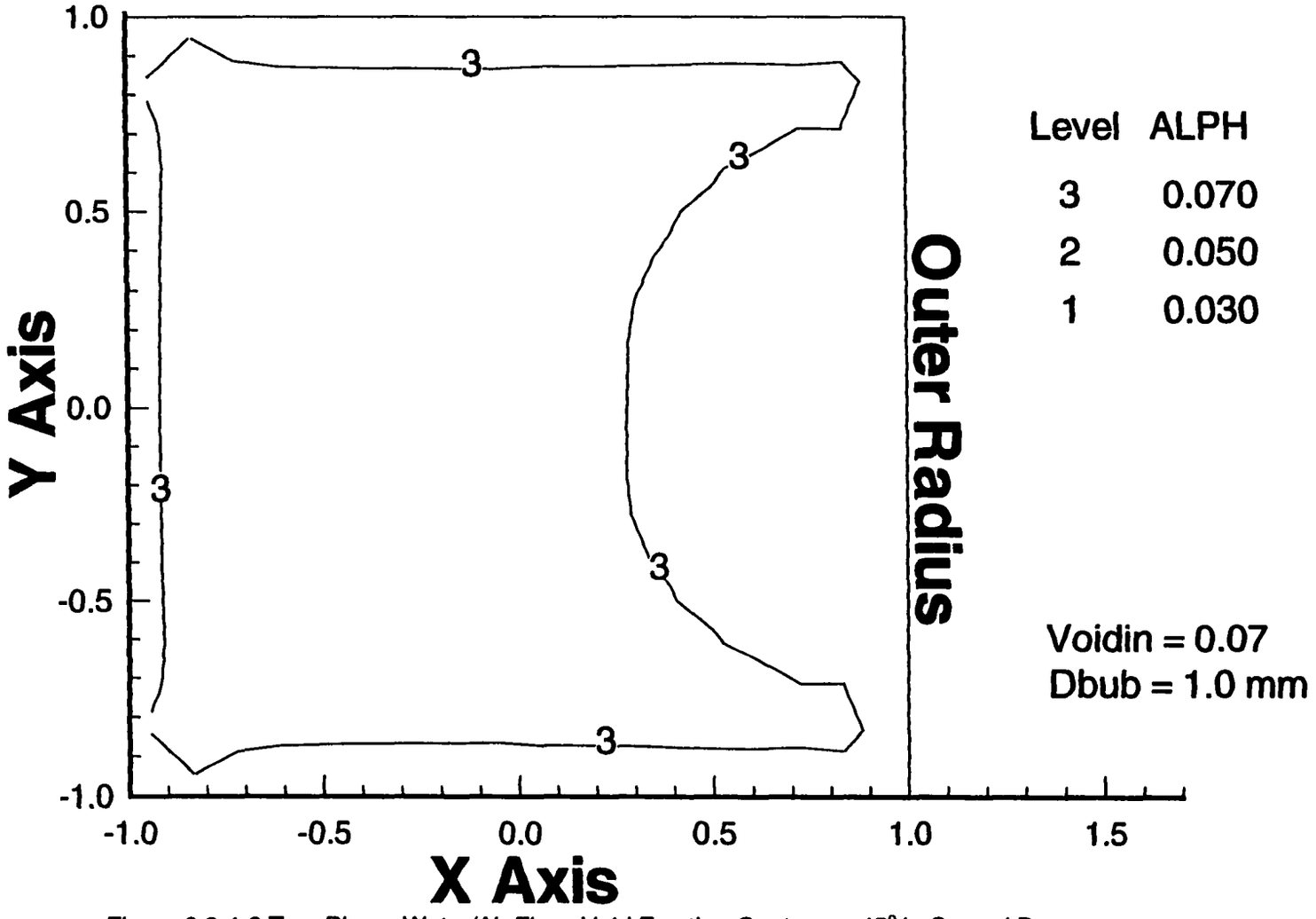

Figure 6.2.4-2 Two-Phase Water/Air Flow; Void Fraction Contours 45° in Curved Duct; Small Bubble Diameter; Re=40,000; d_{bub} = 1 mm; D_H = 25.4 mm

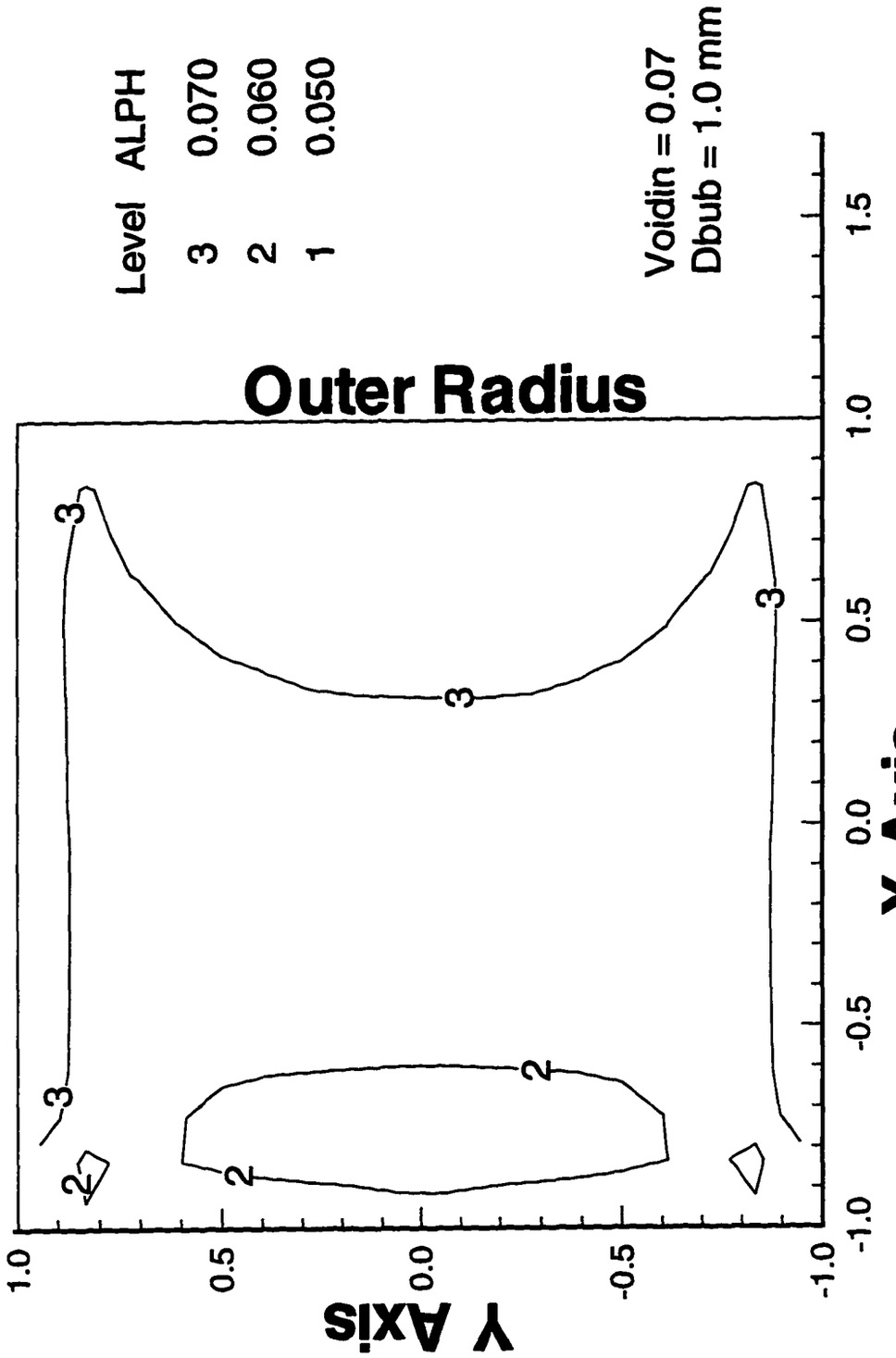

Figure 6.2.4-3 Two-Phase Water/Air Flow; Void Fraction Contours 90° in Curved Duct; Small Bubble Diameter; Re=40,000; d_{bub} = 1 mm; D_H = 25.4 mm

6.2.5 Calculation of Bubbles Flow Rates Based on Void Fraction Distributions in the Lateral Plane

The volumetric flow rate of the distributed phase through a flow area $\Delta x\ \Delta y$ centered at (i,j) is: $W_{2ij}\ \alpha_{2ij}\ \Delta x\ \Delta y$; and the volume of one bubble is $\frac{\pi d_b^3}{6}$; if Δx and Δy are chosen equal to the diameter of a bubble, d_b , then:

Number of bubbles per second passing

through a square with sides equal to d_b $= \frac{6W_2\alpha_2}{\pi d_b}$ [6.2.5-1]

The void fraction data presented above actually represents the passage of a discrete number of bubbles per second at any point in the flow field. The bubble rate is an important parameter in determining the enhancement of heat transfer from a surface. An extension of this work, as recommended in a later section, would compute two-phase heat transfer rates from first principles by the addition of the energy equation. However, an immediate approximation to the two-phase heat transfer rate is possible by applying empirical enhancement correlations with the presently computed bubble rates.

Contour plots of bubbles flowing per second at various stations throughout the straight and curved duct are given in Figures 6.2.5-1 through 6.2.5-4. These contours are proportional to the product of the void fraction and the bubble longitudinal velocity. They are thus somewhat similar to the void fraction contours. However, some of the trends seen in void fraction are

diminished or flattened especially where high void fractions occur in areas that have low velocity. This is the case for the contours at the end of the long straight vertical duct. For fully developed flow in a straight duct peak void fractions occur on the perimeter, but so do the lowest longitudinal velocities. Thus the contours of bubbles per second do not show a significant peaking at the perimeter (see Figure 6.2.5-1) and bubbles passing the plane per second lie in the range of 25 to 30.

The contours at 45° (Figure 6.2.5-2) show a peak in bubble count at the inner diameter, similar to the void fraction contours. The bubble rate is predicted to be 30 along the outer wall and as high as 50 along the inner wall. The bubble rate predicted at the end of the 90° bend is similar to that occurring half way through the bend (Figure 6.2.5-3). Bubbles per second range from 30 on the outer bend to 55 on the inner bend.

Flow through the horizontal duct at 22.5 hydraulic downstream of the bend results in highly stratified water/air flow. The bottom eighty percent of the cross sectional area has a bubble rate of 30 per second (Figure 6.2.5-4). The rate increases dramatically from there to the top wall, where a peak rate of 200 bubbles/second is predicted.

This section has presented contour plots showing the bubble rate, expressed as bubbles per second, at various lateral planes throughout the straight/curved/straight duct geometry. These contour plots, while being similar to the void fraction contour plots, describe the movement of the distributed phase as the main flow traverses the entire test rig in a more straight-forward and physical manner than the concept of the void fraction is able to do. However, the bubble rate does tend to flatten gradients that exist in the void fraction whenever a high void fraction location coincides with low axial velocities.

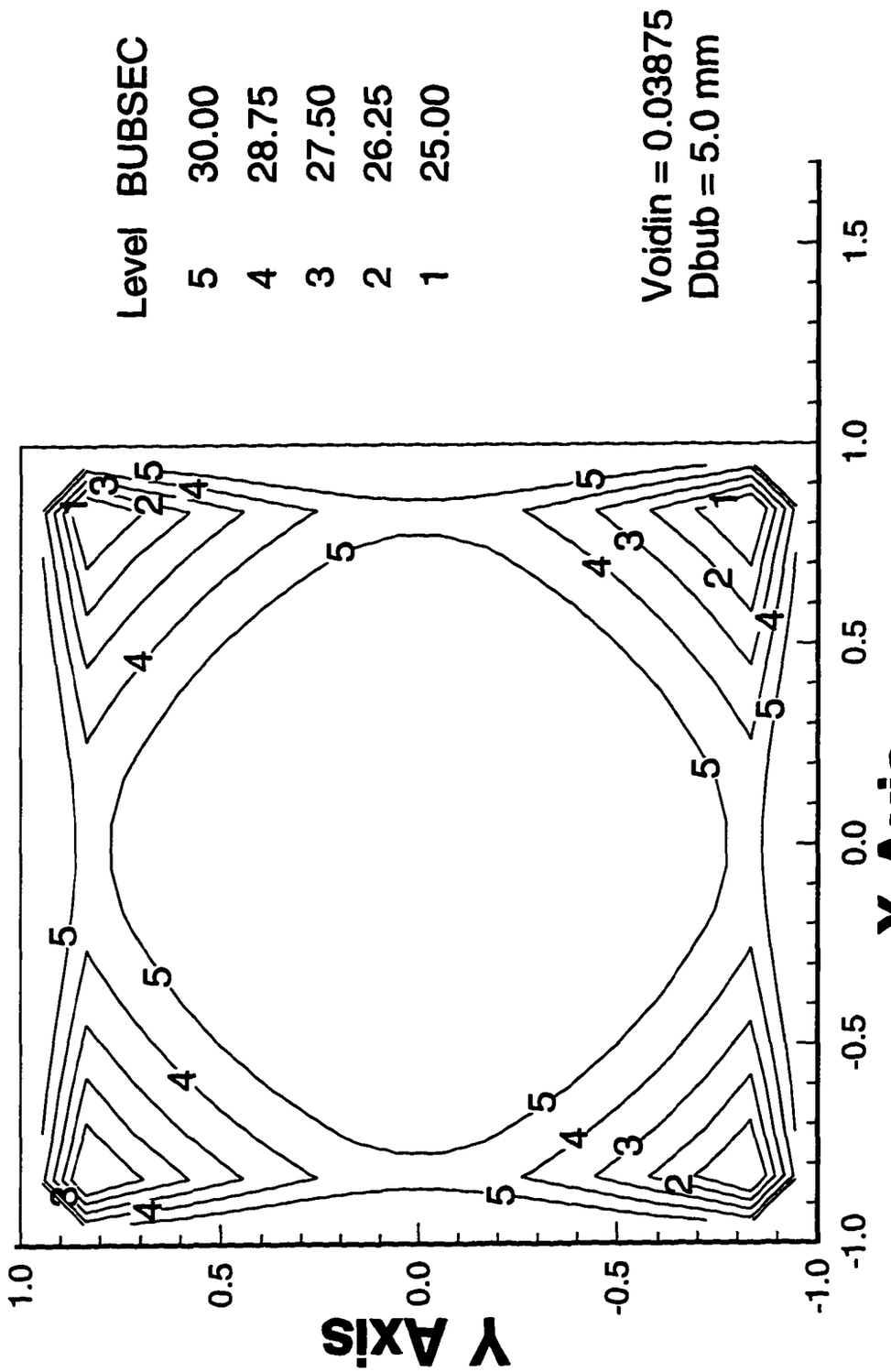

Figure 6.2.5-1 Two-Phase Water/Air Flow; Bubbles/Sec at End of Vertical Duct(Z/D_H=45); Re=40,000; d_{bub} = 5 mm; D_H = 25.4 mm

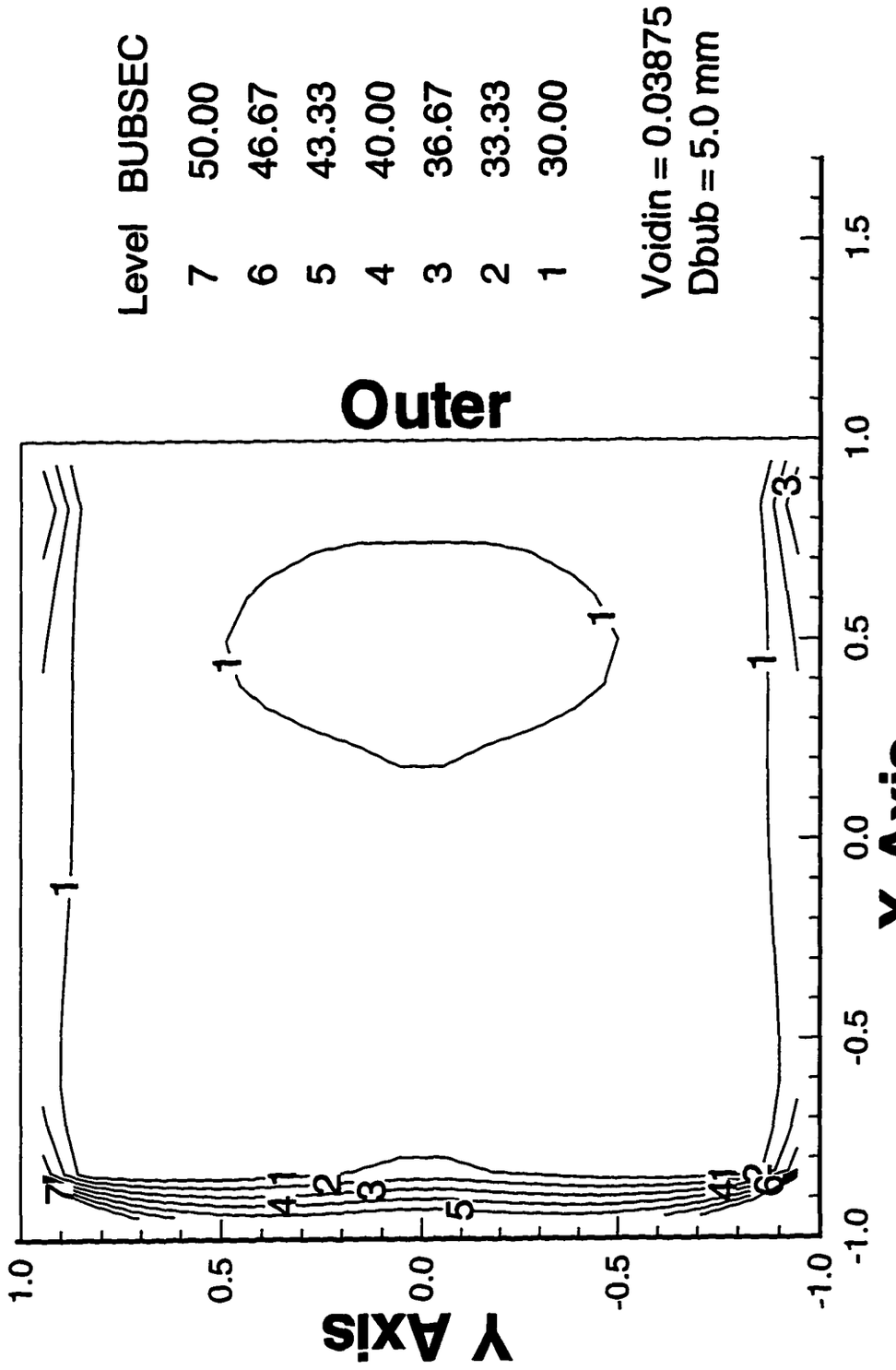

Figure 6.2.5-2 Two-Phase Water/Air Flow; Bubbles/Sec at 45° in Curved Duct; Re=40,000; d_{bub} = 5 mm; D_H = 25.4 mm

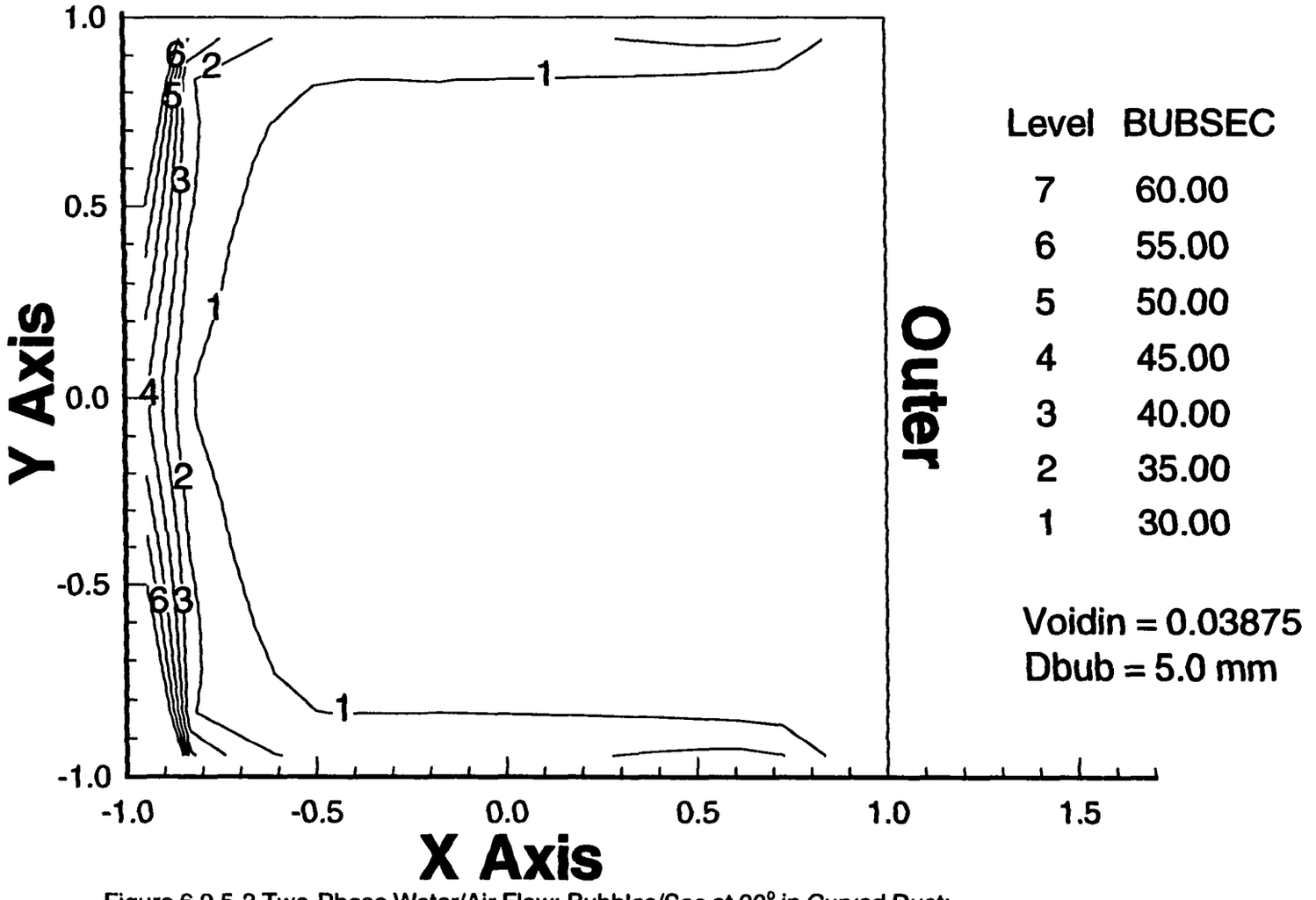

Figure 6.2.5-3 Two-Phase Water/Air Flow; Bubbles/Sec at 90° in Curved Duct; Re=40,000; d_{bub} = 5 mm; D_H = 25.4 mm

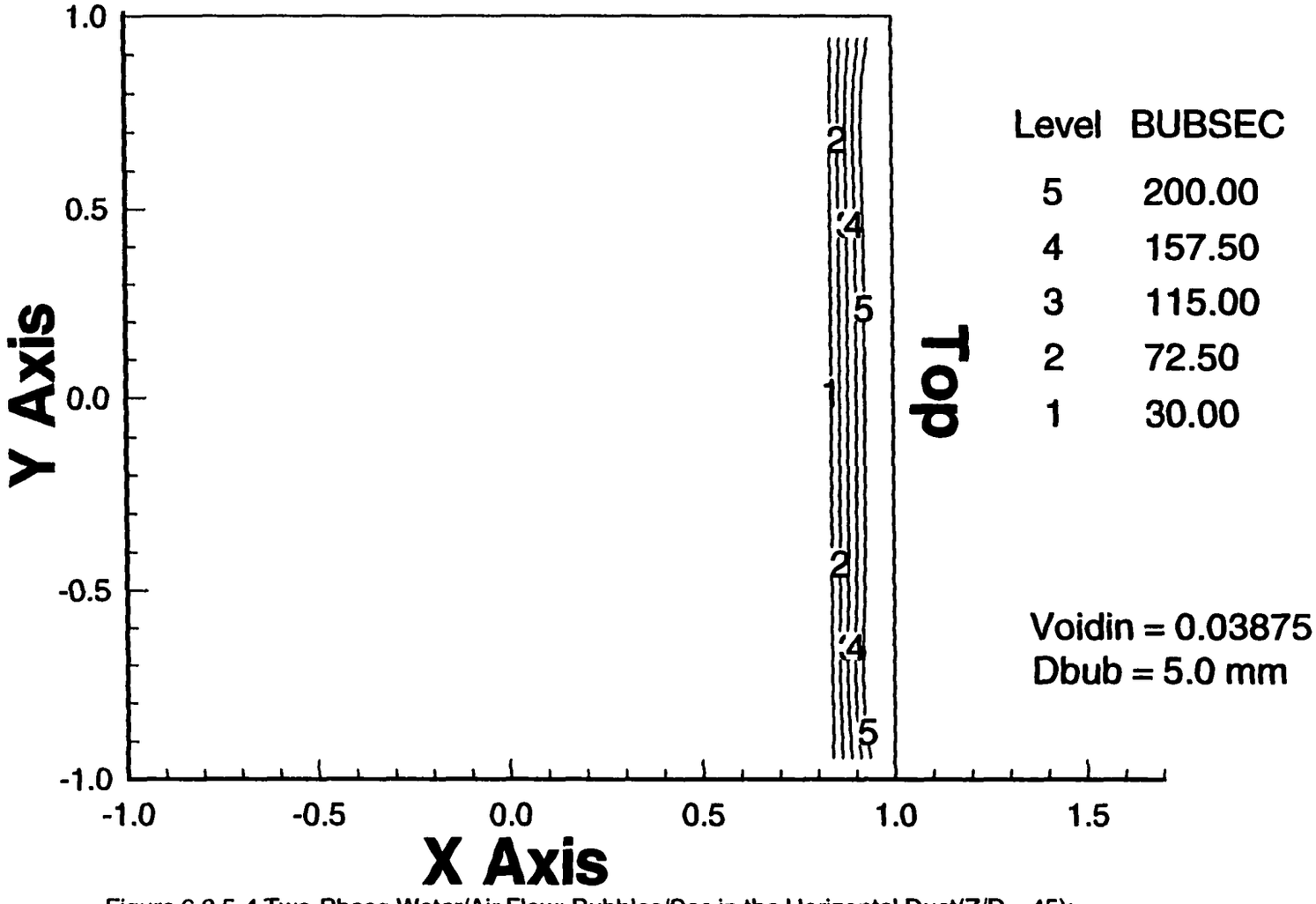

Figure 6.2.5-4 Two-Phase Water/Air Flow; Bubbles/Sec in the Horizontal Duct(Z/D_H=45); Re=40,000; d_{bub} = 5 mm; D_H = 25.4 mm

6.2.6 Overall Two-Phase Loss Predictions

Overall pressure losses have been computed for the bend and for the horizontal and the vertical ducts. This section compares the computational predictions to data found in the literature. Two-phase pressure losses were also measured in the test loop. These measurements were discussed in section 3.4 *Experimental Data and Results*, and are included here also.

The overall two-phase loss multiplier is plotted in Figures 6.2.6-1 through 6.2.6-3 as a function of the Martinelli Flow Parameter as presented in Chisholm and Laird (1958):

$$X = \left(\frac{G_L}{G_g}\right)^{0.875} \left(\frac{\mu_L}{\mu_G}\right)^{0.125} \left(\frac{\rho_G}{\rho_L}\right)^{0.5} \qquad [6.2.6\text{-}1]$$

where G represents the mass flow rates, ρ are the densities and μ are the dynamic viscosities for the gas and liquid phases. The higher the amount of the distributed phase (i.e., air) the lower the value of X will be.

The two-phase loss multiplier is the ratio of the two-phase pressure drop to the pressure drop that would occur if the flow were liquid only. Two-phase loss consists of contributions from frictional loss, acceleration effects and gravitational influence. The change in hydrostatic head for the vertical straight duct and the curved bend results in a change in pressure. However, this pressure change is typically not counted as part of the pressure loss; that is the reason why the Lockhart-Martenelli two-phase loss multiplier is the same for a horizontal or vertical pipe. The Chisholm and Laird (1980) data used to validate the present algorithm's prediction is based on a bend which was tested in a horizontal plane so as to remove the gravitational effect. The loss multiplier for the straight pipe is presented in the format suggested

by Chisholm and Laird (1958) in which the ordinate is given as the two-phase multiplier minus unity. Hsu (1976) present the same Lockhart-Martinelli data with the square root of the two-phase loss multiplier as the abscissa. The two data presentations yield the same value for the two-phase loss multiplier.

The present predicted two-phase loss multiplier is compared with the loss multiplier as measured by Chisholm (1980) for a 90^{o} bend in a circular pipe. Chisholm's data is for R/D = infinite (i.e., straight pipe), 5.02, and 2.36. Using this data an experimental curve fit covering the above non-dimensional pipe radii has been determined. The present R/D ratio of the test loop, (5.5), is within the range covered by data. The curved duct data is presented by Chisholm and others as the square root of the two-phase loss multiplier versus the flow Martinelli parameter. The comparison of the 'DUCT' computational predictions to those measured by Chisholm shows good agreement. The computed results are for 5 mm bubbles. The empirical loss correlation depends only on the amount of gas present (i.e., the void fraction) and does not differentiate between bubble diameters. The computed loss is 10% higher for 1 mm bubbles than 5 mm bubbles. The existing experimental data base is insufficient to presently determine whether the two-phase loss multiplier has a weak dependency on bubble size. The relatively small change (when compared to typical two-phase flow measurement scatter) will make resolving this question by additional experiments difficult. The present numerical computation somewhat underestimates the increase in the pressure losses for two-phase flow.

The computed loss in the horizontal section downstream of the bend is compared to data using the Lockhart-Martinelli correlation (Wallis, 1969). The correlation does not distinguish between vertical and horizontal flows. Figure 6.2.6-2 shows that the present numerical computation again underpredicts the two-phase loss increment; however, the trend and level is in

reasonable agreement with the data. The horizontal flow may have too much stratification which might explain some of the discrepancy.

The computed loss in the vertical section upstream of the bend is compared to data again using the Lockhart-Martinelli correlation. The empirical fit of the data is the same as for the horizontal flow case (Figure 6.2.6-3). The present numerical prediction shows slightly less of a loss multiplier for this vertical flow than computed for the horizontal flow. Again the computed results underestimate the increase in loss due to the second phase.

The present numerical predictions consistently underestimate the two-phase loss multiplier compared to data in the literature. This is probably an indication that the log-law wall function which describes the turbulent boundary layer profile is not appropriate for two-phase flows. The modification to this profile through the two-phase flow multiplier may require further investigation to improve the predictive capability of the present procedure. None the less it is gratifying to note that the two-phase pressure losses computed are reasonably close to empirical data. This is significant since the predictions presented here came from first principles but with empirical data for the modeling of the interfacial forces; otherwise the interpenetrating continuum and the associated momentum exchange models seem adequate to determine the pressure losses described here.

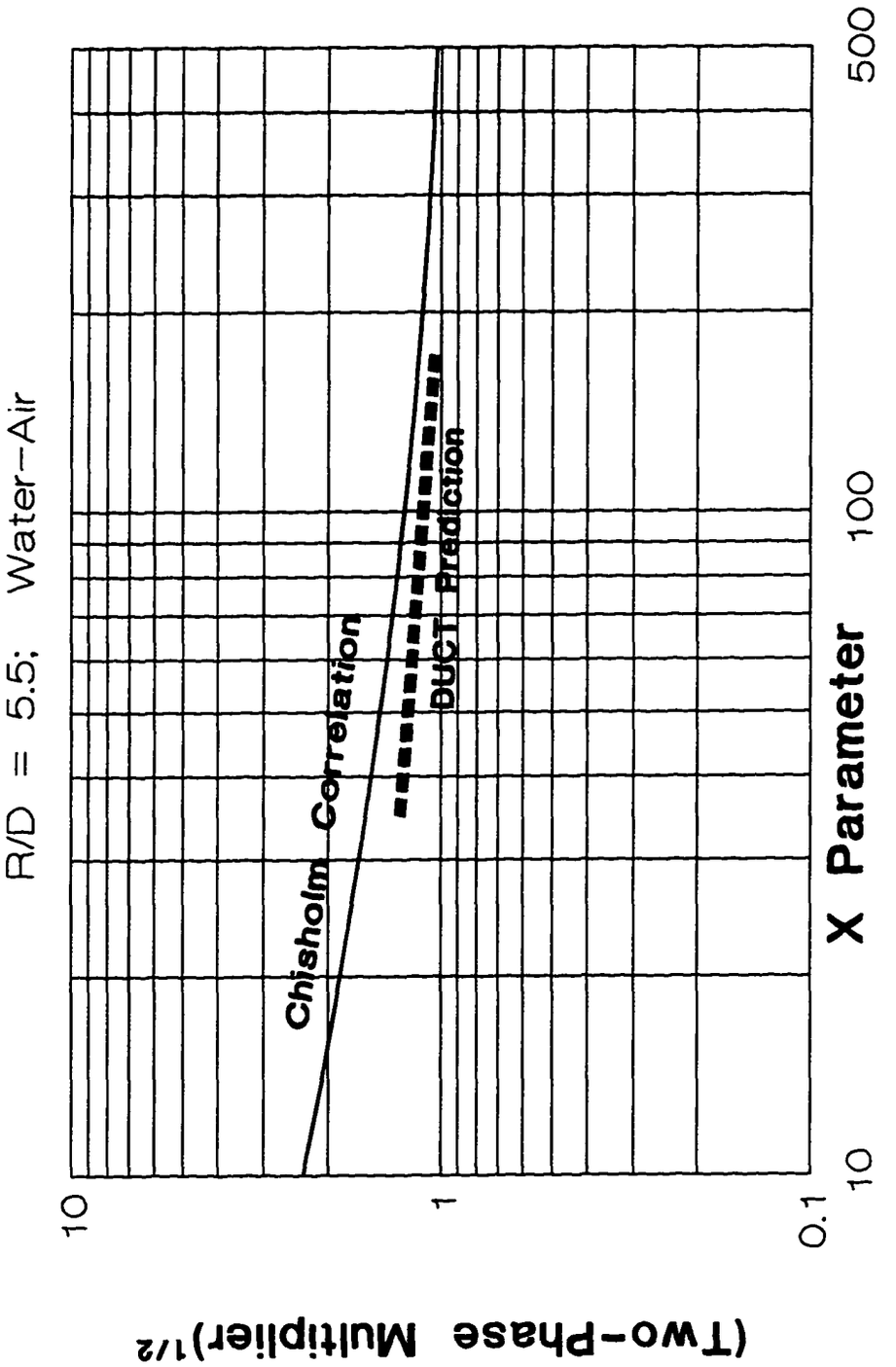

Figure 6.2.6-1 Two-Phase Loss Multiplier for 90° Curved Duct Flow
R/Dh=5.5; Square Cross-Section Duct

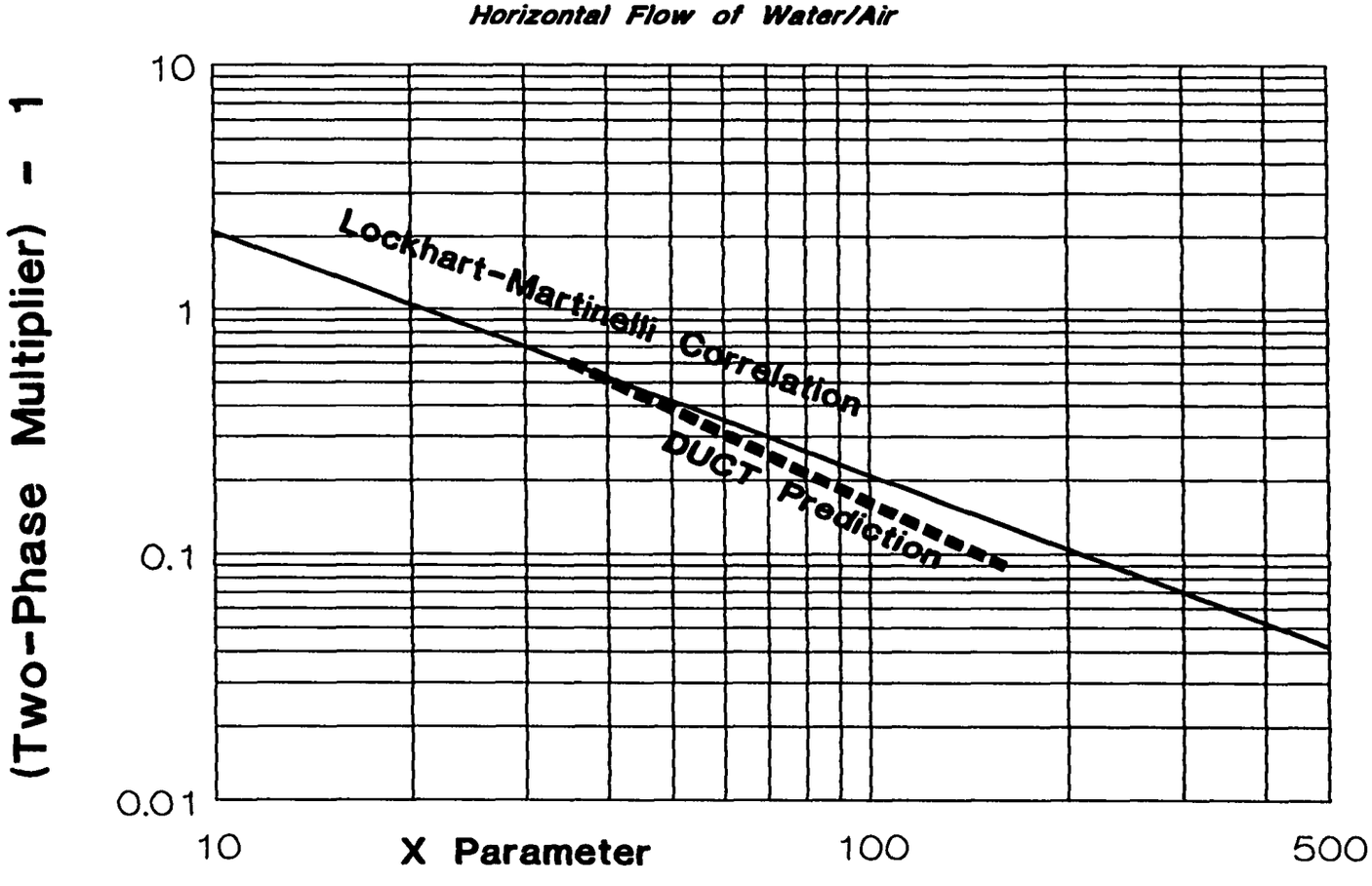

Figure 6.2.6-2 Two-Phase Loss Multiplier for Horizontal Duct Flow
Present Computed Prediction vs Data

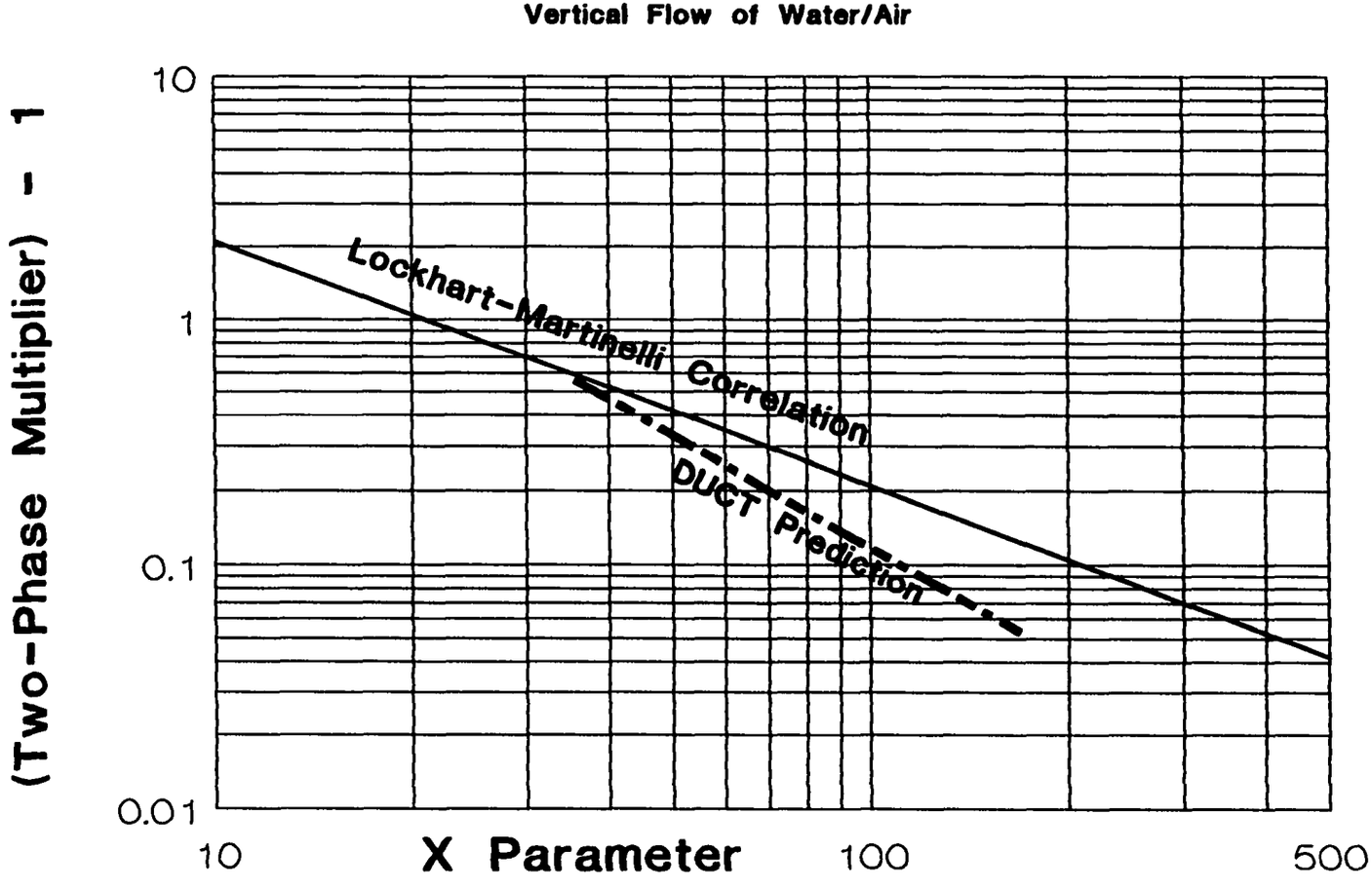

Figure 6.2.6-3 Two-Phase Loss Multiplier for Vertical Duct Flow
Present Computed Prediction vs Data

7. SUMMARY OF RESULTS

The experimental data obtained in the course of this work is given in *Section 3.4 Data and Results*. Single phase and two-phase losses were measured for straight up-flow; straight horizontal flow and for flow in a curved duct with a square cross section.

Computational results for various single phase and two-phase geometries was presented in the previous section on *Computational Results*. Details of the flow, such as velocity profiles and wall shear stresses and secondary flow patterns are compared to data and other investigators' numerical results where applicable. An overview of the two-phase flow measurements and computations can be obtained by comparing the digital photographs recorded in the test flow loop with the predictions from the present two-fluid model.

The bubble distribution at the inlet of the curved duct are shown in Figure 7-1. The bubbles are fairly uniformly dispersed across the section. Figure 7-2 shows the bubbly flow in the curved portion of the duct. The bubbles can be seen to migrate towards the inner radius, although there are still some bubbles along the outer radius of the bend. Figure 7-3 shows a zoom photograph at the 45° location in the bend. Again, the bubble concentration is highest near the inner bend, but some bubbles can still be found along the outer wall. The flow conditions at the exit of the curved section are pictured in Figure 7-4. The bubbles start to move from the inner wall towards the top of the horizontal section.

Numerical predictions of the two-phase flow can be summarized with a series of three-dimensional iso-contour plots. A predicted iso-surface of low void fraction in the duct is shown in Figure 7-5. The predicted low void fraction areas correspond to the outer region of the bend, much as the digital photograph of Figure 7-2. The high void fraction area is predicted to lie along

the inner bend, see Figure 7-3. This iso-surface agrees with the digital photograph of Figure 7-2 which shows a high concentration of bubbles along the inner radius. The numerical prediction of high void region in the straight horizontal section downstream of the bend is shown in Figure 7-7. This prediction shows that the high void fraction area has shifted to the top of the duct, much as the digital photograph of Figure 7-4. Computational results for the fully developed flow in the vertical section, immediately before the bend, shows a central core of void fraction less than the average void fraction (see Figure 7-8). The peaking of the void fraction along the periphery of the cross section is predicted by the present algorithm (see Figure 7-9), where a surface of void fraction higher than the average value is shown to surround the central low void-fraction core.

This series of photographs and three-dimensional contour predictions summarizes the basic features of the two-phase flow as well as the predictive capabilities of the computational algorithm developed here. Overall pressure loss parameters have been measured, computed and compared. In general the agreement for both single-phase and two-phase flow is good. This is extremely gratifying particularly for two-phase flows since the predictions were made from first principles.

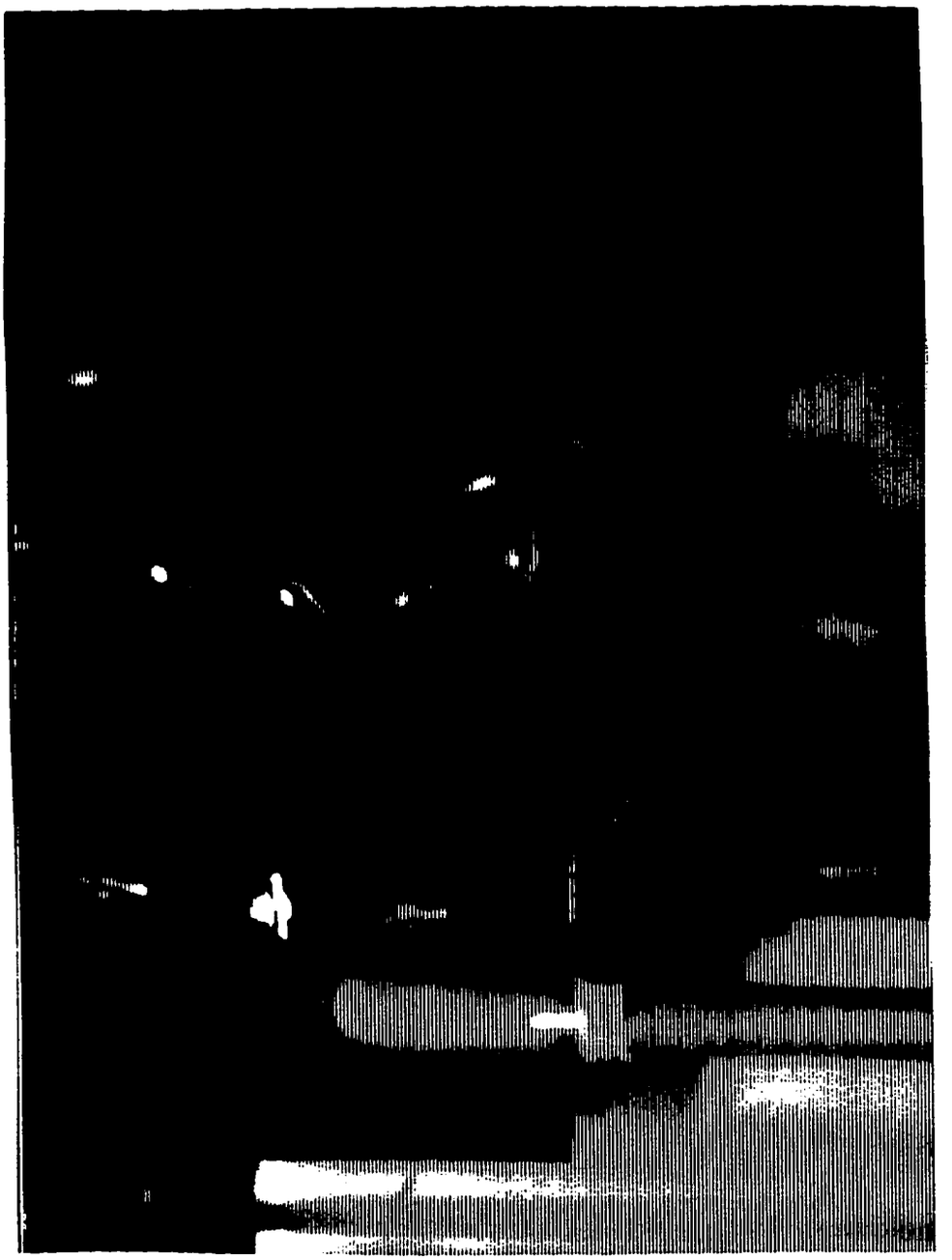

Figure 7-1 Digital Photograph of Bubble Distribution at the Inlet of the Curved Duct

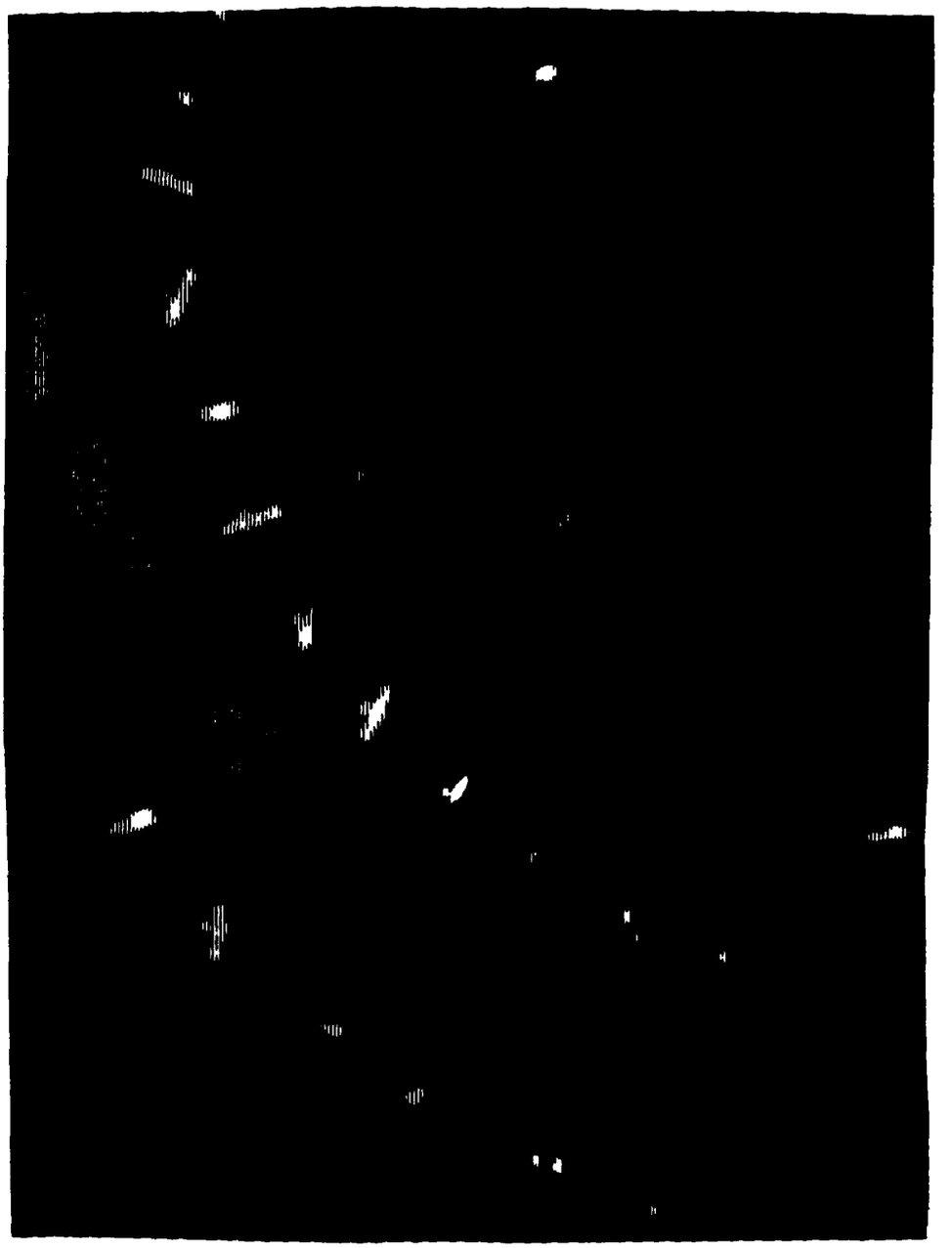

Figure 7-2 Digital Photograph of Bubble Distribution Inside the Curved Duct

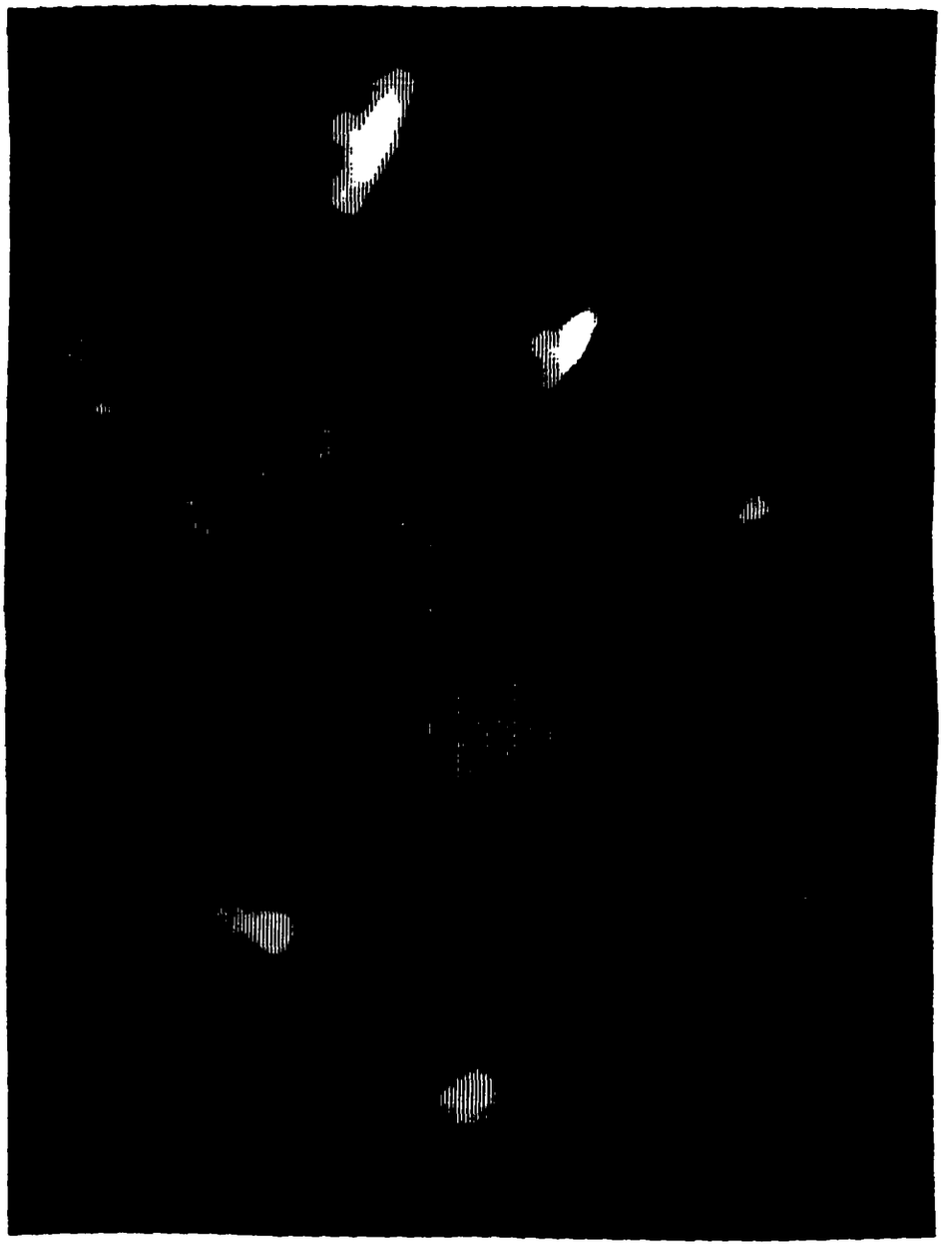

Figure 7-3 Digital Photograph (Zoomed) of Bubble Distribution Inside the Curved Duct at 45°

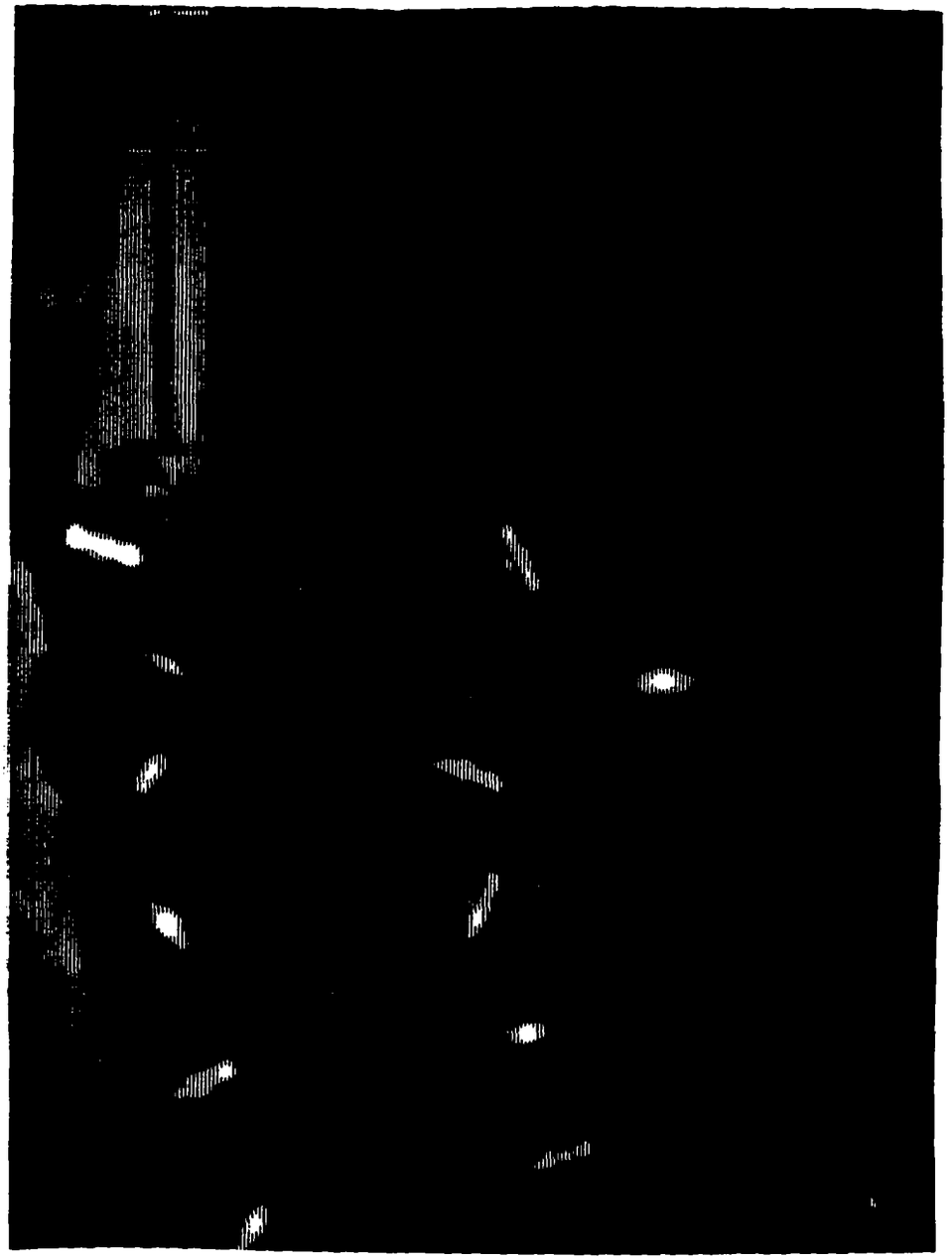

Figure 7-4 Digital Photograph of Bubble Distribution at the Exit of the Curved Duct

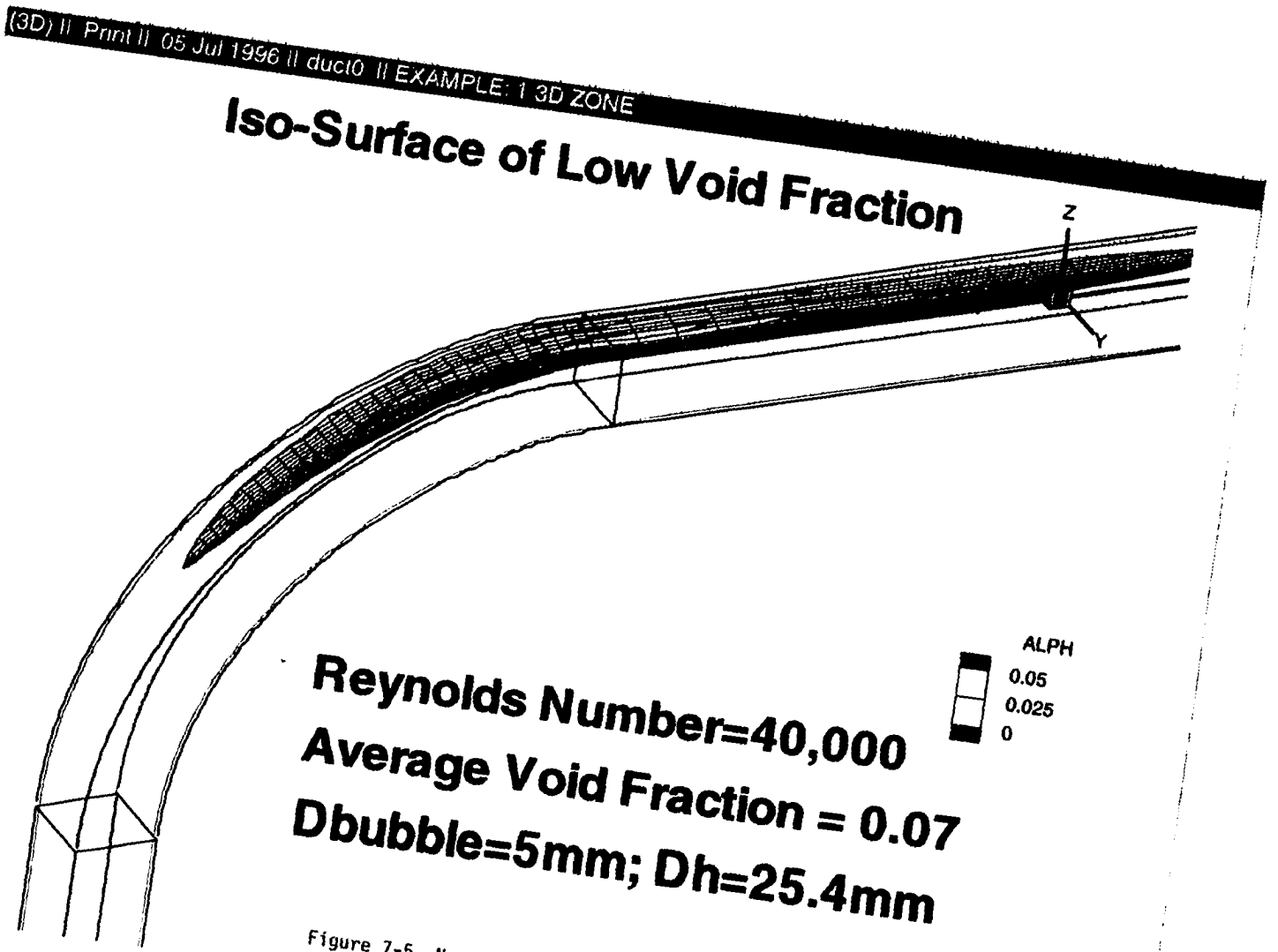

Figure 7-5 Numerical Prediction of Low Void Region Inside the Curved Duct

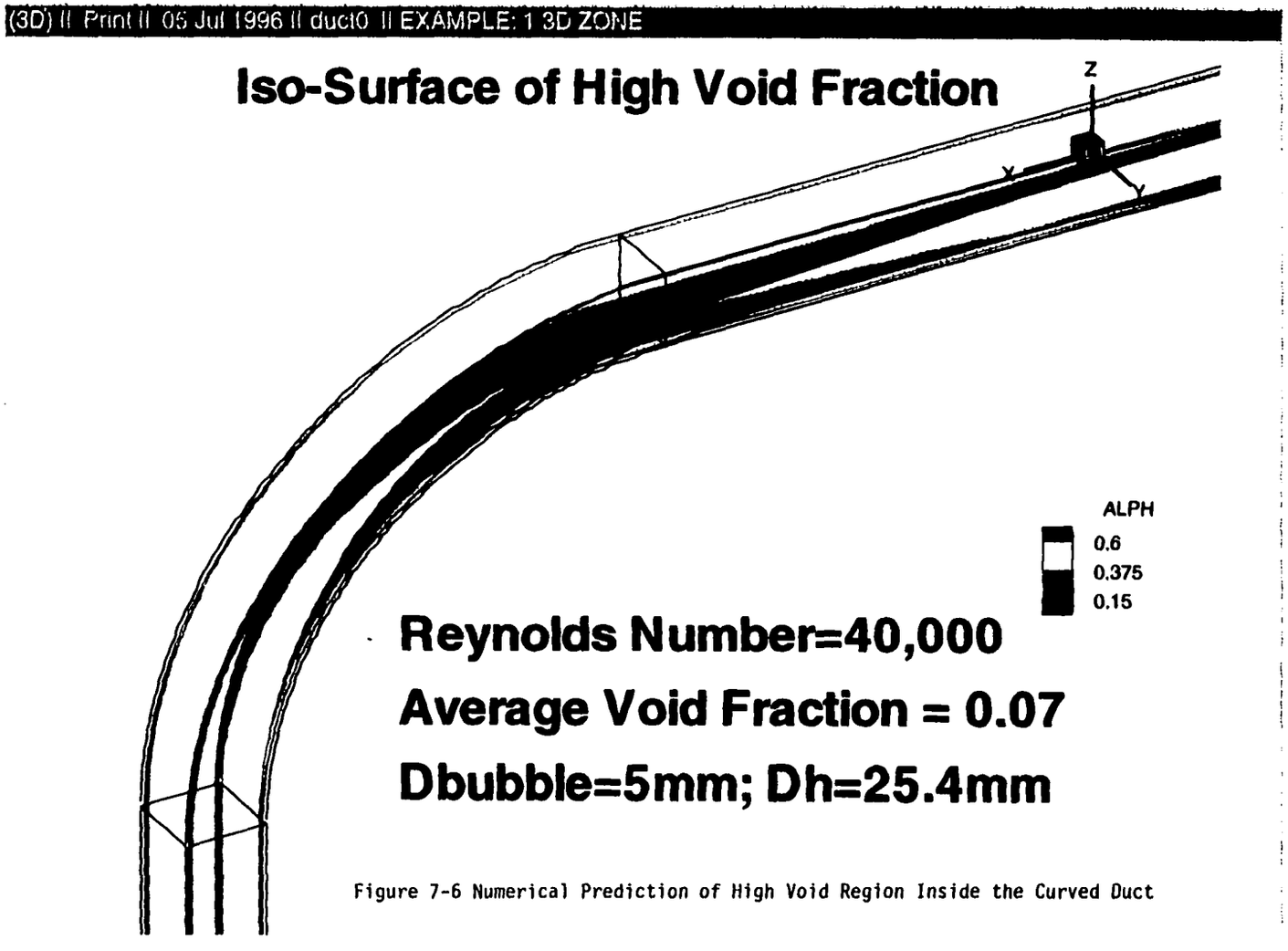

Figure 7-6 Numerical Prediction of High Void Region Inside the Curved Duct

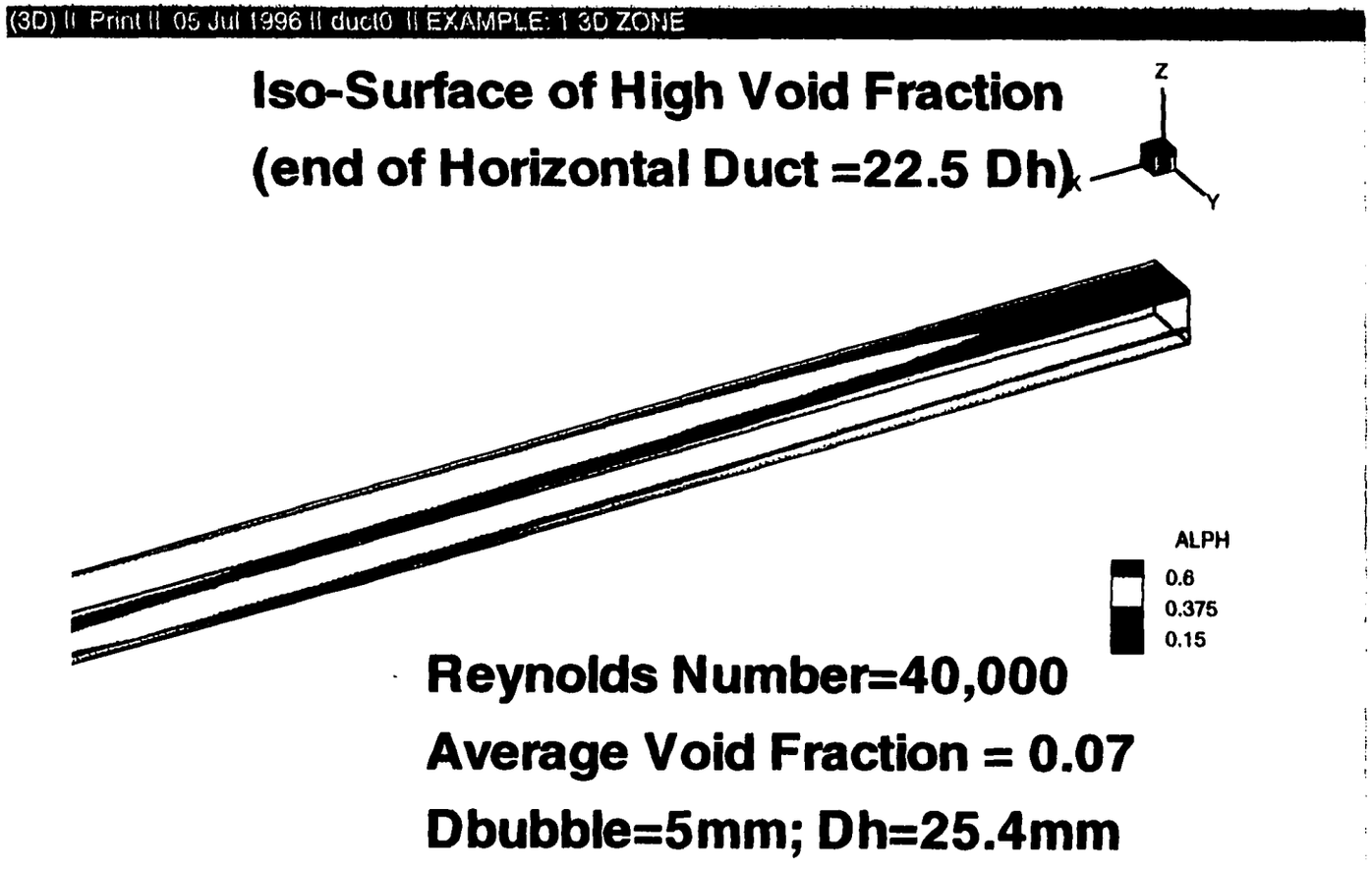

Figure 7-7 Numerical Prediction of High Void Region at the Horizontal Section at Bend Exit

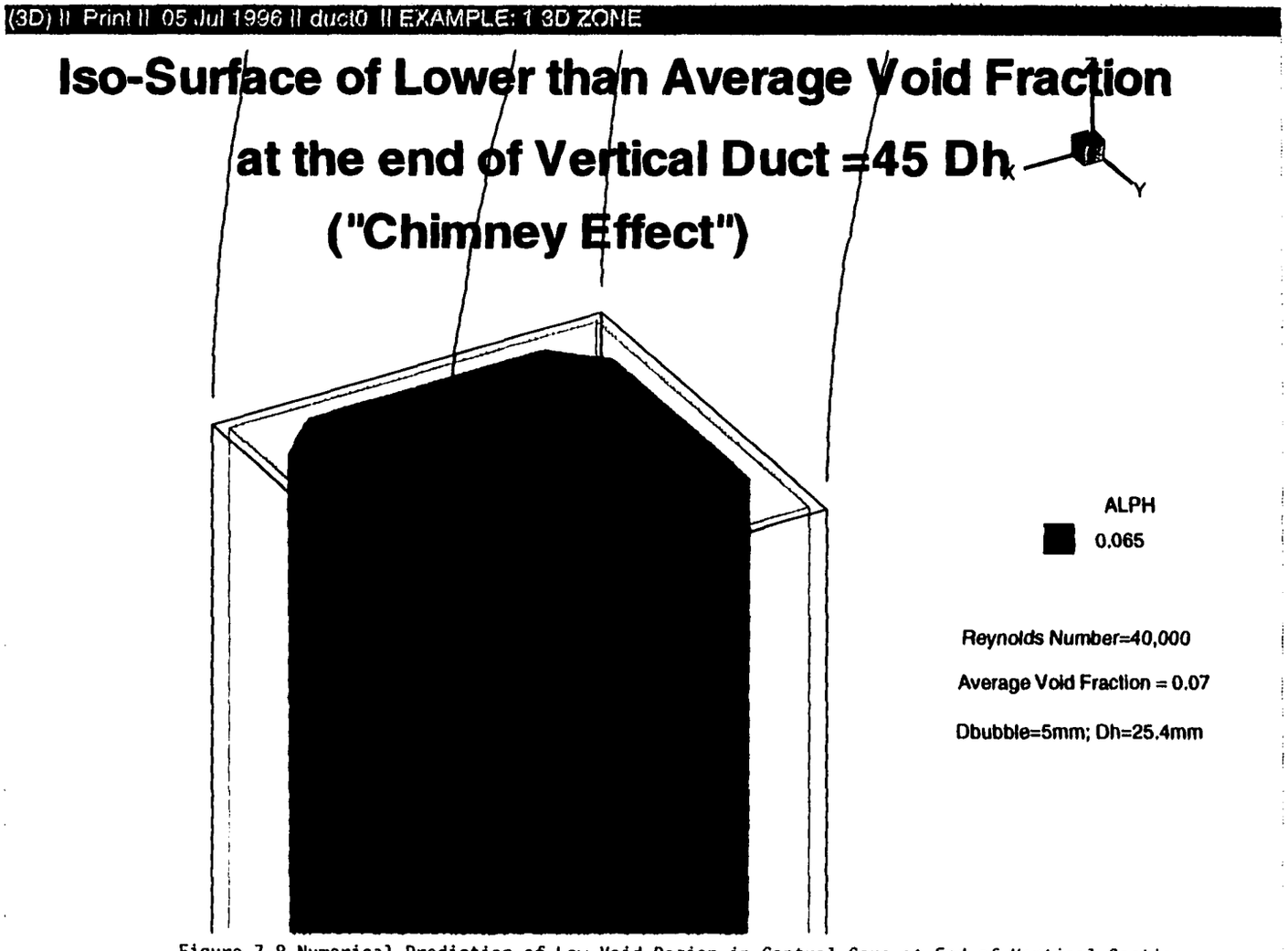

Figure 7-8 Numerical Prediction of Low Void Region in Central Core at End of Vertical Section

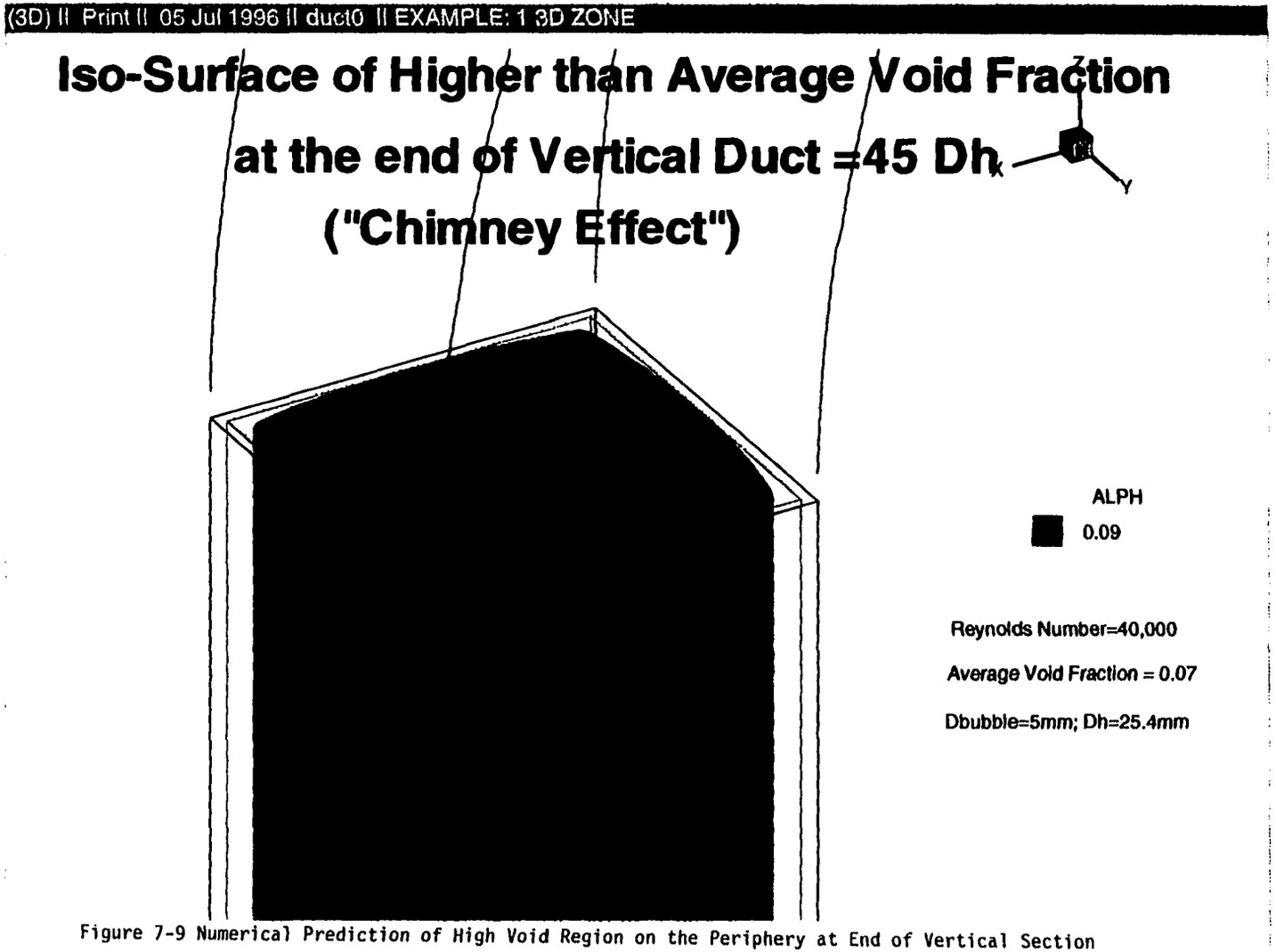

Figure 7-9 Numerical Prediction of High Void Region on the Periphery at End of Vertical Section

8. CONCLUSIONS

- A two-fluid model has been successfully developed that captures the essential features of vertical up-flow, flow in curved ducts and flow in horizontal straight ducts for both single and two-phase flows.
- The algorithm has been verified by comparison with pressure drop data taken in a test loop built in the laboratory
- The computed results have been verified by comparison with both qualitative flow features and quantitative loss data reported in the literature.
- Bubble peaking at the walls of a vertical section has been properly predicted in the present work. The lateral lift force has been modeled with use of modified Saffman theory.
- The interphase drag correlation used has successfully predicted the difference in the distributed void fraction patterns with bubble diameter. Small bubbles are predicted to follow the flow unlike the larger bubbles that tend to segregate.
- The void fraction algorithm is a critical component in the assembly of a robust and stable two-fluid model that can successfully compute phases with widely disparate densities. The presently used void fraction algorithm and lessons learned during its development are reviewed in detail in this dissertation.
- Turbulence transport equations have been developed for two-phase flows. The isotropic k and ε equations contain additional source terms due to the interpenatration and interaction of the phases.

- Bubbly water/air flows can be predicted using a simple turbulence model for the dispersed phase. The use of a second two-equation turbulence model for the dispersed phase does not seem warranted.
- Two phase flows in which the density of the distributed phase is comparable to that of the continuous phase seem to be improved with the addition of the second two-equation turbulence model for the distributed phase.
- Computations of the two-phase driven cavity problem at various gravities indicate that the critical flow pattern differences in labyrinth seals and other turbomachinery components due to microgravity compared to earth gravity at which they were developed can be studied with the present procedure.

9. RECOMMENDATIONS

- Further development of the constitutive models used presently in this two-fluid model numerical algorithm awaits detailed velocity measurements. The collection of such data in the present test loop should be given a high priority.
- The present algorithm is an acceptable vehicle for testing competing two-phase flow turbulence models, since reliable, detailed parametric distributions can be computed.
- The present methodology should be extended to compute heat transfer properties, first for single phase and then for two-phase flows.
- Single component, two-phase flows could be computed in the present algorithm by the addition of the proper source terms in the continuity and momentum equations. Additionally, the energy equation would need to be solved. (The energy equation would have a form very similar to the transport equations for turbulent kinetic energy and the dissipation rate of turbulent kinetic energy.) This would be of great interest in studying water/steam flows where the liquid phase may be evaporated as elevated temperature or low pressure regions are encountered by the continuous phase.
- Particle laden flows could be studied by the addition of a pseudo-kinetic energy equation for predicting the solids' pressure. The prediction of particle trajectories for such flows is of great interest for the proper design of commercial hot gas expanders and many other applications that are susceptible to erosion.

Nomenclature

k	turbulent kinetic energy = 1/2 ($u'^2+v'^2+w'^2$)
x	coordinate direction in the lateral plane that is also in the radial direction for the curved duct problem
y	coordinate direction in the lateral plane
z	coordinate direction in the longitudinal direction (becomes Φ in the curved duct portion of the duct)
u	velocity component in the x direction
v	velocity component in the y direction
w	velocity component in the z or Φ direction

Greek letters

α	volume fraction of phase 2 the distributed phase
ε	dissipation of turbulence
μ	dynamic viscosity (i.e., a property of the fluid alone)
μ_t	turbulent eddy diffusivity
τ	shear stress

Subscript

i,j	index for velocity component
k	index for phase; =1 is continuous phase; =2 is distributed phase

Nomenclature, continued

Superscripts

‘	denotes time varying component

References

Ahmed,S. and Brundrett,E., "Turbulent Flow in Non-Circular Ducts. Part 1", Journal of Fluid Mechanics, Volume 14, pp. 365-375, 1971

Cheng,K.C., Akiyama,M., Endo,Y., Suzuki,M.and Nishwaki,I., "Numerical Visualization of the Elliptic Nature of Laminar Flow in Square Bend Ducts", Heat Transfer and Fluid Flow in Rotating Machinery, Hemisphere Publishing Company, 1987, editor Yang, W.J. , pp. 193-200

Antal, S.P., Lahey, R.T. and Flaherty,J.E., "Analysis of Phase Distribution in Fully Developed Laminar Bubbly Two-Phase", International Journal of Multiphase Flow, Volume 17, Number 5, pp. 635-652, 1991

Batchelor, G., "On Steady Laminar Flow with Closed Streamlines at Large Reynolds Number", Journal of Fluid Mechanics, Volume 1, pp. 177-190, 1956

Berger, S.A. and Talbor, L., "Flow in Curved Pipes", Annual Review of Fluid Mechanics, Volume 15 , pp. 461-512, 1983

Bergstrom,D.,Adamopoulos,G. and Postlethwaite,J., "Numerical Prediction of Two-Dimensional Flow in a Curved Channel with Separation", Separated Flows, pp. 209-216, FED-Volume 149 ASME 1993

Besnard,D.C., Kataoka,I. and Serizawa,A., "Turbulence Modification and Multiphase Turbulence Transport Modeling", Fluids Engineering Division, Volume 110, Turbulence Modification in Multiphase Flows , pp. 51-57, 1991

Blevins, R.D., Applied Fluid Dynamics Handbook, Van Nostrand Reinhold Company, 1984

Brundrett,E and Baines,W.D., "The production and diffusion of vorticity in duct flow",Journal of Fluid Mechanics, Volume 19, pp. 375-394, 1964

Burggraf, O.R., "Analytical and Numerical Studies of the Structure of Steady Separated Flows", Journal of Fluid Mechanics, Volume 24, Part 1, pp. 113-151, 1966

Carver, M.B., "A Method of Limiting Intermediate Values of Volume Fraction in Iterative Two-Fluid Computations", Journal of Mechanical Engineering Science, Volume 24, Number 4, pp. 221-224, IMechE 1982

Carver,M.B., "Numerical Computation of Phase Separation in Two Fluid Flow", Journal of Fluids Engineering, Volume 106, pp. 147-153, June 1984

Carver,M.B. and Salcudean,M., "Three-Dimensional Numerical Modeling of Phase Distribution of Two-Fluid Flow in Elbows and Return Bends", Numerical Heat Transfer, Volume 10, pp. 229-251, 1986

Carver, M.B., "Development and Application of a Three-Dimensional Two-Fluid Numerical Algorithm for Simulation of Phase Redistribution by Bends and Obstructions", Ph.D. Thesis, University of Ottawa, 1988

Chen,J.C., "Some Phenomenological Questions in Post-CHF Heat Transfer", NATO Advanced Research Workshop on Two-Phase Flows and Heat Transfer, 1982

Cheng,K.C., Lin,R.C. and Ou, J.W., "Graetz Problem in Curved Square Channels", Transactions of the ASME, pp. 244-248, May 1975

Cheng,K.C., Lin,R.C and Ou,J.W., "Fully Developed Laminar Flow in Curved Rectangular Channels", ASME, Journal of Fluids Engineering, pp. 41-48, March 1976

Cheng, G.C. and Farokhi,S., "On Turbulent Flows Dominated by Curvature Effects", Transactions of the ASME, Volume 114, pp. 52-56, March 1992

Chisholm,D., "Two-Phase Flow in Bends", International Journal of Multiphase Flow, Volume 6, pp. 363-367, 1980.

Chisholm,D. and Laird, D.K., "Two-Phase Flow in Rough Tubes", Transactions of the ASME, pp. 276-286, February 1958

Cooper,P., "Analysis of Single- and Two-Phase Flows in Turbopump Inducers", ASME Journal of Engineering for Power, pp 577-588, October 1967

Dean, W.R., "The Streamline Motion of Fluid in a Curved Pipe", Philosphical Magazine, Volume 5, 7 th Series, pp. 673-695, April 1928

Drew, D.A. and Lahey, R.T., "Phase Distribution Mechanisms in Turbulent Two-Phase Flow in Channels of Arbitrary Cross Section", Journals of Fluid Engineering, Volume 103, pp. 583-589, December 1981

Drew, D.A. and Lahey, R.T.,"Phase-Distribution Mechanisms in Turbulent Low-Quality Two-Phase Flow in a Circular Pipe", Journal of Fluid Mechanics, Volume 117, pp. 91-106, 1982

Drew,D. , "Mathematical Modeling of Two-Phase Flows", Annual Review of Fluid Mechanics, Volume 15, pp. 261-291, 1983

Drew, D.A. and Lahey, R.T., "The Virtual Mass and Lift Force on a Sphere in Rotating and Straining Inviscid Flow", International Journal of Multiphase Flow, Volume 13, Number 1, pp. 113-121, 1987

Dykhuizen, R.C., Roy, R.P. and Kalra,S.P., "Numerical Method for the Solution of Simultaneous Nonlinear Equations and Application to Two-Fluid Model Equations of Boiling Flow", Numerical Heat Transfer, Volume 7, pp. 225-234, 1984

Elghobashi,S., Abou-Arab,T., Rizk,M. and Mostafa,A., "Prediction of the Particle-Laden Jet with a Two-Equation Turbulence Model", International Journal of Multiphase Flow, Volume 10, Number 6, pp. 697-710, 1984

Elghobashi,S. and Abou-Arab, "A Two-Equation Turbulence Model of Two-Phase Flows", Physics of Fluids, Volume 26(4), pp. 931-938, April 1983

Emery,A.F., Neighbors,P.K. and Gessner,F.B., "The Numerical Prediction of Developing Turbulent Flow and Heat Transfer in a Square Duct", Journal of Heat Transfer, Volume 102, pp. 51-57, February 1980

Founti,M. and Klipfel,A., "The Shear Lift Effects on the Particle Motion in Two-Phase Sudden Expansion Flows", Fluids Engineering Division Volume 185, Numerical Methods in Multiphase Flows, pp. 81-87, 1994

Gardner,G.C. and Neller,P.H., "Phase Distributions in Flow of an Air Water Mixture Round Bends and Past Obstructions", Proceedings of the Institute of Mechanical Engineers, Volume 184, Number 3C

Ghia,K.N. and Sokhey,J.S., "Analysis and Numerical Solution of Viscous Flow in Curved Ducts of Regular Cross sections", ASME Publication, Numerical/Laboratory Computer Methods in Fluid Mechanics, pp 53-72, December 1976

Gidaspow, D., Ding,J. and Jayaswal, U.K., "Multiphase Navier-Stokes Equation Solver", ASME FED Volume 91, Numerical Methods for Multiphase Flows, pp. 47-56, 1991

Gosman,A.D., Lekakou,C.,Politis,S.,Issa,R.and Looney,M.K., "Multidimensional Modeling of Turbulent Two-Phase Flows in Stirred Vessels", AIChE Journal, Volume 1938, Number 12, pp. 1946-1956, December 1992

Gore,R.A. and Crowe,C.T., "Effect of Particle Size on Modulating Turbulent Intensity", International Journal of Multiphase Flow, Volume 15,Number 2, pp. 279-285, 1989

Govier, G.W. and Aziz,K., The Flow of Complex Mixtures in Pipes, Van Nostrand Reinhold Company, 1972

Graf, E. and Neti, S., "Computations of Laminar and Turbulent Two-Phase Flow in a Driven Cavity", ASME Fluids Engineering Division, Volume 236, pp. 127-135, 1996

Hetsroni, G., "Particles-Turbulence Interaction", International Journal of Multiphase Flow, Volume 15, Number 5, pp. 735-746, 1989

Hino,M., "Turbulent Flow with Suspended Particles", Proceedings, American Society of Chemical Engineers, Volume 89, HY 4, pp. 161-185, July 1963

Hsu,Y.Y and Graham, R.W., "Transport Processes in Boiling and Two-Phase Systems", Hemisphere Publishing Corporation, 1976

Humphrey, J.A.C, Taylor,A.M. and Whitelaw, J.H., "Laminar Flow in a Square Duct of Strong Curvature", Journal of Fluid Mechanics, Vol 83, Part 3, pp. 509-527, 1977

Humphrey, J.A.C., "Flow in Ducts with Curvature and Roughness", Doctoral Thesis, Imperial College, London, 1977

Humphrey, J.A.C., Whitelaw, J.H. and Yee, G., "Turbulent Flow in a Square Duct with Strong Curvature", Journal of Fluid Mechanics, Vol ume 103, pp. 443-463, 1981

Idelchik, I.E., Malyavskaya,G., Martynenko,O. and Fried,E., Hankbook of Hydraulic Resistance, Springer-Verlag, 1976

Ishii,M. and Mishima,K., "Two-Fluid Model and Hydrodynamic Constitutive Relations", Nuclear Engineering and Design 82, pp. 107-126, Elsevier Science Publishers, 1984

Ishii, M., "State of the Art in Modeling Two-Phase Flows", lecture at Purdue University, September 1992

Ito,H., "Pressure Losses in Smooth Pipe Bends", Journal of Basic Engineering, ASME, pp. 131-143, March 1960

Jayanti,S. and Hewitt,G.F., "Review of Literature on Dispersed Two-Phase Flow with a View to CFD Modelling", AEA Technology Report AEA-APS-0099, 1991

Kashiwa,B.A. and Gore, R.A., "A Four Equation Model for Multiphase Turbulent Flow", Fluids Engineering Division, Volume 110, Turbulence Modification in Multiphase Flows, pp. 23-27, 1991

Kataoka,I. and Serizawa,A., "Analyses of the Radial Distributions of Average Velocity and Turbulent Velocity of the Liquid Phase in Bubbly Two-Phase Flow", JSME International Journal, Series B, Volume 36, Number 3, pp. 404-411, 1993

Kays,W.M., Convective Heat and Mass Transfer, McGraw Hill Book Co., NY 1966

Launder, B.E. and Spalding,D.B., Lectures in Mathematical Models of Turbulence, Academic Press , 1972

Launder, B.E. and Ying, W. M., "Secondary flows in ducts of square cross section", Journal of Fluid Mechanics, Volume 54, Part 2, pp. 289-295, 1972

Launder, B.E. and Ying, W. M., "Prediction of Flow and Heat Transfer in Ducts of Square Cross section", Heat and Fluid Flow, Volume 3, Number 2, pp. 115-121, 1973

Leschziner, M.A. and Rodi, W., "Calculation of Annular and Twin Parallel Jets Using Various Discretization Schemes and Turbulence Model Variants", Journal of Fluids Engineering, Volume 103, Number 2, pp. 352-360, 1981

Leutheusser, H.J., "Turbulent Flow in Rectangular Ducts", Journal of the Hydraulics Division, Proceedings of the American Society of Civil Engineers, Section HY 3, 3508; pp. 1-19, May 1963

Liu,C.H. and Liou,T.M., "Developing Turbulent Flow in a Curved Square Duct", Proceedings of the Eigth National Conference on Theoretical and Applied Mechanics, Taiwan, December 1984

Lo,S.M., "Mathematical Basis of a Multi-Phase Flow Model", United Kingdom Atomic Energy Authority Harwell Laboratory Report AERE R 13432

Lo,S.M., "Multiphase Flow Model in the Harwell-Flow3D Computer Code",", United Kingdom Atomic Energy Authority Harwell Laboratory Report AEA-InTec-0062

Los Alamos personnel, "TRAC-P1: An Advanced Best Estimate Computer Program for PWR LOCA Analysis", Volume 1, NUREG/CR-0063; LA-7279-MS, 1978

McComas,S.T., "Hydrodynamic Entrance Lenghts for Ducts of Arbitrary Cross Section", Journal of Basic Engineering, pp. 847-850, December 1967

Mei, R. and Klausner,J.F., "Shear Lift Forces on Spherical Bubbles", International Jounal of Heat and Fluid Flow, Volume 15, Number 1, pp. 62-65, February 1994

Melling, A, Investigation of Flow in Non-Circular Ducts and other Configurations by Laser-Doppler Anemometry", Ph. D. Thesis, University of London, 1975

Mishima,K. and Ishii,M., "Flow Regime Transition Criteria for Upward Two-Phase Flow in Vertical Tubes", International Journal of Heat and Mass Transfer, Volume 27, Number 5, pp. 723-737, 1984

Mohamed, O., "Prediction of Turbulent Two-Phase Bubbly Flows in Vertical Pipes", Ph.D. Dissertation, Lehigh University, 1988

Morrison,G.L., Johnson,M.C.and Tatterson,G.B., "3-D Laser Anemometer Measurements in a Labyrinth Seal", ASME Paper 88-GT-63, 1963

Mostafa,A.A. and Mongia,H.C., "On the Modeling of Turbulent Evaporating Sprays: Eulerian versus Lagrangian Approach", International Journal of Heat and Mass Transfer, Pergamon Journals, Volume 30, pp. 2583-2592, 1987.

Moujaes,S. and Dougall,R.S., "Experimental Investigation of Cocurrent Two-phase Flow in A Vertical Rectangular Channel", *Canadian Journal of Chemical Engineering* , Volume 65, pp. 705-715, 1987

Naot,D., Shavit,A. and Wolfshtein,M., "Numerical Calculation of Reynolds Stresses in a Square Duct with Secondary Flow", Warme- und Stoffubertragung, Springer Verlag, pp. 151-161, 1974

Narasimhan,J.L., Ramjee,V., Diwakar,P.M. and Tulapurkara,E.G., "Prediction of a Wake in a Curved Duct", International Journal for Numerical Methods in Fluids, Volume 13, pp 907-916, 1991

Neti,S. and Eichorn,R. , "Computations of Developing Turbulent Flow in a Square Duct", Turbulent Boundary Layers, ASME Publication, editor Weber, H., 1979

Neti,S. and Colella,G.M., "Development of a Fiber Optic Doppler Anemometer for Bubbly Two-Phase Flows", EPRI Report NP-2802, 1983

Neti,S. and Mohamed,O., "Numerical Simulation of Turbulent Two-Phase Flows", International Journal of Heat and Fluid Flow, Volume 11, pp. 204-213, September 1990

Neti,S. and Mohamed,O., "Bubble Distributions in Two-Phase Flows", 1996

Nikuradse, J. "Untersuchugen uber de Geschwindigkeits in Turbulenten Stromungen", VDI Forschungsheft, Number 28, 1926

Oshinowo, T. and Charles,M.E. , "Vertical Two-Phase Flow; Part I, Flow Pattern Correlations", Canadian Journal of Chemical Engineering, Volume 52, pp. 25-35, February 1974

Parthasarathy,R. and Faeth,G., "Structure of Particle-Laden Turbulent Water Jets in Still Water", International Journal of Multiphase Flow, Volume 13, Number 5, pp. 699-716, 1987

Parsons, D.J. and Hill, P.G., "Effects of Curvature on Two-Dimensional Diffusere Flow", ASME Journal of Fluids Engineering, pp. 349-360, September 1973

Patankar,S.V. and Spalding, D.B., "A Calculation Procedure for Heat, Mass and Momentum Transfer in Three-Dimensional Parabolic Flows", International Journal of Heat and Mass Transfer, Volume 15, pp. 1787-1806, 1972

Patankar,S.V., Pratap,V.S.,and Spalding,D.B., "Prediction of Turbulent Flow in Curved Pipes", Journal of Fluid Mechanics, Vol 67, Part 3, pp. 583-595, 1975

Patankar, S.V. Numerical Heat Transfer and Fluid Flow, Hemisphere Publishing Corporation , 1980

Peskin, R.L., "Some Effects of Particle-Particle and Particle-Fluid Interaction in Two-Phase Turbulent Flow", Ph.D. Thesis, Princeton University, Princeton, NJ, 1959

Pourahmadi,F. and Humphrey,J.A.C., "Prediction of Curved Channel Flow with an Extended k-ε Model of Turbulence", AIAA Journal, Volume 21, Number 10, pp. 1365-1373, October 1983

Pratap,V.S. and Spalding,D.B., "Numerical Computations of the Flow in Curved Ducts", Aeronautical Quaterly, pp. 219-228, August 1975

Pratap,V.S. and Spalding,D.B., "Fluid Flow and Heat Transfer in Three-Dimensional Duct Flows" , International Journal of Heat and Mass Transfer, Vol 19, pp. 1183-1188, 1976

Pratap,V.S., "Flow and Heat Transfer in Curved Ducts", Ph.D. Thesis, 1976, University of London

Randelman,R., Benkrid,A. and Caram,H. "Investigation of the Solid Flow Pattern in a Spouted Bed", AICHe Symposium Series, New Development in Fluidization and Fluid-Particle Systems, pp 23-28, 1987

Rivard, W.V. and Torrey,M.D., "KFIX: A Program for Transient Two Dimensional Two-Fluid Flow", LA-NUREG-6623, 1978

Rodi,W., "A New Algebraic Relation for Calculating the Reynolds Stresses", Zeitschrift fur Angewandte Mathematik und Mechanik, Volume 56, T219-T221

Rouson,D.W.I. and Eaton,J., "Direct Numerical Simulation of Turbulent Channel Flow with Immersed Particles", ASME FED Volume 185, Numerical Methods in Multiphase Flows, pp. 47-57, 1994

Saffman, P.G., "The Lift on a Small Sphere in a Slow Shear Flow", Journal of Fluid Mechanics, Volume 22, Part 2, pp. 385-400, 1965

Saffman, P.G., Corrigendum to "The Lift on a Small Sphere in a Slow Shear Flow", Journal of Fluid Mechanics, Volume 31, page 624, 1968

Shah,R.K. and London,A.L., Laminar Flow Forced Convection in Ducts, Academic Press, NY 1978

Shah, V.L , "Numerical Procedures for Calculating Steady/Unsteady Single/Two Phase Three Dimensional Fluid Flow with Heat Transfer", NUREG-CR-0789

Shuen, JS, "A Theoretical and Experimental Investigation of Dilute Particle-Laden Turbulent Gas Jets", Ph. D. Dissertation, Pennyslvania State University, 1984

Simonin,O. and Viollet,P.L., "Prediction of an Oxygen Droplet Pulverization in a Compressible Subsonic Coflowing Hydrogen Flow", ASME FED, Numerical Methods for Multiphase Flows, Volume 91, pp. 73-79, 1991

Soo, S.L., Fluid Dynamics of Multiphase Systems, Blasisdell Publishing Company, 1967

Spalding,D.B., "Mathematical Methods in Nuclear Reactor Thermalhydraulics", Proceedings ANS Meeting, Saratoga, NY 1980

Sparrow,E.M., Hixon,C.W. and Shavit,G., "Experiments on Laminar Flow Development in Rectangular Ducts", Journal of Basic Engineering,Transactions of the ASME, pp. 116-124, March 1967

Sun, T.Y. "A Theoretical and Experimental Study of Noncondensible Turbulent Bubbly Jets", Ph.D. Dissertation, Pennsylvania State University, 1985

Sun, T.Y. and Faeth, G.M., "Structure of Turbulent Bubbly Jets--I. Methods and Centerline Properties", International Journal of Multiphase Flow, Volume 12,Number 1, pp. 99-114, 1986

Squire,H.B. and Winter,K.G., "The Secondary Flow in a Cascade of Airfoils in a Non-Uniform Stream", Journal of Aeronautical Sciences, Number 4, 271-277, April 1951

Tamamidis,P. and Assanis, D.N., "Numerical Simulation of Turbulent Flows in Complex Geometries Using Curvature Modified k-ε Models", ASME Fluid Engineering Division, Volume 155, pp. 113-117, 1993

Taylor,A.M, Whitelaw,J.H., Yianneskis,M., "Curved Ducts with Strong Secondary Motion: Velocity Measurements of Developing Laminar and Turbulent Flow", Transactions of the ASME, Vol 104, pp. 350-359, September 1982

Taylor,G.I., "The Criterion for Turbulence in Curved Pipes", Proceedings of the Royal Society, London, Volume 124 A, pp. 243-249, 1929

Tchen, C.M., Dissertation, Delft, Martinus Nijhoff, The Hague, 1947

Tsuji,Y., "Review: Turbulence Modification in Fluid-Solid Flows", Fluids Engineering Division, Volume 110, Turbulence Modification in Multiphase Flows, pp. 1-6, 1991

Unal, C., Tuzla, K., Cokmez-Tuzla, A., and Chen, J.C., "Vapor Generation Rate Model for Dispersed Drop Flow", Nuclear Engineering and Design, Volume 125, pp. 161-173, 1991

Van Doormaal, J.P.and Raithby,G.D., "Enhancements of the SIMPLE Method for Prediction Incompressible Fluid Flows", Numerical Heat Transfer, Volume 7, pp. 147-163, 1984

Wallis, G.B., One-Dimensional Two-Phase Flow, McGraw Hill Publishing Company, 1969

Walker,J.D.A., Abbott,D.E., Scharnhorst,R.K. and Weigand,G.G., "Wall-Layer Model for the Velocity Profile in Turbulent Flows", AIAA Journal, Volume 27, Number 2, pp 140- 149, 1989

Wang, S.K., Lee, S.J., Jones, O.C. and Lahey, R.T., "3-D Turbulence Structure and Phase Distribution Measurements in Bubbly Two-Phase Flows", International Journal of Multiphase Flow, Volume 13, Number 3, pp. 327-343, 1987

Wang,D.M., Issa,R. and Gosman,A.D., "Numerical Prediction of Dispersed Bubbly Flow in a Sudden Enlargement", Fluids Engineering Division, Numerical Methods in Multiphase Flows, Volume 185, pp. 141-148, 1991

Weisman, J. "Flow Pattern Identification in Concurrent Vapor-Liquid Flow", Two-Phase Flow Dynamics , edited Bergles and Ishigai, 1981

White, C.M., "Streamline Flow through Curved Pipes", Procedings of the Royal Society, A123 1929

Zun,I., "The Transverse Migration of Bubbles Influenced by Walls in Vertical Bubbly Flow", International Journal of Multiphase Flow, Volume 6, pp. 583-588, 1980

Zun,I., "The Role of Void Peaking in Vertical Two-Phase Bubbly Flow", 2nd International Conference on Multi-Phase Flow, Paper C3, pp. 127-139, London, England, June 1985

Appendices

Appendix I: Φ Momentum Equation

Toroidal Coordinates (Incompressible & μ = const.) CONSERV. FORM:

$$\rho\left(\frac{\partial wu}{\partial x}+\frac{\partial v w}{\partial y}+\frac{\partial w^2}{R''\partial\theta}+\delta_{ln}\frac{2\rho u w}{R}\right)$$

$$\rho\left(u\frac{\partial w}{\partial x}+v\frac{\partial w}{\partial y}+\frac{w}{R''}\frac{\partial w}{\partial\phi}+\delta_{ln}\frac{uw}{R}\right)=-\frac{\partial p}{R\partial\phi}+$$

$$\underbrace{\mu\left[\frac{\partial^2 w}{\partial x^2}+\frac{\delta_{ln}}{R}\frac{\partial w}{\partial x}+\frac{\partial^2 w}{\partial y^2}+\frac{\partial^2 w}{R^2\partial^2\phi}\right]}_{\nabla^2 w}+\delta_{ln}\mu\left[2\frac{\partial u}{R^2\partial\phi}-\frac{w}{R^2}\right]$$

Φ Momentum Equation - First Consider Terms that are straight duct-like only

for a CV: $R_{local\,inner}=\frac{x_p+x_w}{2}+\overline{R}_i=\frac{x_i+xi_{i-1}}{2}+\overline{R}_i$

$$R_{local\,outer}=\frac{x_P+x_E}{2}+\overline{R}_i=\frac{x_i+x_{i+1}}{2}+\overline{R}_i$$

$$R_p=x_p+\overline{R}_i=x_i+\overline{R}_i$$

and

$$dz=R_{local}\Delta\theta$$

let

$R_0=R_{local\ outer}$ $\quad$ $R_i=R_{local\ inner}$ $\quad$ $R_p=\overline{R}_{local}$

$dz_0=R_0\Delta\theta$ $\quad$ $dz_i=R_i\Delta\theta$ $\quad$ $dz_p=R_p\Delta\theta$

Then:

$$\left\{u_{E_U}\left(\frac{w_{P_P}+w_{E_P}}{2}\right)dydz_0-\rho u_{P_P}\left(\frac{w_{P_P}+w_{W_P}}{2}\right)dydz_i\right\}$$

$$+\left\{\rho v_{N_P}\left(\frac{w_{P_P}+w_{N_P}}{2}\right)-\rho v_{P_P}\left(\frac{w_{P_P}+w_{S_P}}{2}\right)\right\}dxdz_P$$

$$+\left\{\rho w_{P_U}w_{P_D}-\rho w_{P_U}w_{P_U}\right\}dxdy=-(p_D-p_S)dxdy$$

$$+\mu dydz_P\left[\frac{(w_{E_P}-w_{P_P})}{\frac{\Delta x_P+\Delta x_E}{2}}-\frac{(w_{P_P}-w_{W_P})}{\frac{\Delta x_P+\Delta x_W}{2}}\right]+\mu dxdz_P\left[\frac{(w_{N_P}-w_{P_P})}{\frac{\Delta y_N+\Delta y_P}{2}}-\frac{(w_{P_P}-w_{S_P})}{\frac{\Delta y_S+\Delta y_P}{2}}\right]$$

Divide by dz_p:

$$w_{P_P}\left\{\left(\tfrac{1}{2}\rho u_{E_P}\frac{dz_0}{dz_P}-\tfrac{1}{2}\rho u_{P_P}\frac{dz_i}{dz_P}\right)dy+\left(\tfrac{1}{2}\rho v_{N_P}-\tfrac{1}{2}\rho N_{P_P}\right)dx\right.$$

$$\left.+\rho w_{P_P}\frac{dxdy}{dz_P}+\frac{\mu dy}{\frac{1}{2}(\Delta x_P+\Delta x_E)}+\frac{\mu dy}{\frac{1}{2}(\Delta x_P+\Delta x_W)}+\frac{\mu dx}{\frac{1}{2}(\Delta y_N+\Delta y_D)}+\frac{\mu dx}{\frac{1}{2}(\Delta y_S\Delta y_P)}\right\}$$

$$=w_{E_P}\left\{(-\tfrac{1}{2}\rho u_{E_P})dy\frac{dz_0}{dz_P}+\frac{\mu dy}{\frac{1}{2}(\Delta x_P+\Delta x_E)}\right\}$$

$$+w_{W_P}\left\{(\tfrac{1}{2}\rho u_{P_P})dy\frac{dz_i}{dz_P}+\frac{\mu dy}{\frac{1}{2}(\Delta x_P+\Delta x_W)}\right\}$$

$$+w_{N_P}\left\{(-\tfrac{1}{2}\rho v_{N_P})dx+\frac{\mu dx}{\frac{1}{2}(\Delta y_N+\Delta y_P)}\right\}$$

$$+w_{S_P}\left\{(\tfrac{1}{2}\rho v_{P_P})dx+\frac{\mu dx}{\frac{1}{2}(\Delta y_S+\Delta y_P)}\right\}-(p_D-p_P)\frac{dxdy}{dz_P}+\rho w_{P_P}w_{P_P}\frac{dxdy}{dz_P}$$

From Mass Conservation

$$\text{Mass Resid.} = \left(CE dz_0 - CW dz_i + CN dz_P - CS dz_P + CD - CV + \delta_{ln}\rho\left(\frac{u_{E_P} + u_{P_D}}{2}\right)\frac{dxdydz}{R_P}\right)$$

$$\text{so Mass Resid./}dz_P = CE\frac{dz_0}{dz_P} - CW\frac{dz_i}{dz_P} + CN - CS + \delta_{in}\tfrac{1}{2}(CE + CW)\frac{dx}{R_P}$$

Define

$$\hat{C}\hat{E} = CE\frac{dz_0}{dz_P}$$

$$\hat{C}\hat{W} = CW\frac{dz_i}{dz_P}$$

and

$$SMP = \hat{C}\hat{E} - \hat{C}\hat{W} + CN - CS + \delta_{ln}\tfrac{1}{2}(CE + CW)\frac{dx}{R_P}$$

Φ Momentum Equation. - Curved Duct Terms

$$\delta_{ln}\rho\frac{(u_{E_P} + u_{P_P})}{2}\frac{w_{P_P}}{R_P}(dxdyR_P d\theta) = \frac{\delta_{ln}}{R_P}\mu\left(\frac{w_{P_P} + w_{E_D}}{2} - \frac{w_{P_P} + w_{W_P}}{2}\right)dyR_P d\theta$$

$$+\delta_{ln}\mu\left[\frac{2}{R_P}\frac{\left(\frac{u_{E_P} + u_{P_P}}{2} - \frac{u_{E_v} + u_{P_v}}{2}\right)}{R_P d\theta}dxdyR_P d\theta\right] + \delta_{ln}\mu\left[\frac{-w_{P_D}}{R_P^2}\right]R_P d\theta dxdz$$

or

$$\tfrac{1}{2}\mu_{ln}\rho(u_{E_P} + u_{P_P})dxdyd\theta\, w_{P_P} = \delta_{ln}\mu\left[\frac{w_{E_P} - w_{W_P}}{2}\right]dyd\theta$$

$$+\delta_{ln}\frac{\mu}{R_P}\left[(u_{E_P} + u_{P_P} - u_{E_v} - u_{P_v})dxdy\right] - \delta_{ln}\frac{\mu}{R_P}w_{P_P} - w_{P_P}dxdyd\theta$$

Divide by $dz_P = R_P d\theta$

$$\tfrac{1}{2}\delta_{ln}\rho(u_{E_P}+u_{P_P})\frac{dxdy}{R_P}w_{P_P}=\delta_{ln}\mu\left[\frac{w_{E_P}-w_{w_P}}{2}\right]\frac{dy}{R_P}$$

$$+\delta_{ln}\frac{\mu}{R_P dz_P}\left[(u_{E_P}+u_{P_P}-u_{E_v}-u_{P_v})dxdy\right]-\delta_{ln}\frac{\mu}{R_P^2}dxdy\,w_{P_P}$$

Note: CE = GEdy and $GE=\rho u_{E_P}$

CW = GWdy and $GW=\rho u_{P_P}$

or

$$\delta_{in}\,w_{P_P}\left[\tfrac{1}{2}\rho u_{E_P}dy\frac{dxd\theta}{dz_P}\frac{dz_0}{dz_0}+\tfrac{1}{2}\rho u_{P_P}dy\frac{dxd\theta}{dz_P}\frac{dz_i}{dz_i}\right]=\delta_{ln}\mu\left[\frac{w_{E_P}-w_{W_P}}{2}\right]\frac{dy}{R_P}$$

$$+\delta_{ln}\frac{\mu}{R_P dz_P}\left[\left(u_{E_P}+u_{P_P}-u_{E_v}-u_{P_v}\right)dxdy\right]-\delta_{ln}\frac{\mu}{R_P^2}dxdy\,w_{P_P}$$

or

$$\delta_{ln}\left[\frac{\hat{C}\hat{E}}{2}\frac{dxd\theta}{dz_0}+\frac{\hat{C}\hat{W}}{2}\frac{dxd\theta}{dz_i}\right]w_{P_P}=\delta_{ln}\mu\left[\frac{w_{E_P}-w_{W_P}}{2}\right]\frac{dy}{R_P}$$

$$+\delta_{ln}\frac{\mu}{R_P dz_P}\left[\left(u_{E_P}+u_{P_P}-u_{E_v}-u_{P_v}\right)dxdy\right]-\delta_{ln}\frac{\mu}{R_P^2}dxdy\,w_{P_P}$$

These terms go into S_U and S_P.

Φ Momentum Equation - Toroidal Coordinates (Incompressible & μ = const.)

CONSERV. FORM

$$\rho\left(\frac{\partial wu}{\partial x}+\frac{\partial v w}{\partial y}+\frac{\partial w^2}{R^n\partial\theta}+\delta_{ln}\frac{2\rho u w}{R}\right)$$

$$\rho\left(u\frac{\partial w}{\partial x}+v\frac{\partial w}{\partial y}+\frac{w}{R^n}\frac{\partial w}{\partial\phi}+\delta_{ln}\frac{uw}{R}\right)=-\frac{\partial p}{R\partial\phi}+$$

$$\underbrace{\mu\left[\frac{\partial^2 w}{\partial x^2}+\frac{\delta_{ln}}{R}\frac{\partial w}{\partial x}+\frac{\partial^2 w}{\partial y^2}+\frac{\partial^2 w}{R^2\partial^2\phi}\right]}_{\nabla^2 w}+\delta_{ln}\mu\left[2\frac{\partial u}{R^2\partial\phi}-\frac{w}{R^2}\right]$$

Note: curved duct $n=1$ $\delta_{ln}=1$

straight duct $n = 0$ $\delta_{ln} = 0$ (Reduces to straight duct result)

Note: $R = R_P \equiv R_i + x_{w_P}$

So add the following terms:

$$2\delta_{ln}\rho\frac{\left(u_{E_P}+u_{P_P}\right)}{2}\frac{w_{P_P}}{R}(dxdyRd\theta)=\frac{\delta_{ln}}{R}\mu\left(\frac{w_{P_P}+w_{E_D}}{2}-\frac{w_{P_P}+w_{W_D}}{2}\right)dyRd\theta$$

$$+\delta_{ln}\mu\left[\frac{2}{R}\frac{\left(\frac{u_{E_P}+u_{P_P}}{2}-\frac{u_{E_V}+u_{P_V}}{2}\right)}{Rd\theta}dxdyRd\theta\right]$$

$$+\delta_{ln}\mu\left[-\frac{w_{P_P}}{R^2}\right]dxdyRd\theta$$

Additional Terms for Curved Φ Momentum Equation

$$\delta_{ln}\rho\left(u_{E_P}+u_{P_P}\right)dxdyd\theta w_P=\delta_{ln}\mu\left[\frac{w_{E_P}-w_{W_P}}{2}\right]dyd\theta$$

$$+\delta_{ln}\frac{\mu}{R}\left[\left(u_{E_P}+u_{P_P}-u_{E_V}-u_{P_V}\right)dxdy\right]-\frac{\delta_{ln}\mu w_{P_P}dxdy}{R}$$

Additional Terms:

$$(CE+CW)dxd\theta \Rightarrow \hat{A}_E\hat{A}_W$$

$$w_{P_P}\left[\overbrace{\delta_{\ln}\left\{\rho(u_{E_P}+u'_{P_P})dxdyd\theta\right.}+\frac{\mu}{R}dxdyd\theta\right]=$$

$$w_{E_P}\left[\delta_{\ln}\left\{\frac{\mu dyd\theta}{2}\right\}\right]-w_{w_P}\left[\delta_{\ln}\left\{\frac{\mu dyd\theta}{2}\right\}\right]$$

$$+\delta_{\ln}\frac{\mu}{R}\left[\left(u_{E_P}+u_{P_P}-u_{E_U}-u_{P_U}\right)dxdy\right]$$

For Mass Conserv. $\left(\frac{\partial u}{\partial x}+\frac{\partial v}{\partial y}+\frac{\partial w}{Rd\theta}+\delta_{\ln}\frac{u}{R}\right)dxdyRd\theta=0$

$$0=\rho\left(u_{out}-u_{in}\right)dyRd\theta+\rho\left(v_{out}-v_{in}\right)dxRd\theta+\rho\left(w_{out}-w_{in}\right)dxdy+\delta_{\ln}\rho\frac{u}{R}dxdyRd\theta$$

$$Rd\theta\left(CE-CW+CN-CS+CD-CU+\delta_{\ln}\rho\overbrace{\left(\frac{u_{E_P}+u_{P_P}}{2}\right)\frac{dxdy}{R}}^{\frac{1}{2}(CE+CW)\frac{dx}{R}}\right)=0$$

The coefficient of w_{P_P} becomes (on subtracting $\frac{\text{Continuity Eqn.}}{Rd\theta}$):

$$\left[\frac{1}{2}(CE-CW+CN-CS)+CU+\delta_{\ln}\left\{(CE+CW)\frac{dx}{R}+\frac{\mu}{R^2}dxdy\right\}\right.$$

$$\left.-\left(CE-CW+CN-CS+\delta_{\ln}\frac{1}{2}(CE+CW)\frac{dx}{R}\right)+DN+DS+DE+DW\right]$$

or

$$\left[\frac{1}{2}(-CE+CW-CN+CS)+\delta_{\ln}\frac{1}{2}(CE+CW)\frac{dx}{R}+CV+\delta_{\ln}\frac{\mu}{R^2}dxdy+DN+DS+DE+DW\right]$$

Then the coefficient of w_{P_P} becomes

$$w_{P_P}\left[(DN-\tfrac{1}{2}CN)+(DS+\tfrac{1}{2}CS)+(DE-\tfrac{1}{2}\hat{C}\hat{E})+(DW+\tfrac{1}{2}\hat{C}\hat{W})+SMP+CU+\frac{\mu}{R^2}dxdy\right]$$

Define $\hat{SP}(I,J) = -SMP - \frac{\mu}{R^2}dxdy; \quad CU = AU$

Then coeffficient of w_{P_P} is: $w_{P_P}\left[A_N + A_S + A_E + A_W - \hat{SP} + AU\right.$

- Use Hybrid Discretization, i.e. $A_E = AMAX(ABS(\frac{1}{2}CE); D_e) - \frac{1}{2}CE$, on $(\hat{A}_E \text{ and } D_E)$ and $(\hat{A}_W + D_W)$ for coefficient w_{P_D}.
- For coefficient of w_{P_P} use Hybrid on original (A_E and D_E) and (A_w and D_w).

  but let coefficient of $\quad w_{E_P} = A_E + \delta_{ln}\frac{\mu dy}{2R}$

  and let coefficient of $\quad w_{W_P} = A_W - \delta_{ln}\frac{\mu dy}{2R}$
- Let $S(I,J) = \delta_{ln}\frac{\mu}{R}\left[(u_{E_P} + u_{P_P} - u_{E_U} - u_{P_U})dxdy\right.$

  (was zero for straight duct)
- Redefine SP to $\hat{SP} = -SMP - \frac{\mu}{R^2}dxdy$.

Φ Momentum Equation - Toroidal Coordinates: (1Φ and Laminar)
for n = 1 curved duct

$$\rho\left(U_x\frac{\partial U_\phi}{\partial x} + U_y\frac{\partial U_\phi}{\partial y} + \frac{U_\phi}{R}\frac{\partial U_\phi}{\partial \phi} + \frac{U_x U_\phi}{R}\right) =$$

$$-\frac{\partial p}{R\partial\phi} + \frac{\partial \tau_{x\phi}}{\partial x} + \frac{\partial \tau_{y\phi}}{\partial y} + \left\{\frac{\partial \tau_{\phi\phi}}{R\partial\phi}\right\} + \frac{\partial \tau_{x\phi}}{R} + \rho g_\phi$$

Consider the Viscous Tenns:

$$\frac{\partial}{\partial x}\left[\frac{\partial U_\phi}{\partial x}-\frac{U_\phi}{R}+\frac{1}{R}\frac{\partial U_x}{\partial \phi}\right]+\mu\frac{\partial}{\partial y}\left[\frac{\partial U_\phi}{\partial y}+\frac{\partial U_y}{R\partial\phi}\right]+2\mu\frac{\partial}{R\partial\phi}\left[\frac{1}{R}\frac{\partial U_\phi}{\partial\phi}+\frac{U_x}{R}\right]$$

$$+2\mu\left[\left(\frac{1}{R}\frac{\partial U_\phi}{\partial x}-\frac{U_\phi}{R^2}\right)+\frac{1}{R^2}\frac{\partial U_x}{\partial\phi}\right]$$

or

$$\frac{\partial}{\partial x}\left[\frac{\partial U_\phi}{\partial x^2}-\frac{\partial U_\phi}{R\partial x}+\frac{U_\phi}{R^2}+\frac{\partial^2 U_x}{R\partial\phi\partial x}-\frac{1}{R^2}\frac{\partial U_x}{\partial\phi}\right]+\mu\left[\frac{\partial^2 U_\phi}{\partial y^2}+\frac{\partial^2 U_y}{R\partial\phi\partial y}\right]$$

$$+2\mu\left[\frac{\partial^2 U_\phi}{R^2\partial\phi^2}+\frac{\partial U_x}{R^2\partial\phi}\right]+2\mu\left[\left(\frac{1}{R}\frac{\partial U_\phi}{\partial x}-\frac{U_\phi}{R^2}+\frac{1}{R^2}\frac{\partial U_x}{\partial\phi}\right)\right]$$

Note: $\frac{\mu\partial}{R\partial\phi}$ (Continuity Eqn.) is: $\frac{\mu\partial}{R\partial\phi}\left(\frac{\partial U_x}{\partial x}+\frac{\partial U_y}{\partial y}+\frac{\partial U_\phi}{R\partial\phi}+\frac{U_x}{R}\right)=0$

or

$$\mu\left[\frac{\partial^2 U_x}{R\partial\phi\partial x}+\frac{\partial^2 U_y}{R\partial\phi\partial y}+\frac{\partial^2 U_\phi}{R^2\partial\phi^2}+\frac{\partial U_x}{R^2\partial\phi}\right]=0$$

So combining with Continuity Equation gives for Viscous terms:

$$\mu\left[\underbrace{\frac{\partial^2 U_\phi}{\partial x^2}+\frac{1}{R}\frac{\partial U_\phi}{\partial x}+\frac{\partial^2 U_\phi}{\partial y^2}+\frac{\partial^2 U_\phi}{R^2\partial\phi^2}}_{\nabla^2 U_\phi}\right]+\mu\left[-\frac{\partial U_\phi}{R\partial x}+\frac{U_\phi}{R^2}-\frac{1}{R^2}\frac{\partial U_x}{\partial\phi}\right]$$

$$+\mu\left[\frac{\partial U_x}{R^2\partial\phi}\right]+\mu\left[\frac{1}{R}\frac{\partial U_\phi}{\partial x}-\frac{2U_\phi}{R^2}+\frac{2}{R^2}\frac{\partial U_x}{\partial\phi}\right]=\mu\nabla^2 U_\phi+\mu\left[-\frac{U_\phi}{R^2}+\frac{2\partial U_x}{R^2\partial\phi}\right]$$

Thus the Momentum Equation becomes:

$$\rho\left[U_x\frac{\partial U_\phi}{\partial x}+U_y\frac{\partial U_\phi}{\partial y}+\frac{U_\phi}{R}\frac{\partial U_\phi}{\partial \phi}+\frac{U_xU_\phi}{R}\right]=-\frac{\partial p}{R\partial\phi}+\mu\nabla^2U_\phi+\mu\left[\frac{2\partial U_x}{R^2\partial\phi}-\frac{U_\phi}{R^2}\right]$$

Z Momentum Equation in Cartesian Coordinates (Incompr. and μ = const.)

$$\frac{\partial(\rho wu)}{\partial x}+\frac{\partial(\rho vw)}{\partial y}+\frac{\partial(\rho w^2)}{\partial z}=-\frac{\partial p}{\partial z}+\mu\frac{\partial^2 w}{\partial x^2}+\mu\frac{\partial^2 w}{\partial y^2} \qquad \text{(A)}$$

Discretize (A) using: central differences for all terms but convective term in z direction (use upwind).

$$\left\{\rho u_{E_P}\frac{(w_{P_P}+w_{E_P})}{2}-\rho u_{P_P}\frac{(w_{P_P}+w_{W_P})}{2}\right\}dy\underbrace{R_P d\theta}_{dz}$$

$$+\left\{\rho v_{N_P}\frac{(w_{P_P}+w_{N_P})}{2}-\rho v_{P_P}\frac{(w_{P_P}+w_{S_P})}{2}\right\}dx\underbrace{R_P d\theta}_{dz}$$

$$+\left\{\rho w_{P_P}w_{P_P}-\rho w_{P_P}\frac{(w_{P_P}+w_{P_U})}{2}\right\}dxdy=$$

$$-(p_D-p_P)dxdy+\mu\frac{dxdz}{dy}\left[\frac{(w_{E_P}-w_{P_P})}{\frac{(\Delta x_P+\Delta x_E)}{2}}-\frac{(w_{P_P}-w_{W_P})}{\frac{(\Delta x_P+\Delta x_W)}{2}}\right]$$

$$+\mu dxdz\left[\frac{w_{N_P}-w_{P_D}}{\frac{(\Delta y_N+\Delta y_P)}{2}}-\frac{w_{P_P}-w_{S_P}}{\frac{(\Delta y_S+\Delta y_P)}{2}}\right]$$

and divide by dz

$$w_{P_P}\left(\tfrac{1}{2}\rho u_{E_P}-\tfrac{1}{2}\rho u_{P_P}\right)dydz+\left(\tfrac{1}{2}\rho v_{N_P}-\tfrac{1}{2}\rho v_{P_P}\right)dxdz+\left(\rho w_{P_P}\right)\frac{dxdy}{dz}+\frac{\mu dzdy/dz}{\tfrac{1}{2}\left(\Delta x_P+\Delta x_E\right)}$$

$$+\frac{\mu dzdy/dz}{\tfrac{1}{2}\left(\Delta x_P+\Delta x_W\right)}+\frac{\mu dxdz}{\frac{\left(\Delta y_N+\Delta y_P\right)}{2}}+\frac{\mu dydz}{\frac{\left(\Delta y_S+\Delta y_P\right)}{2}}=$$

$$w_{E_P}\left\{\left(-\tfrac{1}{2}\rho u_{E_P}\right)dydz+\frac{\mu dydz}{\tfrac{1}{2}\left(\Delta x_P+\Delta x_E\right)}\right\}$$

$$-w_{W_P}\left\{\left(+\tfrac{1}{2}\rho u_{P_P}\right)dydz+\frac{\mu dydz}{\tfrac{1}{2}\left(\Delta x_P+\Delta x_W\right)}\right\}$$

$$+w_{N_P}\left\{\left(-\tfrac{1}{2}\rho v_{N_P}\right)+\frac{\mu dxdz}{\tfrac{1}{2}\left(\Delta y_N+\Delta y_P\right)}\right\}$$

$$w_{S_P}\left\{\left(\tfrac{1}{2}\rho v_{P_D}\right)dxdz+\frac{\mu dxdz}{\tfrac{1}{2}\left(\Delta y_S+\Delta y_P\right)}\right\}-\left(p_D-p_P\right)\frac{dxdy}{dz}+\left(\rho w_{P_P}w_{P_P}\right)\frac{dxdy}{dz}$$

Define:

$GN=\rho v_{N_P}$ $\quad GU=\rho w_{P_P}$ $\quad CN=GNdx$ $\quad CU=GU\dfrac{dxdy}{dz}$

$GS=\rho v_{P_P}$ $\quad CS=GPdx$

$GE=\rho u_{E_P}$ $\quad CE=GEdy$

$GW=\rho u_{P_P}$ $\quad CW=GWdy$

$DN=\dfrac{\mu dx}{\tfrac{1}{2}(\Delta y_p+\Delta y_N)}$ $\quad DE=\dfrac{\mu dy}{\tfrac{1}{2}(\Delta x_P+\Delta x_E)}$

$DS=\dfrac{\mu dx}{\tfrac{1}{2}(\Delta y_S+\Delta y_D)}$ $\quad DW=\dfrac{\mu dy}{\tfrac{1}{2}(\Delta x_P+\Delta x_W)}$

Hence (AA) becomes:

$$w_{P_P}\left\{\tfrac{1}{2}CE-\tfrac{1}{2}CW+\tfrac{1}{2}CN-\tfrac{1}{2}CS+\tfrac{1}{2}CU+DN+DS+DE+DW\right\}=$$

$$w_{E_P}\left\{-\tfrac{1}{2}CE+DE\right\}+w_{W_P}\left\{\tfrac{1}{2}CW+DW\right\}+w_{N_P}\left\{-\tfrac{1}{2}CN+DN\right\}$$

$$+w_{S_P}\left\{\tfrac{1}{2}CS+DS\right\}-(P(I,J)_D-(P(I,J)_P)\frac{dxdy}{dz}+CU\omega_{P_P}$$

From Mass Conservation:

$$\text{Mass Residual} = dz(CE-CW+CN-CS+CD-CU)$$

$$\text{Define}\quad SMP=\frac{\text{Mass Res.}}{dz}=(CE-CW+CN-CS)$$

Rewrite the coefficient of w_{P_P} as:

$$\left\{-\tfrac{1}{2}(CE-CW+CN-CS)+CU-\underbrace{(CE-CW+CN-CS)}+DN+DS+DE+DW\right\}$$

$$=0 \text{ by Continuity}$$

which can be rewritten as:

$$\left\{-\tfrac{1}{2}(CE+\tfrac{1}{2}CW-\tfrac{1}{2}CN+\tfrac{1}{2}CS)+CU+DN+DS+DE+DW\right.$$

Now add SMP to A_P {thus adding $w_{P_P}(i,j)SMP_i$} and add SMP U_{P_P} to SU (on RHS of the equation.) Thus the coefficient of w_{P_P} becomes

$$\left\{\underbrace{(DN-\tfrac{1}{2}CN)}_{\equiv A_N}+\underbrace{(DS+\tfrac{1}{2}CS)}_{\equiv A_S}+\underbrace{(DE-\tfrac{1}{2}CE)}_{\equiv A_E}-\underbrace{(DW+\tfrac{1}{2}CW)}_{\equiv A_W}+SMP+CU\right\}$$

Substitute the above in for a_{P_P} (i.e., the coefficient of w_{P_P}) to get:
and define: SP(I,J) = -SMP
AU = CU

$$w_{P_P}\{A_N + A_S + A_E + A_W + AU - SP(I,J)\} =$$
$$w_{E_P}A_E + w_{W_P}A_W + w_{N_P}A_N + w_{S_P}A_S$$
$$-(P(I,J)_D - P(I,J)_P)\frac{dxdy}{dz} + AUw_{P_U} + SMPw_{P_U}$$

Φ Momentum Equation

Φ Momentum Equation (Single Phase)

$$\rho\left(u\frac{\partial w}{\partial x} + v\frac{\partial w}{\partial y} + \frac{w}{R^n}\frac{\partial w}{\partial \phi} + \delta_{1n}\frac{uw}{R}\right) = -\frac{\partial p}{R^n\partial\phi} + \frac{\partial \tau_{x\phi}}{\partial x} + \frac{\partial \tau_{y\phi}}{\partial y} + \delta_{1n}\frac{2\tau_{x\phi}}{R} + \rho g\phi$$

Rewrite momentum equation in conserv. form by adding ($\rho w \times$ Continuity Equation) to the original momentum equation, i.e.

$$\rho w\frac{\partial u}{\partial x} + \rho w\cdot\frac{\partial v}{\partial y} + \rho w\cdot\frac{\partial w}{R^n\partial\phi} + \delta_{1n}\rho\frac{uw}{R} = 0$$

$$\frac{\partial(\rho wu)}{\partial x} + \frac{\partial(\rho vw)}{\partial y} + \frac{\partial(\rho w^2)}{R^n\partial\phi} + \delta_{1n}\frac{2\rho uw}{R} = -\frac{\partial p}{R^n\partial\phi} + \frac{\partial \tau_{x\phi}}{\partial x} + \frac{\partial \tau_{y\phi}}{\partial y} + \delta_{1n}\frac{2\tau_{x\phi}}{R} + \rho g\phi$$

Appendix II: X Momentum Equation

X Momentum Equation in Toroidal Coordinates (Single Phase)

$$\rho\left(u\frac{\partial u}{\partial x}+v\frac{\partial u}{\partial y}+\frac{w}{R^M}\frac{\partial u}{\partial \phi}-\delta_{ln}\frac{w^2}{R}\right)=-\frac{\partial p}{\partial x}+\mu\nabla^2 u-\mu\frac{u}{R^2}-2\mu\frac{\partial w}{R^2\partial\phi}$$

Consider first the X Momentum Equation in Cartesian Coordinates:
(refer to Figure 5.2-6 Control Volume for U velocity:
R_P is the radius to node P; R_W is the radius to node W)

$$\frac{\partial \rho u^2}{\partial x}+\frac{\partial(\rho uv)}{\partial y}+\frac{\partial(\rho uw)}{\partial z}=-\frac{\partial p}{\partial x}=+\text{ viscous terms}$$

$$\frac{\partial(\rho u^2)}{\partial x}+\frac{\partial(\rho uv)}{\partial y}+\frac{\partial(\rho uw)}{\partial z}=-\frac{\partial p}{\partial x}+\mu\left\{\frac{\partial^2 u}{\partial x^2}+\frac{\partial^2 u}{\partial y^2}\right\}\qquad\text{Eqn[X-1]}$$

Discretize Eqn[X-1] :

$$\left\{\frac{(\rho u_{E_U}+\rho u_{P_U})}{2}\frac{(u_{E_P}+u_{P_P})}{2}R_P-\frac{(\rho u_{w_U}+\rho u_{P_U})}{2}\frac{(u_{w_P}+u_{P_P})}{2}R_w\right\}d\theta dy$$

$$+\left\{\frac{(\rho v_{N_U}+\rho v_{NW_U})}{2}\frac{(u_{P_P}+u_{N_P})}{2}-\frac{(\rho v_{P_U}+\rho v_{W_U})}{2}\frac{(u_{P_P}+u_{s_P})}{2}\right\}\left(\frac{R_P+R_W}{2}\right)d\theta dx$$

$$\left\{\frac{(\rho w_{P_P}+\rho w_{w_P})}{2}u_{P_P}-\frac{(\rho w_{P_U}+\rho w_{w_U})}{2}u_{P_v}\right\}dxdy=$$

$$(p_P-p_w)\Delta y\left(\frac{R_w+R_P}{2}\right)d\theta+d\theta dy\frac{(R_w+R_P)}{2}\left\{\frac{\mu(u_E-u_P)_P}{\frac{1}{2}(\Delta x_P+\Delta x_E)}-\frac{\mu(u_P-u_w)}{\frac{1}{2}(\Delta x_P+\Delta x_w)}\right\}$$

$$+dxd\theta\frac{(R_w+R_P)}{2}\left\{\frac{\mu(u_{N_P}-u_{P_P})}{\frac{1}{2}(\Delta y_P+\Delta y_N)}-\frac{\mu(u_{P_P}-u_{s_P})}{\frac{1}{2}(\Delta y_P+\Delta y_s)}\right\}$$

Define:

$GN=\rho v_{N_v}=\rho v(1,J+1)$ $\qquad$ CN = 0.5(GN+GNW)dx

$GS = \rho v_{P_s} = \rho v(1, J)$ CS = 0.5(GS+GSW)dx

$GNW = \rho v_{NW_v} = \rho v(I-1, J+1)$ CE = 0.5(GE+GP)dy

$GE = \rho u_{E_v} = \rho u(I+1, J)$ CW = 0.5(GP+GW)dy

$GW = \rho u_{W_v} = \rho u(I-1, J)$ GU = ((ρw(I − 1, J) + ρw(I, J))

$GP = \rho u_{P_v} = \rho u(I, J)$ $CU = 0.5\ GU\ \frac{dxdy}{dz}$

$GSW = \rho v_{W_v} = \rho v(I-1, J)$ $CD = 0.5\ GD\ \frac{dxdy}{dz}$

$GD = (\rho w(I-1, J) + \rho w(I, J))_{Down}$

$DN = \frac{\mu dx}{\frac{1}{2}(\Delta y_P + \Delta y_N)}$ $DE = \frac{\mu dy}{\frac{1}{2}(\Delta x_P + \Delta x_E)}$

$DS = \frac{\mu dx}{\frac{1}{2}(\Delta y_P + \Delta y_s)}$ $DW = \frac{\mu dy}{\frac{1}{2}(\Delta x_P + \Delta x_w)}$

Thus the coefficient of u_{P_P} is:

$$\left\{\frac{1}{2}(CE - CW + CN - CS) + CU + DN + DS + DE + DW\right.$$

Rewrite as:

$$\left\{\frac{1}{2}(CE-CW+CN-CS)-(CE-CW+CN-CS+CD-CU)+CU+(DN+DS+DE+DW)\right\}$$

or

$$\left\{\frac{1}{2}(-CE+CW-CN+CS)+CU+(DN+DS+DE+DW)\right\}$$

since from Mass Conserv: (CE - CW + CN - CS + CD - CU) = 0

Mass Residual = dz(CE - CW + CN - CS + CD - CU)

$$\text{Define SMP} = \frac{\text{Mass Res}}{dz} = \text{CE - CW + CN - CS}$$

Add SMP to the coefficient of A_P {i.e., LHS of Eqn.} and SMP $U_{upstream}$ to RNS of the equation. Hence coefficient of u_{Pp} becomes:

$$\left\{\frac{1}{2}(-CE + CW - CN + CS) + SMP + CU + (DN + DS + DE + DW)\right.$$

or

$$u_P\left\{DN - \tfrac{1}{2}CN) + (DS + \tfrac{1}{2}CS) + (DE - \tfrac{1}{2}CE) + (DW + \tfrac{1}{2}CW) + CU - SMP\right.$$

or

$$u_P\{A_N + A_S + A_E + A_W + AU + SMP$$

where: SP = -SMP; A_N = DN - $\frac{1}{2}$CN; A_S = DS + $\frac{1}{2}$CS; etc.

Further, define

$$A'_{E_P} = \frac{A_{E_P}}{A_{P_P}};\ A'_{W_P} = \frac{A_{W_P}}{A_{P_P}};\ \text{etc.}$$

and

$$A_P = A_N + A_S + A_E + A_W + AU - SP(I,J).$$

Then the X Momentum Equation becomes:

$$u_{P_P} = A'_{E_P} u_{E_P} + A'_{W_P} u_{W_P} + A'_{N_P} u_{N_P} + A'_{S_P} u_{S_P}$$

$$\underbrace{+\frac{u_{P_P} A_U}{A_P} + \frac{dy}{A_{P_P}}\{P(I-1,J) - P(I,J)\} + \frac{SMP * u_{P_U}}{A_{P_P}}}_{SU(I,J)}$$

Equation Formulation (How to handle the viscous terms)

For incompressible flow, u equation is

$$---= -\frac{\partial p}{\partial x} + \underbrace{\frac{\partial \tau_{xx}}{\partial x} + \frac{\partial \tau_{xy}}{\partial y} + \frac{\partial \tau_{xz}}{\partial z}}_{(A)}$$

$$\tau_{xx} = 2\mu \frac{\partial u}{\partial x}$$

$$\tau_{xy} = \mu\left\{\frac{\partial u}{\partial y} + \frac{\partial v}{\partial x}\right\}$$

$$\tau_{xz} = \mu\left\{\frac{\partial w}{\partial x} + \frac{\partial u}{\partial z}\right\}$$

so that (A) gives: (for μ = const.)

$$= 2\mu \frac{\partial^2 u}{\partial x^2} + \mu \frac{\partial^2 u}{\partial y^2} + \mu \frac{\partial^2 v}{\partial x \partial y} + \mu \frac{\partial^2 w}{\partial x \partial z} + \mu \frac{\partial^2 u}{\partial z^2}$$

$$= \mu \frac{\partial^2 u}{\partial x^2} + \mu \frac{\partial^2 u}{\partial x^2} + \mu \frac{\partial^2 u}{\partial y^2} + \mu \frac{\partial^2 v}{\partial x \partial y} + \mu \frac{\partial^2 w}{\partial x \partial z} + \mu \frac{\partial^2 u}{\partial z^2}$$

$$= \mu\left\{\frac{\partial^2 u}{\partial x^2} + \frac{\partial^2 u}{\partial y^2} + \mu \frac{\partial^2 u}{\partial z^2}\right\} + \mu \frac{\partial}{\partial x}\underbrace{\left(\frac{\partial v}{\partial x} + \frac{\partial v}{\partial y} + \frac{\partial w}{\partial z}\right)}$$

$= 0$ by continuity

Hence for Cartesian coordinates and no body forces, RHS of momentum equation becomes

$$= -\frac{\partial p}{\partial x} + \mu\left\{\frac{\partial^2 u}{\partial x^2} + \frac{\partial^2 u}{\partial y^2} + \frac{\partial^2 u}{\partial z^2}\right\}$$

Partially Parabolic:
Neglect diffusion in z direction
compared to the convective flow

$$= -\frac{\partial p}{\partial x} + \mu \frac{\partial}{\partial x}\left(\frac{\partial u}{\partial x}\right) + \mu \frac{\partial}{\partial y}\left(\frac{\partial u}{\partial y}\right)$$

Note: no
$\frac{\partial}{\partial y}\left(\mu \frac{\partial v}{\partial x}\right)$ TERM

Viscous Terms in Momentum Equation for 2ϕ Flow (In Cartesian Coordinates)

$$\nabla \cdot \alpha\tau$$

Consider X Momentum Equation

$$= \underbrace{\frac{\partial(\alpha\tau_{xx})}{\partial x} + \frac{\partial(\alpha\tau_{xy})}{\partial y} + \frac{\partial(\alpha\tau_{xz})}{\partial z}}_{(A)}$$

where

$$\tau_{xx} = 2\mu\frac{\partial u}{\partial x}$$

$$\tau_{xy} = \mu\left(\frac{\partial u}{\partial y} + \frac{\partial v}{\partial x}\right)$$

$$\tau_{xz} = \mu\left(\frac{\partial w}{\partial x} + \frac{\partial u}{\partial z}\right)$$

so that (A) gives: (for μ = constant)

$$= 2\mu\alpha\frac{\partial^2 u}{\partial x^2} + \mu\alpha\frac{\partial^2 u}{\partial y^2} + \mu\alpha\frac{\partial^2 v}{\partial x\partial y} + \mu\alpha\frac{\partial^2 w}{\partial x\partial z} + \mu\alpha\frac{\partial^2 u}{\partial z^2}$$
$$\underbrace{+ 2\mu\frac{\partial u}{\partial x}\frac{\partial \alpha}{\partial x} + \mu\frac{\partial u}{\partial y}\frac{\partial \alpha}{\partial y} + \mu\frac{\partial v}{\partial x}\frac{\partial \alpha}{\partial y} + \mu\frac{\partial w}{\partial x}\frac{\partial \alpha}{\partial z} + \mu\frac{\partial u}{\partial z}\frac{\partial \alpha}{\partial z}}_{= \text{Terms (B)}} \qquad (A_1)$$

Note: Continuity Equation is

$$\frac{\partial(\rho\alpha u)}{\partial x} + \frac{\partial(\rho\alpha v)}{\partial y} + \frac{\partial(\rho\alpha w)}{\partial z} = 0$$

Write (A_1) as:

$$= \mu\alpha\left[\frac{\partial^2 u}{\partial x} + \frac{\partial^2 u}{\partial y^2} + \frac{\partial^2 u}{\partial z^2}\right] + \mu\alpha\frac{\partial}{\partial x}\left[\frac{\partial u}{\partial x} + \frac{\partial v}{\partial y} + \frac{\partial w}{\partial z}\right]$$
$$+ \text{Terms (B)}$$

$$= \mu\alpha\left[\frac{\partial^2 u}{\partial x^2}+\frac{\partial^2 u}{\partial y^2}+\frac{\partial^2 u}{\partial z^2}\right]+\mu\frac{\partial}{\partial x}\left[\frac{\partial(\alpha u)}{\partial x}+\frac{\partial(\alpha v)}{\partial y}+\frac{\partial(\partial w)}{\partial z}\right]= \text{ 0 by Continuity}$$

$$-\mu\frac{\partial}{\partial x}\left[u\frac{\partial\alpha}{\partial x}+v\frac{\partial\alpha}{\partial y}+w\frac{\partial\alpha}{\partial z}\right]-\mu\frac{\partial\alpha}{\partial x}\frac{\partial u}{\partial x}-\mu\frac{\partial v}{\partial y}\frac{\partial\alpha}{\partial x}-\mu\frac{\partial w}{\partial z}\frac{\partial\alpha}{\partial x}$$

+ Terms (B)

Hence, can write (A_1) as:

$$= \mu\alpha\left[\frac{\partial^2 u}{\partial x^2}+\frac{\partial^2 u}{\partial y^2}+\frac{\partial^2 u}{\partial z^2}\right]-\mu\frac{\partial u}{\partial x}\frac{\partial\alpha}{\partial x}-\mu u\frac{\partial^2\alpha}{\partial x^2}-\mu\frac{\partial v}{\partial x}\frac{\partial\alpha}{\partial y}-\mu v\frac{\partial^2\alpha}{\partial x\partial y}$$

$$-\mu\frac{\partial w}{\partial x}\frac{\partial\alpha}{\partial z}-\mu w\frac{\partial^2\alpha}{\partial x\partial z}$$

$$+\mu\frac{\partial u}{\partial x}\frac{\partial\alpha}{\partial x}+\mu\frac{\partial u}{\partial y}\frac{\partial\alpha}{\partial y}+\mu\frac{\partial v}{\partial x}\frac{\partial\alpha}{\partial y}+\mu\frac{\partial w}{\partial x}\frac{\partial\alpha}{\partial z}+\mu\frac{\partial u}{\partial z}\frac{\partial\alpha}{\partial z}$$

Note that:

$$\mu\frac{\partial}{\partial x}\left[\frac{\partial(\alpha u)}{\partial x}+\frac{\partial(\alpha v)}{\partial y}+\frac{\partial(\alpha w)}{\partial z}\right]$$

can be expanded to:

$$\mu\frac{\partial}{\partial x}\left[u\frac{\partial\alpha}{\partial x}+\alpha\frac{\partial u}{\partial x}+v\frac{\partial\alpha}{\partial y}+\alpha\frac{\partial v}{\partial y}+w\frac{\partial\alpha}{\partial z}+\alpha\frac{\partial w}{\partial z}\right]$$

which is:

$$\mu\frac{\partial}{\partial x}\left[u\frac{\partial\alpha}{\partial x}+v\frac{\partial\alpha}{\partial y}+w\frac{\partial\alpha}{\partial z}\right]+\underbrace{\mu\alpha\frac{\partial}{\partial x}\left[\frac{\partial u}{\partial x}+\frac{\partial v}{\partial y}+\frac{\partial w}{\partial z}\right]}$$

Presently in X Mom. Eqn.

$$+\mu\frac{\partial\alpha}{\partial x}\frac{\partial u}{\partial x}+\mu\frac{\partial v}{\partial y}\frac{\partial\alpha}{\partial x}+\mu\frac{\partial w}{\partial z}\frac{\partial\alpha}{\partial x}$$

Therefore:

$$\underbrace{\alpha\frac{\partial}{\partial x}\left[\frac{\partial u}{\partial x}+\frac{\partial v}{\partial y}+\frac{\partial w}{\partial z}\right]}=\mu\frac{\partial}{\partial x}\left[\frac{\partial(\alpha u)}{\partial x}+\frac{\partial(\alpha v)}{\partial y}+\frac{\partial(\alpha w)}{\partial z}\right]$$

Presently in X Mom. Eqn.

$$-\mu\frac{\partial}{\partial x}\left[u\frac{\partial\alpha}{\partial x}+v\frac{\partial\alpha}{\partial y}+w\frac{\partial\alpha}{\partial z}\right]$$

$$-\mu\frac{\partial\alpha}{\partial x}\frac{\partial u}{\partial x}-\mu\frac{\partial v}{\partial y}\frac{\partial\alpha}{\partial x}-\mu\frac{\partial w}{\partial z}\frac{\partial\alpha}{\partial x}$$

Since (A_1) can be written as

$$=\mu\alpha\left[\frac{\partial^2 u}{\partial x^2}+\frac{\partial^2 u}{\partial y^2}+\frac{\partial^2 u}{\partial z^2}\right]$$

$$+\mu\frac{\partial u}{\partial x}\frac{\partial\alpha}{\partial x}+\mu\frac{\partial u}{\partial y}\frac{\partial\alpha}{\partial y}+\mu\frac{\partial u}{\partial z}\frac{\partial\alpha}{\partial z}$$

$$-\mu\left[u\frac{\partial^2\alpha}{\partial x^2}+v\frac{\partial^2\alpha}{\partial x\partial y}+w\frac{\partial^2\alpha}{\partial x\partial z}\right]$$

$$=\mu\alpha\left[\frac{\partial^2 u}{\partial x^2}+\frac{\partial u}{\partial y^2}+\frac{\partial^2 u}{\partial z^2}\right]+\mu\frac{\partial u}{\partial x}\frac{\partial\alpha}{\partial x}+\mu\frac{\partial u}{\partial y}\frac{\partial\alpha}{\partial y}+\mu\frac{\partial u}{\partial z}\frac{\partial\alpha}{\partial z}$$

$$\underbrace{-\mu\left[u\frac{\partial}{\partial x}\left(\frac{\partial\alpha}{\partial x}\right)+v\frac{\partial}{\partial x}\left(\frac{\partial\alpha}{\partial y}\right)+w\frac{\partial}{\partial x}\left(\frac{\partial\alpha}{\partial z}\right)\right]}$$

$$-\left[u\frac{\partial}{\partial x}\left(\frac{\partial\alpha}{\partial x}\right)+v\frac{\partial}{\partial y}\left(\frac{\partial\alpha}{\partial x}\right)+w\frac{\partial}{\partial z}\left(\frac{\partial\alpha}{\partial x}\right)\right]$$

$$(A_1)=\mu\alpha\left[\frac{\partial^2 u}{\partial x^2}+\frac{\partial^2 u}{\partial y^2}+\frac{\partial^2 u}{\partial z^2}\right]+\underbrace{\mu\nabla u\cdot\nabla\alpha-u\bar{V}\cdot\nabla\left(\frac{\partial\alpha}{\alpha x}\right)}$$

Note: $\nabla\bar{u}\cdot\nabla\alpha-\bar{u}\cdot\nabla\frac{\partial\alpha}{\partial x}$; From Continuity $\frac{\partial(\alpha u)}{\partial x_i}=0$

$$\rightarrow u\frac{\partial\alpha}{\partial x}=\alpha\frac{\partial u}{\partial x}$$

$\underbrace{\frac{\partial u}{\partial x}\frac{\partial\alpha}{\partial x}}$ $-$ $\underbrace{u\frac{\partial}{\partial x}\left(\frac{\partial\alpha}{\partial x}\right)+v\frac{\partial}{\partial y}\left(\frac{\partial\alpha}{\partial x}\right)}$

$\left(\frac{u}{\alpha}\frac{\partial\alpha}{\partial x}\right)\frac{\partial\alpha}{\partial x}$ $\quad u\frac{\partial}{\partial x}\left(\frac{\partial\alpha}{\partial x}\right)+v\frac{\partial}{\partial x}\left(\frac{\partial\alpha}{\partial y}\right)$

$\underbrace{\textit{and}\ \frac{\partial\alpha}{\partial x}\ \text{is small}\equiv\varepsilon}_{\varepsilon^2=\varepsilon_1}$ $\quad \underbrace{\approx\frac{\partial}{\partial x}\left[\frac{\partial(\alpha u)}{\partial x}+\frac{\partial}{\partial y}(\alpha v)\right]}_{\textit{Hence}\equiv\varepsilon_2}$ $= 0$ by Continuity

$$\Rightarrow\varepsilon_1-\varepsilon_2\approx 0$$

X Momentum Equation in Toroidal Coordinates (Single Phase)

$$\rho\left(\mu\frac{\partial u}{\partial x}+v\frac{\partial u}{\partial y}+\frac{w}{R''}\frac{\partial u}{\partial\phi}-\delta_{ln}\frac{w^2}{R}\right)=-\frac{\partial p}{\partial x}+\mu\nabla^2 u-\mu\frac{u}{R^2}-2\mu\frac{\partial w}{R^2\partial\phi}$$

Note: $u\{\text{Continuity Equation}\}=0=u\frac{\partial u}{\partial x}+u\frac{\partial v}{\partial y}+u\frac{\partial w}{R\partial\phi}+\delta_{ln}\frac{u^2}{R}=0$

Hence:

$$\rho\left(\frac{\partial u^2}{\partial x}+\frac{\partial uw}{\partial y}+u\frac{\partial uw}{R\partial\phi}-\delta_{ln}\frac{w^2}{R}+\delta_{ln}\frac{u^2}{R}\right)=-\frac{\partial p}{\partial x}$$

$$+\mu\left(\frac{\partial^2 u}{\partial x^2}+\delta_{ln}\frac{\partial u}{R\partial x}+\frac{\partial^2 y}{\partial y^2}-2\delta_{ln}\frac{\partial w}{R^2\partial\phi}-\delta_{ln}\frac{u}{R^2}\right)$$

Note: $R = R_i + \frac{(R_P + R_w)}{2}$

So add to the terms of Cartesian development the following terms:

$$-\delta_{ln}\rho\frac{w^2}{R}+\delta_{ln}\rho\frac{u^2}{R}=\mu\frac{\partial u}{R\partial x}-2\mu\frac{\partial w}{R^2\partial\phi}-\mu\frac{u}{R^2}$$

or

$$-\delta_{ln}\frac{\rho}{R}\left(\frac{w_{P_v}+w_{w_v}}{2}\right)^2+\delta_{ln}\rho\frac{u_{P_v}+u_{P_P}}{R}=\frac{\mu}{R}\delta_{ln}\frac{\left(\frac{u_{P_P}+u_{E_P}}{2}-\frac{u_{P_P}+u_{w_P}}{2}\right)}{\Delta x}$$

$$\frac{-\frac{2\mu\delta_{ln}}{R}\left(\frac{w_{P_v}+w_{w_v}}{2}-\frac{w_{P_{vv}}+w_{w_{vv}}}{2}\right)}{R\partial\phi}-\frac{\delta_{ln}}{R^2}\mu u_{P_P}$$

Then the additional terms for X Momentum Equation are:

$$u_{P_P}\left[\delta_{ln}\frac{\rho u_{P_v}}{R}+\delta_{ln}\frac{\mu}{R^2}\right]dxdyRd\theta$$

$$=u_{E_P}\left[\frac{\delta_{ln}\mu}{2R\Delta x}\right]dxdyRd\theta-u_{w_P}\left[\frac{\delta_{ln}\mu}{2R\Delta x}\right]dxdyRd\theta+\delta_{ln}\frac{\rho}{R}\left[\frac{w_{P_v}+w_{w_U}}{2}\right]^2dxdyRd\theta$$

$$-\delta_{ln}\frac{\mu}{R}\left[\frac{w_{P_v}+w_{w_v}+w_{P_U}+w_{w_U}}{R\Delta\theta}\right]dxdyRd\theta$$

From Mass Conservation: u_{p_p} (Continuity Equation):

$$u_{P_P}\left\{Rd\theta\left(CE-CW+CN-CS+CD-CU+\delta_{ln}\frac{u_{P_U}}{R}dxdy\right)\right\}=0$$

Divide both the additional terms of the Momentum Equation and Continuity Equation by Rdθ:

Subtract Continuity Equation from Coefficient of u_{p_p} to get

$$u_{P_P}\left\{\tfrac{1}{2}(-CE+CW-CN+CS)+SMP+CU+(DN+DS+DE+DW)+\delta_{ln}\frac{\mu}{R^2}dxdy\right\}$$

Note: AE; AW; etc., defined as for straight duct

$$=u_{E_P}\left[\text{as before }+\delta_{ln}\frac{\mu\Delta y}{2R}\right]+u_{w_P}\left[\text{as before }-\delta_{ln}\frac{\mu dy}{2R}\right]$$

$$\underbrace{+\delta_{ln}\frac{\rho}{R}\left(\frac{w_{P_P}+w_{w_U}}{2}\right)^2 dxdy-\delta_{ln}\frac{\mu}{R}\left[\frac{w_{P_P}+w_{w_P}-w_{P_U}-w_{w_U}}{R\Delta\theta}\right]}$$

Source terms for S_u

X Momentum Equation - Toroidal Coordinates: Viscous Terms (Single Phase) for n = 1 curved duct

Consider RHS of Momentum Equation

$$-\frac{\partial p}{\partial x}+\frac{\partial \tau_{xx}}{\partial x}+\frac{\partial \tau_{xy}}{\partial y}+\left\{\frac{\partial \tau_{x\phi}}{R\partial\phi}\right\}+\frac{\tau_{xx}-\tau_{\theta\theta}}{R}+\rho g_x$$

↓

can neglect
with partially
parabolic

The viscous terms give

$$\frac{\partial}{\partial x}\left(2\mu\frac{\partial U_x}{\partial x}\right)+\mu\frac{\partial}{\partial y}\left(\frac{\partial U_x}{\partial y}+\frac{\partial U_y}{\partial x}\right)+\mu\frac{\partial}{\partial\phi}\left(\frac{\partial}{\partial x}\frac{U_\phi}{R}\right)+\frac{1}{R^2}\frac{\partial^2 U_x}{\partial\phi^2}$$

$$\underbrace{+\frac{2\mu}{R}\frac{\partial U_x}{\partial x}}_{\tau_{xx}}\underbrace{-\frac{2\mu}{R^2}\frac{\partial U_\phi}{\partial\phi}-2\mu\frac{U_x}{R^2}}_{-\tau_{\theta\theta}}$$

or

$$\mu\left[2\frac{d^2U_x}{\partial x^2}+\frac{\partial^2U_x}{\partial y^2}+\frac{\partial^2U_y}{\partial x\partial y}+\frac{\partial^2U_\phi}{\partial xR\partial\theta}+\frac{1}{R^2}\frac{\partial^2U_x}{\partial\phi^2}+\frac{2\mu}{R}\frac{\partial U_x}{\partial x}\right.$$

$$\left.-\frac{2}{R^2}\frac{\partial U_\phi}{\partial\phi}-2\mu\frac{U_x}{R^2}\right]$$

Note: $\frac{\partial}{\partial x}$ (Continuity Equation) is:

$$\frac{\partial}{\partial x}\left[\frac{\partial U_x}{\partial x}+\frac{\partial U_y}{\partial y}+\frac{\partial U_\phi}{R\partial\theta}+\frac{U_x}{R}\right]=0$$

$$\left[\frac{\partial^2U_x}{\partial x^2}+\frac{\partial^2U_y}{\partial x\partial y}+\frac{\partial^2U_\phi}{R\partial\phi\partial x}-\frac{1}{R^2}+\frac{\partial U_\phi}{\partial\phi}+\frac{1}{R}\frac{\partial U_x}{\partial x}-\frac{U_x}{R^2}\right]=0$$

Hence the viscous terms become:

$$\mu\left[\frac{\partial^2U_x}{\partial x^2}+\frac{\partial^2U_x}{\partial y^2}+\frac{1}{R^2}\frac{\partial^2U_x}{\partial\theta^2}-\left(\frac{2\frac{\partial U_\phi}{R\partial\phi}+\frac{U_x}{R}}{R}\right)\right.$$

so that the X Momentum Equation is:

$$\rho\left(U_x\frac{\partial U_x}{\partial x}+V_y\frac{\partial U_x}{\partial y}+\frac{U_\phi}{R}\frac{\partial U_x}{\partial\phi}-\frac{U_\phi^2}{R}\right)$$

$$=-\frac{\partial p}{\partial x}+\underbrace{\mu\left\{\frac{\partial^2U_x}{\partial x^2}+\frac{\partial^2U_x}{\partial y^2}+\frac{1}{R^2}\frac{\partial^2U_x}{\partial\phi^2}+\frac{\partial U_x}{R\partial x}\right\}}_{\mu\nabla^2U_x}-\underbrace{\left\{\frac{2\mu\frac{\partial U_\phi}{R\partial\phi}+\mu\frac{U_x}{R}}{R}\right\}}$$

↓

& then neglect with
Part. Parabolic

or

$$\rho\left(U_x\frac{\partial U_x}{\partial x}+U_y\frac{\partial U_x}{\partial y}+\frac{U_\phi}{R}\frac{\partial U_x}{\partial \phi}-\frac{U_\phi^2}{R}\right)$$

$$=-\frac{\partial p}{\partial x}+\mu\nabla^2 U_x-\mu\frac{U_x}{R^2}-2\mu\frac{\partial U_\phi}{R^2\partial\phi}$$

Appendix III: Y Momentum Equation

Y Momentum Equation in Toroidal Coordinates

$$U_x \frac{\partial U_y}{\partial x} + U_y \frac{\partial U_y}{\partial y} + \frac{U_\phi}{R''} \frac{\partial U_y}{\partial \phi} = -\frac{\partial p}{\partial y} + \frac{\partial \tau_{xy}}{\partial x} + \frac{\partial \tau_{yy}}{\partial y} + \delta_{ln} \frac{\tau_{xy}}{R} + \rho g$$

Y Momentum Equation (Terms that are Straight duct-like only)

$$R_{\text{local inner}} = \frac{x_P + x_w}{2} + \overline{R}_i = \frac{x_i + x_{i-1}}{2} + \overline{R}_i$$

$$R_{\text{local inner}} = \frac{x_P + x_E}{2} + \overline{R}_i = \frac{x_i + x_{i+1}}{2} + \overline{R}_i$$

Let $R_0 = R_{\text{local outer}}$ $\quad R_i = R_{\text{local inner}}$ $\quad R_P = \overline{R}_{\text{local}}$

$dz_0 = R_0 \Delta\theta$ $\quad dz_i = R_i \Delta\theta$ $\quad dz_P = R_P \Delta\theta$

Then:

$$\left\{\left(\frac{\rho u_{E_U} + \rho u_{SEU}}{2}\right)\left(\frac{v_{P_P} + v_{E_P}}{2\Delta x_E}\right) dy dz_0 dx - \left(\frac{\rho u_{P_U} + \rho u_{S_U}}{2}\right)\left(\frac{v_{P_P} + v_{W_P}}{2\Delta x_P}\right) dy dz_i dx\right\}$$

$$+\left\{\left(\frac{\rho v_{P_U} + \rho v_{NU}}{2}\right)\left(\frac{v_{P_P} + v_{N_P}}{2}\right) - \left(\frac{\rho v_{P_U} + \rho v_{S_U}}{2}\right)\left(\frac{v_{P_P} + v_{S_P}}{2}\right)\right\} dx dz_P$$

$$+\left\{\left(\frac{\rho w_{P_U} + \rho w_{SU}}{2}\right)\left(\frac{v_{P_D} + v_{P_P}}{2}\right) - \left(\frac{\rho w_{P_U} + \rho w_{S_U}}{2}\right)\left(\frac{v_{P_U} + v_{P_P}}{2}\right)\right\} dx dy = -(P_P - P_S) dx dz$$

$$+\mu\left[\frac{(v_{E_P} - v_{P_P})}{\frac{1}{2}(\delta x + \delta x_E)} - \frac{(v_{P_P} - v_{W_P})}{\frac{1}{2}(\delta x + \delta x_W)}\right] dy dz_P + \mu\left[\frac{(v_{N_P} - v_{P_P})}{\frac{1}{2}(\delta y + \delta y_N)} - \frac{(v_{P_P} - v_{S_P})}{\frac{1}{2}(\delta y_P + \delta y_S)}\right] dx$$

Divide by $dz_P \Rightarrow$ (Will cancel everywhere but for 1st {}).

Define $\hat{C}\hat{E} = CE\frac{dz_o}{dz_P}$

$$\hat{C}\hat{W} = CW\frac{dz_i}{dz_P}$$

and

$$SMP = \hat{C}\hat{E} - \hat{C}\hat{W} + CN - CS + \delta_{ln}\tfrac{1}{2}(CE + CW)\frac{dx}{R_P}$$

Y Momentum Equation (Extra Curvature Terms /dz_P)

$$\delta_{ln}\left[\left(\frac{\rho u_{E_U} + \rho u_{SE_U}}{4R_P}\right)v_{P_P}dxdyR_Pd\theta + \left(\frac{\rho u_{U_U} + \rho u_{S_U}}{4R_P}\right)v_{P_P}dxdyR_Pd\theta\right] =$$

$$\mu\delta_{ln}\frac{\left(\frac{v_{P_P} + v_{E_P}}{2} - \frac{v_{P_P} + v_{W_P}}{2}\right)}{R_Pdx}R_Pd\theta dxdy$$

or

$$\delta_{ln}\left[\tfrac{1}{2}\frac{CE\,dx}{R_P}\left(\frac{dz_0}{dz_0}\right)\left(\frac{d\theta}{d\theta}\right)v_{P_P} + \tfrac{1}{2}\frac{CWdx}{R_P}\left(\frac{dz_i}{dz_i}\right)\left(\frac{d\theta}{d\theta}\right)v_{P_P}\right] = \frac{\mu}{2}\delta_{ln}\left(v_{E_P} - v_{W_P}\right)\frac{dy}{R_P}$$

Note: $CE\frac{dz_0}{R_Pd\theta} = \hat{C}\hat{E}$

or

$$\delta_{ln}\left[\tfrac{1}{2}\hat{C}\hat{E}\frac{dxd\theta}{dz_0} + \tfrac{1}{2}\hat{C}\hat{W}\frac{dxd\theta}{dz_i}\right]v_{P_P} = \delta_{ln}\frac{\mu}{2}\left(v_{E_P} - v_{W_P}\right)\frac{dy}{R_P}$$

These terms go into S_U and S_P.

Y Momentum Equation (Toroidal;1ϕ)

$$U_x\frac{\partial U_y}{\partial x} + U_y\frac{\partial U_y}{\partial y} + \frac{U_\phi}{R^n}\frac{\partial U_y}{\partial \phi} = -\frac{\partial p}{\partial y} + \frac{\partial \tau_{xy}}{\partial x} + \frac{\partial \tau_{yy}}{\partial y} + \delta_{ln}\frac{\tau_{xy}}{R} + \rho g_y$$

Note: $U_y\{\text{Continuity Equation}\} = 0 = U_y\frac{\partial U_x}{\partial x} + U_y\frac{\partial U_y}{\partial y} + U_y\frac{\partial U_\phi}{R^n\partial\phi} + \delta_{ln}\frac{U_yU_x}{R}$.

Hence the Y Momentum Eqn. can be written as:

$$\frac{\partial U_x U_y}{\partial x}+\frac{\partial U_y^2}{\partial y}+\frac{\partial U_\phi U_y}{R^n \partial \phi}+\delta_{1n}\frac{U_y U_x}{R}=-\frac{\partial p}{\partial y}+\frac{\partial \tau_{xy}}{\partial x}+\frac{\partial \tau_{yy}}{\partial y}+\delta_{1n}\frac{\tau_{xy}}{R}+\rho g_y$$

or

$$\frac{\partial (U_x U_y)}{\partial x}+\frac{\partial U_y^2}{\partial y}+\frac{\partial U_\phi U_y}{R^n \partial \phi}+\delta_{1n}\frac{U_y U_x}{R}=-\frac{\partial p}{\partial y}+\mu\left[\frac{\partial^2 U_y}{\partial x^2}+\frac{\partial^2 U_y}{\partial y^2}+\frac{\delta_{1n}\partial^2 U_y}{R\partial x}\right]+\rho g_y$$

and

$$R \equiv R_i+\left(\frac{R_P+R_W}{2}\right).$$

So new additional terms are:

$$\delta_{1n}\rho\frac{v_{P_P}(u_{E_U}+u_{P_U}+u_{SE_U}+u_{S_U})\Delta Vol.}{4R}=\delta_{1n}\frac{\left(\frac{v_{P_P}+v_{E_P}}{2}-\frac{v_{P_P}+v_{W_P}}{2}\right)}{R\Delta x}\Delta Vol.$$

or

$$\delta_{1n}\rho v_{P_P}\frac{(u_{E_U}+u_{P_U}+u_{SE_U}+u_{S_U})}{4R}\{dxdyRd\theta\}=(\delta_{1n}\mu)\frac{(v_{E_P}-v_{W_P})}{2R\Delta x}(dxdyRd\theta).$$

Note:

$$\rho u_{SE_U}=GSE$$
$$\rho u_{S_U}=GSW$$
$$\rho u_{P_U}=GW$$
$$\rho u_{E_U}=GE$$

and

$$CE=0.5(GE+GSE)\delta y$$
$$CW=0.5(GW+GSW)\delta y.$$

Thus the additional terms can be written

$$v_{P_P}\left[\delta_{1n}\frac{0.5CEdx}{R}+\frac{\delta_{1n}0.5CWdx}{R}\right]=v_{E_P}\left[\delta_{1n}\mu\frac{dy}{2R}\right]-v_{W_P}\left[\delta_{1n}\mu\frac{dy}{2R}\right]$$

From Mass Conservation:

$$v_{P_P}\left(\frac{\partial u}{\partial x}+\frac{\partial v}{\partial y}+\frac{\partial w}{Rd\theta}+\delta_{ln}\frac{u}{R}\right)=U$$

or

$$0=v_{P_P}\left\{CE-CW+CN-CS+CD-CU+\delta_{ln}\rho\frac{(u_{E_{PU}}+u_{SE_U}+u_{P_U}+u_{S_U})dxdy}{4R}\right\}Rd\theta$$

$$0=v_{P_P}Rd\theta\left\{CE-CW+CN-CS+\delta_{ln}0.5CE\frac{dx}{R}+\delta_{ln}0.5CW\frac{dx}{R}\right\}.$$

Then the coefficient of v_{P_P} becomes (after subtracting $\frac{\text{Cont. Eqn.}}{Rd\theta}$):

$$\left\{\left[\tfrac{1}{2}(-CE+CW-CN+CS)-\delta_{in}\,0.5CE\frac{dx}{R}-\delta_{ln}\,0.5CW\frac{dx}{R}\right]+DE+DW+DN+DS\right\}$$

or

$$v_{P_P}\left\{\hat{A}\hat{E}+\hat{A}\hat{W}+AN+AS+AU+SMP\right.$$

where

$$\hat{A}\hat{E}=\left(-\tfrac{1}{2}\hat{C}\hat{E}+DE\right)$$

$$\text{and } \hat{C}\hat{E}=CE\left\{1+\delta_{ln}\frac{dx}{R}\right\}$$

$$\hat{A}\hat{W}=\left(\tfrac{1}{2}CW+DW\right)$$

$$\text{and } \hat{C}\hat{W}=CW\left\{1-\delta_{ln}\frac{dx}{R}\right\}.$$

Use $\hat{A}\hat{E}$ and $\hat{A}\hat{W}$ with DE & DW for hybrid discretization.

II.

Let coefficient of v_{E_P} be: $A_E+\frac{\delta_{ln}\mu dy}{2R}$

v_{W_P} be: $A_W-\frac{\delta_{ln}\mu dy}{2R}$

Y Momentum Equation -Toroidal Coordinates: Viscous Terms

$$\frac{\partial\tau_{xy}}{\partial\phi}+\frac{\partial\tau_{yy}}{\partial y}+\left\{\frac{\partial\tau_{y\phi}}{R\partial\phi}\right\}+\frac{\tau_{xy}}{R}\ ;\ \text{they can be written:}$$

$$\mu\left[\frac{\partial^2 U_x}{\partial x \partial y}+\frac{\partial^2 U_y}{\partial x^2}+2\frac{\partial^2 U_y}{\partial y^2}+\left(\frac{1}{R}\frac{\partial U_x}{\partial y}+\frac{1}{R}\frac{\partial U_y}{\partial x}\right)+\left(\frac{\partial^2 U_\phi}{R\partial\phi\partial y}+\frac{\partial^2 U_y}{R^2\partial\phi^2}\right)\right] \quad \text{Eqn[Y-1]}$$

Note: $\frac{\partial}{\partial y}$ (Continuity Eqn.) is: $\frac{\partial^2 U_x}{\partial x \partial y}+\frac{\partial^2 U_y}{\partial y^2}+\frac{\partial^2 U_\phi}{R\partial\phi dy}+\frac{\partial U_x}{R\partial y}=0.$ Eqn[Y-2]

subtracting Eqn [Y-2] from Eqn [Y-1] yields:

$$\mu\left[\frac{\partial^2 U_y}{\partial x^2}+\frac{\partial^2 U_y}{\partial y^2}+\frac{\partial^2 U_y}{R^2\partial\phi^2}+\frac{1}{R}\frac{\partial U_y}{\partial x}\right].$$

Thus the Y Momentum Equation becomes:

$$\rho\left(U_x\frac{\partial U_y}{\partial x}+U_y\frac{\partial U_y}{\partial y}+\frac{U_\phi}{R}\frac{\partial U_y}{\partial\phi}\right)=-\frac{\partial p}{\partial y}+\mu\left[\frac{\partial^2 U_y}{\partial x^2}+\frac{\partial^2 U_y}{\partial y^2}+\frac{\partial^2 U_y}{R^2\partial\phi^2}+\frac{1}{R}\frac{\partial U_y}{\partial x}\right]+\rho g_y$$

Y Momentum Equation: In Cartesian Coordinates

$$\frac{\partial(\rho uv)}{\partial x}+\frac{\partial(\rho v^2)}{\partial y}+\frac{\partial(\rho vw)}{\partial z}=-\frac{\partial p}{\partial y}+\frac{\partial\tau_{xy}}{\partial x}+\frac{\partial\tau_{yy}}{\partial y}+\frac{\partial\tau_{zy}}{\partial z}.$$

Note: $\tau_{xy}=\mu\left(\frac{\partial\mu}{\partial y}+\frac{\partial v}{\partial x}\right)$

$$\tau_{yy}=2\mu\frac{\partial v}{\partial y}$$

$$\tau_{zy}=\mu\left(\frac{\partial w}{\partial y}+\frac{\partial v}{\partial z}\right)$$

so viscous stresses become:

$$\mu\frac{\partial}{\partial x}\left(\frac{\partial u}{\partial y}\right)+\mu\frac{\partial^2 v}{\partial x^2}+2\mu\frac{\partial^2 v}{\partial y^2}+\mu\frac{\partial}{\partial z}\left(\frac{\partial w}{\partial y}\right)+\mu\frac{\partial^2 v}{\partial z^2}$$

$$\mu\frac{\partial}{\partial y}\underbrace{\left\{\frac{\partial u}{\partial x}+\frac{\partial v}{\partial y}\frac{\partial w}{\partial z}\right\}}_{=0 \text{ if incompressible}}$$

Hence RHS becomes

$$-\frac{\partial p}{\partial y}+\mu\frac{\partial^2 v}{\partial x^2}+\frac{\partial^2 v}{\partial y^2}$$

Divide Momentum Equation by dz to get:

$$\left\{\left(\frac{\rho u_{E_U}+\rho u_{SEU}}{2}\right)\left(\frac{v_{P_P}+v_{E_P}}{2\Delta x_E}\right)-\left(\frac{\rho u_{P_U}+\rho u_{S_U}}{2}\right)\left(\frac{v_{P_P}+v_{W_P}}{2\Delta x_P}\right)\delta y\delta x\right\}$$

$$+\left\{\left(\frac{\rho v_{P_U}+\rho v_{NU}}{2}\right)\left(\frac{v_{P_P}+v_{N_P}}{2}\right)-\left(\frac{\rho v_{P_U}+\rho v_{S_U}}{2}\right)\left(\frac{v_{P_P}+v_{S_P}}{2}\right)\right\}\delta x$$

$$+\left\{\left(\frac{\rho w_{P_U}+\rho w_{S_U}}{2}\right)\left(\frac{v_{P_P}+v_{P_D}}{2}\right)-\left(\frac{\rho w_{P_U}+\rho w_{S_U}}{2}\right)\left(\frac{v_{P_U}+v_{P_P}}{2}\right)\right\}\delta x$$

$$=-(P_P-P_S)\delta x+\mu\left[\frac{(v_{E_P}-v_{P_P})}{\frac{1}{2}(\delta x+\delta x_E)}-\frac{(v_{P_P}-v_{W_P})}{\frac{1}{2}(\delta x+\delta x_W)}\right]\delta y$$

$$+\mu\left[\frac{(v_{N_P}-v_{P_P})}{\frac{1}{2}(\delta y_P+\delta y_N)}-\frac{(v_{P_P}-v_{S_P})}{\frac{1}{2}(\delta y_P+\delta y_S)}\right]\delta x$$

Hence:

$$v_{P_P}\left\{\left(\frac{\rho u_{E_U}+\rho u_{SEU}}{4}\right)\delta y-\left(\frac{\rho u_{P_U}+\rho u_{S_U}}{4}\right)\delta y+\left(\frac{\rho v_{P_U}+\rho v_{N_U}}{4}\right)\delta x\right.$$
$$-\left(\frac{\rho v_{P_U}+\rho v_{S_U}}{4}\right)\delta x+\left(\frac{\rho w_{P_U}+\rho w_{S_U}}{2}\right)\frac{\delta x\delta y}{\delta z}+\frac{\mu\delta y}{\frac{1}{2}(\delta x+\delta x_E)}$$
$$\left.+\frac{\mu\delta y}{\frac{1}{2}(\delta x+\delta x_W)}+\frac{\mu\delta x}{\frac{1}{2}(\delta y_P+\delta y_N)}+\frac{\mu\delta x}{\frac{1}{2}(\delta y_P+\delta y_S)}\right\}=-(P_P-P_S)\delta x$$

$$+v_{E_P}\left\{-\left(\frac{\rho u_{E_U}+\rho u_{SE_U}}{4}\right)\delta y+\frac{\mu\delta y}{\frac{1}{2}(\delta x+\delta x_E)}\right\}$$

$$+v_{W_P}\left\{\left(\frac{\rho u_{P_U}+\rho u_{S_U}}{4}\right)\delta y+\frac{\mu\delta y}{\frac{1}{2}(\delta x+\delta x_W)}\right\}$$

$$+v_{N_P}\left\{-\left(\frac{\rho v_{P_U}+\rho v_{N_U}}{2}\right)\delta x+\frac{\mu\delta x}{\frac{1}{2}(\delta y_P+\delta y_N)}\right\}$$

$$+v_{S_P}\left\{\left(\frac{\rho v_{P_U}+\rho v_{S_U}}{2}\right)\delta x+\frac{\mu\delta x}{\frac{1}{2}(\delta y_P+\delta y_S)}\right\}$$

$$-v_{P_U}\left\{\left(\frac{\rho w_{P_U}+\rho w_{S_U}}{2}\right)\frac{\delta x\delta y}{\partial z}\right\}$$

DEFINE:

$$DN=\frac{\mu dx}{\frac{1}{2}(\Delta y_P+\Delta y_N)} \qquad DE=\frac{\mu dy}{\frac{1}{2}(\Delta x_P+\Delta x_E)}$$

$$DS=\frac{\mu dx}{\frac{1}{2}(\Delta y_P+\Delta y_S)} \qquad DW=\frac{\mu dy}{\frac{1}{2}(\Delta x_P+\Delta x_W)}$$

$$GN=\rho v_{N_U} \qquad CN=0.5(GN+GP)\delta x$$

$$GS=\rho v_{S_U} \qquad CS=0.5(GS+GP)\delta x$$

$$GP=\rho v_{P_U} \qquad CE=0.5(GE+GSE)\delta y$$

$$GE=\rho u_{E_U} \qquad CW=0.5(GW+GSW)\delta y$$

$$GSE=\rho u_{SE_U} \qquad CU=GU\frac{\delta x\delta y}{\delta z}$$

$$GW=\rho u_{P_U} \qquad GD=\frac{\rho w_{P_P}+\rho w_{S_P}}{2}$$

$$GSW=\rho u_{S_U} \qquad CD=GD\frac{\delta x\delta y}{\delta z}$$

$$GU = \frac{\rho w_{P_U} + \rho w_{SU}}{2}$$

Then the Y Momentum Equation becomes:

$$v_{P_P}\left\{\frac{1}{2}CE + DE - \frac{1}{2}CW + DW + \frac{1}{2}CN + DN - \frac{1}{2}CS + DS - CU\right\} =$$
$$-(P_P - P_S)fx + v_{E_P}\left\{-\frac{1}{2}CE + DE\right\} + v_{W_P}\left\{\frac{1}{2}CW + DW\right\}$$
$$+ v_{N_P}\left\{-\frac{1}{2}CN + DN\right\} + v_{S_P}\left\{\frac{1}{2}CS + DS\right\} + v_{P_V}CU$$

If we subtract (CE - CW + CN - CS + CD - CU) = 0 {by Continuity Equation} from the coefficient of v_{P_P} we get:

$$v_{P_P}\left\{-\frac{1}{2}CE + DE + \frac{1}{2}CW + DW - \frac{1}{2}CN + DN + \frac{1}{2}CS + DS + CU\right\} =$$
$$-(P_P - P_S)\delta x + v_{E_P}\left\{-\frac{1}{2}CE + DE\right\} + v_{W_P}\left\{\frac{1}{2}CW + DW\right\}$$
$$+ v_{N_P}\left\{-\frac{1}{2}CN + DN\right\} + v_{S_P}\left\{\frac{1}{2}CS + DS\right\} + v_{P_U}CU$$

Define:

$$AE = -\frac{1}{2}CE + DE$$
$$AW = \frac{1}{2}CW + DW$$
$$AN = -\frac{1}{2}CN + DN$$
$$AS = \frac{1}{2}CS + DS$$
$$AU = CU$$

Then the Momentum Equation becomes:

$$v_{P_P}\{AE + AW + AN + AS + AU\} = -(P_P - P_S)\delta x + v_{E_P}A_E + v_{W_P}A_W$$
$$+ v_{N_P}A_N + v_{S_P}A_S + v_{P_V}CU$$

Add $v_{P_P}SMP$ to the LHS
and $v_{P_V}SMP$ to the RHS

$$v_{P_P}\{AE + AW + AN + AS + AU + SMP\} = -(P_P - P_S)\delta x + v_{E_P}A_E + v_{W_P}A_W$$
$$+ v_{N_P}A_N + v_{S_P}A_S + v_{P_U}CU + SMP\,v_{P_U}$$

Define

$$A_P = AE + AW + AN + AS + AU + SMP$$

and

$$A'_E = \frac{A_E}{A_P}; \quad A'_W = \frac{A_W}{A_P}; \quad A'_S = \frac{A_S}{A_P}; \quad A'_N = \frac{A_N}{A_P}.$$

Then:

$$v_{P_P} = v_{E_P} A'_E + v_{W_P} A'_W + v_{N_P} A'_N + v_{S_P} A'_S + \frac{v_{P_U} CU}{A_P} + \frac{SMP}{A_P} v_{P_U} - (P_P - P_S)\frac{\delta x}{A_P}$$

Appendix IV: Pressure Correction Equation

DERIVATION: Use Momentum Eqns. plus Continuity Eqns. for the Two Phases:

Note: u {Continuity Eqn.} = $u\frac{\partial(\alpha u)}{\partial x}+u\frac{\partial(\alpha v)}{\partial y}+u\frac{\partial(\alpha w)}{R\partial\theta}+\delta_{ln}\frac{\alpha u}{R}=$

Hence:

$$\frac{\partial(\rho\alpha u^2)}{\partial x}+\frac{\partial(\rho\alpha uv)}{\partial y}+\frac{\partial(\rho\alpha uw)}{R\partial\phi}-\delta_{ln}\rho\frac{\alpha w^2}{R}+\delta_{ln}\rho\frac{\alpha u^2}{R}=-\frac{\partial p}{\partial x}+Viscous\ Terms$$

$$u'_{P_k}=-\frac{(\alpha_P+\alpha_W)}{2}D_u\left\{p'_{P_P}-p'_{W_P}\right\}\quad D_u=\frac{dy}{A_P^u};\quad A_P^u=\left(\frac{\partial_N+\partial_{NW}}{2}\right)A_N+\left(\frac{\partial_P+\alpha_{W_P}}{2}\right)A_S$$

$$+\left(\frac{\alpha_E+\alpha_P}{2}\right)A_E+\left(\frac{\alpha_W+\alpha_P}{2}\right)A_W$$

$$+\alpha_U A_U-SP$$

$$u'_{E_P}=-\frac{(\alpha_P+\alpha_E)}{2}D_u\left\{p'_{Ep}-p'_{Pp}\right\}$$

$$v'_{N_P}=-\frac{(\alpha_P+\alpha_W)}{2}D_v\left\{p'_{Np}-p'_{Pp}\right\}\qquad \text{where}\quad D_v=\frac{dx}{A_P^V}$$

$$v'_{P_P}=-\frac{(\alpha_P+\alpha_S)}{2}D_v\left\{p'_P-p'_S\right\}$$

$$w'_{P_P}=+\alpha_P D_W p'_P\qquad \text{where}\quad D_w=\frac{dx\,dy}{dz\,A_P^W}$$

$$w'_{P_U}=-\frac{(\alpha_P+\alpha_U)}{2}D_W p'_P$$

and $p=p^*+p'$

Substitute $u=u^*+u'$, etc., for the velocity into Continuity Equation. Also divide by $\overline{\rho}_k$:

$$O=\frac{\dot{m}^*_{P1}}{\overline{\rho}_1}-p'_P\left\{-C_xD_u\left(\frac{\rho_E+\rho_P}{2\overline{\rho}_1}\right)\left(\frac{\alpha_E+\alpha_P}{2}\right)^2_1-C_xD_u\left(\frac{\rho_W+\rho_P}{2\overline{\rho}_1}\right)\left(\frac{\alpha_W+\alpha_P}{2}\right)^2_1\right.$$

$$-C_yD_v\left(\frac{\rho_W+\rho_P}{2\overline{\rho}_1}\right)_1\left(\frac{\alpha_N+\alpha_P}{2}\right)^2_1-C_yD_v\left(\frac{\rho_S+\rho_P}{2\overline{\rho}_1}\right)_1\left(\frac{\alpha_S+\alpha_P}{2}\right)^2_1$$

$$+\frac{\delta_{ln}D_u\rho_P\alpha_p(\alpha_P+\alpha_W)dxdydz_i}{4R_P\overline{\rho}_1}-\frac{\alpha_P^2\rho_P}{\overline{\rho}_k}C_ZD_W$$

$$\left.-\left(\frac{\alpha_P+\alpha_U}{2}\right)^2\left(\frac{\rho_P+\rho_U}{2\overline{\rho}_1}\right)C_ZD_W-\frac{\delta_{ln}\rho_P\alpha_PD_u}{2R_P\overline{\rho}_1}\frac{(\alpha_P+\alpha_E)}{2}dxdydz_0\right\}$$

$$-p'_E\left\{C_xD_u\left(\frac{\rho_E+\rho_P}{2\overline{\rho}_1}\right)\left(\frac{\alpha_E+\alpha_P}{2}\right)^2_1+\frac{\delta_{ln}D_u\rho_P\alpha_p(\alpha_p+\alpha_E)dz_0dxdy}{4R_P\overline{\rho}_1}\right\}$$

$$-p'_W\left\{C_xD_u\left(\frac{\rho_W+\rho_P}{2\overline{\rho}_1}\right)\left(\frac{\alpha_W+\alpha_P}{2}\right)^2_1-\frac{\delta_{ln}D_u\rho_P\alpha_P(\alpha_P+\alpha_W)dz_idxdy}{4R_P\overline{\rho}_1}\right\}$$

$$-p'_N\left\{C_yD_v\left(\frac{\rho_N+\rho_P}{2\overline{\rho}_1}\right)\left(\frac{\alpha_N+\alpha_P}{2}\right)^2_1\right\}-p'_S\left\{C_yD_v\left(\frac{\rho_S+\rho_P}{2\overline{\rho}_1}\right)\left(\frac{\alpha_S+\alpha_P}{2}\right)^2_1\right\}$$

Add the same equation for the distributed phase (i.e., "2") to this equation to get the full equation for p′ and divide by dz_P:

$$O=\frac{\dot{m}_{P_1}{}^*}{\overline{\rho}_1dz_P}+\frac{\dot{m}_{P_2}{}^*}{\overline{\rho}_2dz_P}-p'_P\left[-\frac{C_X}{dz_P}\left\{D_u\left(\frac{\rho_E+\rho_P}{2\overline{\rho}_1}\right)\left(\frac{\alpha_E+\alpha_P}{2}\right)^2_1\right.\right.$$

$$+D_u\left(\frac{\rho_E+\rho_P}{2\overline{\rho}_2}\right)_2\left(\frac{\alpha_E+\alpha_P}{2}\right)^2_2+D_u\left(\frac{\rho_W+\rho_P}{2\overline{\rho}_1}\right)\left(\frac{\alpha_W+\alpha_P}{2}\right)^2_1$$

$$\left.+D_u\left(\frac{\rho_W+\rho_P}{2\overline{\rho}_2}\right)\left(\frac{\alpha_W+\alpha_P}{2}\right)^2_2\right\}$$

$$-\frac{C_y}{dz_P}+\left\{D_v\left(\frac{\rho_N+\rho_P}{2\overline{\rho}_1}\right)_1\left(\frac{\alpha_N+\alpha_P}{2}\right)^2_2+D_v\left(\frac{\rho_N+\rho_P}{2\overline{\rho}_2}\right)\left(\frac{\alpha_N+\alpha_P}{2}\right)^2\right.$$

$$+ D_v\left(\frac{\rho_S+\rho_P}{2\bar{\rho}_1}\right)_1\left(\frac{\alpha_S+\alpha_P}{2}\right)_1^2 + D_v\left(\frac{\rho_S+\rho_P}{2\bar{\rho}_2}\right)_2\left(\frac{\alpha_S+\alpha_P}{2}\right)_2^2\Bigg\}$$

$$-\frac{C_Z}{dz_P}\Bigg\{D_W\left(\frac{\rho_P}{\bar{\rho}_1}\right)_1\alpha_{P_1}^2 + D_W\left(\frac{\rho_P}{\bar{\rho}_2}\right)\alpha_{P_2}^2 + D_W\left(\frac{\rho_P+\rho_U}{2\bar{\rho}_1}\right)\left(\frac{\alpha_P+\alpha_U}{2}\right)_1^2$$

$$+D_W\left(\frac{\rho_P+\rho_U}{2\bar{\rho}_2}\right)\left(\frac{\alpha_P+\alpha_u}{2}\right)_2^2\Bigg\}$$

$$+\frac{\delta_{ln}D_u\rho_{P_1}\alpha_{P_1}(\alpha_P+\alpha_W)_1 dx\,dy\,dz_i}{4R_P\bar{\rho}_1 dz_P} + \frac{\delta_{ln}D_u\rho_{P_2}\alpha_{P_2}(\alpha_P+\alpha_W)_2 dx\,dy\,dz_i}{4R_P\bar{\rho}_2 dz_P}$$

$$-\frac{\delta_{ln}D_u\rho_{P_1}(\alpha_P+\alpha_E)_1 dx\,dy\,dz_o}{4R_P\bar{\rho}_1 dz_P} - \frac{\delta_{ln}D_u\rho_{P_2}(\alpha_P+\alpha_E)_2 dx\,dy\,dz_o}{4R_P\bar{\rho}_2 dz_P}$$

$$-p'_E\Bigg[\frac{C_X}{dz_P}\Bigg\{D_u\left(\frac{\rho_E+\rho_P}{2\bar{\rho}_1}\right)\left(\frac{\alpha_E+\alpha_P}{2}\right)_1^2 + D_u\left(\frac{\rho_E+\rho_P}{2\bar{\rho}_2}\right)_2\left(\frac{\alpha_E+\alpha_P}{2}\right)_2^2\Bigg\}$$

$$+\frac{\delta_{ln}D_u\rho_{P_1}\alpha_{P1}(\alpha_P+\alpha_E)_1 dx\,dy\,dz_o}{4R_P\bar{\rho}_1 dz_P} + \frac{\delta_{ln}D_u\rho_{P_2}\alpha_{P_2}(\alpha_P+\alpha_E)_2 dx\,dy\,dz_o}{4R_P\bar{\rho}_2 dz_P}$$

$$-p'_W\Bigg[\frac{C_X}{dz_P}\Bigg\{D_u\left(\frac{\rho_W+\rho_P}{2\bar{\rho}_1}\right)_1\left(\frac{\alpha_W+\alpha_P}{2}\right)_1^2 + D_u\left(\frac{\rho_W+\rho_P}{2\bar{\rho}_2}\right)\left(\frac{\alpha_W+\alpha_P}{2}\right)_2^2\Bigg\}$$

$$-\frac{\delta_{ln}D_u\rho_{P_1}\alpha_{P1}(\alpha_P+\alpha_W)_1 dx\,dy\,dz_i}{4R_P\bar{\rho}_1 dz_P} - \frac{\delta_{ln}D_u\rho_{P_2}\alpha_{P_2}(\alpha_P+\alpha_W)_2 dx\,dy\,dz_i}{4R_P\bar{\rho}_2 dz_P}\Bigg]$$

$$-p'_N\Bigg[\frac{C_y}{dz_P}\Bigg\{D_v\left(\frac{\rho_N+\rho_P}{2\bar{\rho}_1}\right)_1\left(\frac{\alpha_N+\alpha_P}{2}\right)_1^2 + D_v\left(\frac{\rho_N+\rho_P}{2\bar{\rho}_2}\right)_2\left(\frac{\alpha_N+\alpha_P}{2}\right)_2^2\Bigg\}\Bigg]$$

$$-p'_S\Bigg[\frac{C_y}{dz_P}\Bigg\{D_v\left(\frac{\rho_S+\rho_P}{2\bar{\rho}_1}\right)_1\left(\frac{\alpha_S+\alpha_P}{2}\right)_1^2 + D_v\left(\frac{\rho_S+\rho_P}{2\bar{\rho}_2}\right)\left(\frac{\alpha_S+\alpha_P}{2}\right)_2^2\Bigg\}\Bigg]$$

Note: This equation is of the form:

$$A_P p'_P = \underbrace{-\frac{\dot{m}^{\bullet}_{P_1}}{\overline{\rho}_1 dz} - \frac{\dot{m}^{\bullet}_{P_2}}{\overline{\rho}_2 dz}}_{S_U} + A_E p'_E + A_W p'_W + A_N p'_N + A_S p'_S$$

This PRESSURE CORRECTION EQUATION can be solved for p' 's and used to correct pressure and velocities.

Note:

$$\frac{\dot{m}_P{}^*}{dz_P} = \frac{dy}{dz_P}\left[(\alpha\rho u^*)_{out} dz_o - (\alpha\rho u^*)_{in} dz_i + \mathrm{dx}\left[(\alpha\rho \mathrm{v}^*)_{\mathrm{OUT}} - (\alpha\rho \mathrm{v}^*)_{\mathrm{IN}}\right]\right.$$

$$+\frac{dx\,\mathrm{dy}}{dz_P}\left[\alpha_P \rho_P w^{\bullet}_{P_P} - \alpha_U \rho_U w^{\bullet}_{P_U} + \frac{\delta_{\mathrm{In}} \alpha_P \left(u^{\bullet}_{E_P} + u^{\bullet}_{P_P}\right) \rho_P dx\,dy}{2R_P}\right.$$

$c_x = \Delta y \Delta z$

$c_y = \Delta x \Delta z$

$c_z = \Delta x \Delta y$

$D_u = \frac{\Delta y}{A_P^U}$ Note: A_P^u from Subroutine CALCU

$D_v = \frac{\Delta x}{A_P^v}$ A_P^v from Subroutine CALCV

$D_w = \frac{\Delta x \Delta y}{A_P^W \Delta z}$ A_P^w from Subroutine CALCW

Appendix V: Void Fraction Equation

Continuity equation for two-phase flow:

$$\frac{\partial(\rho_k\alpha_k u)}{\partial x}+\frac{\partial(\rho_k\alpha_k v)}{\partial y}+\frac{\partial(\rho_k\alpha_k w)}{R\partial\phi}+\delta_{1n}\frac{\rho_k\alpha_k u}{R}=0$$

where: k=1 is the continuous phase
2 is the distributed phase

Discretize to get:

$$\frac{dy}{dz}\left[\left(\frac{\rho_e+\rho_p}{2}\right)\left(\frac{\alpha_e+\alpha_p}{2}\right)u_{e_p}\left(\frac{dz_o+dz_p}{2}\right)-\left(\frac{\rho_w+\rho_p}{2}\right)\left(\frac{\alpha_w+\alpha_p}{2}\right)u_{p_p}\left(\frac{dz_i+dz_p}{2}\right)\right]$$

$$dx\left[\left(\frac{\rho_n+\rho_p}{2}\right)\left(\frac{\alpha_n+\alpha_p}{2}\right)v_{n_p}-\left(\frac{\rho_s+\rho_p}{2}\right)\left(\frac{\alpha_s+\alpha_p}{2}\right)v_{p_p}\right]+$$

$$\frac{dx\,dy}{dz}\left[(\rho_p\alpha_p w_p)-\left(\frac{\rho_u+\rho_p}{2}\right)\left(\frac{\alpha_u+\alpha_p}{2}\right)w_{p_u}\right]$$

$$+\delta_{1n}\rho_p\alpha_p\frac{\left(u_{e_p}+u_{p_p}\right)}{2R_p}dx\,dy=0$$

Subtract the equation for Phase 1 from the equation for Phase 2 and normalize by each phases's reference density:

$$\frac{dy}{dz}\left[\left(\frac{\rho_e+\rho_p}{2\bar{\rho}_2}\right)_2\left(\frac{\alpha_e+\alpha_p}{2}\right)_2 u_{e_{p_2}}\left(\frac{dz_o+dz_p}{2}\right)\left(\frac{\rho_w+\rho_p}{2\bar{\rho}_2}\right)_2\left(\frac{\alpha_w+\alpha_p}{2}\right)_2 u_{p_{p2}}\left(\frac{dz_i+dz_p}{2}\right)\right]$$

$$dx\left[\left(\frac{\rho_n+\rho_p}{2\bar{\rho}_2}\right)_2\left(\frac{\alpha_n+\alpha_p}{2}\right)_2 v_{n_{p_2}}-\left(\frac{\rho_s+\rho_p}{2\bar{\rho}_2}\right)_2\left(\frac{\alpha_s+\alpha_p}{2}\right)_2 v_{p_{p2}}\right]+$$

$$\frac{dx\,dy}{dz}\left[\left(\frac{\rho_p}{\bar{\rho}_2}\alpha_p w_p\right)_2-\left(\frac{\rho_u+\rho_p}{2\bar{\rho}_2}\right)_2\left(\frac{\alpha_u+\alpha_p}{2}\right)_2 w_{p_{u2}}\right]$$

$$+\delta_{1n}\frac{\rho_{p_2}}{\bar{\rho}_2}\alpha_{p_2}\frac{\left(u_{ep}+u_{pp}\right)_2}{2R_p}dx\,dy -$$

$$\frac{dy}{dz}\left[\left(\frac{\rho_e+\rho_p}{2\bar{\rho}_1}\right)_1\left(\frac{\alpha_e+\alpha_p}{2}\right)_1 u_{e_{p_1}}\left(\frac{dz_o+dz_p}{2}\right)-\left(\frac{\rho_w+\rho_p}{2\bar{\rho}_1}\right)_1\left(\frac{\alpha_w+\alpha_p}{2}\right)_1 u_{p_{p_1}}\left(\frac{dz_i+dz_p}{2}\right)\right]$$

$$-dx\left[\left(\frac{\rho_n+\rho_p}{2\bar{\rho}_1}\right)_1\left(\frac{\alpha_n+\alpha_p}{2}\right)_1 v_{n_{p_1}}-\left(\frac{\rho_s+\rho_p}{2\bar{\rho}_1}\right)_1\left(\frac{\alpha_s+\alpha_p}{2}\right)_1 v_{p_{p_1}}\right]+$$

$$\frac{dx\,dy}{dz}\left[\left(\frac{\rho_p}{\bar{\rho}_1}\alpha_p w_p\right)_1-\left(\frac{\rho_u+\rho_p}{2\bar{\rho}_1}\right)_1\left(\frac{\alpha_u+\alpha_p}{2}\right)_1 w_{p_{p_1}}\right]$$

$$+\delta_{1n}\frac{\rho_{p_1}}{\bar{\rho}_1}\alpha_{p_1}\frac{\left(u_{ep}+u_{pp}\right)_1}{2R_p}dx\,dy = 0$$

i) Substitute $\alpha_1 = 1 - \alpha_2$

ii) add $\alpha_{p_2}\left[\frac{-\text{"Modified" Continuity Eqn Phase 1}}{\bar{\rho}_1}+\frac{-\text{"Modified" Continuity Eqn Phase 1}}{\bar{\rho}_1}\right]$

"Modified" means that just for this step inside the multiplier of α_{p2} (which is A_P) it is assumed that $\alpha_{n2}=\alpha_{s2}=\alpha_{e2}=\alpha_{w2}=\alpha_{p2}$ for a given node

iii) on completion of the above and rearranging, the result is:

Define:

$$A_e = -\frac{dy}{dz}\left(\frac{dz_o+dz_p}{2}\right)\left\{\left(\frac{\rho_{e1}+\rho_{p1}}{2\bar{\rho}_1}\right)\frac{u_{ep1}}{2}+\left(\frac{\rho_{e2}+\rho_{p2}}{2\bar{\rho}_2}\right)\frac{u_{ep2}}{2}\right\}$$

$$A_w = +\frac{dy}{dz}\left(\frac{dz_i+dz_p}{2}\right)\left\{\left(\frac{\rho_{w1}+\rho_{p1}}{2\bar{\rho}_1}\right)\frac{u_{pp1}}{2}+\left(\frac{\rho_{w2}+\rho_{p2}}{2\bar{\rho}_2}\right)\frac{u_{p_{p2}}}{2}\right\}$$

$$A_n = -dx\left\{\left(\frac{\rho_{n1}+\rho_{p1}}{2\bar{\rho}_1}\right)\frac{v_{np1}}{2}+\left(\frac{\rho_{n2}+\rho_{p2}}{2\bar{\rho}_2}\right)\frac{v_{n_{p2}}}{2}\right\}$$

$$A_s = +dx\left\{\left(\frac{\rho_{s1}+\rho_{p1}}{2\bar{\rho}_1}\right)\frac{v_{pp1}}{2}+\left(\frac{\rho_{s2}+\rho_{p2}}{2\bar{\rho}_2}\right)\frac{v_{s_{p2}}}{2}\right\}$$

$$A_u = \frac{+dx\,dy}{dz_p}\left\{\left(\frac{\rho_{p1}+\rho_{u1}}{2\bar{\rho}_1}\right)\frac{w_{pu1}}{2}+\left(\frac{\rho_{p2}+\rho_{u2}}{2\bar{\rho}_2}\right)\frac{w_{p_{u2}}}{2}\right\}$$

$$A_p = A_e + A_w + A_n + A_s + A_u$$

Then the governing equation for the void fraction is:

$$\alpha_{p_2}A_p = \alpha_{e_2}A_e + \alpha_{e_2}A_e + \alpha_{e_2}A_e + \alpha_{e_2}A_e + \alpha_{e_2}A_e + S_{\alpha_2}$$

where :

$$S_{\alpha_2} = \frac{dy}{dz_p}\left[\left(\frac{\rho_e+\rho_p}{2\overline{\rho_1}}\right)u_{e_{p_1}}\left(\frac{dz_o+dz_p}{2}\right)-\left(\frac{\rho_w+\rho_p}{2\overline{\rho_1}}\right)u_{p_{p_1}}\left(\frac{dz_i+dz_p}{2}\right)\right]$$

$$+dx\left[\left(\frac{\rho_n+\rho_p}{2\overline{\rho_1}}\right)_1 v_{n_{p_1}}-\left(\frac{\rho_s+\rho_p}{2\overline{\rho_1}}\right)_1 v_{p_{p_1}}\right]$$

$$+\frac{dx\,dy}{dz_p}\left[\left(\frac{\rho_{p_1}}{\overline{\rho_1}}\right)_1 w_{p_{p_1}}-\left(\frac{\rho_u+\rho_p}{2\overline{\rho_1}}\right)_1 w_{p_{u_1}}\right]+$$

$$\delta_{1n}\frac{\rho_{p_1}}{\bar{\rho}_1}\frac{\left(u_{ep_1}+u_{pp_1}\right)}{2R_p}\,dx\,dy$$

Appendix VI: Turbulent Kinetic Energy in Toroidal Coordinates

Begin by Summing: $u'[U\,Mom]+v'[V\,Mom]+u'[W\,Mom]$

$$u'(u'+\overline{u})\frac{\partial(u'+\overline{u})}{\partial x} + u'(v'+\overline{v})\frac{\partial(u'+\overline{u})}{\partial y} + u'(w'+\overline{w})\frac{\partial(u'+\overline{u})}{R\partial\phi} - \frac{u'(w'+\overline{w})^2}{R}$$

$$= -\frac{u'}{\rho}\frac{\partial(p'+\overline{p})}{\partial x} + u'\frac{\mu}{\rho}\nabla^2(u'+\overline{u}) - \frac{\mu}{\rho}\frac{u'(u'+\overline{u})}{R^2}$$

$$-\frac{2\mu}{\rho}u'\frac{\partial(w'+\overline{w})}{R^2\partial\phi} \quad ;$$

$$v'(u'+\overline{u})\frac{\partial(v'+\overline{v})}{\partial x} + v'(v'+\overline{v})\frac{\partial(v'+\overline{v})}{\partial y} + v'\frac{(w'+\overline{w})}{R}\frac{\partial(v'+\overline{v})}{\partial\phi}$$

$$= -\frac{v'}{\rho}\frac{\partial(p'+\overline{p})}{\partial y} + v'\frac{\mu}{\rho}\nabla^2(v'+\overline{v}) \;;$$

$$w'(u'+\overline{u})\frac{\partial(w'+\overline{w})}{\partial x} + w'(v'+\overline{v})\frac{\partial(w'+\overline{w})}{\partial y} + \frac{w'(w'+\overline{w})}{R}\frac{\partial(w'+\overline{w})}{\partial\phi}$$

$$+\frac{w'(u'+\overline{u})(w'+\overline{w})}{R} = -\frac{w'}{\rho}\frac{\partial(p'+\overline{p})}{R\partial\phi} + w'\frac{\mu}{\rho}\nabla^2(w'+\overline{w})$$

$$+\frac{\mu}{\rho}w'\left[2\frac{\partial(u'+\overline{u})}{R^2\partial\phi} - \frac{(w'+\overline{w})}{R^2}\right] \;;$$

Note: $(u'+\overline{u})(w'+\overline{w}) = u'w' + u'\overline{w} + \overline{u}w' + \overline{u}\overline{w}$

and $\frac{w'}{R}(u'+\overline{u})(w'+\overline{w}) = \frac{u'w'^2}{R} + \frac{u'w'\overline{w}}{R} + \frac{\overline{u}w'^2}{R} + \frac{\overline{u}\overline{w}w'}{R}$

Collect Terms:

$$u'\overline{u}\frac{\partial\overline{u}}{\partial x} + u'^2\frac{\partial\overline{u}}{\partial x} + u'\overline{u}\frac{\partial u'}{\partial x} + u'^2\frac{\partial u'}{\partial x} +$$

$$u'\overline{v}\,\frac{\partial\overline{u}}{\partial y} + u'v'\,\frac{\partial\overline{u}}{\partial y} + u'\overline{v}\,\frac{\partial u'}{\partial y} + u'v'\,\frac{\partial u'}{\partial y} +$$

$$u'\overline{w}\,\frac{\partial\overline{u}}{R\partial\phi} + u'w'\,\frac{\partial\overline{u}}{R\partial\phi} + u'\overline{w}\,\frac{\partial u'}{R\partial\phi} + u'w'\,\frac{\partial u'}{R\partial\phi} - \frac{u'w'^2}{R} - \frac{u'\overline{w}^2}{R} - \frac{2u'w'\overline{w}}{R} +$$

$$v'\overline{u}\,\frac{\partial\overline{v}}{\partial x} + v'u'\,\frac{\partial\overline{v}}{\partial x} + v'\overline{u}\,\frac{\partial v'}{\partial x} + v'u'\,\frac{\partial v'}{\partial x} +$$

$$v'\overline{v}\,\frac{\partial\overline{v}}{\partial y} + v'^2\,\frac{\partial\overline{v}}{\partial y} + v'\overline{v}\,\frac{\partial v'}{\partial y} + v'^2\,\frac{\partial v'}{\partial y} +$$

$$v'\overline{w}\,\frac{\partial\overline{v}}{R\partial\phi} + v'w'\,\frac{\partial\overline{v}}{R\partial\phi} + v'\overline{w}\,\frac{\partial v'}{R\partial\phi} + v'w'\,\frac{\partial v'}{R\partial\phi} +$$

$$w'\overline{u}\,\frac{\partial\overline{w}}{\partial x} + w'u'\,\frac{\partial\overline{w}}{\partial x} + w'\overline{u}\,\frac{\partial w'}{\partial x} + w'u'\,\frac{\partial w'}{\partial x} +$$

$$w'\overline{v}\,\frac{\partial\overline{w}}{\partial y} + w'v'\,\frac{\partial\overline{w}}{\partial y} + w'\overline{v}\,\frac{\partial w'}{\partial y} + w'v'\,\frac{\partial w'}{\partial y}$$

$$w'\overline{w}\,\frac{\partial\overline{w}}{\partial z} + w'^2\,\frac{\partial\overline{w}}{\partial z} + w'\overline{w}\,\frac{\partial w'}{\partial z} + w'^2\,\frac{\partial w'}{\partial z} + \frac{w'^2u'}{R} + \frac{w'u'\overline{w}}{R} + \frac{w'^2\overline{u}}{R} + \frac{w'\overline{u}\overline{w}}{R} =$$

$$-\frac{u'}{\rho}\,\frac{\partial(\overline{p}+p')}{\partial x} - \frac{v'}{\rho}\,\frac{\partial(\overline{p}+p')}{\partial y} - \frac{w'}{\rho}\,\frac{\partial(\overline{p}+p')}{R\partial\phi} +$$

$$\nu\left\{u'\,\frac{\partial^2\overline{u}}{\partial x^2} + u'\,\frac{\partial^2u'}{\partial x^2} + u'\,\frac{\partial^2\overline{u}}{\partial y^2} + u'\,\frac{\partial^2u'}{\partial y^2} + \frac{u'\partial^2\overline{u}}{R^2\partial\phi^2} + u'\,\frac{\partial^2u'}{R^2\partial\phi^2} + u'\,\frac{\partial\overline{u}}{R\partial x} + \frac{u'\partial u'}{R\partial x}\right.$$

$$\left. - \frac{u'^2}{R^2} - \frac{u'\overline{u}}{R^2} - 2u'\,\frac{\partial w'}{R^2\partial\phi} - 2u'\,\frac{\partial\overline{w}}{R^2\partial\phi}\right\} +$$

$$\nu\left\{v'\,\frac{\partial^2\overline{v}}{\partial x^2} + v'\,\frac{\partial^2v'}{\partial x^2} + v'\,\frac{\partial^2\overline{v}}{\partial y^2} + v'\,\frac{\partial^2v'}{\partial y^2} + v'\,\frac{\partial^2\overline{v}}{R^2\partial\phi^2} + v'\,\frac{\partial^2v'}{R^2\partial\phi^2} + v'\,\frac{\partial\overline{v}}{R^2\partial\phi^2}\right.$$

$$\left. + v'\,\frac{\partial\overline{v}}{R\partial x} + \frac{v'\partial v'}{R\partial x}\right\}$$

$$\nu\left\{ w' \frac{\partial^2 \overline{w}}{\partial x^2} + w' \frac{\partial^2 w'}{\partial x^2} + w' \frac{\partial^2 \overline{w}}{\partial y^2} + w' \frac{\partial^2 w'}{\partial y^2} + w' \frac{\partial^2 \overline{w}}{R^2 \partial \phi^2} + \frac{w' \partial^2 \overline{w}}{R^2 \partial \phi^2} + \frac{w' \partial \overline{w}}{R \partial x} + \frac{w' \partial w'}{R \partial x} \right\}$$

Now Time Average:

$$\overline{u'^2} \frac{\partial \overline{u}}{\partial x} + \overline{\overline{u}\, u' \frac{\partial u'}{\partial x}} + \overline{u'^2 \frac{\partial u'}{\partial x}} + \overline{u'v'} \frac{\partial \overline{u}}{\partial y} + \overline{v}\, \overline{u' \frac{\partial u'}{\partial y}} + \overline{u'v' \frac{\partial u'}{\partial y}} +$$

$$\overline{u'w'} \frac{\partial \overline{u}}{R \partial \phi} + \overline{\overline{w}\, \overline{u' \frac{\partial u'}{R \partial \phi}}} + \overline{u'w' \frac{\partial u'}{R \partial \phi}} - \frac{\overline{u'w'^2}}{R} - 2\overline{w} \frac{\overline{u'w'}}{R} +$$

$$\overline{v'u'} \frac{\partial \overline{v}}{\partial x} + \overline{\overline{u}\, v' \frac{\partial v'}{\partial x}} + \overline{v'u' \frac{\partial v'}{\partial x}} + \overline{v'^2} \frac{\partial \overline{v}}{\partial y} + \overline{v}\, \overline{v' \frac{\partial v'}{\partial y}} + \overline{v'^2 \frac{\partial v'}{\partial y}} +$$

$$\overline{v'w'} \frac{\partial \overline{v}}{R \partial \phi} + \overline{\overline{w}\, \overline{v' \frac{\partial v'}{R \partial \phi}}} + \overline{v'w' \frac{\partial v'}{R \partial \phi}}$$

$$\overline{w'u'} \frac{\partial \overline{w}}{\partial x} + \overline{\overline{u}\, w' \frac{\partial w'}{\partial x}} + \overline{w'u' \frac{\partial w'}{\partial x}} + \overline{w'v'} \frac{\partial \overline{w}}{\partial y} + \overline{v}\, \overline{w' \frac{\partial w'}{\partial y}} + \overline{w'v' \frac{\partial w'}{\partial y}}$$

$$\overline{w'} \frac{\partial \overline{w}}{R \partial \phi} + \overline{\overline{w}\, \overline{w' \frac{\partial w'}{R \partial \phi}}} + \overline{w'^2 \frac{\partial w'}{R \partial \phi}} + \frac{\overline{w'^2 u'}}{R} + \overline{w} \frac{\overline{w'u'}}{R} + \overline{u} \frac{\overline{w'^2}}{R} =$$

$$-\frac{\overline{u'} \frac{\partial p'}{\partial x}}{\rho} - \frac{\overline{v'} \frac{\partial p'}{\partial y}}{\rho} - \frac{\overline{w'} \frac{\partial p'}{\partial z}}{\rho}$$

$$+ \nu \left\{ \overline{u' \frac{\partial^2 u'}{\partial x^2}} + \overline{u' \frac{\partial^2 u'}{\partial y^2}} + \overline{u' \frac{\partial^2 u'}{R^2 \partial \phi^2}} + \overline{v' \frac{\partial^2 v'}{\partial x^2}} + \overline{v' \frac{\partial^2 v'}{\partial y^2}} + \overline{v' \frac{\partial^2 v'}{R^2 \partial \phi^2}} \right.$$

$$\left. + \overline{w' \frac{\partial^2 w'}{\partial x^2}} + \overline{w' \frac{\partial^2 w'}{\partial y^2}} + \overline{w' \frac{\partial^2 w'}{R^2 \partial \phi^2}} \right.$$

$$+\underline{\underline{\frac{\overline{u'\frac{\partial u'}{\partial x}}}{R}}} - \frac{\overline{u'^2}}{R} - 2\frac{\overline{u'\frac{\partial w'}{\partial \phi}}}{R^2} + \underline{\underline{\frac{\overline{v'\frac{\partial w'}{\partial x}}}{R}}} + \underline{\underline{\frac{\overline{w'\frac{\partial w'}{\partial x}}}{R}}}\Bigg\}$$

Define $k = \frac{1}{2}(u'^2 + v'^2 + w'^2)$

$$\frac{dk}{\partial v} = u'\frac{\partial u'}{\partial x} + v'\frac{\partial v'}{\partial x} + w'\frac{\partial w'}{\partial x}$$

Hence the 9 double underlined terms represent $\underline{\overline{V}} \bullet \frac{dk}{d\underline{x}}$

or the Advection of TKE

$$= u\frac{\partial k}{\partial x} + v\frac{\partial k}{\partial y} + w\frac{\partial k}{R\partial \phi}$$

Now, noting that the continuity equation is:

$$\frac{\partial u}{\partial x} + \frac{\partial v}{\partial y} + \frac{\partial w}{R\partial \phi} + \frac{u}{R} = 0$$

and gathering the inviscid triple correlations:

$$\underline{\underline{u'^2\frac{\partial u'}{\partial x}}} + \underline{u'v'\frac{\partial u'}{\partial y}} + u'w'\frac{\partial u'}{R\partial \phi} - \frac{u'w'^2}{R} + \underline{\underline{v'u'\frac{\partial v'}{\partial x}}} + \underline{v'^2\frac{\partial v'}{\partial y}}$$

$$+ v'w'\frac{\partial v'}{R\partial \phi} + \underline{\underline{w'u'\frac{\partial w'}{\partial x}}} + \underline{w'v'\frac{\partial w'}{\partial y}} + w'^2\frac{\partial w'}{R\partial \phi} + \frac{w'^2u'}{R}$$

Add to these above terms the following terms {which=0}

$$\frac{u'^2}{2}\left(\underline{\underline{\frac{\partial u'}{\partial x}}} + \underline{\frac{\partial v'}{\partial y}} + \frac{\partial w'}{R\partial \phi} + \frac{u'}{R}\right)$$

$$+ \frac{v'^2}{2}\left(\underline{\underline{\frac{\partial u'}{\partial x}}} + \underline{\frac{\partial v'}{\partial y}} + \frac{\partial w'}{R\partial \phi} + \frac{u'}{R}\right.$$

$$+\frac{w'^2}{2}\left(\underline{\underline{\frac{\partial u'}{\partial x}}}+\underline{\frac{\partial v'}{\partial y}}+\frac{\partial w'}{R\partial\phi}+\frac{u'}{R}\right)$$

Note: $$\frac{\partial}{\partial x_i}\{u_j'k\}=\underbrace{\frac{\partial}{\partial x}\{u'k\}}_{I}+\underbrace{\frac{\partial}{\partial y}\{v'k\}}_{II}+\underbrace{\frac{\partial}{R\partial\phi}\{w'k}}_{III}$$

Consider the first term I:

$$\frac{\partial}{\partial x}\left\{u'\left[\frac{u'^2}{2}+\frac{v'^2}{2}+\frac{w'^2}{2}\right]\right\}=u'^2\frac{\partial u'}{\partial x}+\frac{u'^2}{2}\frac{\partial u'}{\partial x}+u'v'\frac{\partial v'}{\partial x}+\frac{v'^2}{2}\frac{\partial u'}{\partial x}$$
$$+u'w'\frac{\partial w'}{\partial x}+\frac{w'^2}{2}\frac{\partial u'}{\partial x}$$

Hence the 6 double underlined terms make up $\frac{\partial}{\partial x}\left\{u'\left[\frac{u'^2}{2}+\frac{v'^2}{2}+\frac{w'^2}{2}\right]\right\}$

and the single underlined terms make up $\frac{\partial}{\partial y}\{v'k\}$ [i.e. II] ; the same format is followed for $\frac{\partial}{R\partial\phi}\{w'k\}$

Therefore the inviscid triple correlations can be written as

$$\frac{\partial}{\partial x_i}\{u_i'k\}+\frac{u'}{2R}\left(u'^2+v'^2+w'^2\right)=\frac{\partial}{\partial x_i}\{u_i'k\}+\frac{u'k}{R}$$

and

$$\frac{\partial}{\partial x_i}\{u_i'k\}=\frac{\partial}{\partial x}\left\{\frac{\mu_t}{\sigma_k}\frac{\partial k}{\partial x}\right\}+\frac{\partial}{\partial y}\left\{\frac{\mu_t}{\sigma_k}\frac{\partial k}{\partial y}\right\}+\frac{\partial}{R\partial\phi}\left\{\frac{\mu_t}{\sigma_k}\frac{\partial k}{R\partial\phi}\right\}$$

and $$\frac{u'k}{R}=\frac{\mu_t}{R\sigma_k}\frac{\partial k}{\partial x}$$

by the same argument i.e., assume diffusive action of turbulence to be similar to molecular diffusion; the rate of transport of turb. energy is proportional to the spatial gradient of k: $u_i'k=\mu_t\nabla k$.

Bring these inviscid triple correlation tensors to RHS and combine with the pressure gradient terms to get

$$-\frac{\partial}{\partial x_i}\left[u_i'\left(k+\frac{p'}{\rho}\right)\right]$$ This is the convective diffusion of TKE.

Also take to RHS the terms:

$$\overline{u'^2}\frac{\partial\overline{u}}{\partial x} + \overline{u'v'}\frac{\partial\overline{u}}{\partial y} + \overline{u'w'}\frac{\partial\overline{u}}{R\partial\phi} + \overline{u'v'}\frac{\partial\overline{v}}{\partial x} + \overline{v'^2}\frac{\partial\overline{v}}{\partial y}$$

$$+ \overline{v'w'}\frac{\partial\overline{v}}{R\partial\phi} + \overline{w'u'}\frac{\partial\overline{w}}{\partial x} + \overline{w'v'}\frac{\partial\overline{w}}{\partial y} + \overline{w'^2}\frac{\partial\overline{w}}{R\partial\phi}$$

which on the RHS can be written as $$-\rho\ \overline{u_i'u_j'}\frac{\partial\overline{u}_j}{\partial x_i}$$

Therefore, remaining on LHS are:

$$-2\overline{w}\frac{\overline{u'w'}}{R} + \overline{w}\frac{\overline{w'u'}}{R} + \overline{u}\frac{\overline{w'^2}}{R}$$

or

$$\overline{u}\frac{\overline{w'^2}}{R} - \overline{w}\frac{\overline{w'u'}}{R}$$

PRODUCTION OF TKE IN TOROIDAL COORDS

$$-\rho \left\{\overline{u'_i u'_j}\right\}\frac{\partial u_i}{\partial x_j} = \mu_t \left\{e_{ij}\right\}\frac{\partial u_i}{\partial x_j}$$

↑

Rate of Strain Tensor

$$2e_{xy} = \frac{\partial u}{\partial y} + \frac{\partial v}{\partial x} = -\frac{\rho\overline{u'_1 u'_2}}{\mu_t} \qquad 2e_{xx} = 2\frac{\partial u}{\partial x} = \frac{-\rho\overline{u'^2}}{\mu_t}$$

$$2e_{y\phi} = \frac{\partial v}{R\partial\phi} + \frac{\partial w}{\partial y} = -\frac{\rho\overline{u'_2 u'_3}}{\mu_t} \qquad 2e_{yy} = 2\frac{\partial v}{\partial y} = \frac{-\rho\overline{v'^2}}{\mu_t}$$

$$2e_{x\phi} = \frac{\partial w}{\partial x} + \frac{\partial u}{R\partial\phi} - \frac{w}{R} = -\frac{\rho\overline{u'_1 u'_3}}{\mu_t} \qquad 2e_{\phi\phi} = 2\left(\frac{\partial w}{R\partial\phi} + \frac{u}{R}\right) = \frac{-\rho\overline{v'^2}}{\mu_t}$$

We need 9 terms:

$$-\rho u_1 u_1 \frac{\partial u_1}{\partial x_1} + -\rho u_1 u_2 \frac{\partial u_1}{\partial x_2} + -\rho u_1 u_3 \frac{\partial u_1}{\partial x_3} +$$

$$-\rho u_2 u_1 \frac{\partial u_2}{\partial x_1} + -\rho u_2 u_2 \frac{\partial u_2}{\partial x_2} + -\rho u_2 u_3 \frac{\partial u_2}{\partial x_3} +$$

$$-\rho u_3 u_1 \frac{\partial u_3}{\partial x_1} + -\rho u_3 u_2 \frac{\partial u_3}{\partial x_2} + -\rho u_3 u_3 \frac{\partial u_3}{\partial x_3} +$$

where

$$\frac{\partial u_1}{\partial x_1} = \frac{\partial u}{\partial x}; \quad \frac{\partial u_1}{\partial x_2} = \frac{\partial u}{\partial y}; \quad \frac{\partial u_1}{\partial x_3} = \frac{\partial u}{R\partial\phi}$$

$$\frac{\partial u_2}{\partial x_1} = \frac{\partial v}{\partial x}; \quad \frac{\partial u_2}{\partial x_2} = \frac{\partial v}{\partial y}; \quad \frac{\partial u_2}{\partial x_3} = \frac{\partial v}{R\partial\phi}$$

$$\frac{\partial u_3}{\partial x_1} = \frac{\partial w}{\partial x}; \quad \frac{\partial u_3}{\partial x_2} = \frac{\partial w}{\partial y}; \quad \frac{\partial u_3}{\partial x_3} = \frac{\partial w}{R\partial\phi}$$

Thus $-\rho \left\{\overline{u'_i u'_j}\right\}\frac{\partial u_i}{\partial x_j}$ becomes:

$$2\left(\frac{\partial u}{\partial x}\right)^2 + \left(\frac{\partial u}{\partial y} + \frac{\partial v}{\partial x}\right)\frac{\partial u}{\partial y} + \left(\frac{\partial w}{\partial x} + \frac{\partial u}{R\partial\phi} - \frac{w}{R}\right)\frac{\partial u}{R\partial\phi} +$$

$$\left(\frac{\partial u}{\partial y} + \frac{\partial v}{\partial x}\right)\frac{\partial v}{\partial x} + 2\left(\frac{\partial v}{\partial y}\right)^2 + \left(\frac{\partial v}{R\partial\phi} + \frac{\partial w}{\partial y}\right)\frac{\partial v}{R\partial\phi} +$$

$$\left(\frac{\partial w}{\partial x} + \frac{\partial u}{R\partial\phi} - \frac{w}{R}\right)\frac{\partial w}{\partial x} + \left(\frac{\partial v}{R\partial\phi} + \frac{\partial w}{\partial y}\right)\frac{\partial w}{\partial y} + 2\left(\frac{\partial w}{R\partial\phi}\right)^2 + 2\frac{u}{R}\frac{\partial w}{R\partial\phi} =$$

$$2\left(\frac{\partial u}{\partial x}\right)^2 + 2\left(\frac{\partial v}{\partial y}\right)^2 + 2\left(\frac{\partial w}{R\partial\phi}\right)^2 + \left(\frac{\partial u}{\partial y}\right)^2 + \frac{\partial v}{\partial x}\frac{\partial u}{\partial y} + \frac{\partial w}{\partial x}\frac{\partial u}{R\partial\phi} + \left(\frac{\partial u}{R\partial\phi}\right)^2 - \frac{w\partial u}{R^2\partial\phi} +$$

$$\frac{\partial u}{\partial y}\frac{\partial v}{\partial x} + \left(\frac{\partial v}{\partial x}\right)^2 + \left(\frac{\partial v}{R\partial\phi}\right)^2 + \frac{\partial w}{\partial y}\frac{\partial v}{R\partial\phi} + \left(\frac{\partial w}{\partial x}\right)^2 + \frac{\partial u}{R\partial\phi}\frac{\partial w}{\partial x} - \frac{w}{R}\frac{\partial w}{\partial x}$$

$$+ \frac{\partial v}{R\partial\phi}\frac{\partial w}{\partial y} + \left(\frac{\partial w}{\partial y}\right)^2 + 2\frac{u}{R^2}\frac{\partial w}{\partial\phi} = \{\text{Neglecting terms with } \frac{\partial}{\partial\phi} \text{ for Partially Parb.}\}$$

$$= 2\left\{\left(\frac{\partial u}{\partial x}\right)^2 + \left(\frac{\partial v}{\partial y}\right)^2 + \left(\frac{\partial w}{R\partial\phi}\right)^2\right\} + \underbrace{\left(\frac{\partial u}{\partial y} + \frac{\partial v}{\partial x}\right)^2}_{\left(\frac{\partial u}{\partial y}\right)^2 + 2\frac{\partial u}{\partial y}\frac{\partial v}{\partial x} + \frac{\partial v^2}{\partial x}} + \left(\frac{\partial w}{\partial x}\right)^2 - \frac{w}{R}\frac{\partial w}{\partial x} + \left(\frac{\partial w}{\partial y}\right)^2$$

$$= 2\left\{\left(\frac{\partial u}{\partial x}\right)^2 + \left(\frac{\partial v}{\partial y}\right)^2\right\} + \left(\frac{\partial u}{\partial y} + \frac{\partial v}{\partial x}\right)^2 + \left(\frac{\partial w}{\partial y}\right)^2 + \left(\frac{\partial w}{\partial x}\right)^2 - \frac{w}{R}\frac{\partial w}{\partial x} \quad [A]$$

Plus the terms bring to RHS - $\left(-\bar{w}\frac{\overline{w'u'}}{R} + \bar{u}\frac{\overline{w'^2}}{R}\right) = -\left(\bar{w}\left(\frac{\overline{w'u'}}{R}\right) - \bar{u}\left(\frac{\overline{-w'^2}}{R}\right)\right)$

These 2 terms equal:

$$-\frac{w}{R}\left\{\frac{\partial w}{\partial x}+\frac{\partial u}{R\partial\phi}-\frac{w}{R}\right\}+\frac{u}{R}\left\{2\frac{\partial w}{R\partial\phi}+2\frac{u}{R}\right\}$$

and on neglecting $\frac{\partial}{R\partial\phi}$ terms:

$$-\frac{w}{R}\frac{\partial w}{\partial x}+\frac{w^2}{R^2}+2\frac{u^2}{R^2}$$

Adding these terms to line [A] gives

$$\text{Production of TKE} = \mu_t\left[2\left\{\left(\frac{\partial u}{\partial x}\right)^2+\left(\frac{\partial v}{\partial y}\right)^2\right\}+\left(\frac{\partial u}{\partial y}+\frac{\partial v}{\partial x}\right)^2+\left(\frac{\partial w}{\partial y}\right)^2+\left(\frac{\partial w}{\partial x}\right)^2\right.$$

$$\left.-2\frac{w}{R}\frac{\partial w}{\partial x}+\frac{w^2}{R^2}+2\frac{u^2}{R^2}\right]\equiv G$$

Note: u,v,w are mainflow time averaged quantities.

[Note, error in Pratap/Spalding paper]

$$\text{Addtl terms in G neglected by Pratap: } 2\left(\frac{\partial w}{R\partial\phi}\right)+\frac{\partial w}{\partial x}\frac{\partial u}{R\partial\phi}+\left(\frac{\partial u}{R\partial\phi}\right)^2-2w\frac{\partial u}{R^2\partial\phi}$$

$$+\left(\frac{\partial v}{R\partial\phi}\right)^2+\frac{\partial w}{\partial y}\frac{\partial v}{R\partial\phi}+\frac{\partial u}{R\partial\phi}\frac{\partial w}{\partial x}+\frac{\partial v}{R\partial\phi}\frac{\partial w}{\partial y}+4\frac{u}{R^2}\frac{\partial w}{\partial\phi}\ =$$

$$2\left(\frac{\partial w}{R\partial\phi}\right)^2+2\frac{\partial w}{\partial x}\frac{\partial u}{R\partial\phi}+\left(\frac{\partial u}{R\partial\phi}\right)^2+\left(\frac{\partial v}{R\partial\phi}\right)^2-2w\frac{\partial u}{R^2\partial\phi}+2\frac{\partial w}{\partial y}\frac{\partial v}{R\partial\phi}+4\frac{u}{R^2}\frac{\partial w}{\partial\phi}$$

VISCOUS TERMS

$$u'\frac{d^2u'}{\partial x^2} \; ; \qquad \frac{\partial}{\partial x}\left(u'\frac{du'}{dx}\right) = \left(\frac{\partial u}{\partial x}\right)^2 + u'\frac{\partial^2 u}{\partial x^2}$$

so that

$$u'\frac{\partial^2 u'}{\partial x^2} = \frac{\partial}{\partial x}\left(u'\frac{\partial u'}{\partial x}\right) - \left(\frac{\partial u'}{\partial x}\right)^2$$

$$u'\frac{\partial^2 u'}{\partial y^2} = \frac{\partial}{\partial y}\left(u'\frac{\partial u'}{\partial y}\right) - \left(\frac{\partial u'}{\partial y}\right)^2$$

$$u'\frac{\partial^2 u'}{R^2\partial\phi^2} = \frac{\partial}{R\partial\phi}\left(u'\frac{\partial u'}{R\partial\phi}\right) - \left(\frac{\partial u'}{R\partial\phi}\right)^2$$

$$v'\frac{\partial^2 v'}{\partial x^2} = \frac{\partial}{\partial x}\left(v'\frac{\partial v'}{\partial x}\right) - \left(\frac{\partial v'}{\partial x}\right)^2$$

$$v'\frac{\partial^2 v'}{\partial y^2} = \frac{\partial}{\partial y}\left(v'\frac{\partial v'}{\partial y}\right) - \left(\frac{\partial v'}{\partial y}\right)^2$$

$$v'\frac{\partial^2 v'}{R^2\partial\phi^2} = \frac{\partial}{R\partial\phi}\left(v\frac{\partial v'}{R\partial\phi}\right) - \left(\frac{\partial v'}{R\partial\phi}\right)^2$$

$$w'\frac{\partial^2 w'}{\partial x^2} = \frac{\partial}{\partial x}\left(w'\frac{\partial w'}{\partial x}\right) - \left(\frac{\partial w'}{\partial x}\right)^2$$

$$w'\frac{\partial^2 w'}{\partial y^2} = \frac{\partial}{\partial y}\left(w'\frac{\partial w'}{\partial y}\right) - \left(\frac{\partial w'}{\partial y}\right)^2$$

$$w'\frac{\partial^2 w'}{R^2\partial\phi^2} = \frac{\partial}{R\partial\phi}\left(w'\frac{\partial w}{R\partial\phi}\right) - \left(\frac{\partial w'}{R\partial\phi}\right)^2$$

Note $\frac{\partial k}{\partial x} = \frac{\partial}{\partial x}\left\{\frac{1}{2}\left(u'^2 + v'^2 + w'^2\right)\right\} = u'\frac{\partial u'}{\partial x} + v'\frac{\partial v'}{\partial x} + w'\frac{\partial w'}{\partial x}$

$\frac{\partial k}{\partial y} = \qquad\qquad = u'\frac{\partial u'}{\partial y} + v'\frac{\partial v'}{\partial y} + w'\frac{\partial w'}{\partial y}$

$\frac{\partial k}{R\partial\phi} = \qquad\qquad = u'\frac{\partial u'}{R\partial\phi} + v'\frac{\partial v'}{R\partial\phi} + w'\frac{\partial w'}{R\partial\phi}$

so that $\frac{\partial}{\partial x}\left(\frac{\partial k}{\partial x}\right) + \frac{\partial}{\partial y}\left(\frac{\partial k}{\partial y}\right) + \frac{\partial}{R\partial\phi}\left(\frac{\partial k}{R\partial\phi}\right) =$

$\frac{\partial}{\partial x}\left(u'\frac{\partial u'}{\partial x}\right) + \frac{\partial}{\partial x}\left(v'\frac{\partial v'}{\partial x}\right) + \frac{\partial}{\partial x}\left(w'\frac{\partial w'}{\partial x}\right) +$

$\frac{\partial}{\partial y}\left(u'\frac{\partial u'}{\partial y}\right) + \frac{\partial}{\partial y}\left(v'\frac{\partial v'}{\partial y}\right) + \frac{\partial}{\partial y}\left(w'\frac{\partial w'}{\partial y}\right) +$

$\frac{\partial}{R\partial\phi}\left(u'\frac{\partial u'}{R\partial\phi}\right) + \frac{\partial}{R\partial\phi}\left(v'\frac{\partial v'}{R\partial\phi}\right) + \frac{\partial}{R\partial\phi}\left(w'\frac{\partial w'}{R\partial\phi}\right)$

Thus the terms in _____ on pg 4 and page 1-D can be written:

$$\frac{1}{\rho}\left[\frac{\partial}{\partial x}\left(\mu_\ell\frac{\partial k}{\partial x}\right) + \frac{\partial}{\partial y}\left(\mu_\ell\frac{\partial k}{\partial y}\right) + \frac{\partial}{R\partial\phi}\left(\mu_\ell\frac{\partial k}{R\partial\phi}\right)\right]$$

ϵ: Dissipation

Note: $\frac{1}{R}\frac{\partial k}{\partial x} = \frac{1}{R}\left\{u'\frac{\partial u'}{\partial x} + v'\frac{\partial v'}{\partial x} + w'\frac{\partial w'}{\partial x}\right\}$

So that the circled terms on page 4 give:

$$\frac{\mu_\ell}{\rho}\ \frac{1}{R}\ \frac{\partial k}{\partial x}$$

Neglecting $u' \frac{\partial w'}{R\partial\phi}$ that leaves the terms:

$$-\frac{\mu_\ell}{\rho}\left\{\left(\frac{\partial u'}{\partial x}\right)^2+\frac{u'^2}{R^2}+\left(\frac{\partial u'}{\partial y}\right)^2+\left(\frac{\partial u'}{R\partial\phi}\right)^2\right.$$

$$+\left(\frac{\partial v'}{\partial x}\right)^2+\left(\frac{\partial v'}{\partial y}\right)^2+\left(\frac{\partial v'}{R\partial\phi}\right)^2$$

$$\left.+\left(\frac{\partial w'}{\partial x}\right)^2+\left(\frac{\partial w'}{\partial y}\right)^2+\left(\frac{\partial w'}{R\partial\phi}\right)^2\right\} \equiv -\epsilon$$

dissipation of tke

---

if $\Gamma_k \equiv \mu_\ell + \frac{\mu_t}{\sigma_k}$, the Transport Eqn for k is

$$\rho\left(u\frac{\partial k}{\partial x}+v\frac{\partial k}{\partial y}+w\frac{\partial k}{R\partial\phi}\right) \equiv \frac{\partial}{\partial x}\left(\Gamma_k\frac{\partial k}{\partial x}\right)+\frac{\partial}{\partial y}\left(\Gamma_k\frac{\partial k}{\partial y}\right) +\Gamma_k\frac{1}{R}\frac{\partial k}{\partial x}+G-\rho\epsilon$$

where:

$$G = \mu_t\left[2\left\{\left(\frac{\partial u}{\partial x}\right)^2+\left(\frac{\partial v}{\partial y}\right)^2\right\}+\left(\frac{\partial u}{\partial y}+\frac{\partial v}{\partial x}\right)^2+\left(\frac{\partial w}{\partial y}\right)^2+\left(\frac{\partial w}{\partial x}\right)^2-2\frac{w}{R}\frac{\partial w}{\partial x}+\frac{w^2}{R^2}+2\frac{u^2}{R^2}\right]$$

and

$$\epsilon\equiv\frac{\mu_\ell}{\rho}\left\{\left(\frac{\partial u'}{\partial x}\right)^2+\frac{u'^2}{R^2}+\left(\frac{\partial u'}{\partial y}\right)^2+\left(\frac{\partial u'}{R\partial\phi}\right)^2 +\left(\frac{\partial v'}{\partial x}\right)^2+\left(\frac{\partial v'}{\partial y}\right)^2+\left(\frac{\partial v'}{R\partial\phi}\right)^2\right.$$

$$\left.+\left(\frac{\partial w'}{\partial x}\right)^2+\left(\frac{\partial w'}{\partial y}\right)^2+\left(\frac{\partial w'}{R\partial\phi}\right)^2\right\}$$

Additional terms due to Interphase Momentum Exchange in the Momentum Equations--i.e. Source of Turbulence Modification due to Dispersed Phase

$$u_1'\left[CNST2*\left(u_1'+\bar{u}_1-u_2'-\bar{u}_2\right)\right]+$$

$$v_1'\left[CNST2*\left(v_1'+\bar{v}_1-v_2'-\bar{v}_2\right)\right]+$$

$$w_1'\left[CNST2*\left(w_1'+\bar{w}_1-w_2'-\bar{w}_2\right)\right.$$

where:

$$\text{CNST2} = \frac{\frac{3}{4}\alpha_2\rho_1 C_D \quad V_{rel}\,\Delta x\Delta y}{d_{bubble}}$$

where: C_D is the drag coefficient which is a function of duct Reynolds number

Now time average:

$$\text{CNST2}*\left\{\overline{\left[u_1'^2\right]}-\overline{u_1'u_2'}\right\}+\left\{\overline{\left[v_1'^2\right]}-\overline{v_1'v_2'}\right\}+\left\{\overline{\left[w_1'^2\right]}-\overline{w_1'w_2'}\right\}$$

$$= \underbrace{\text{CNST2}*2k}_{\text{terms I}} - \underbrace{\text{CNST2}*\left[\overline{u_1'u_2'}+\overline{v_1'v_2'}+\overline{w_1'w_2'}\right]}_{\text{terms II}}$$

According to Besnard et. al. (1991) the coupling between phases is usually small; hence, terms II are neglected in comparison to terms I

Appendix VII: Derivation of the Dissipation Transport Equation: ε

The Mean Momentum Equations (or Time Averaged Equations) can be written:

I) X direction

$$\rho\left(\underline{u}\bullet\nabla u_x-\frac{u_\phi'^2}{R}-\frac{u_\phi^2}{R}\right)=-\frac{\partial p}{\partial x}+\mu\nabla^2u_x-\frac{\partial\left(u_x'u_{x_i}'\right)}{\partial x_i}-\mu\frac{u_x}{R^2}-2\mu\frac{\partial u_\phi}{R^2\partial\phi}$$

II) Y Direction

$$\rho(\underline{u}\bullet\nabla u_y)=-\frac{\partial p}{\partial y}+\mu\nabla^2u_y$$

III) ϕ Direction

$$\rho\left(\underline{u}\bullet\nabla u_\phi+\frac{u_xu_\phi}{R}+\frac{u_x'u'_\phi}{R}\right)=-\frac{\partial p}{R\partial\phi}+\mu\nabla^2u_\phi-\frac{\partial\left(u_\phi'u_{x_i}'\right)}{\partial x_i}-\mu\frac{u_\phi}{R^2}+2\mu\frac{\partial u_\phi}{R^2\partial\phi}$$

{Note: $\nabla^2=\frac{\partial^2}{\partial x^2}+\frac{1}{R}\frac{\partial}{\partial x}+\frac{\partial^2}{\partial y^2}+\frac{\partial^2}{R^2\partial\phi^2}$ }

Note: the Instantaneous Equations can be written:

I) X Direction

$$\rho\left[\underline{u}\bullet\nabla u_x+\underline{u}'\bullet\nabla u_x+\underline{u}\bullet\nabla u_x'-\frac{u_\phi'^2}{R}-\frac{u_\phi^2}{R}-\frac{2u_\phi'u_\phi}{R}\right]=-\frac{\partial(p+p')}{\partial x}+\mu\nabla^2u_x$$

$$+\mu\nabla^2u_x'-\frac{\partial\left(u_x'u_{x_i}'\right)}{\partial x_i}-\mu\frac{\left(u_x+u_x'\right)}{R}-2\mu\frac{\partial\left(u_\phi+u_\phi'\right)}{R^2\partial\phi}$$

II) Y Direction

$$\rho\left[\underline{u}\bullet\nabla u_y+\underline{u}'\bullet\nabla u_y+\underline{u}\bullet\nabla u_y'\right]=-\frac{\partial(p+p')}{\partial y}+\mu\nabla^2 u_y+$$

$$\mu\nabla^2 u_y'-\frac{\partial\left(u_y'u_{y_i}'\right)}{\partial x_i}$$

III)ϕ Direction

$$\rho\left[\underline{u}\bullet\nabla u_\phi+\underline{u}'\bullet\nabla u_\phi+\underline{u}\bullet\nabla u_\phi'+\frac{u_x u_\phi}{R}+\frac{u_x'u_\phi'}{R}+\frac{u_x'u_\phi}{R}-\frac{u_\phi'u_x}{R}\right]=-\frac{\partial(p+p')}{R\partial\phi}$$

$$+\mu\nabla^2 u_{\phi+}\mu\nabla^2 u_\phi'-\frac{\partial\left(u_\phi'u_{x_i}'\right)}{\partial x_i}+2\mu\frac{\partial u_\phi}{R^2\partial\phi}+2\mu\frac{\partial u_\phi'}{R^2\partial\phi}-\mu\frac{u_\phi}{R}-\mu\frac{u_\phi'}{R}$$

From the Instantaneous Equations Subtract the Time Averaged Equations:

I) X Equation

$$\rho\left[\underline{u}'\bullet\nabla u_x+\underline{u}\bullet\nabla u_x'-2\frac{u_\phi'u_\phi}{R}\right]=-\frac{\partial p'}{\partial x}+\mu\nabla^2 u_x'-\frac{\mu u_x'}{R}-\frac{2\mu\partial u_\phi'}{R\partial\phi}$$

II) Y Equation

$$\rho\left[\underline{u}'\bullet\nabla u_y+\underline{u}\bullet\nabla u_y'\right]=-\frac{\partial p'}{\partial y}+\mu\nabla^2 u'$$

III) ϕ Equation

$$\rho\left[\underline{u}'\bullet\nabla u_\phi+\underline{u}\bullet\nabla u_\phi'+\frac{u_x'u_\phi}{R}+\frac{u_\phi'u_x}{R}\right]=-\frac{\partial p'}{R\partial\phi}+\mu\nabla^2 u_\phi'+2\mu\frac{\partial u_\phi'}{R\partial\phi}-\mu\frac{u_\phi'}{R}$$

Differentiate the three equations above with respect $x_l\left\{i.e.,\frac{\partial}{\partial x}+\frac{\partial}{\partial y}+\frac{\partial}{R\partial\phi}\right\}$

where l =1,2,3

and multiply by $\mu\frac{\partial u_i'}{\partial x_m}$ where m =1,2,3

Add the three resulting equations.

After considerable algebraic manipulation it can be shown that the transport equation for ε in toroidal coordinates reduces to:

$$\rho\left(u_x\frac{\partial\varepsilon}{\partial x}+u_y\frac{\partial\varepsilon}{\partial y}+u_\phi\frac{\partial\varepsilon}{R\partial\phi}\right)=\frac{\partial\left(\Gamma_\varepsilon\frac{\partial\varepsilon}{\partial x}\right)}{\partial x}+\frac{\partial\left(\Gamma_\varepsilon\frac{\partial\varepsilon}{\partial y}\right)}{\partial y}+\Gamma_\varepsilon\frac{\partial\varepsilon}{R\partial x}$$

$$+C_1\frac{\varepsilon}{k}G-C_2\frac{\rho\varepsilon^2}{k}$$

where is G is the production of turbulent kinetic energy. Its form here is consistent with that dervied in tht transport equation for turbulent kinetic energy.

Vita

Edward Graf was born in Philadelphia, Pennsylvania on May 26, 1950. He was graduated from Father Judge High School in Philadelphia, Pennsylvania on June 1968.

He was graduated from University of Pennsylvania in 1972 with a Bachelor of Science Degree in Mechanical Engineering. He was graduated from California Institute of Technology in 1973 with a Master of Science in Mechanical Engineering.

From 1973 through 1976 he was employed in the Westinghouse Thermodynamics Development Section of the Large Steam Turbine Division. Between 1973 and 1981 he was a Senior Engineer at Westinghouse Marine Division. Mr. Graf worked in the Aerodynamics Development Section of the Ingersoll-Rand Corporation between 1981 and 1987. Between 1987 and the present he has been employed as a Senior Engineering Consultant in the Research and Development Group of Ingersoll-Dresser Pumps.

Mr. Graf has published fifteen technical articles in ASME journals, Pumping Symposiums and NASA publications in the area of turbomachinery, computational fluid dynamics and cavitation.